Université Pierre et Marie Curie (ParisVI)
Ecole Doctorale de Physique Quantique de la reg. parisiènne
LKB

*pour obtenir le titre de Docteur de l'Université ParisVI*

Università degli Studi di Firenze
Facoltà di Scienze Matematiche Fisiche e Naturali
LENS

*Tesi di Dottorato in Fisica - ciclo XXIII*

# Coherent manipulation of the internal state of an atomic gas: from atomic memories to atomic interferometers

***Pietro Ernesto Lombardi***

| | |
|---|---|
| Mme Elisabeth Giacobino | **directeur de thèse** |
| M. Francesco Saverio Cataliotti | **examinateur** |
| M. Francesco Marin | **directeur de thèse** |
| Mme Laurence Pruvost | **rapporteur** |
| M. Maurizio Artoni | **rapporteur** |
| Mme Agnès Maitre | **examinateur** |

# Abstract

This thesis work is dedicated to the exploration of coherent methods for the manipulation of atomic internal states. The final aim is to create a robust scheme for the realization of a quantum memory capable of storing the quantum state of a light pulse in an atomic spin state superposition.

I have explored two very different experimental realizations, both based on electromagnetically induced transparency in a three level $\Lambda$ scheme. The first realization was based on Zeeman sub-levels of Cesium atoms in a room temperature cell. This experiment was realized in the *groupe d'optique quantique* of Elisabeth Giacobino at LKB.

In this experiment we characterized a memory based on the $D2$ line of $^{133}Cs$. In the presence of Doppler broadening the $EIT$ effect is strongly reduced due to the presence of adjacent transitions. We theoretically developed a model to describe the optical response of the complete system including off-resonant transitions and integrating over atoms belonging to different velocity classes. We then experimentally verified the model and found a method to enhance the transparency based on velocity selective optical pumping. These results are very promising for the realization of a robust quantum memory and constitute a general recipe for the enhancement of $EIT$ in inhomogeneously broadened media.

The second realization was instead based on hyperfine states of ultracold Rubidium atoms held in a magnetic microtrap. This experiment was realized in the group of Francesco S. Cataliotti at the European laboratory for non-linear spectroscopy (LENS) in Firenze. In this experiment we found the optimal regime for trapping to mode match the atomic cloud to the light pulse in order to maximize the interaction. We then observed a strong reduction (almost 6 orders of magnitude) in the speed of light within the atomic sample, a promising step towards the realization of coherent information storage. Finally we developed a method to measure the relative phase of light pulses using atomic interferometry. These findings open an interesting alternative route for the detection of quantum coherences and non-classical states.

# Resumé

Ce travail de thèse est dédié á l'exploration de méthodes pour la manipulation cohérente des variables internes d'un ensemble d'atomes. L'objectif final est de créer une procédure pour la réalisation d'une mémoire quantique capable de stocker l'état quantique d'une impulsion lumineuse dans une superposition d'états de spin atomique.

J'ai exploré deux réalisations expérimentales très différentes, toutes deux basées sur la transparence induite électromagnétiquement ($EIT$) dans un schema atomique à trois niveaux en configuration $\Lambda$. La première réalisation a été basée sur des sous-niveaux Zeeman des atomes de Césium dans une cellule à température ambiante. Cette expérience a été réalisée dans le *groupe d'optique quantique* d'Elisabeth Giacobino au LKB.

Dans le cadre de cette expérience, nous avons caractérisé une mémoire basée sur la raie $D2$ du $^{133}Cs$. En présence de l'élargissement Doppler l'effet $EIT$ est fortement réduit en raison de la présence de transitions adjacentes. Nous avons développé un modèle théorique pour décrire la réponse optique du système atomique comprenant les transitions hors résonance, et moyennée sur les réponses des atomes appartenant à des classes de vitesse différentes. Nous avons ensuite vérifié expérimentalement le modèle, qui a aussi permis de trouver une méthode, basée sur un pompage optique sélectif en vitesse, pour améliorer la transparence. Ces résultats sont une étape fondamentale dans la direction d'une mémoire quantique robuste, et constituent une méthode générale pour l'amélioration de l'$EIT$ dans les milieux qui présentent un élargissement inhomogène.

La seconde réalisation a été basée sur une cohérence entre états hyperfins d'atomes de Rubidium ultrafroids piegié dans une micropiège magnétique. Cette expérience a été réalisée dans le groupe de Francesco S. Cataliotti au laboratoire européen pour la spectroscopie non-linéaire (LENS) à Firenze. Dans cette expérience on a trouvé tout d'abord le régime optimal de piégeage pour maximiser l'interaction entre le nuage atomique et le mode du champ de l'impulsion de lumière à stocker. Nous avons observé une forte réduction (près de 6 ordres de grandeur) de la vitesse de la lumière au sein de l'ensemble atomique, ce qui est une étape prometteuse vers la réalisation du stockage cohérent de l'information contenue dans une impulsion de lumière. Enfin, nous avons développé une méthode pour mesurer la phase relative

d'impulsions lumineuses co-propagatives à l'aide d'interférométrie atomique. Ces résultats ouvrent une voie alternative intéressante pour la détection des cohérences quantiques et d'états atomiques non-classiques.

# Contents

# Introduction

My PhD work has been done in the framework of a collaboration between two laboratories with expertise in different but complementary fields:
- on the one hand the *groupe d'optique quantique* of Elisabeth Giacobino at LKB, which focuses on continous variables quantum optics;
- on the other hand, the *quantum gases group* of M.Inguscio at LENS, which is expert in production and manipulation of ultracold and degenerate atomic clouds.
The aim of the collaboration being the promotion of continous variables quantum memory experiments with ultacold gases, I spent a first part of the doctorate in Paris, to get the know-how developed at LKB about quantum memories (applied there to warm gases); then a second part in Firenze, to implement a similar experiment in one of the degenerate samples available at Lens.

When I joined the group of E. Giacobino in March 2008, a set-up to store and release a coherent pulse of light without adding noise in a $40^oC$ cell of Cesium atoms was already running; details about its implementation can be found in the PhD thesis of former students J.Cviklinki [20] and J.Ortalo [91]. The period of my stay was devoted to the exploration of the limits and optimization of this set-up, in collaboration with two PhD students: J.Ortalo and M.Scherman. My activity in the laboratory was always in close relationship with their one, and what I report here is a sort of "bridge" between their thesis ([91], [103]).
The principal aim of the work has been to understand the fundamental mechanism responsible for the weak $EIT$ effect attainable on the D2 line of alkali atoms (in our case $^{133}Cs$) in the presence of inhomogeneous broadening. For this we have theoretically defined a model that takes into account the multiple excited levels of the line and identifies the influence of each of them on the $EIT$ [83]). It has been concluded that some particular velocity classes of atoms are responsible for the loss of

the collective induced transparency response. We then have proposed an original method that permits to restore the transparency by velocity distribution shaping, which is generally applicable to inhomogeneously broadened media. The validity of the method has been experimentally demonstrated for our system, the measured increase of transparency matching the value estimated by a simulation based on the model ([104]).

When I returned to Firenze in September 2009, I joined the group of F.S.Cataliotti, which was at that time involved in restructuring their set-up for condensation of $^{87}Rb$. Therefore, while working on the specific system for the generation of light beams for memory experiments, I also had the opportunity to participate in the setting up of the vacuum system, and in the development of the laser circuits and magnetic coils around the vacuum cell. The set-up is of the "atom chip" family ([35], [93], [53], [101]). Considering that the production of the condensate was the PhD subject of another student, I.Herrera, and that I did not directly participate in the design of the set-up, I will give only a short description of it in this thesis, quoting Herrera's thesis [54] as reference for details. The main steps concerning the set-up implementation have been: ultra high vacuum (UHV) up to $10^{-10}\,mbar$ in December 2009; magneto-optical trap (MOT) in January 2010; magnetic trapping with chip's structures in May 2010; condensation in October 2010; stabilization of the experimental procedure in December 2010.
My work in the group of Cataliotti has then concerned the development of the experimental loading procedure able to give an optimal ultracold cloud for $EIT$ and memory experiments. Indeed a different trapping regime, with respect to the one leading to condensation, was necessary in order to mode match the atomic cloud to the light pulse and maximize the field-atoms coupling. We were able to observe a marked reduction (almost 6 orders of magnitude) in the speed of light within the atomic sample, a promising step towards the realization of coherent information storage.
In the mean time we have exploited the Rubidium condensate for the implementation of a multipath Ramsey-like atom interferometry based on RF coupling of the Zeeman manifold of the hyperfine level $F = 2$. In the framework of the long term target of quantum computation, we were able to demonstrate the possibility to modify the output of the interferometer by means of interaction with an out-from-resonance

light. As a second step, we have demonstrated that the RF atomic interferometer can detect the multi-component quantum superposition atomic state built by Raman pulses able to couple all the successive sub-levels of the Zeeman manifold.

The manuscript is divided in four parts. The first part contains the main theoretical issue I had to face during my work and is divided in three chapters: the first chapter contains subjects of general use, concerning treatments covered by general manuals of advanced physics; the second chapter focuses on the theory of $EIT$ and $EIT$ based quantum memories in a simple three-level $\Lambda$ scheme; the third chapter provides an introduction to multi-path atomic interferometry.
The second and the third parts of the manuscript are devoted to the illustration of the protocols and the experimental results obtained during the PhD. In the second part I report my work on electromagnetically induced transparency and light pulse storage. The report is separated in two sections describing the contribution given in the two different experimental contexts: hot vapor cell in Paris (chapter 4) and ultracold trapped cloud in Firenze (chapter 5). In the third part I describe the results obtained in Firenze on atomic mutipath interferometry by means of the degenerate sample (chapter 6). The fourth part concerns a detailed description of the planning work, the construction strategies and the characteristics of the apparatus I have developed in Firenze for the optical interrogation of the cold sample (chapters 7,8,9).
Entering into the details of Chapter 1, which is not monothematic, it includes:
(1) a section where I recall some elements of the electromagnetic field representation in quantum mechanics. It is concluded by the expressions of the quantities experimentally measured by means of the homodyne detection;
(2) a section where I recall the common semi-classical theory of light-matter interaction, focusing attention on particular aspects as the determination of the group velocity and the Rabi oscillations induced by coherent interaction;
(3) a section where a door is opened over the wide world of Bose-Einstein condensates. As this was not the main subject of my PhD work, I just give a qualitative description of the main features which characterize its behavior;
(4) a last section devoted to the common interaction tools used to handle atomic samples. Magnetic potential as well as optical potential are considered, together with two-photon Raman transitions.

## Historical context

A storage device able to keep the quantum properties of the stored state (that is, a quantum memory) nowadays represents a challenge for fundamental and applied physics. Such a device is indeed the fundamental brick on which relevant research fields, such as quantum information [26, 8] and quantum communication [7], are based.

The field of quantum information requires the ability to exchange, store and perform operations on quantum bits (qubits). Photons are excellent carriers in this sense: they are characterized by a high propagation velocity, can be modulated up to high frequencies, and are relatively robust against decoherence. However it is not easy either to store them or to have some interaction among them. For these tasks, material media (atoms, ions, molecules, quantum-dots, Josephson junctions) are instead the natural candidates. The long lived coherences between ground states, characterized by lifetime scales that can vary from *microseconds* to minutes, can be exploited either for storage or for complex quantum operations implementation.
On the other hand, the transmission of photons over long distances is subjected to the low but non zero absorption induced by the propagation in optical fibers (attenuation of the order of $0.2\,dB/km$), showing hence exponential decrease with distance. In classical system of communication, amplification is provided periodically in order to restore the amplitude of the signal. This is not possible in the case of quantum variables, the amplification process progressively destroying the quantum characteristics. An original protocol has been developed for this purpose, based on a scheme which realizes the entanglement of two distant points by means of a series of entangling processes engaging intermediate nodes. With the help of quantum memories (which provide the storage of the photons at each node), the transfer of the entanglement on longer segments up to the edge points is possible even if all the entanglement exchanging measurements do not take place at the same moment. This relaxation of the limits of validity allows the entanglement of the two distant points with a cost in term of entangled photons that increases as a polynomial (not exponential) function of the distance [13]. The realization of efficient quantum memories is thus a crucial step also in the perspective of the construction of a network based on quantum communications.

In the light of the considerations reported above, we may say that the development of a process that allows an efficient, reversible and coherent exchange of information between photons and atoms is an experimental challenge of general interest[75].
In this framework, two main regimes have been developed during last decades. One is focused on handling a low number of atoms and enhancing the atom-field coupling. In this case the coupling is maximized using high finesse cavities within which the field oscillates: this is the field of cavity $QED$ (quantum electro-dynamics) [81]. Even if this approach has provided good results, the intrinsic complexity associated to these set-ups has maintained them far from possible scalable protocols. The second approach is intended to overcome these problems. In this case, the enhancement of the interaction is realized by involving a large number of atoms, while the light is left in single pass configuration. These protocols are based on the modification of the optical properties of a medium by means of a coherent preparation. In a variant of this phenomenon, electromagnetically induced transparency ($EIT$) [49], the field and the atomic medium are mutually modified during the interaction and they map their own variables on the ones of the other [23, 24]. Another fundamental aspect of this type of protocol relies on the fact that distributing the information on a large ensemble of atoms, the storage results to be more robust against loss mechanisms: the loss of a small number of atoms, does not substantially change the collective state of the sample.

The realization of efficient quantum memory protocols based on the $EIT$ has been an experimental challenge of the past ten years [46].
Storage of quantum states of the electromagnetic field is however only a small part of the applications of the phenomenon of electromagnetically induced transparency. The cancellation of the linear susceptibility of the medium due to destructive quantum interference is also accompanied by enhancement of the nonlinear susceptibilities [32]. This amplification of the nonlinear effects can allow an effective interaction between pulses containing a low number of photons and, ultimately, the realization of single photons logic gates. The high complexity which characterizes the coherent interaction in hot atomic gases often prevents the use of simple experimental apparatuses based on vapor cells, forcing experiment implementation by exploiting cold atomic clouds. This is the case, for instance, of the $EIT$ on the $D2$ line of alkali gases, which suffers

from a strong reduction with respect to the Doppler free case due to the destructive interplay of the different velocity classes contained in the thermal distribution. The development of a recovery technique for $EIT$ effect in hot atomic samples, as the one reported in this thesis, is therefore a field of investigation of widespread interest.

## State of the art

In this section a general overview on the experimental realization of classical and quantum memory devices for light pulses is reported. A number of techniques can be exploited for this aim, namely (considering the most commonly exploited) photon echo, Raman coupling and $EIT$.

Many storage protocols use the principle of the photon echo. This method exploits the inhomogeneous broadening of particular media. In such a medium, the coherences excited by the passage of a signal field accumulate a differential phase shift relative to each other. If the broadening is due to a stationary processes in the time scale of the memory, the phase shifts are deterministic. They can therefore be reversed, leading to the reconstruction of the macroscopic dipole momentum and the consequent re-emission of an echo pulse by the medium.
The first realization of such a memory protocol in a two level system ([69]), realized the inversion of the phases of the coherences by means of an inversion of population, obtained with a $\pi$ pulse of resonant light. The procedure was hence exposed to large spontaneous emission, an aspect that makes the protocol not suitable for storage of quantum properties. In the last years however, techniques for the reversal of the phases of the coherence without resonant interaction have been elaborated, leading to excellent results. $CRIB$ (Controlled Reversible Inhomogeneous Broadening) and $GEM$ (Gradient Echo Memory) are based on the same principle, that is, having an external parameter responsible for a displacement of the resonant frequency of the medium which can be modulated both in space and in time. By inverting the value of the parameter in point of the medium, one obtains the reflection of the induced inhomogeneity with respect to the central frequency of resonance, and hence the inversion of all the detunings. In the first case (CRIB), a static electric field gradient modulates the resonant frequency of a crystal at cryogenic temperature by means of the induced Stark shift. The maximal efficiency detected attains 69% without

addition of noise [51]. The second protocol is based on a vapor cell (hot atoms), the spatial modulated inhomogeneity given in this case by the Zeeman effect. A gradient of magnetic field is produced by a Zeeman-slower solenoid. Actually, the apparatus is composed of two such solenoids spatially merged and set in opposite configuration, so that switching the current from one to the other results in a switch of the spatial gradient. By using a $\Lambda$ scheme so as replacing the optical coherence with a Raman coherence characterized by a smaller decay rate, the protocol has shown very wide potentialities. A highly multimode nature [61], the possibility of a coherent control of the stored pulse [14], storage efficiencies up to 87% [60], and fidelity beyond the classical limit for weak coherent states [59], have been experimentally demonstrated in such a system.

Storage protocols based on Raman pulses are exhaustively described by Gorshkov et al. in [42]. The experimental realization is very similar to the one in $EIT$ configuration, but here one-photon detuned fields are exploited. Near resonance, the storage is similar to that occurring in $EIT$ (described in chapter 3) [66]. For large detuning instead, the quantum interference responsible for the $EIT$ vanishes, and the process of storage is no longer linked neither to a group velocity reduction, nor to a transparency peak. The most recent experiment exploiting this configuration has been performed on a hot Cesium vapor [102] used on the $D2$ line. Pulses of duration less than a *nanosecond* ($300\,ps$) can be effectively stored, proving an available bandwidth for the memory process larger than one *gigahertz*. This is made possible by the distance of the atomic resonance and by the spectral width of the control field, which is obtained from the same pulsed laser as the signal, and shows the same temporal profile. The storage efficiency is 30% and the lifetime of the memory is evaluated in $1.5\,\mu s$, i.e. 5000 times the duration of the pulse. Finally, the low noise measured on the retrieved impulse makes the process compatible with experimental quantum information protocols.

### $EIT$ based memories

The first realizations of memories exploiting the $EIT$ effects date back to 2001, following the first theoretical paper from M.Fleischauer on the subject [33]. Almost at the same time storage of a classical pulse of light was demonstrated in a Rubid-

ium vapor with $5\,torr$ of $He$ buffer gas ([97]) by means of a Zeeman ground state coherence ($|F = 2, m_F = +2\rangle$, $|F = 2, m_F = 0\rangle$) and in a ultracold sample of $Na$ atoms by exploiting the clock states ($|F = 2, m_F = +1\rangle$, $|F = 1, m_F = -1\rangle$)In the first case a storage with an efficiency of 10% showing a decay constant of $150\,\mu s$ was obtained. In the second case, only a small part of the signal pulse was detected (the one passing through the axis of the cold cloud), because the interest was focused on the determination of the lifetime of the memory. The retrieved signal was visible for a storage time up to $1\,ms$ (5%).

Successively, a number of spectacular experiments have been performed exploiting pulse storage, as, e.g., [6] and [38]. In the first paper the realization of pulses of light with stationary envelopes bound to an atomic spin coherence (in a hot Rubidium vapor) is reported. The signal pulse is first stored in the medium in the usual way. Then, control field is switched back on as standing wave instead of as traveling wave, hence inducing both the regeneration of the signal pulse and the formation of a periodic modulation of the atomic susceptibility, seen by the signal field as a kind of photonic crystal. The geometry of the system makes the signal field fall into the band gap of the "structure", and therefore it cannot escape the medium.

In the second paper, the momentum transfer relative to a velocity selective two-photon transition is exploited to make the wavefuction component in the final state migrate from one condensate to an other. The collective coherence characterizing these samples involves the formation of a macroscopic dipole momentum resulting from the combination of the two components coming from the two condensates, hence allowing the reading procedure in the second sample.

The first storage experiments in a solid state medium have been performed in 2005 by exploiting $Pr : Y_2SiO_5$ crystals at cryogenic temperature (few $kelvin$) [73]. Using counterpropagating signal and control fields[1], and a rephasing technique counteracting the inhomogeneous broadening, it has been possible to attain very long storage times, up to $2.3\,s$. The low optical depth of the sample (15% absorption at resonance) limited the memory efficiency to 1%, but it opened the way to condensed matter based protocols [86], [70], [51]. Even if strong $EIT$ and $EIA$ (electromagnetically induced absorption, which corresponds a superluminal group velocity) have been detected on solid state samples at room temperature [11], until now no storage

[1] which does not involve any difference with respect to the copropagating configuration in a solid state system, due to the absence of motion

has been demonstrated in such conditions.
Still in the framework of classical storage, it has been demonstrated that in real physical systems, where the optical density is finite, the temporal profiles of both signal and control fields play a role in the overall efficiency of the storage process. An iterative procedure for experimental optimization of the profiles has been suggested [88] and verified [98], resulting in a storage up to $100\,\mu s$ for $10\,\mu s$-long pulses with a efficiency of 43% in hot vapors ($60^oC$) $^{87}Rb$ in the presence of $30\,torr$ of neon (2008).
Studies on the possibility of multiplexing the stored information have been carried out both in frequency modes and transversal spatial modes. In [15] a control field with complex temporal shape is exploited in order to generate a comb-shaped transparency spectrum. The delay-bandwidth product and the light storage capacity for a probe pulse with a similar profile are enhanced by a factor of about 50 with respect to what is obtained for a monochromatic control field.
Concerning spatial transverse structure, in [116] the storage of complex images has been demonstrated in hot vapors of Rubidium, with a lifetime up to $30\,\mu s$. The storage has been made robust against diffusion of atoms by storing the Fourier transform of the image. Storage times up to $\sim 15\,\mu s$ of a superpositions of non-zero orbital moments modes has been realized in a free falling ultracold cloud of Cesium atoms by a technique very similar to $EIT$, employing Bragg diffraction to retrieve the stored optical information imprinted into the atomic coherence via a non collinear configuration of control and signal fields [85]. More recently (2010), image storage has been performed successfully in a crystal of $Pr : Y_2SO_5$. A technique of the same type as those used in photon echo protocols, able to rephasing the spatially inhomogeneous coherences of the sample, has given a lifetime of the memory of the order of a *millisecond* ([52]).

The coherent nature of the storage, which is a fundamental feature of interest for this protocols, has been experimentally demonstrated for the first time in [77]. The mutual mapping of the phase between the light pulse and the atomic spin is verified in this paper by observing a modulation of the phase of the retrieved pulse as a consequence of the direct modification of the phase of the Zeeman coherence via a pulse of DC magnetic field.
The storage of a coherent state in a hot vapor of $^{133}Cs$ carried out by J.Cviklinski and J.Ortalo [21] (2008), which is the starting point of my PhD work, has given

another verification of this characteristic. In the paper the linear dependence of the phase of the retrieved state with respect to the phase of the incoming state is verified, showing moreover the relation between the two phases is quantitatively determined by the two-photon detuning of the fields. On the other hand, the storage of complex images is itself a demonstration of the coherent mapping of the phase, the spatial features being the result of specific interference among eigenmodes of propagation of laser beams in free space [116].

The quantum nature of the memory protocol has been directly demonstrated by successfully storing non-classical state of the light. In both free falling cold cloud and hot vapor cell based set-ups, storage and retrieval of single photons (respectively [17] and [28], both in 2005) and squeezed vacuum pulses (respectively [57] and [2], both in 2008) has been demonstrated. The storage time was however shorter than a *microsecond* in all of these experiments. Finally, also in 2008, a delocalized single photon was stored in two different atomic ensembles[2] at the same time, allowing the formation of entanglement between two separated macroscopic objects for the first time [18].

[2]within the same cloud cold of cesium atoms

# Part I

# Theoretical background

# Chapter 1

# Quantum interaction of light and atoms

## 1.1 Electromagnetic field representation

Quantum optics is generally divided in two branches: the photons counting and the continuous variables domains. In the first case, detectors able to measure single photons (as avalanche photodiodes) are required, and the experimental procedures for studying quantum properties of light consist in the study of the of arrival time for a finite number of single excitations. The second branch works instead in the presence of any number of photons, with a detection stage focused on photon fluxes. It is accomplished with regular photodetectors that measure local intensity of light, thus providing an output which can take values in a continuous range. The relevant quantities in this case are the fluctuations of the measured fields. This thesis belongs to the second branch, so I will first introduce the formalism to handle the electromagnetic field in its free multimode form.
Classically, ignoring spatial dependence, a single mode of the electromagnetic field with polarization $\bar{e}$ and pulsation $\omega$ is defined by two real parameters[1], and can be expressed under two equivalent forms

$$\vec{E}(t) = 2\bar{e}E_0\, cos(\omega_0\, t + \varphi) = \bar{e}E_0 \left(e^{i\omega\, t + i\varphi} + e^{-i\omega\, t - i\varphi}\right) \tag{1.1}$$

$$= \bar{e}\,(X\, cos(\omega\, t) + Y\, sin(\omega\, t)) \tag{1.2}$$

[1] or one complex parameter

In the first form the mode is specified by amplitude ($E_0$) and phase ($\varphi$), while in the second one by two "quadratures" ($X_\varphi = 2E_0\, cos(\varphi)$, $Y_\varphi = 2E_0\, sin(\varphi)$). Throughout the whole thesis, we will define the amplitude of the electric field according to expression 1.1 . A useful representation of field states shows them as vectors in a $(x, y)$ Cartesian reference, named Fresnel reference plane, where the two coordinates correspond to the two quadratures. Defining the field in terms of $E_0$ and $\varphi$ corresponds to switching to polar coordinates in the same reference, as shown in fig1.1. Quadratures can be chosen arbitrarily within the $2\pi$ range of the angular variable. A new couple of quadratures rotated by an angle $\phi$ can be derived from a previous one by replacing $cos(\omega\, t + \varphi)$ with $cos(\omega\, t + (\varphi - \phi))$, as it is shown in fig1.1.

### 1.1.1 Quantization of light

Interpreting the normal modes as independent harmonic oscillators leads to a quantum description of the electromagnetic field, with the complex amplitude $E_0 e^{i\varphi}$ replaced by operators ($\hat{a}_\omega$, $\hat{a}^\dagger_\omega$). This couple of operators fulfill the commutation rule for conjugate variables $[\hat{a}_\omega, \hat{a}^\dagger_\omega] = 1$ and they can be interpreted, respectively, as annihilation ($\hat{a}_\omega$) and creation ($\hat{a}^\dagger_\omega$) operators of quanta of field.
The corresponding electric field operator takes the form

$$\hat{E} = \mathcal{E}\,(\hat{a}_\omega e^{-i\phi}\, e^{-i\omega\, t} + \hat{a}^\dagger_\omega e^{i\phi}\, e^{i\omega\, t}) = \mathcal{E}\,(\hat{X}^\phi\, cos(\omega t) + \hat{Y}^\phi\, sen(\omega t)) \tag{1.3}$$

where $\mathcal{E} = \sqrt{\frac{\hbar\omega}{2\epsilon_0 V}}$ represents the electric field of a single photon[2] ($V$ is the quantization volume), while $\phi$ accounts for the arbitrary choice of the phase reference.
Quadrature operators are defined as

$$\hat{X}^\phi = \hat{a}^\dagger_\omega e^{i\phi} + \hat{a}_\omega e^{-i\phi} \qquad \hat{Y}^\phi = i(\hat{a}^\dagger_\omega e^{i\phi} - \hat{a}_\omega e^{-i\phi}) \tag{1.4}$$

Following definition 1.4, we see that quadrature operators are also conjugate variables, and a Heisenberg uncertainty relation holds for their variances[3] $\Delta^2(\hat{X}^\phi)$

$$\Delta^2(\hat{X}^\phi) = \langle \hat{X}^{\phi\,2} - \langle \hat{X}^\phi \rangle^2 \rangle$$

[2]In this way the operator $\hat{a}_\omega$ is dimensionless

[3]For three observables $\hat{A}$, $\hat{B}$ and $\hat{C}$ which obey the commutation relations $[\hat{A}, \hat{B}] = i\hat{C}$, it holds

$$\langle \hat{A}^2 \rangle \langle \hat{B}^2 \rangle \geq 1/4 \langle \hat{C} \rangle^2 \tag{1.5}$$

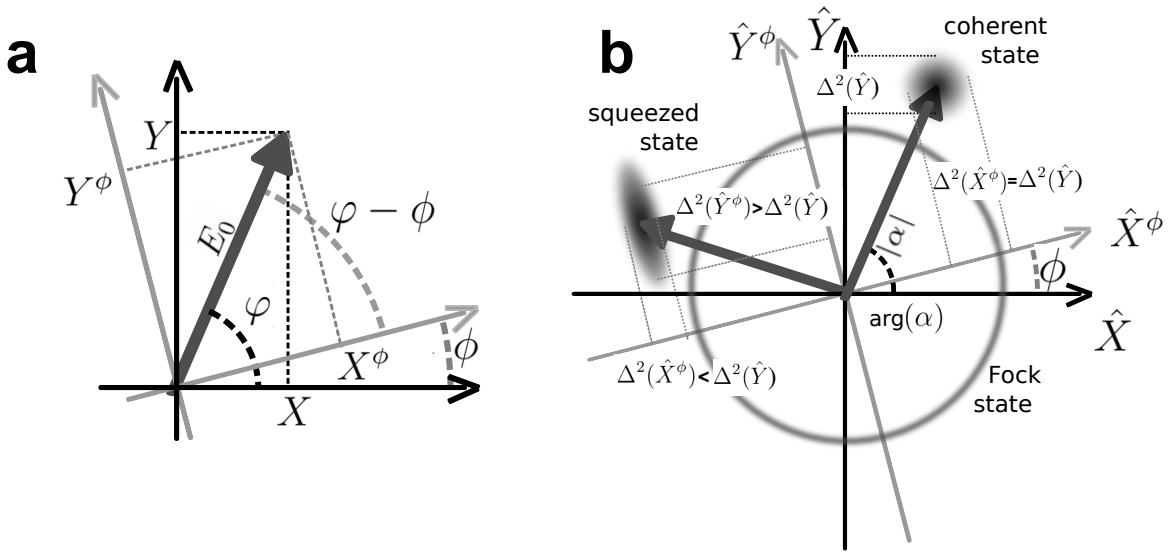


Figure 1.1: **a** - Representation of a classical state of the electromagnetic field in the Fresnel reference plane (dark gray arrow). The physical meaning of the two couples of parameters $(X, Y)$ and $(E_0, \varphi)$ is illustrated. The decomposition on a different basis rotated by an angle $\phi$ with respect to the original one is also visible in light gray. The amplitudes of the new quadratures can be derived from the previous ones by replacing $cos(\omega\, t + \varphi)$ with $cos(\omega\, t + (\varphi - \phi))$.
**b** - Quantum representation of three states of the electromagnetic field in the Fresnel reference plane. A coherent state (in the first quadrant) and a squeezed state with mean amplitude differing from zero (in the second quadrant) are represented. The circle represents a number state (Fock state). The meaning of $\alpha$ is also shown. Focusing on the uncertainty halos, one can see how the projection on a general quadrature gives the same distribution in the case of a coherent state, while squeezed states have a preferential base in which the ratio between the projected variances of the two quadratures is maximized.

$$\left[\hat{X}^{\phi},\, \hat{Y}^{\phi}\right] = i\left[\hat{a}_{\omega}^{\dagger}e^{i\phi} + \hat{a}_{\omega}e^{-i\phi},\, \hat{a}_{\omega}^{\dagger}e^{i\phi} - \hat{a}_{\omega}e^{-i\phi}\right] = 2i$$

$$\Rightarrow \quad \Delta^2(\hat{X}^{\phi})\,\Delta^2(\hat{Y}^{\phi}) \geq 1 \tag{1.6}$$

Hence it's not possible to know at the same time with arbitrary precision the expectation values of the two quadratures, and their representation in the Fresnel reference corresponds to a halo around the "classical" vector, as displayed in fig1.1 (right). This halo can get any ellipticity but respecting the Heisenberg constraint 1.6.
To study the fluctuations of a particular field mode, that is the statistical distribution of its quadratures, a common strategy is to simplify the related equations of motion by linearization around the mean values. This is done by separating each operator in two contributions: a c-number equal to its expectation value, and an operator for its fluctuations. Hence the remaining operator does not affect the expectation values, while completely defining the variances. For the field operator one gets

$$\hat{E} = \langle\hat{E}\rangle + \delta\hat{E}$$

$$\langle\delta\hat{E}\rangle = 0 \qquad \Delta^2(\hat{E}) = \Delta^2(\delta\hat{E}) = \langle\delta\hat{E}^{\,2}\rangle \tag{1.7}$$

From 1.4 we see that quadratures operators can be defined for every value of $\phi$. In particular, setting $\phi$ equal to the phase of the "classical" field $\varphi$ ($\langle\hat{a}\rangle = Ae^{i\varphi}$), one gets couple of quadratures named amplitude and phase quadratures (respectively $\hat{X}^I$ and $\hat{X}^{\varphi}$) characterized by $\langle\hat{X}^I\rangle = A$ and $\langle\hat{X}^{\varphi}\rangle = 0$. Such quadratures are closely related to the number operator $\hat{N} = \hat{a}^{\dagger}\hat{a}$, which has a mean value $\langle\hat{N}\rangle = |A|^2$, and the phase parameter $\varphi$. Concerning the operators describing the fluctuations, one finds the relations

$$\delta\hat{N} \sim \langle\hat{a}\rangle\delta\hat{a}^{\dagger} + \langle\hat{a}^{\dagger}\rangle\delta\hat{a} = Ae^{i\varphi}\delta\hat{a}^{\dagger} + Ae^{-i\varphi}\delta\hat{a} = A\,\delta\hat{X}^I$$

$$\delta\varphi \sim \frac{\hat{X}^{\varphi}}{2A} \tag{1.8}$$

which leads the number-phase Heisenberg uncertainty relation

$$\Delta^2(\hat{N})\Delta^2(\varphi) \geq \frac{1}{4} \tag{1.9}$$

This point of view is useful in the regime of photon counting. It shows, for example, that a Fock state $|n\rangle$ (i.e. a state with perfectly determined number of photons $n$) has no defined phase, and hence is represented in the Fresnel reference as a circle

centered on the origin (fig1.1).

A fundamental role in continuous variable quantum optics is played by coherent states [40]. These states are defined as eigenstates of the annihilation operator $\hat{a}$:

$$\hat{a}|\alpha\rangle = \alpha|\alpha\rangle \tag{1.10}$$

Let's consider the displacement operator which produces a shift in the Fresnel reference by quantities $\xi$ and $\eta$ respectively in the quadratures $\hat{X}$ and $\hat{Y}$. It takes the form

$$\hat{D}(\beta) = e^{-i(\xi\hat{Y}-\eta\hat{X})} = e^{\beta\hat{a}^\dagger - \beta^*\hat{a}} \qquad \text{with } \beta = \xi + i\eta \tag{1.11}$$

Since it can be shown that $\hat{D}(\beta)\hat{a}\hat{D}^\dagger(\beta) = \hat{a} - \beta\hat{\mathbb{I}}$, coherent states are obtained from the ground state $|0\rangle$ by application of such a displacement operator. For a coherent state $|\gamma\rangle$ indeed (since definition 1.10)

$$(\hat{a} - \gamma\hat{\mathbb{I}})|\gamma\rangle = 0 = \hat{D}(\gamma)\hat{a}\hat{D}^\dagger(\gamma)|\gamma\rangle \Rightarrow \hat{a}\hat{D}^\dagger(\gamma)|\gamma\rangle = 0 \Rightarrow \hat{D}^\dagger(\gamma)|\gamma\rangle = |0\rangle \tag{1.12}$$

On the other hand, definition 1.6 makes variances $\Delta^2(\hat{X}^\phi)$ invariant with respect to a simple translation. Therefore, whatever its amplitude, a coherent state shows the same characteristic fluctuations as the ground state of the field. A nice representation depicts them as the vacuum halo moved away from the origin of the Fresnel reference[4]. For this reason these states are usually taken as reference for "calibration" of quantum fluctuations of the field, and their variance ($\Delta^2(\hat{X}^\theta) = \textit{constant}\ \forall\,\theta$), named "standard quantum limit" (or "shot noise"), is defined as units of measurements of the variances ($\Delta^2(\hat{X}^\theta) = 1$).
Using Feynman's disentangling techniques, the $\hat{D}(\alpha)$ operator can be factorized in terms of fundamental operators as $\hat{D}(\alpha) = e^{-\frac{|\alpha|}{2}} e^{\alpha\hat{a}^\dagger} e^{\alpha^*\hat{a}}$, from which one can write the expansion of $|\alpha\rangle$ in terms of Fock states

$$|\alpha\rangle = \hat{D}(\alpha)|0\rangle = e^{-\frac{|\alpha|}{2}} e^{\alpha\hat{a}^\dagger} e^{\alpha^*\hat{a}}|0\rangle = e^{-\frac{|\alpha|}{2}} e^{\alpha\hat{a}^\dagger}|0\rangle = e^{-\frac{|\alpha|^2}{2}} \sum_{n=0}^{\infty} \frac{\alpha^n}{\sqrt{n!}}|n\rangle \tag{1.13}$$

A physical interpretation of the complex amplitude $\alpha$ is found from the calculation of the probability of measuring a photon number

$$|\langle n|\alpha\rangle|^2 = \frac{|\alpha|^{2n}}{n!} e^{-|\alpha|^2} \tag{1.14}$$

[4] it matches indeed the equality limit of the Heisenberg relation 1.6 with isotropic uncertainty

where one can recognizes $|\alpha|^2$ as the mean value of a Poissonian distribution[5]. This last aspect reflects the fact that a coherent state is obtained by removing all the sources of classical noise, allowing the statistics of a random variable to emerge. This is achieved in laser beams well above threshold, and it is in general well verified also in sufficiently attenuated beams. Coherent states are considered as the quantum field state that is the closest to a classical representation[6], the quantum frontier being (in the continuous variables domain) represented by variance smaller than shot noise. This can be obtained without violating Heisenberg principle 1.6, by compensating the reduction of fluctuations in one variable with an excess noise in the conjugate quantity (that corresponds to squeezing the uncertainty halo, from which the name "squeezed states").

Until now I have considered single mode variables, corresponding to waves defined in an infinite range of time. This description simplifies the theoretical work but can not represent the experimental situation. Both for limited coherence time of laser sources and for time shaping of the beam (for example by pulsing it), one needs to consider some frequency band around the carrier frequency $\omega_L$ to characterize a field state. This is also necessary to study the fluctuation properties of the field.
The multimode electric field operator, considering just one polarization, can be calculated as a sum over an ensemble of longitudinal modes

$$\hat{E}(t) = \int_{\omega_L-\Delta\omega/2}^{\omega_L+\Delta\omega/2} \sqrt{\frac{\hbar\omega}{2\epsilon_0 Sc}}(\hat{a}_\omega\, e^{-i\omega\, t} + \hat{a}_\omega^\dagger\, e^{i\omega\, t})\frac{d\omega}{2\pi} \tag{1.15}$$

where $\Delta\omega$ is the full considered bandwidth. In order to neglect the spatial dependence[7], we have defined a section of interest $S$ where we consider the field amplitude as constant. For laser light we have $\Delta\omega \ll \omega_L$, therefore it is possible to define a "slowly varying envelope" operator $\hat{A}(t)$ as[8]

$$\hat{A}(t) = \int_{-\Delta\Omega/2}^{\Delta\Omega/2} \hat{a}_{\omega_L+\Omega}\, e^{-i\Omega\, t}\frac{d\Omega}{2\pi} \Rightarrow \hat{E}(t) \sim \mathcal{E}_L\left(\hat{A}(t)\, e^{-i\omega_L\, t} + \hat{A}^\dagger(t)\, e^{i\omega_L\, t}\right) \tag{1.16}$$

[5]The phase of $\alpha$ determines the repartition of the excitation between the quadratures $\hat{X}$ and $\hat{Y}$

[6]which is a simple vector in the Fresnel reference

[7]with not extremely focused beams, laser light can be considered mostly as a plane wave in a section within its waist

[8]The sign $\sim$ in the expression for $\hat{E}$ in terms of $(\hat{A}, \hat{A}^\dagger)$ is due to the simplification obtained by replacing $\omega$ with $\omega_L$ inside the square root

where $\Omega = \omega - \omega_L$ and $\mathcal{E}_L = \sqrt{\frac{\hbar\omega_L}{2\epsilon_0 Sc}}$. With the definition of $\mathcal{E}_L$, $\langle \hat{A}^\dagger \hat{A} \rangle$ represents the photon flux throw $S$. Similarly to the single mode case, a commutation relation between $\hat{A}(t)$ and $\hat{A}^\dagger(t)$ can be written:

$$\left[\hat{A}(t), \hat{A}^\dagger(t')\right] = \int_{-\Delta\Omega/2}^{\Delta\Omega/2} e^{-i\Omega(t-t')} \frac{d\Omega}{2\pi} \xrightarrow{\frac{1}{|t-t'|} \ll \Delta\Omega} \delta(t-t') \tag{1.17}$$

the constrain $\frac{1}{|t-t'|} \ll \Delta\Omega$ meaning that the relation is valid only for fluctuations of frequency much smaller than the detection bandwidth (long integration times). Within this limit, it is possible to obtain equations similar to those involving single mode variables by replacing single mode annihilation/creation operators $(\hat{a}, \hat{a}^\dagger)$ with their slowly varying envelopes counterparts $(\hat{A}, \hat{A}^\dagger)$. In particular, it is possible to get a Heisenberg uncertainty relation between variances of the quadrature operators

$$\left[\hat{X}(t), \hat{Y}(t')\right] = \left[\delta\hat{X}(t), \delta\hat{Y}^\dagger(t')\right] = 2i\delta(t-t') \tag{1.18}$$

In general experiments, we have access to field fluctuations by measuring quadrature spectral densities $S_X(\omega)$, that is, evaluating noise amplitude within a particular frequency bandwidth by demodulating the time sequence of the detected signal. As shown in [91], in the frequency domain an expression equivalent to 1.18 holds

$$\xrightarrow{FT\colon f(\omega)=\int dt\, f(t)\, e^{i\omega t}} \left[\delta\hat{X}(\omega), \delta\hat{Y}(-\omega')\right] = 4i\pi\, \delta(\omega-\omega') \tag{1.19}$$

and exploiting the spectral density definition
$\langle \delta\hat{X}(\omega)\, (\delta\hat{X}(-\omega'))^\dagger \rangle = 2\pi S_X(\omega)\, \delta(\omega-\omega')$
one can determine an uncertainty relation in terms of spectral densities

$$S_X(\omega) S_Y(\omega) \geq 1 \tag{1.20}$$

The actual quantity obtained by demodulating the signal at a frequency $\omega_0/2\pi$ for a time $\Delta t$, denoted as $X^\theta_{\omega_0;\Delta t}$, is related to the noise spectral density through its variance

$$\Delta^2(X^\theta_{\omega_0;\Delta t}) = 2\frac{1}{2\pi\Delta t} S_{X^\theta}(\omega_0) \tag{1.21}$$

where $\frac{1}{2\pi\Delta t} = F$ is the frequency resolution, that is the integration bandwidth. So, for the experimentally accessible quantities $X^\theta_{\omega_0;\Delta t}$, the Heisenberg inequality becomes

$$\Delta^2(X_{\omega_0;\Delta t}) \Delta^2(Y_{\omega_0;\Delta t}) \geq 4\, F^2 \tag{1.22}$$

where one finds the well-known property that shot noise is proportional to the demodulation bandwidth.

### 1.1.2 Continuous wave measurement: homodyne detection

Homodyne detection allows to measure any quadrature of the electric field, exploiting the interference with another beam of much larger intensity (called local oscillator). In fig1.2 I report a standard set-up scheme, where the definitions of the variables for the treatment are given. After merging the signal $E_s$ to be characterized with the local oscillator $E_{l.o.}$ in a 50/50 beam-splitter, one gets two outputs of the form $E_\pm = \frac{1}{\sqrt{2}}(E_{l.o.} \pm E_s)$. Hence the two photodiodes read the same stationary intensity $(|E_s|^2 + |E_{l.o.}|^2)$, but also an interference term with opposite phases, which can be isolated by subtraction of the two outputs

$$i_\pm = \frac{1}{2}|E_{l.o.} \pm E_s|^2 = \frac{1}{2}(|E_{l.o.}|^2 + |E_s|^2 \pm 2|E_{l.o.}||E_s|\, cos(\phi))$$

$$i = i_+ - 1_- = 2|E_{l.o.}||E_s|\, cos(\phi) \tag{1.23}$$

If the local oscillator is close to a coherent state, that is its fluctuations are mostly independent of the intensity, and assuming $|E_s| \ll |E_{l.o.}|$, one can simplify the linearized expression for fluctuations leaving only the term depending from $E_s$

$$\delta i \sim |E_s|\, cos(\phi)\, \delta(|E_{l.o.}|) + |E_{l.o.}|\, \delta(|E_s|\, cos(\phi)) \sim |E_{l.o.}|\, \delta(|E_s|\, cos(\phi)) \tag{1.24}$$

It means that the homodyne output mostly shows the features of the fluctuations of $E_s$, achieving moreover a kind of amplification of the signal proportional to the local oscillator amplitude $|E_{l.o.}|$.

Switching to quantum operators, with the above constraints on the local oscillator spectral properties, one can leave it as a c-number (as a classical field), while using $\hat{a}, \hat{a}^\dagger$ operator for the signal mode

$$\hat{a}_\pm = \frac{1}{\sqrt{2}}(\hat{a}_{l.o.} \pm \hat{a}_s) = \frac{1}{\sqrt{2}}(\, |E_{l.o.}|e^{i\phi} \pm \hat{a}_s) \tag{1.25}$$

$$\hat{i} = |E_{l.o.}|\, (e^{-i\phi}\hat{a}_s + e^{i\phi}\hat{a}_s^\dagger) = |E_{l.o.}|\, \hat{X}_s^\phi$$

where $\hat{X}_s^\phi$ represents the projection of the signal field on the axis of the amplitude quadrature of the local oscillator.Therefore, slightly changing the optical path of one of the two beams (e.g. by acting with a piezoelectric-transducer on a mirror before the merging point), one can change the relative phase $\phi$ and observe the signal projection over any quadrature.

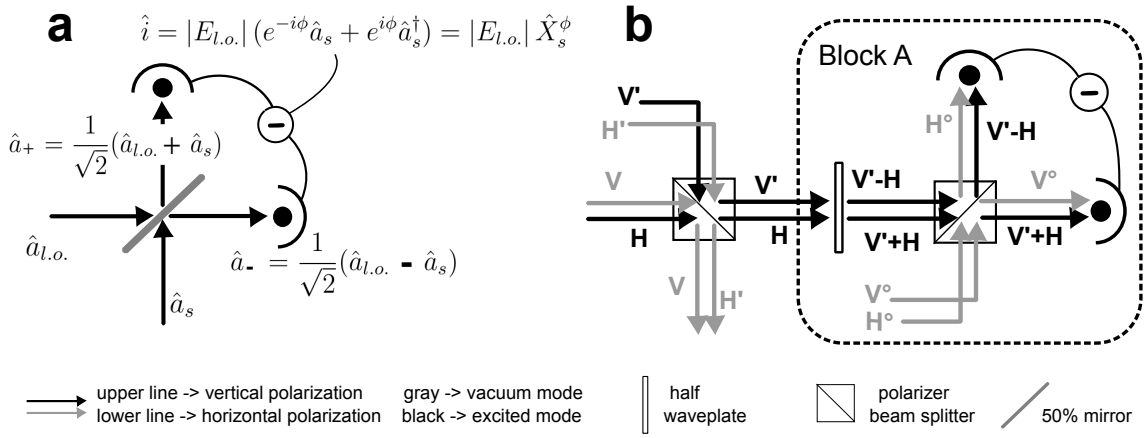


Figure 1.2: **a** - Diagram of a homodyne detection scheme. The difference in the expressions for $\hat{a}_+$ and $\hat{a}_-$ is determined by the reflection on opposite interfaces. The value for $\hat{i}$ as reported is obtained by considering the quantum operator for the field to be analyzed and the classic value $|\alpha|e^{i\phi}$ for the strong field acting as local oscillator (phase reference).
**b** - Experimental realization of a homodyne detection scheme using birefringent elements (polarizing beam-splitters). In this case two stages are needed, a first one to merge the two fields and a second one to decompose their superposition on a basis rotated by $45^o$ relative to their polarization axes. The opposite phases for the interference terms detected by the two photodiodes results from projection into the new basis. The presence of more than one mixing element mixes the fields of interest with an independent vacuum state (in the second cube). This fact however has no consequences on the detection statistics, since the added vacuum field does not beat with the other fields because it is orthogonally polarized to them.

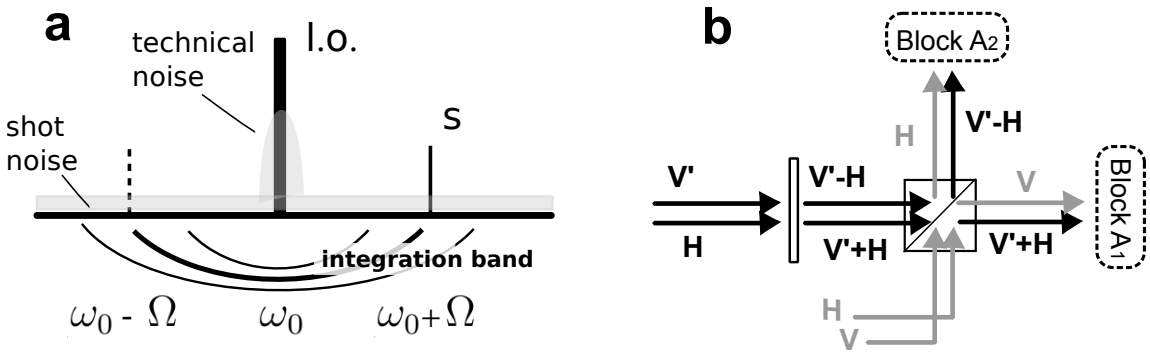


Figure 1.3: **a** - Frequency components entering the signal output of the homodyne detection for the case of a local oscillator displaced by $\Omega$ from the frequency of interest, after a frequency filtering centered on $\Omega$. By exploiting this method it is possible to avoid the technical noise present at low frequencies close to the local oscillator. As a counterpart, the mode at opposite frequency (with respect to the local oscillator) can not be eliminated and influences the output.
**b** - Set-up for the implementation of two simultaneous homodyne detections performed on the same signal beam. Splitting the signal when it is already mixed with the local oscillator requires an additional polarizing cube with respect the usual configuration (fig1.2). This operation mixes the field of interest with an uncorrelated vacuum state before the last polarizing beam splitter, which hence mixes the two field projecting them into the same polarizations. As a consequence the detection is influenced by an additional beat note due to the interference of the field of interest with an additional uncorrelated vacuum state.

For a multimode signal, measuring fluctuations for modes at different frequencies with respect to that of the local oscillator can be important. Shifting the local oscillator respect to the frequency of interest is also the usual technique exploited to avoid the technical noise present at low frequencies. Considering a mode $\hat{a}_\Omega$ at a frequency $\Omega$ far away from the local oscillator, one finds that the mean value of the homodyne detection gives a beat note at $\Omega$, while fluctuations can be observed as amplitude and phase noise on this oscillation.

Actually it is not possible to isolate a single mode, because, while the contribution of other frequencies can be removed by acting with a bandpass filter centered at $\Omega$,

the mode at opposite frequency (respect to local oscillator) $\hat{a}_{-\Omega}$ enters this selective port (fig1.3). Indeed the expression for the homodyne output at $\Omega$ shows a mix of quadratures of the two modes

$$\hat{i} = |E_{l.o.}|^2 \left( cos(\Omega t)(\hat{X}^{\phi}_{s,\Omega} + \hat{X}^{\phi}_{s,-\Omega}) + sin(\Omega t)(\hat{Y}^{\phi}_{s,\Omega} - \hat{Y}^{\phi}_{s,-\Omega}) \right) \tag{1.26}$$

where $\hat{X}^{\phi}_{s,\Omega}$ represents a quadrature of the mode detuned by $\Omega$ from the local oscillator frequency ($\hat{X}^{\phi}_{s,\Omega} = e^{i\phi + i\Omega t}\hat{a}^{\dagger}_{s} + e^{-i\phi - i\Omega t}\hat{a}_{s}$). One finds that simultaneous measurements of both observables ($\hat{X}^{\phi}_{s,\Omega} + \hat{X}^{\phi}_{s,-\Omega}$) and ($\hat{Y}^{\phi}_{s,\Omega} - \hat{Y}^{\phi}_{s,-\Omega}$) are possible[9]. These quantities are the relevant ones for the detection of squeezed states, in which quantum correlations between symmetric sidebands are present (and which the homodyne detection is mainly made for). In our case, we use this technique to measure mean value and fluctuations of weak beams at frequency $\Omega$ away from the local oscillator, that is we are interested in the single sideband properties $\hat{X}^{\phi}_{s,\Omega}$, $\hat{Y}^{\phi}_{s,\Omega}$, $\Delta^2(\hat{X}^{\phi}_{s,\Omega})$, $\Delta^2(\hat{Y}^{\phi}_{s,\Omega})$. As we have shown, homodyne detection does not give direct access to such observables, but, considering vacuum state for the $-\Omega$ sideband, one gets

$$\langle \hat{X}^{\phi}_{s,\Omega} + \hat{X}^{\phi}_{s,-\Omega} \rangle = \langle \hat{X}^{\phi}_{s,\Omega} \rangle \qquad \langle \hat{Y}^{\phi}_{s,\Omega} - \hat{Y}^{\phi}_{s,-\Omega} \rangle = \langle \hat{Y}^{\phi}_{s,\Omega} \rangle$$

$$\Delta^2(\hat{X}^{\phi}_{s,\Omega} + \hat{X}^{\phi}_{s,-\Omega}) = 1 + \Delta^2(\hat{X}^{\phi}_{s,\Omega}) \qquad \Delta^2(\hat{Y}^{\phi}_{s,\Omega} - \hat{Y}^{\phi}_{s,-\Omega}) = 1 + \Delta^2(\hat{Y}^{\phi}_{s,\Omega}) \tag{1.27}$$

where I have used $\Delta^2(X^{\phi}_{vacuum})$ as units of measurement for the variances ($\Delta^2(X^{\phi}_{vacuum})$ = 1, as defined before). This technique gives a variance equal to 2 in case of detection of a coherent state (or the vacuum state). Simultaneous measurements of the two quadratures of a field state are in fact possible at the expense of an additional unity of shot noise in the variance. This is because the proposed operation is similar to splitting the mixed beam into two parts to be sent to separated homodyne detections: the fluctuations of an uncorrelated vacuum state enter through the second port of the beam-splitter (see fig1.3).

[9] by analyzing the output with a double phase lock-in amplifier or recording it and performing a numerical demodulation off-line

## 1.2 Light-matter interaction, semi-classical model

In this section I will recall the basic equations governing the interaction between atomic systems and electromagnetic radiation. The treatment is limited to a semi-classical model with a two level atom, where the fields are classical waves. The whole section is written in terms of the density matrix formalism [74] and follows reference [121], except when indicated.

With the basic assumption of a two level atom (with $|1\rangle, |2\rangle$ eigenstates of the unperturbed Hamiltonian $\hat{H}_0$) excitable through a dipolar type interaction ($\hat{H}' = -\hat{\mu}\, E(t)$ such that $\mu_{11} = \mu_{22} = 0$; $\hat{\mu}$ being the dipole moment component along the direction of the field $E(t)$ ), one can write equations for the density matrix elements in terms of $H_0$ eigenstates as[10]

$$\hat{H} = \hat{H}_0 + \hat{H}' \qquad \hat{H}_0|i\rangle = E_i|i\rangle \quad i = 1, 2 \tag{1.28}$$

$$\frac{d}{dt}\rho_{ij} = -\frac{i}{\hbar}[(H_0 + H'),\, \rho]_{ij} \;\Rightarrow\; \frac{d}{dt}\rho_{12} = \frac{i}{\hbar}(H'_{12}(t)\,\rho_{22} - E_1\rho_{12} + E_2\rho_{12} - \rho_{11}\,H'_{12}(t))$$

Setting conveniently the phases of the basis states (without loss of generality) such that $\mu_{12} = \mu_{21} = \mu$ and defining $\omega_0 = (E_2 - E_1)/\hbar$ one gets the system of equations

$$\frac{d}{dt}\rho_{12} = i\omega_0\rho_{12} + i\frac{\mu}{\hbar}E^*(t)(\rho_{22} - \rho_{11})$$

$$\frac{d}{dt}(\rho_{22} - \rho_{11}) = i\frac{\mu}{\hbar}(E(t) + E^*(t))(\rho^*_{12} - \rho_{12}) \tag{1.29}$$

A more realistic model needs to includes decay rates, both for population ($\rho_{22} - \rho_{11}$) and for coherence $\rho_{12}$. The two being of different nature, one have to consider different time scale for them: $T_1$ for change in populations (mostly due to spin-changing collisions and spontaneous emission), $T_2$ for collisions and inhomogeneities that cause loss of coherence through temporal modulation of the energy eigenvalue. The decay terms to be added in 1.29 take different forms $\left(-\frac{\rho_{12}}{T_2}\right)$ and $\left(\frac{(\rho_{22}-\rho_{11})-(\rho_{22}-\rho_{11})_0}{T_1}\right)$ due

[10]The assumption of two levels atoms is justified when the perturbing field frequency is much closer to the considered atomic resonance than to others.
$\mu_{ii} = \langle i|\mu|i\rangle = 0$ for electric dipole momenta is true in case of eigenstates of defined parity (which is the case for atoms, if not in static electric fields); for magnetic dipoles it is true in case of transitions between the states $m_s = \pm 1/2$ of a spin 1/2 system

to the fact that coherence always goes to zero, while population can have any asymptotic value $(\rho_{22} - \rho_{11})_0$ due to external pumping.
Moreover, for harmonic perturbing fields $E(t) = 2E_0\, cos(\omega\, t) = E_0(e^{i\omega\, t} + e^{-i\omega\, t})$ close to the atomic resonance $\omega_0$ (i.e. $\omega \sim \omega_0$), it is useful to define slowly varying variables for coherence terms as $\rho_{12}(t) = \sigma_{12}\, e^{i\omega\, t}$, and rewrite equations in terms of such variables. Eventually, neglecting all the terms that are not slowly varying[11] (the so called rotating wave approximation (RWA)), the system takes the form

$$\frac{d}{dt}\sigma_{12} = -i(\omega - \omega_0)\sigma_{12} + i\frac{\mu E_0}{\hbar}(\rho_{22} - \rho_{11}) + \left[-\frac{\sigma_{12}}{T_2}\right]$$

$$\frac{d}{dt}(\rho_{22} - \rho_{11}) = 2i\frac{\mu E_0}{\hbar}(\sigma_{12} - \sigma_{12}^*) + \left[-\frac{(\rho_{22} - \rho_{11}) - (\rho_{22} - \rho_{11})_0}{T_1}\right] \tag{1.30}$$

I have put decay terms into square brackets [.], so that it is simple to ignore them if useful.
The expectation value for the dipole moment $\langle\mu\rangle$ can be evaluated within the density matrix formalism as

$$\langle\mu\rangle = tr(\rho\mu) = \mu(\rho_{12} + \rho_{21}) = \mu(\sigma_{12}e^{i\omega\, t} + \sigma_{21}e^{-i\omega\, t}) =$$

$$= 2\mu[\, Re(\sigma_{12}(t))\, cos(\omega t) + \, Im(\sigma_{12}(t))\, sin(\omega t)] \tag{1.31}$$

where the Hermitian character of the dipole moment ($\sigma_{21} = \sigma_{12}^*$) is used to obtain the second line.

[11] that is the ones with exponential $e^{\pm i\, n\, \omega\, t}$ $(n = 1, 2)$, which is physically justified since they average out to zero in any time scale of interest (remind that $\omega$ is within the optical domain)

### 1.2.1 Steady state limit: atomic susceptibility ($\chi$)

By imposing derivatives equal to zero in system 1.30 one finds the asymptotic steady state for the elements of the density matrix, and eventually for the population distribution $\Delta N = N\,(\rho_{22} - \rho_{11})$ and the macroscopic polarization $\vec{P} = \bar{e}_\mu P\, N\, \langle \mu \rangle$ ($N$ number of atoms).
With some algebra we find

$$Im(\sigma_{12}) = \Omega T_2 \, \frac{1}{1 + (\omega - \omega_0)^2 T_2^2 + 4\Omega^2 T_2 T_1} \, (\rho_{22} - \rho_{11})_0$$

$$Re(\sigma_{12}) = \Omega T_2^2 \, \frac{(\omega - \omega_0)}{1 + (\omega - \omega_0)^2 T_2^2 + 4\Omega^2 T_2 T_1} \, (\rho_{22} - \rho_{11})_0$$

$$(\rho_{22} - \rho_{11}) = \frac{1 + (\omega - \omega_0)^2 T_2^2}{1 + (\omega - \omega_0)^2 T_2^2 + 4\Omega^2 T_2 T_1} \, (\rho_{22} - \rho_{11})_0 \tag{1.32}$$

where the Rabi frequency is $\Omega = \frac{\mu E_0}{\hbar}$. So, according to 1.31, the expression for $P$ reads

$$P = 2\frac{\mu}{\hbar} \Omega T_2 \, \Delta N_0 \left( \frac{(\omega - \omega_0) T_2 \, cos(\omega t) - sin(\omega t)}{1 + (\omega - \omega_0)^2 T_2^2 + 4\Omega^2 T_2 T_1} \right) \tag{1.33}$$

with $\Delta N_0 = N\,(\rho_{22} - \rho_{11})_0$. From the macroscopic polarization one can determine the atomic susceptibility $\chi = \chi' + i\chi''$, that is the parameter which drives the propagation of light (as it will be shown in the next section). Comparing the definition of susceptibility valid in the case of an isotropic, linear, not magnetic and not charged medium[12]

$$\vec{P} = \epsilon_0 \, \chi \, \vec{E}$$

$$\bar{e}_\mu = \bar{e} \qquad P(t) = 2\, Re(\epsilon_0 \chi \, E_0 \, e^{i\omega t}) = 2\epsilon_0 E_0 (\chi' \, cos(\omega t) - \chi'' \, sin(\omega t)) \tag{1.34}$$

with 1.33, one finds for real ($\chi'$) and imaginary ($\chi''$) components

$$\chi'(\omega) = \frac{1}{\epsilon_0} \frac{\mu^2}{\hbar} \, \frac{(\omega - \omega_0)\, T_2^2}{1 + (\omega - \omega_0)^2 T_2^2 + 4\Omega^2 T_2 T_1} \, \Delta N_0$$

$$\chi''(\omega) = \frac{1}{\epsilon_0} \frac{\mu^2}{\hbar} \, \frac{T_2}{1 + (\omega - \omega_0)^2 T_2^2 + 4\Omega^2 T_2 T_1} \, \Delta N_0 \tag{1.35}$$

One can see that $\chi'$ is an odd while $\chi''$ is an even function. They both show extrema near the resonance $\omega = \omega_0$ and contain an intensity dependent term that broadens

[12] all of these properties are assumed by choosing the interaction term of the Hamiltonian

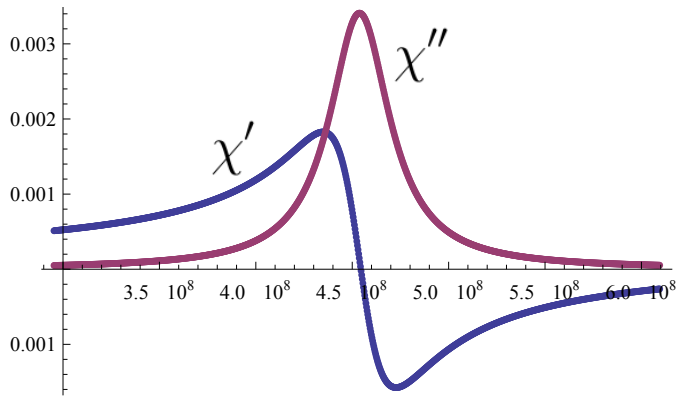


Figure 1.4: Real (blue curve) and imaginary (red curve) parts of the susceptibility of a medium in the vicinity of a resonance. The real part (related to the dispersion properties of the medium) has an odd profile around the resonance, while the imaginary part (related to the absorbance of the medium) has an even profile.

and reduces the peaks, hence reducing the effect of the medium on the light. This is the so called intensity saturation effect, which becomes relevant for

$$4\Omega^2 T_1 T_2 > 1 \quad \Rightarrow \quad \Omega > \frac{\Gamma}{2} \tag{1.36}$$

the second (simpler) form obtained by approximating $T_1 \sim T_2 \sim 1/\Gamma$ .

### 1.2.2 Interpretation of $\chi$

In this section I show how the susceptibility acts on waves propagation, focusing on the effects on light pulses , such as: temporal broadening and changes in the group velocity. According to Maxwell's equations, the presence of a polarization $\bar{P}$ modifies the dielectric constant thus causing differences in the propagation of light with respect to the vacuum case. Indeed the wave equation reads

$$\triangle \vec{E}(\bar{r},t) - \frac{n^2}{c^2}\frac{\partial^2}{\partial t^2}\vec{E}(\bar{r},t) = -\mu_0 \frac{\partial^2}{\partial t^2}\vec{P}(\bar{r},t) \qquad \epsilon_r = n^2 \tag{1.37}$$

where we consider in $\vec{P}$ just the resonant component of the polarization, leaving in $\epsilon_r$ the almost constant part related to far detuned contributions ($n$ is the far from resonance index of refraction). $P(\vec{r},t)$ is related to $P(t)$ as defined in 1.34

by replacing $\Delta N_0$ with its local density (for homogeneous density $\Delta N_0/V$, with $V$ interaction volume). To study the effect of the susceptibility it is useful to switch to the frequency domain. The general solution for a plane wave can than be reported back to the time domain according to

$$\left(\triangle + \frac{\omega^2}{c^2}(n^2+\chi)\right)\vec{E}(\vec{r},\omega) \quad \Rightarrow \quad \vec{E}(\vec{r},t) = \bar{e}\, Re(E\, e^{i(\omega\, t - k'\, z)}) \tag{1.38}$$

The effect of a resonance can thus be expressed through a modified wave vector $k'$, defined as

$$k' = \frac{\omega}{c}\sqrt{n^2+\chi} \sim k\, n(1+\frac{\chi}{2n^2}) = k\, n\left[\left(1+\frac{\chi'}{2n^2}\right) + i\left(\frac{\chi''}{2n^2}\right)\right] \tag{1.39}$$

where $k = \frac{\omega}{c}$ is the wave vector related to the mode $\omega$ in vacuum. The approximation holds if $|\chi| \ll 1$, which is usually well satisfied in atomic physics, due to the low density of gases. In the presence of an atomic transition the wave propagates according to

$$\vec{E}(\vec{r},t) = \bar{e}\, Re(E\, e^{i(\omega\, t - k\, n(1+\frac{\chi'}{2n^2})z) + k\frac{\chi''}{2n^2}z}) \tag{1.40}$$

which means that after a distance $L$, a monochromatic wave shows both a reduction in amplitude and a shift in phase: the first effect is related to the imaginary part through the term $\chi$ as $e^{\frac{k\chi''}{2n}L}$, that gives a transmission coefficient

$$t = |E(L)|^2/|E(0)|^2 = e^{kL\frac{\chi''}{n}} \tag{1.41}$$

the second effect is related to the real part of $\chi$ and originates from the term $e^{i(\omega\, t - k\, n(1+\frac{\chi'}{2n^2})\, z)}$, which gives a phase delay $\Delta\phi$ with respect to the propagation in vacuum

$$\Delta\phi(\omega) = \frac{\omega}{c}L(n-1+\frac{\chi'(\omega)}{2n}) \tag{1.42}$$

This phase shift is related to the wave front propagation velocity in the medium, i.e., the phase velocity $v_p$, that can be written as

$$v_p(\omega) = \omega/k' = c/(n+\frac{\chi'(\omega)}{2n}) \tag{1.43}$$

In general $n$ is a smooth function of $\omega$; for a dilute gas however, it is considered as constant and close to unity $n \simeq 1$, due to the weak polarization obtainable at these densities. This approximation will be introduced in the final expressions, leaving $n$

unspecified during the calculations for the seek of clarity.

A pulse of monochromatic light (that is a monochromatic wave with an envelope which vanishes outside a defined time interval) can be seen as a superposition of an ensemble of monochromatic waves with a choice of the relative phases such that at a time $t_0$ the ensemble forms constructive interference in a position $z_0$. The propagation velocity of the envelope (i.e. the group velocity $v_g$) follows the propagation of this phase matching condition: it is determined by the mean phase velocity $\langle v_p \rangle$ within the frequency spectrum of the pulse, after considering the spreading of $v_p$ in the same bandwidth. Indeed the spreading accounts for a change in the relative phase among the components with respect to the initial state, which induces a change in the conditions to achieve a constructive interference[13].
A simple way to derive the expression for $v_g$ is described in the following.
Let's consider a pulse of light[14] in the time domain, represented in terms of its Fourier transform as

$$E(x,t) = \frac{1}{\sqrt{2\pi}} \int_{-\infty}^{\infty} A(\omega) e^{i(\omega\, t - k'\, x)} d\omega \tag{1.44}$$

The wave vector $k'$ can be expressed in terms of pulsation $\omega$ throw 1.39, and thus it can be replaced around the resonance $\omega_0$ by the polynomial expansion $k' \simeq k'_0 + \frac{d}{d\omega} k'|_{\omega_0} (\omega - \omega_0)$; here we consider just the real part of $k'$.
The expression for the pulse takes the form

$$E(x,t) = e^{-i\, k_0\, x} e^{i \frac{d}{d\omega} k'|_{\omega_0} \omega_0\, x} \frac{1}{\sqrt{2\pi}} \int_{-\infty}^{\infty} A(\omega) e^{i(\omega\, t - \frac{d}{d\omega} k'|_{\omega_0} \omega\, x)} d\omega \tag{1.45}$$

Considering the absolute value of the field amplitude $|E(x,t)|$, one can recognize in the factor $\frac{d}{d\omega} k'|_{\omega_0}$ the inverse of the envelope velocity $(1/v_g)$

$$|E(x,t)| = |E(0, t - \frac{d}{d\omega} k'|_{\omega_0}\, x)| = |E(0, t - \frac{x}{v_g})| \quad \Rightarrow v_g = \left( \frac{d}{d\omega} k' \right)^{-1} \tag{1.46}$$

[13] In a far from resonance medium with constant index of refraction, wave fronts of different components move together (phase velocity $v_p(\omega) = c/n = \textit{costante}$), leading to an envelope moving in the same way (group velocity $v_g = v_p$). Otherwise, one can show that for $\partial v_p / \partial \omega \neq 0$ the group velocity $v_g$ can strongly differ from the phase velocity. A transparent medium is generally characterized by $v_g < v_p$, since the real part of $n$ between two transitions shows a weak monotonously increasing shape, which brings to a small phase gradient changing the phase matching condition of a pulse

[14] defined as a generic envelope multiplied by a monochromatic plane wave propagating along $x$

By taking the definition 1.39 for $k'$, one finds for $v_g$ [15]

$$v_g = \left(\frac{d}{d\omega}k'\right)^{-1} = \left(\frac{d}{d\omega}\left[\frac{\omega}{c}n(1+\frac{\chi'}{2n^2})\right]\right)^{-1} = \frac{1}{\frac{d}{d\omega}\left(\frac{\omega}{v_p}\right)} = v_p\,\frac{1}{1-\frac{\omega}{v_p}\frac{d}{d\omega}v_p} \qquad (1.47)$$

Around a resonance, the phase velocity $v_p$ can show a sharp derivative in $\omega$: in this cases one gets $v_g$ very different from $v_p$.
In terms of susceptibility $\chi$ one finds

$$v_g = \left(\frac{1}{c}n(1+\frac{\chi'}{2n^2}) + \frac{\omega}{c}\frac{d}{d\omega}\left[n(1+\frac{\chi'}{2n^2})\right]\right)^{-1} \sim \frac{c}{1+\frac{\omega}{2}\frac{d}{d\omega}\chi'} \qquad (1.48)$$

where to get the second expression, approximations that hold with diluted gases are applied ($n \simeq 1\,;\ \chi \ll 1$), which correspond to consider $v_p \sim c\,$.

It is instructive to look at the dispersion effects on pulse envelopes directly in time domain, where the group velocity explicitly appears. Starting from 1.37, one can find the equation for the slowly varying envelopes

$$\left(\frac{\partial}{\partial z} + \frac{n}{c}\frac{\partial}{\partial t}\right)E = -i\frac{\mu_0 c\,\omega_0}{2n}P \qquad (1.49)$$

which is the expression normally used for describing light-matter interaction with pulses. Replacing again the polarization $P(\omega)$ with a polynomial expansion in $(\omega - \omega_0)$, one can calculate an approximate expression for the slowly varying $P(t)$ by Fourier transform

$$P(\omega-\omega_0) = \epsilon_0\,\chi(\omega-\omega_0)E(\omega-\omega_0) = \epsilon_0\,\left(\chi(\omega_0) + \frac{\partial}{\partial\omega}\chi|_{\omega_0}\,(\omega-\omega_0) + ...\right)E(\omega-\omega_0)$$

$$\xrightarrow{FT} \quad P(t) = \epsilon_0\left(\chi(\omega_0)E(t) - i\frac{\partial}{\partial\omega}\chi|_{\omega_0}\,\frac{\partial}{\partial t}E(t) + ...\right) \qquad (1.50)$$

The 1.49 takes the form

$$\left(\frac{\partial}{\partial z} + \frac{1}{c}\left(n + \frac{\omega_0}{2n}\frac{\partial}{\partial\omega}\chi|_{\omega_0}\right)\frac{\partial}{\partial t}\right)E = -i\frac{\omega_0}{2nc}\chi(\omega_0)\,E \qquad (1.51)$$

[15] the usual form $v_g = c/(n+\omega\frac{dn}{d\omega})$ is obtained by replacing $\sqrt{n^2+\chi'} = n$, in which case $v_p = c/n$ and the expression follows after $v_g = (\frac{d}{d\omega}(k\,n))^{-1}$

where we recognize the expression related to the group velocity 1.48, for $\omega_0$ matching exactly the resonance condition the expression is further simplified by $\chi'(\omega_0) = 0$.

If $v_p$ is not linear in $\omega$ (that is one cannot truncate the polynomial expansion to first order) the envelope of the wave packet not only moves, but is also distorted, eventually getting stretched out. Distortion can be related also to a differential absorption within the pulse spectrum, due to a change of $\chi''$ in the frequency band of interest.

### 1.2.3 Before the steady state: coherent interaction

The solution obtained in the previous sections is valid in an equilibrium situation, that is for interaction times longer than the time scale given by the decay rates of the atomic system ($T_1$ and $T_2$). On the contrary with long coherence systems (as atomic clouds under favorable conditions), or by using strong coupling, the initial "transient" period plays a relevant role, and the system shows features different from what we have seen previously. Within these time scales, indeed, one cannot consider the atomic polarization as an explicit function of the instantaneous electric field, therefore it is not possible to interpret the response of the medium in terms of susceptibility: to determine the evolution of the system, one needs to solve the single atom equations of motion 1.29.
In this framework, it is convenient to cast 1.29 in a geometrical form that allows a representation of the atomic state as a fictitious 3-D pseudo-vector, and of its evolution as a precession around an axis defined by the characteristics of the perturbation. Even if an atomic state is determined by three parameters (the amplitude probabilities for the two levels and their relative phase), the normalization condition reduces them to two, which corresponds to fixing the amplitude of the vector reducing its dynamics on the surface of a sphere. Defining three vector components as $r_1 = 2\,Re(\rho_{12})$, $r_2 = 2\,Im(\rho_{12})$ and $r_3 = (\rho_{22} - \rho_{11})$, and rearranging 1.29 to obtain expressions for these new variables, one finds that the vector $\bar{r}$ obeys the simple equation

$$\frac{d}{dt}\vec{r} = \vec{\omega}(t) \times \vec{r} \tag{1.52}$$

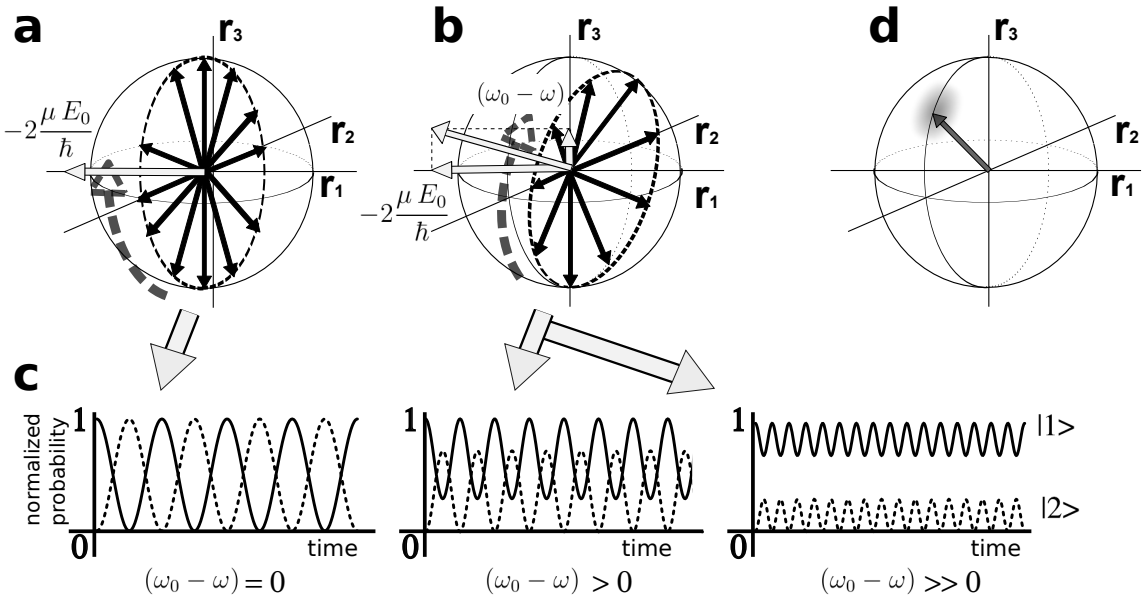


Figure 1.5: Bloch sphere representation of the evolution of a two level atom under an external perturbation. In **a** and **b**, the Rabi flopping phenomenon is represented, respectively for a resonant and for a slightly out of resonance perturbation. The state of the atom, as it evolves in time, is represented by the black arrows. The perturbation is represented by the light arrows. In **c**, the corresponding occupation probabilities for the two states is reported in the resonant, near resonance, and far from resonance cases (respectively from left to right). For larger detunings, the frequency of the oscillations is enhanced while their amplitude is reduced. In **d** the representation in the Bloch sphere of an atomic coherent state (see section 1.2.4) is reported.

where

$$\begin{cases} \omega_1 = -\frac{\mu}{\hbar}(E(t) + E(t)^*) & \left(\omega_1 = \frac{H'_{21}+H'_{12}}{\hbar}\right) \\ \omega_2 = i\frac{\mu}{\hbar}(E(t) - E(t)^*) & \left(\omega_2 = i\,\frac{H'_{21}-H'_{12}}{\hbar}\right) \\ \omega_3 = \omega_0 & \left(\omega_3 = \frac{H_{22}-H_{11}}{\hbar}\right) \end{cases} \tag{1.53}$$

with $\mu = \mu_{12} = \mu_{21} \in \mathbb{R}$ as set in sec2.2 . In bracket I show the form of $\vec{\omega}$ for a generic two states Hamiltonian $H = H_0 + H'$ with a perturbative term $H'$. The meaning of $\vec{r}$ components follows from their definitions: $r_3$ represents the imbalance in occupation probability for the two states, while $r_1$ and $r_2$ contain the information about amplitude and phase of the non diagonal elements of the density matrix[16]. Actually they can be seen as the counterparts of the quadratures operators for the states of light, in the sense that they are defined as the quadratures components of $\rho_{12}$.

To proceed with the calculation we have to specify the characteristics of both the transition and the applied electromagnetic field.

For the very simple case of an harmonic linear perturbation $E = E_0(e^{i\omega t} + e^{-i\omega t})$, one gets

$$\omega_1 = -4\frac{\mu\, E_0}{\hbar}\, cos(\omega\, t) \qquad \omega_2 = 0 \qquad \omega_3 = \omega_0$$

In this form the evolution of $\vec{r}$ is not simple to understand, but one can manipulate the equations as we have done to get 1.30 for the slowly varying variables $\sigma_{ij}$. Here we obtain the system 1.52 for a "slowly varying" Bloch vector [17] $\vec{\tilde{r}} = (2\, Re(\sigma_{12}),\ 2\, Im(\sigma_{12}),\ (\rho_{22} - \rho_{11}))$ :

$$\frac{d}{dt}\vec{\tilde{r}} = \vec{\tilde{\omega}}(t)\ \times\ \vec{\tilde{r}} \qquad \vec{\tilde{\omega}}(t) = \left(-2\frac{\mu\, E_0}{\hbar}\ ,\ 0\ ,\ (\omega_0 - \omega)\right) \tag{1.54}$$

From 1.52, 1.53 and 1.54 one finds that:

- without any perturbation, $\vec{r}$ rotates around the third axis with angular velocity $\omega_0$, keeping constant both the $r_3$ component and the coherent amplitude $r_1^2 +$

[16] Considering a dipole transition, $r_1$ and $r_2$ correspond to the dipole moment components in the normal plane of real space with respect to the quantization direction

[17] The first step by switching to a rotating frame following the angular velocity $\vec{\Omega} = (0, 0, \omega)$, in which $\vec{\omega}$ becomes $\vec{\tilde{\omega}} = (\omega_1\, cos(\omega t) + \omega_2\, sin(\omega t)\ ,\ -\omega_1\, sin(\omega t) + \omega_2\, cos(\omega t)\ ,\ \omega_0 - \omega)$; the second step calculating time averaged values for the terms oscillating at optical frequencies (RWA):
$\tilde{\omega}_1 = -4\mu E_0/\hbar\, cos^2(\omega t) \to -2\mu E_0/\hbar$; $\tilde{\omega}_2 = 4\mu E_0/\hbar\, cos(\omega t)\, sin(\omega t) \to 0$; $\tilde{\omega}_3 = (\omega_0 - \omega) \to (\omega_0 - \omega)$

$r_2^2$, while the phase of the latter oscillates at a rate equal to the difference in energy between the two levels. This reflects the fact that with no applied field no transition can take place, the possibility of spontaneous transitions being excluded from in the model due to the classical representation of the field.

- in the presence of some perturbation ($E_0 \neq 0$), the problem is reduced to the precession of $\vec{\tilde{r}}$ about a stationary vector such as $\vec{\tilde{\omega}}$ in 1.54. The rate of precession is

$$|\vec{\tilde{\omega}}| = \sqrt{\left(2\frac{\mu\, E_0}{\hbar}\right)^2 + (\omega_0 - \omega)^2} \tag{1.55}$$

resulting in an oscillation of the occupation probability (in the case that we start with the atom in the state $|1\rangle$) as

$$\tilde{r}_3 = r_3 = 2\frac{\left(2\frac{\mu\, E_0}{\hbar}\right)^2}{|\bar{\tilde{\omega}}|^2}\, sin^2\left(\frac{|\vec{\tilde{\omega}}|}{2}\, t\right) - 1 \tag{1.56}$$

In terms of single state occupancy probability, the result for $r_3$ leads to

$$\begin{cases} |\rho_{11}|^2 = 1 - \frac{4|\Omega|^2}{4|\Omega|^2+\Delta\omega^2}\; sin^2\left(\frac{\sqrt{4|\Omega|^2+\Delta\omega^2}}{2}\, t\right) \\ |\rho_{22}|^2 = \frac{4|\Omega|^2}{4|\Omega|^2+\Delta\omega^2}\; sin^2\left(\frac{\sqrt{4|\Omega|^2+\Delta\omega^2}}{2}\, t\right) \end{cases} \tag{1.57}$$

where we have defined the Rabi frequency $\Omega = \frac{\mu E_0}{\hbar}$ and the detuning from resonance $\Delta\omega = (\omega_0 - \omega)$, so that $|\bar{\tilde{\omega}}|^2 = 4|\Omega|^2 + \Delta\omega^2$. Thus, at resonance, the occupation probability is transferred completely from one state to the other with an oscillation frequency given by the Rabi frequency $|\Omega|$. The phenomenon is referred to as Rabi flopping. Out of resonance, instead, the transfer is not perfect, but attains a fraction $\frac{4|\Omega|^2}{\sqrt{4|\Omega|^2+\Delta\omega^2}}$, while its oscillation gets faster as $\frac{1}{2}\sqrt{4|\Omega|^2 + \Delta\omega^2}$, which can be referred to as generalized Rabi frequency.

If the coherence time of the field (that is defined as the average time during which it phase remains constant) is shorter than the Rabi oscillation period, the transition is thwarted: it can be considered as an ultimate limit to the coherence time attainable in the system. One needs to use modulation techniques or optical phase locking to establish longer coherence times.

The Bloch vector representation is particularly advantageous when one wants to predict the effect of a series of pulses: e.g. it gives a simple illustration of Ramsey-like interferometry, as shown in chapter 4; another example is the photon echo effect (mentioned in sec 2.2.4 ). In these cases it is useful to speak in terms of "pulse area" $A = \int \Omega(t)\, dt$, which accounts for the effect of the whole envelope of a pulse. It is evaluated in radians and corresponds to the total rotation imposed to $\bar{\bar{r}}$ within the passage of the pulse.

Finally I want to mention another (simpler) system of equations, named "rate equations" [121], which is often sufficient for predictions concerning an ensemble of atoms interacting with an electromagnetic field (e.g. for laser dynamics). Rate equations involve only population and field intensity, discarding phase relations. Actually optical Bloch equations become redundant in two regimes:

- in the limit of broad-band field, that is when field frequency spread exceeds the linewidth of the atomic transition $\gamma' = \gamma_{em} + \gamma_{coll}$ (where $\gamma_{em}$ and $\gamma_{coll}$ stay respectively for spontaneous emission rate and collisional broadening);
- in the limit of large collisional broadening, in which $\gamma' \gg \gamma_{em}$; the equivalence between the two descriptions holds in this case for any bandwidth of the incident light

The same results apply for other forms of broadening, even inhomogeneous such as Doppler broadening [74].

### 1.2.4 Atomic coherent states

To obtain the collective behavior of an atomic sample, one has to sum the Bloch vectors related to each atom. The components of such a collective Bloch vector $\vec{R}$ represent the population imbalance ($R_3$) and the macroscopic coherence ($R_1$ and $R_2$) of the sample. While in single atom systems the norm of the Bloch vector is fixed (equal to $u$), for $N$-atoms states it can take any value in the interval $[\,0; N \times u]$, the latter limit occurring in the special case where all the atoms are in the same state.

If $\vec{r}_1$ and $\vec{r}_2$ are two single atom vectors, one gets from 1.52

$$\frac{d}{dt}(\vec{r}_1 \cdot \vec{r}_2) = (\vec{\omega} \times \vec{r}_1) \cdot \vec{r}_2 + (\vec{\omega} \times \vec{r}_2) \cdot \vec{r}_1 = \vec{\omega} \cdot (\vec{r}_1 \times \vec{r}_2 + \vec{r}_2 \times \vec{r}_1) = 0 \qquad (1.58)$$

So, due to the fact that the evolution in the Bloch sphere is a precession (1.52), the angles between the sub-vectors do not change during any coherent process, and the evolution of the system can be described by the motion of a rigidly connected set of Bloch vectors whose sum $\vec{R}$ obeys 1.52.

The passage from Rabi oscillations to the asymptotic steady state characterized by the susceptibility $\chi$ is due to coherence and population decay rates, which decrease the amplitude of the oscillations till their complete annihilation. In the steady state, atoms keep on undergoing Rabi oscillations, but each with a random phase, so that the collective dynamics average to zero.

This representation is however not complete in quantum mechanics terms, since looking at collective atomic states as exactly defined Bloch vectors is somehow similar to looking at field eigenstates as simple vectors in the Fresnel reference frame: there is no account for quantum fluctuations. Actually any two level system shows the same characteristics as spin 1/2 systems, so it is simple to write expressions for statistical properties. Indeed, operators for the two level system are
populations $\hat{\pi}_1 = |1\rangle\langle 1| \quad \hat{\pi}_2 = |2\rangle\langle 2|$ and coherences $\hat{\sigma}_+ = |2\rangle\langle 1| \quad \hat{\sigma}_- = |1\rangle\langle 2|$
and introducing linear combinations of them as

$$\hat{j}_x = \frac{\hat{\sigma_+} + \hat{\sigma}_-}{2} \qquad \hat{j}_y = \frac{\hat{\sigma}_+ - \hat{\sigma}_-}{2i} \qquad \hat{j}_z = \frac{\hat{\pi}_2 - \hat{\pi}_1}{2} \tag{1.59}$$

one finds that $\hat{j}_i$ operators obey the standard commutation relations for angular momentum

$$\left[\hat{j}_i, \hat{j}_j\right] = i\epsilon_{ijk}\hat{j}_k \qquad \epsilon_{ijk} \text{ Ricci tensor} \tag{1.60}$$

as well as the specific relations for 1/2 spins

$$\hat{j}_i^2 = \frac{\mathbb{I}}{4} \qquad \forall \text{ i;} \qquad \hat{j}^2 = \sum_{i=x,y,z} \hat{j}_i^2 = \frac{3}{4}\mathbb{I} \tag{1.61}$$

Considering an ensemble of $N$ atoms, it is possible to define collective operators as

$$\hat{J}_i = \sum_{i=1}^{N} \hat{j}_x^i \tag{1.62}$$

which, even if they have no well defined expectation values for $\hat{J}_i^2$ operators (due to the possibility of correlations between the spins), still obey commutation rules

analogous to 1.60

$$\hat{J}_x^2 = \underbrace{\sum_{i=1}^{N} (\hat{j}_x^i)^2}_{\frac{N}{4}\mathbb{I}} + \underbrace{\sum_{i \neq j} \hat{j}_x^i \, \hat{j}_x^j}_{correlations} \qquad \left[\hat{J}_i, \hat{J}_j\right] = i\epsilon_{ijk}\hat{J}_k \tag{1.63}$$

It is thus possible to determine Heisenberg uncertainty relations between the collective spin components similar to those concerning the field quadratures, based on the derivation on (1.5, 1.6) after application of the commutation relations 1.63.
The modulus of the collective spin follows $\langle \hat{\vec{J}} \rangle^2 = \langle J_x \rangle^2 + \langle J_y \rangle^2 + \langle J_z \rangle^2 \leq \left(\frac{N}{2}\right)^2$ attaining the maximal value $N/2$ if all the atoms are in the same state (as already said at the beginning of this section). Let's consider the simplest one among these states: an ensemble of $N$ atoms all in the ground state. In this case $\langle \hat{J}_x \rangle = \langle \hat{J}_y \rangle = 0$ while $\langle \hat{J}_z \rangle = N/2$; for the transverse components one finds

$$\Delta^2(\hat{J}_x)\, \Delta^2(\hat{J}_y) \geq \frac{\langle \hat{J}_z \rangle^2}{4} = \frac{1}{4} \times \left(\frac{N}{2}\right)^2 \tag{1.64}$$

If the fluctuations of the atoms are uncorrelated, this uncertainty is isotropic, so that $\Delta^2(\hat{J}_\theta) = N/4$, with $\hat{J}_\theta = \hat{J}_x \, cos\theta + \hat{J}_y \, sin\theta$ generic direction in the transverse plane. Actually this condition is valid for any vector belonging to the Bloch sphere of maximum radius $N/2$ (every atom in the same state), defining the transverse components as directions in the plane orthogonal to the mean vector $\vec{R}$.
As in the case of field coherent states, all these states can be generated by the application of a displacement operator $\hat{D}_\zeta$ to the ground state, so that they are named "atomic coherent states" [3]. Defining collective raising and lowering operators $\hat{R}_\pm$ defined as $\hat{R}_\pm = \sum_{i=1}^{N} \hat{\sigma}_\pm = \hat{R}_1 \pm i \, \hat{R}_2$, it is possible to determine such a displacement operator as

$$\hat{D}_\zeta = e^{\zeta \hat{R}_+ - \zeta^* \hat{R}_-} \tag{1.65}$$

As for the field[18] it is possible to factorize $\hat{D}_\zeta$ and find a simple expression for the states in terms of the complex parameter $\zeta$ defining the displacement

$$|N/2, z\rangle = \prod_{i=1}^{N} \frac{1}{\sqrt{1+|z|^2}} (|1\rangle_i + z|2\rangle_i) \qquad \text{with } z = tg\,(|\zeta|)\; e^{i\, arg(\zeta)} \tag{1.66}$$

[18] even if the calculation is more complicated in this case

As expected, this is a simple product state, in which each atom is in the same pure state. From expectation values for operators $\hat{R}_{\pm}$:

$$\langle N/2, z|\hat{R}_{-}|N/2, z\rangle = \frac{N}{2}\frac{2z}{1+|z|^2} \qquad \langle N/2, z|\hat{R}_{+}|N/2, z\rangle = \frac{N}{2}\frac{2z^*}{1+|z|^2}$$

one can write down expectation values for the $\hat{R}_i \quad (i = 1, 2, 3)$

$$\langle N/2, z|\hat{R}_1|N/2, z\rangle = \frac{N}{2}\frac{1}{1+|z|^2}\,2\,Re(z) \qquad \langle N/2, z|\hat{R}_2|N/2, z\rangle = \frac{N}{2}\frac{1}{1+|z|^2}\,2\,Im(z)$$

$$\langle N/2, z|\hat{R}_3|N/2, z\rangle = \frac{N}{2}\frac{1}{1+|z|^2}\,(|z|^2-1) \tag{1.67}$$

One finds that for a coherent state $\sum_{i=1,2,3}\langle\hat{R}_i\rangle^2 = N/2$ and the expectation values for the collective Bloch vector components are well defined, which confirms that they are a symmetrized generalization of the single atom state.

Last I want to mention that, still in analogy with quantum field theory, coherent states have the physical property of being produced by classical sources. It can be shown indeed ([3]) that the application of a classical field as 1.1 to the collective ground state $|N/2, -N/2\rangle$ results in a coherent state.

### Some features of coherent interaction

Optical coherent effects show exciting features that can be really far from conventional treatment of light propagation in terms of basic medium parameters (such as dielectric susceptibility). Among these, one can mention self-induced transparency, superfluorescence and photon echo. Here I will present the first and the third phenomenon briefly. The second one being more relevant for this thesis will be treated in the next section.

The phenomenon of *self-induced transparency* consists in the fact that above a well defined intensity threshold, short resonant pulses of a given duration propagate through a normally absorbing medium with anomalous low attenuation. This happens when the pulse is short with respect to the relaxation time in the medium. After a few classical absorption lengths, the pulse reaches a steady state in which its width, energy, and shape remain constant, while its group velocity is greatly reduced by several orders of magnitude. A rigorous theoretical demonstration of this effect can be found in [121]. However, the fundamental concept behind it is simple: the absorbing medium

reshapes the pulse until it gets a pulse area $\int \Omega \, dt$ equal to the closest integer multiple of $2\pi$. Once this area is reached, the coherent interaction exactly transforms the whole pulse in atomic excitation and back in photons, and no excitation can be lost by incoherent emission (as spontaneous emission), because no excitation remains in the medium for a long enough time.

In *photon echo*, the basic experiment involves the application of two intense and short optical pulses to an ensemble of resonant absorbing atoms with a small amount of inhomogeneous broadening. One observes a further radiated pulse (the echo), delayed with respect to the second input pulse by a time equal to the separation of the two exciting pulses. The short length of the pulses allows coherent and resonant interaction with the whole ensemble of atoms disregarding the spreading of the frequency of resonance. If the first pulse has an area equal to $\pi/2$, in the time $\tau$ between the two pulses $\vec{r}$ evolves in the $(1,2) - plane$. Due to the inhomogeneous broadening, there will be components $\{\vec{r}_i\}$ turning at different velocities, thus loosing the macroscopic polarization. By applying a second pulse with an area equal to $\pi$, the distribution of vectors $\{\vec{r}_i\}$ in the $(1,2) - plane$ is reversed, bringing to the reconstruction of the macroscopic polarization after a time interval. This phenomenon has as consequence the emission of a superfluorescent echo pulse[19].

### 1.2.5 Superfluorescence

We now consider a coherent atomic state in the $(1,2) - plane$: it has the largest dipole moment possible forthe ensemble, with all the atoms contributing coherently to a single giant dipole moment. In general, the collective atomic states with some component in the $(1,2) - plane$ are called superfluorescent states, the term superfluorescence denoting the increased radiation rate that characterizes the spontaneous decay of the giant dipole.
The general form for these states is

$$|\Phi\rangle = \prod_{j=1}^{N} (a_1|1\rangle + a_2|2\rangle) \tag{1.68}$$

[19] see next section for comments on the concept of superfluorescence

in which $a_1$ and $a_2$ are arbitrary complex numbers, with $(|a_1|^2+|a_2|^2 = 1)$, that are the same for every atom. It can be shown (see for example [78]) that for such a collective state, under the condition of spatial confinement within a radiation wavelength[20], the probability $P(t)$ per unit time for the emission of a photon (summarizing both on wave vector directions and polarizations) is

$$P(t) = A[N|a_2|^2 + N(N-1)|a_2|^2|a_1|^2] \tag{1.69}$$

where $A$ represents the Einstein coefficient for spontaneous emission. In the expression we have two terms:

- one proportional to the number of atoms $N$, as expected for independently radiating atoms; for a fully excited initial state, so that $a_1 = 0$, this is the only non-vanishing term;

- one proportional to $N(N-1)$, associated with a cooperative radiation process (it is present only for $N > 2$), which tends to dominate even for $|a_1|$ close to 0 when $N$ becomes a large number.

It follows that the rate of radiation of $N$ atoms so close to be perturbed by the field emitted by them selves can be much larger than in the case of $N$ independent radiating atoms, provided that the atoms are in a state described in 1.68 (not fully excited). This is the phenomenon called superfluorescence, which is similar but not identical to the superradiance of Dicke states. In the former case indeed one has a giant dipole moment while it is zero in the latter case[21].
To understand the evolution of the system, one can equalize $P(t)$ as defined in equation 1.69 to the definition of energy loss rate $\frac{d}{dt}\langle\hat{H}_0\rangle = -\hbar\omega_0 N\frac{d}{dt}|a_2|^2$ for the atomic ensemble, obtaining an equation of motion

$$-\frac{d}{dt}|a_2|^2 = A|a_2|^2[1 + (N-1)|a_1|^2] \tag{1.70}$$

valid when, during the whole evolution, the electromagnetic field remains close to the vacuum state. For $N = 1$, one recovers the exponential decay rate that is characteristic of spontaneous emission; for $N > 1$ instead, the solution is much more

[20] so that every atom sees the same field

[21] Dicke state are of the form $\prod_i^N |j_i\rangle$, with $j = 1, 2$, in which each atom has zero dipole moment

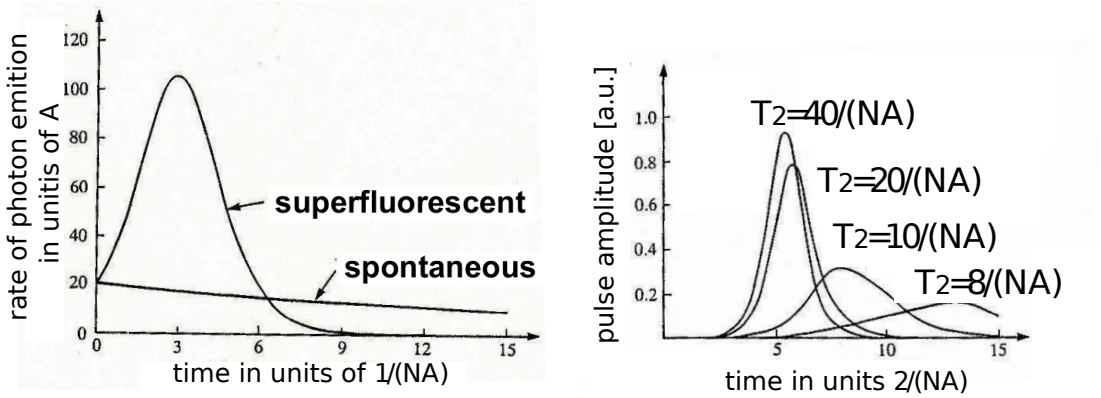


Figure 1.6: Rate of photon emission (left), and temporal profile of the emitted pulse (right) related to the phenomenon of the superfluorescence. At the beginning, the emission rate is equal to the spontaneous emission rate for $N$ non-interacting atoms. After the emission of few photons in random directions, the cooperative effect of the macroscopic dipole moment takes place . The photon flux, instead of following the normal exponentially decreasing profile, has the shape of a pulse. The time delay at which the pulse takes place with respect to the formation of the macroscopic dipole moment, as well as its time spreading, strongly depends on the coherence decay rate $T_2$ characterizing the medium. The curves reported in this figure are taken from [78].

complicated, and gives for the occupation probability $|a_2|^2$ and the rate of photon emission $f(t)$

$$|a_2|^2 = \frac{N}{N + e^{A\,N\,t} - 1} \qquad f(t) = \frac{A\,N^3 e^{A\,N\,t}}{(N + e^{A\,N\,t} - 1)^2} \tag{1.71}$$

At $(t = 0)$ the photon flux is equal to that for $N$ non-interacting atoms[22] $(f(0) = A\,N)$; however, at later times the cooperative effects come into play, greatly modifying the emission rate and leading to the generation of a "compact" pulse (as reported in fig.1.6). It can be shown that intensity peak of this pulse is proportional to $N^2$ and occurs at $t_0 = \frac{ln(N+1)}{N\,A}$ ($t = 0$ is the starting point of existence of the giant dipole), while its width turns out to be of the order of $2/(N\,A)$.

[22] i.e. $N$ times the spontaneous emission rate

To evaluate the effect of a non perfect preparation of the state, one can look back at the collective Bloch vector $\vec{R}$ as the sum of a number of Bloch sub-vectors, each one related to part of the ensemble or even to a single atom. At the end of the superfluorescent pulse, $\vec{R}$ points down, but due to the non perfect alignment of the sub-vectors, some of them still have a transverse component, and some energy remains trapped in the atomic system , to be ultimately dissipated by non-cooperative processes.
When inhomogeneous broadening is taken into account, as shown in [78], its main effect is to limit the amount of cooperative radiation, forcing some energy to be radiated non-cooperatively (fig1.6).

Finally we want to stress some particular characteristics of the fluctuations, that cannot be derived from this mean field treatment. The delay $t_0$ is very sensitive to both the initial excitation state of the atomic system, and the initial radiation rate. The first one undergoes preparation, or at least quantum, fluctuations; while the second one is largely governed by non-cooperative single-atom spontaneous emission, which in turn is subject to very large quantum fluctuations. It is therefore expected that $t_0$ varies widely from pulse to pulse.

## 1.3 Bose-Einstein condensate

In this section I will introduce the main features of a Bose-Einstein condensate (BEC) of alkali gases. I will give a general overview of the subject, stressing fundamental aspects and characteristics that we have exploited in our experiments. General and particular technical aspects for the production of the condensate in our experiment can be found in [54] (as they are the central subject in the thesis of a former PhD student). [65] provide a complete overview on condensation.

BEC is a pure quantum phenomenon consisting in the macroscopic occupation of a single-particle state by an ensemble of identical bosons in thermal equilibrium at finite temperature. The whole system can be represented by a single wave function, most like a single particle wave function times the number of particles. This way we can look at BEC as a macroscopic representation of the microscopic quantum world. From the quantum point of view, in a gas of identical particles at thermal equilibrium, the position of a single particle has a certain amount of uncertainty associated with the thermal momentum distribution, estimated by the *deBroglie* wavelength[23]: $\lambda_{dB} = \frac{h}{2\pi m k_B T}$ . When $\lambda_{dB}$ becomes comparable with the mean inter-particle distance, the quantum indistinguishability of the particles cannot be neglected and the quantum nature of the particles, whether they are bosons or fermions, becomes important. For bosons, a critical temperature $T_c$ exists below which the particles start to macroscopically occupy the lowest energy state and a Bose-Einstein condensate ($BEC$) forms. The same behavior is classically (by Maxwell-Boltzamann statistics) predicted for $T = 0$, where entropic term in the free energy vanishes. Bose statistics allows it to happen for $T = T_c > 0$, basically because at low temperature entropy starts to be maximized by forming a condensate in the ground state and distributing the remaining atoms among higher energy states.

For ideal gases BEC transition occurs when $\quad n\,\lambda_{dB}^3 \simeq 2.6 \qquad \left(n = \frac{N}{V}\right)$

where $n$, $V$, $N$, respectively stay for: number density, available volume and number of particles[24]. In the real world alkali gases are always very far below this condition, and huge efforts have to be made to achieve the density-temperature regime for condensation. Having a look on the phase diagram (fig.1.7.a), we can understand that a

[23] meaning of symbols:

$h$ - Planck constant; $m$ - particle mass; $k_B$ - Boltzmann constant; $T$ - temperature

[24] i.e. mean distance between particles = $(1/\mathrm{n})^{\frac{1}{3}}$

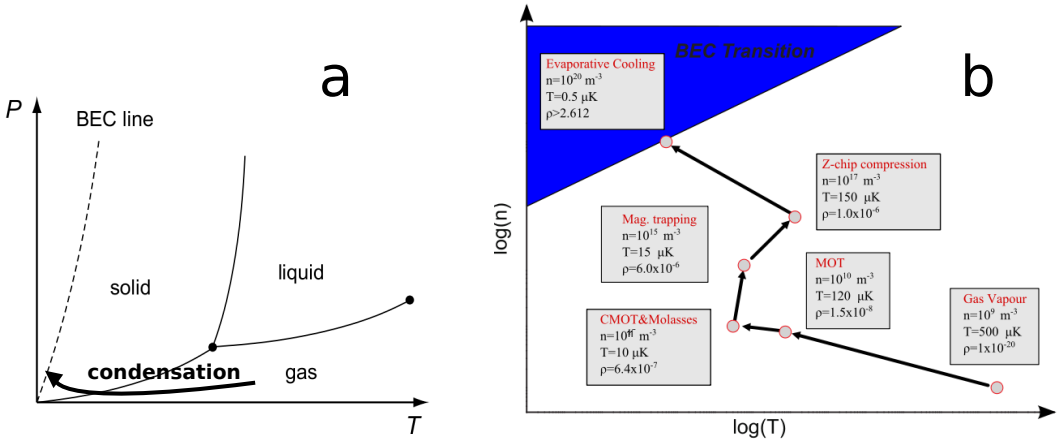


Figure 1.7: **a** - Phase diagram of a typical bosonic element. The *BEC* region is dashed since the true equilibrium state of the system is the solid state. The arrow indicate the road traveled to reach the condensation in the case of cold atoms.
**b** - The road traveled to reach the condensation with our atom chip apparatus. The main aspects are common to many apparatuses for the production of condensates.

high density makes the gas collapse into a solid phase (preventing condensation), the key to observe *BEC* at low temperature being maintaining of $\lambda_{dB}$ greater than the *interaction distance* while both lowering the temperature and increasing the density of the sample. Actually the condensed phase remains a metastable state, recombination processes ($j$-body collisions are proportional to $n^{j-1}$) always providing an ultimate life time limit.
In part b of fig1.7 our *road to condensation of* $^{87}Rb$ (3D mirror-MOT stage + magnetic trapping + RF evaporative cooling) is reported. The work is done by two steps: laser cooling and evaporative cooling. The former stage is able to collects a large number of atoms (up to billions, around $10^8$ in our case) and efficiently cool them down to tens of $\mu K$ temperatures, but holds an ultimate limit on achievable phase space density still $6-7$ order of magnitude far from condensation. This is not the case for evaporative cooling, which in turns has a limited operating time due to recombinations and noise heating of the set-up. Finally, the previous stages are required to get a sufficiently high initial scattering rate, which is proportional to the density and the square root of temperature. Efficient evaporation needs to take place

in a quasi-thermal equilibrium state down to condensation[25]. Various heating rates and loss channels giving a limited life time for any trapped cloud (few seconds in our case), this means a higher limit for time of thermalization, and so a lower limit for the scattering rate.
One fascinating aspect of $BEC$ is the presence of coherence in a macroscopic quantum system. This is possible, like for laser light, by exploiting a mechanism that enhances the population of a single state: bosonic stimulation.
According to this principle, the probability distribution for the final state of a scattering event is modified by the population of these final states. Like for photons, the scattering rate into a certain state is enhanced by a factor of $(N_0 + 1)$ with respect to the case of isolated events, where $N_0$ is the population of the final state.
In a normal gas, atoms scatter among a myriad of possible quantum state. For bosons instead, when the critical temperature $T_c$ is reached, the atoms tend to scatter into the lowest energy state. This discontinuity in the behavior is due to the fact that because of the presence of a $BEC$ (that is a macroscopic population of the ground state), stimulated scattering into this state occurs. This leads to an increase of the population and an enhancement of the stimulation. The scattering rate out of the condensate instead is simply proportional to the condensed fraction, due to the fact that there are no other state macroscopically populated. Thermal equilibrium is reached when the number of collision into and out of the $BEC$ are equal, that is the usual statistical concept of detailed balance.

### 1.3.1 Trapped and free falling atomic clouds characteristics

In this section I show how a magnetically trapped condensate of alkali atoms looks like from the experimental point of view. Geometrical features and fundamental quantities are recalled both for trapped and free falling samples.
Let's consider a trap made of a $3D$ harmonic potential, that is an excellent model in most cases:

$$U(\vec{r}) = \frac{1}{2}m(\omega_x x^2 + \omega_y y^2 + \omega_z z^2) \tag{1.72}$$

[25]Evaporative cooling works by removing high velocity atoms from the sample, waiting for rethermalization before lowering the edge velocity. Advancing in quasi-thermal equilibrium, we maximize the number of atoms that survive for successive steps.

where $\omega_i$ stays for the trap pulsation for the three directions.

**Thermal cloud:** First I recall the case of a thermal cloud, that is a sample at $T \gg T_c$. Normally it also means $k_B T \gg \hbar\omega_i$, making a semi-classical approach valid ([5]) and leading to a density distribution of the form

$$n_{th}(\vec{r}) = \frac{1}{\lambda_{dB}^3} \; g_{\frac{3}{2}}\left(e^{\frac{\mu - U(\vec{r})}{k_B T}}\right) \qquad g_{\frac{3}{2}}(z) = \sum_i \frac{z^i}{i^{\frac{3}{2}}} \quad Bose\ function \tag{1.73}$$

where $\lambda_{dB}$, $k_B$ and $T$ are defined as before, while $\mu$ is the chemical potential.
This is equal to the classical result for distinguishable particles, corrected for the effects of quantum statistics, which gives a density increase by a factor $g_{\frac{3}{2}}(z)/z$. The sample has a Gaussian shape, with spatial dimensions that scale as the inverse of the corresponding trap frequencies.
After the trap is switched off, atoms expand ballistically from their initial position. At sufficiently large times ($t \gg \omega_i^{-1}$), when the cloud is already much larger than its original size, its evolution reduces to an isotropic expansion related to the sample temperature as

$$n_{th,tof}(\vec{r}) = \frac{1}{\lambda_{dB}^3} g_{\frac{3}{2}}\left(e^{\frac{\mu - \vec{r}^2/(2t^2)}{k_B T}}\right) \tag{1.74}$$

This is the basic equation for estimating the temperature of a thermal cloud by density profile imaging.

*BEC* **at zero temperature:** For a condensed sample without excitation, the many-body state can be described by a single complex order parameter $\psi(\vec{r})$ that follows the Gross-Pitaevskii equation

$$i\hbar\frac{d\psi}{dt} = -\frac{\hbar^2}{2m}\nabla^2\psi + U(\vec{r})\psi + g|\psi|^2\psi \qquad g = \frac{4\pi\hbar a}{m} \tag{1.75}$$

U describes the effect of two-body collisions in the regime of $s-wave$ scattering ($a$ is the s-wave scattering length, $|\psi|^2$ represents the density), which is the only relevant contribution in this density/temperature condition.
Solution for the equation 1.75 are simple in two limit cases.
For $\underline{|\psi|^2 U \ll \hbar\omega_i}$ *(ideal gas limit)*, we can neglect the interaction term, turning to a

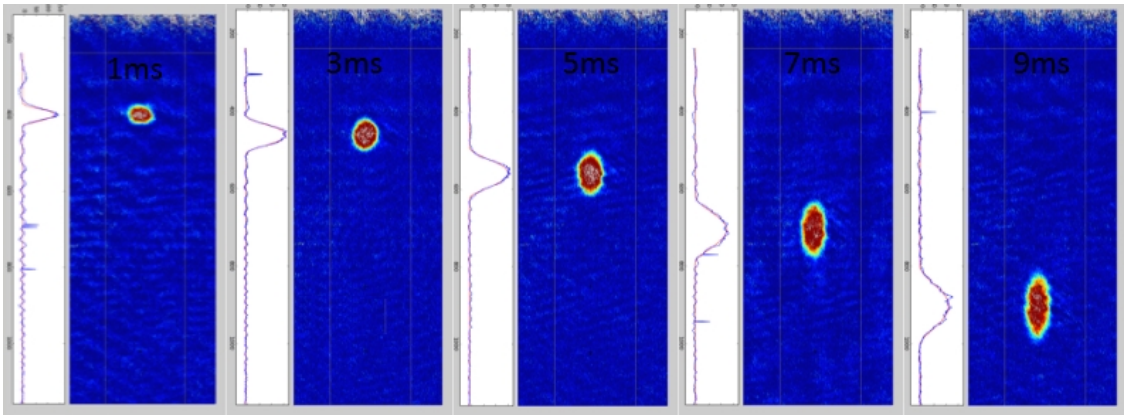


Figure 1.8: Sequence of images of the free falling condensate for different times of flight after releasing. One can see the inversion of the aspect ratio, attained for $3\,ms$ of free expansion. Within the framework of this thesis, manipulation of the sample always takes place in the trap or before the first reported image, while imaging for detection of the induced effects are usually taken at a time close to that of the last image.

simple "single particle in external potential" problem: every atom stays in the single particle ground state, that shows a Gaussian probability distribution of spatial extent inversely proportional to the trap frequencies

$$|\psi(\vec{r})|^2 = n_c(\vec{r}) = \frac{N}{\pi^{3/2}} \prod_{i=1}^{3} \left( \frac{1}{\sqrt{\hbar/(m\omega_i)}} e^{-\frac{r_i^2}{\hbar/(m\omega_i)}} \right) \tag{1.76}$$

The quantity $\sqrt{\frac{\hbar}{m\omega_i}}$ is defined as "oscillator length" $(l_i^{ho})$.
In free expansion, the momentum distribution (determined by the uncertainty principle) tends to invert the ratio between the different spatial dimensions, and for $t \gg \omega_i^{-1}$ the cloud gets a gaussian shape with dimensions given by $r_i^2 = \frac{\hbar\omega_i}{m} t^2$ .
For $|\psi|^2 U \gg \hbar\omega_i$ *(Thomas-Fermi limit)*, equation 1.75 can be simplified by neglecting the kinetic energy term, leading to a time independent form as

$$\mu\,\psi(\vec{r}) = V(\vec{r})\,\psi(\vec{r}) + g|\psi(\vec{r})|^2\,\psi(\vec{r}) \tag{1.77}$$

In this case (which is the most common one, and which the case of our experiment too), one can think of the condensate as a fluid that follows the trap shape, filling the

bottom of the trapping potential up to a certain energy value (corresponding to the chemical potential $\mu$). For harmonic traps, indeed, the density profile is parabolic

$$|\psi(\vec{r})|^2 = n_c(\vec{r}) = \begin{cases} \frac{\mu - U(\vec{r})}{g} = \frac{1}{g}(\mu - \frac{m}{2}\sum_{i=1}^{3}\omega_i^2 r_i^2) & if \quad \mu - U(\vec{r}) > 0 \\ 0 & if \quad \mu - U(\vec{r}) < 0 \end{cases} \tag{1.78}$$

The free falling expansion shows an evolution similar to the previous case: we see a rescaling of the parabolic profile, with a progressive inversion of the spatial aspect ratio[26]. We can recognize three stages. At the very beginning, interaction energy is converted into kinetic energy through an accelerating expansion in the most strongly confined direction(s). In a second stage, expansion becomes constant, and progressively involves the weakly confined direction(s). In the third stage, expansion gets an asymptotic aspect ratio $\frac{r_i}{r_j} \sim \frac{\pi}{2}(\frac{\omega_i}{\omega_j})^2$.
Our set-up is able to produce a cigar shaped condensate, with trap pulsations:
$\omega_x = \omega_z = \omega_\rho \sim 900Hz$; $\omega_y = \omega_\rho/18$. So, during expansion the cigar becomes a disk, overcoming the first stage after $t \sim 1\,ms$ and never reaching the third one (it should happen for $t > 100\,ms$). In fig1.8, a superposition of our $BEC$ pictures for different expansion times is reported. Within the framework of this thesis, manipulation of the sample always takes place in the trap or within the first $ms$ of expansion, while imaging for detection of induced effects on the sample are usually taken around $10\,ms$.

The chemical potential $\mu$ and the spatial extents $r_i$ of the $BEC$ can be calculated in the Thomas-Fermi limit by solving the system of equations[27]

$$\begin{cases} V = \frac{4}{3}\pi\left(\frac{\omega_1\omega_2}{\omega_0^2}\right) r_0^3 \\ \mu = \frac{1}{V}\left(\int_V U(\vec{r})\, d^3r + g\, N\right) \\ \mu = \frac{m}{2}\omega_0^2 r_0^2 \end{cases} \tag{1.79}$$

[26] in this case the final spatial aspect ratio is proportional to the square (rather than the square root) of the trap frequencies ratio

[27] the first equation is the volume formula for a 3D ellipsoid with axial aspect ratios fixed by the trap frequencies, $r_0$ being the extent in the spatial direction related to $\omega_0$; the second equation comes from an integral form of the 1.77 over the volume $V(r_0)$ occupied by the condensate $\int_V \mu\, d^3r = \int_V U(\vec{r})\, d^3r + g\int_V |\psi(\vec{r})|^2\, d^3r$; the third equation is the required equality for chemical and external potential where the wave function $\psi$ vanishes

which gives

$$r_0 = \left(\frac{15}{4\pi}\frac{gN}{m}\frac{\omega_1\omega_2}{\omega_0^4}\right)^{1/5} \qquad \mu = \frac{\hbar\omega_0}{2}\left(\frac{\omega_1\omega_2}{\omega_0^2}\frac{15aN}{l_0^{ho}}\right)^{2/5} \qquad r_{1,2} = \frac{\omega_0}{\omega_{1,2}}r_0 \tag{1.80}$$

The form for the maximal density $n_c(0,0,0) = \mu/g = \frac{1}{8\pi a l_0^{ho}}\left(\frac{\omega_1\omega_2}{\omega_0^2}\frac{15aN}{l_0^{ho}}\right)^{2/5}$ shows an interesting feature: it has no dependence on the mass of the particle, but only on total number of atoms $N$, trap frequencies $\omega_i$ and scattering length $a$.

## 1.4 Atomic sample manipulation tools

To manipulate and excite ultra-cold atomic samples one can use a number of electromagnetic field tools.

### 1.4.1 Magnetic fields

#### Static fields

DC magnetic fields can be used as trapping elements, both in quadrupole and harmonic (Ioffe-Pritchard) configurations. Particularly simple in magnetic traps is to change the shape and the aspect ratio by varying the field parameters. In order to have adiabatic changes (that is eigenstates changes without reducing phase space density), one has to fulfill the condition

$$\frac{d\phi}{dt} \ll \frac{\mu_B |\vec{B}|}{\hbar} = \omega_L \tag{1.81}$$

where $\mu_B$ is the Bohr magneton, $|\vec{B}|^2$ and $\phi$ are the modulus of the magnetic field and its direction[28]. Non-adiabatic passages lead to atom losses, due to transitions to non trapped orientation states. The most limiting aspect of magnetic trapping is in fact its internal state selectivity, that can actually turn optimal to get almost pure collective states.[29]
Adiabatic change is also employed for compressing the sample, that can play a crucial role in BEC experiments, because it leads to an increase of the collision rate before evaporative cooling [65]. In this case, an optimal procedure requires

$$\frac{d\omega_{trap}}{dt} \ll \omega_{trap}^2 \tag{1.82}$$

which can turn really difficult for weak traps. Violation of adiabaticity brings to higher temperatures, but does not have severe consequences: for harmonic traps, a sudden increase of the potential by a factor $\alpha$ gives a factor greater than $\sqrt{\alpha}$ in the

[28] This condition simply reflects the fact that a magnetic dipole can follow a turning magnetic field just if its Larmor period ($\frac{2\pi}{\omega_L}$) is sufficiently short respect to the time scale of the change

[29] Losses can occur even in static traps, due to field variations seen by the atoms in their motion. This phenomenon take the name of Majorana spin flip, and can be avoided by ensuring a minimum amplitude of the field in the whole space occupied by the sample.

scattering rate, to be compared with a factor $\alpha$ gained for a fully adiabatic passage. In our set-up, even if the life time of the magnetically trapped clouds is quite short ($\sim 2s$), the initially high trap frequencies allow an adiabatic compression of the order of $1\,kHz$ (from $200\,Hz$ to $900\,Hz$) in $0.5\,s$.
Magnetic field gradient can be used to launch atoms, providing a useful tool for ultracold atoms, since the standard technique of accelerating molasses severely heats up samples at sub-recoil temperatures.

**RF waves**

Radio-frequency radiation can be used to change the magnetic orientation state of trapped atoms. This is used to switch atoms from a trapped to an untrapped hyperfine state, both for evaporative cooling and for realizing an output coupler for an atom laser.
RF methods are also used for coherent interaction, due to the fact that strong coupling between states is possible with almost zero spontaneous emission decay. Coherence time in those experiments (as for example Ramsey interferometry) is mostly limited by collision induced spin changes and both spatial and temporal inhomogeneity of the magnetic field.

### 1.4.2 Optical dipole forces

Light effects near an atomic resonance are almost dominated by a dissipative force which is the *radiation pressure force* due to absorption of photons from a laser beam followed by spontaneous emission. This force is indeed related to the momentum carried by photons ($\hbar k$, where $k = 2\pi/\lambda$), and is the basic mechanism of the common laser cooling techniques (as MOT and optical molasses).
Sufficiently out of resonance, dissipative effects fall down, leaving dispersive effects dominate. They result in an off-resonance force (*dipole force*) which works without exciting atoms, and is proportional to the intensity gradient of the field.
Starting from the expression for the atomic polarization $\bar{P}$ obtained with a semiclassical model in section 2.2 (1.33, 1.31), one can derive expressions for the two forces by rewriting 1.35 for the single atom in the out-of-resonance limit

$$p = \epsilon_0 \chi E \sim -\frac{\mu^2}{\hbar}\left(\frac{1}{\Delta} + i\frac{\Gamma}{\Delta^2}\right) E \tag{1.83}$$

where we define $1/T_2 = \Gamma$ (the decay rate for the excited state) and $\Delta N_0 = -1$, while[30] $(\omega - \omega_0) = \Delta$.
The average energy absorbed by an atom in a unit time, divided by the photon energy $\hbar\omega$, gives an estimation for the photon scattering rate $\Gamma_{sc}$

$$\Gamma_{sc} = \frac{\left\langle \dot{\vec{p}} \cdot \vec{E} \right\rangle}{2\hbar\omega} = -\frac{1}{2\hbar c} Im(\chi)\, I = \frac{\mu^2}{2\hbar^2 \epsilon_0 c} \frac{\Gamma}{\Delta^2} I =$$

$$= \frac{3\pi c^2}{2\hbar\omega_0^3} \left(\frac{\Gamma}{\Delta}\right)^2 I \quad = \Gamma \left(\frac{\Omega}{\Delta}\right)^2 \tag{1.84}$$

the last two expressions obtained by respectively imposing[31] $I = 2c\epsilon_0 |E_0|^2$, $\Gamma = \frac{\omega_0^3}{3\pi\epsilon_0 \hbar c^3 \Gamma} \mu^2$, and the definition of the Rabi frequency $\Omega = \frac{\mu E_0}{\hbar}$.
With a similar approach, we can derive the dipolar force as the gradient of the dipolar potential (i.e. the interaction energy of the induced dipole $p$ with the driving electric field $E$)

$$\vec{F}_{dip}(\vec{r}) = -\nabla U_{dip}(\vec{r})$$

$$U_{dip}(\vec{r}) = -\frac{1}{2} \left\langle \vec{p} \cdot \vec{E} \right\rangle = -\frac{1}{2c} Re(\chi) I(\vec{r}) = \frac{\mu^2}{2c\epsilon_0 \hbar} \frac{1}{\Delta} I(\vec{r}) =$$

$$= \frac{3\pi c^2}{2\omega_0^3} \frac{\Gamma}{\Delta} I(\vec{r}) \quad = \hbar \frac{\Omega^2(\vec{r})}{\Delta} \tag{1.85}$$

From 1.85 one finds that the *dipole force* can be either attractive or repulsive depending on the sign of $\Delta$ ( attractive for red detuning: $\Delta < 0$). Moreover, increasing both $|\Delta|$ and $I$, allow one to lower the spontaneous scattering while keeping the potential height constant.

### Dipolar traps

Focused and far from resonance red detuned light can be used for trapping cold atoms. Optical traps have several qualities, as for example the fact that they can be internal state insensitive, even for different atomic species (in the second case by carefully choosing the wavelength of the light). Moreover optical beams can have

[30] $\omega$ and $\omega_0$ are respectively the laser and the atomic resonance pulsations

[31] for $I$: due to the definition of field amplitude: $E(t) = 2E_0\, cos(\omega t)$;
for $\Gamma$: determined with approximation by considering only the dipole matrix element between ground and excited state [44]

a faster temporal dynamics than magnetic fields (of the order of $\mu s$ rather than $ms$). However, spatial movement with dipole traps are more difficult to implement than in the case of magnetic trap, where only a change in the current intensity is needed. A seriously limiting aspect of dipole traps is their relative weakness, limited to *millikelvin* scale even for tens of *watt* available power.
In the work reported here no optical traps were implemented in our set-up, the first project in this direction has just launched during the redaction of this thesis.

### Optical lattices

A very important feature of optical beams is the possibility of generating almost perfectly periodical "miniaturized" potential down to the optical wavelength scale ($\mu m$), that is made possible by interference patterns between coherent beams. The simplest case of this kind is obtained by retro-reflecting a single laser beam: this way one gets a standing wave with successive nodes at a distance of $\lambda/2$, which is seen by non-resonant atoms as a periodic potential, named *optical lattice*. Approximating the system with two counter-propagating plane waves of the form 1.1 (with $k_2 = k_1$, $\bar{e}_2 = \bar{e}_1$ and $\omega_2 = -\omega_1$), after some mathematics and averaging on the terms oscillating at the optical frequencies, one finds

$$I(z) = \frac{\epsilon_0 c}{2}|\vec{E}_1(z,t) + \vec{E}_2(z,t)|^2 = c\epsilon_0 E^2\, cos^2(kz+\phi) = I_0\, cos^2(kz+\phi)$$

$$U_{dip}(z) = \frac{3\pi c^2}{2\omega_0^3}\frac{\Gamma}{\Delta} I_0\, cos^2(kz+\phi) \tag{1.86}$$

where $\phi$ accounts for the phase accumulated while traveling to the mirror and backward[32].

Physics of degenerate gases in multidimensional optical lattices is a huge field that we just touched in this thesis exploiting a 1D lattice for coherent transition between momentum states.
Due to the spatial periodicity, theory as for solid state physics (based on the Bloch theorem) applies, leading to Bloch function type eigenfunctions and band structure for eigenvalues. Eigenvectors are determined by two quantum numbers: band index $n$ and quasi-momentum $q$, which characterizes the phase difference between neighboring lattice sites. Since the potential does not present a complete but discrete

[32] $\phi = 2 \times k\, z_{mirror}$

translational invariance, the eigenvectors are not eigenstates of the momentum operator, and the quasi-momentum $\hbar q$ is defined modulus $\pi/d = k$, $d$ being the spatial period of the lattice ($d = \lambda/2$).

A BEC makes it easy to load a lattice state with a well-defined quasi-momentum. Its small momentum spread (much narrower than the extent of a band ($2\hbar k$)) results in a similar spread of the quasi-momentum $q$.
In general, any free particle momentum eigenfunction can be represented by a superposition of Bloch states from different energy bands but with equal quasi-momentum $q_0$, determined as

$$|p\rangle = \sum_n |n, q_0\rangle \qquad \hbar q_0 = p - \hbar k \left\lfloor \frac{p}{\hbar k} \right\rfloor \tag{1.87}$$

$p$ and $\lfloor \cdot \rfloor$ staying for the momentum of the free particle, and "lower integer part" operator. A $BEC$, taken to be a plane wave, suddenly loaded into a lattice can be described with such a superposition of Bloch states. This statement reflects the fact that the the old ground state occupied by the cloud (a nearly flat wave function) is very different from the new ground state (which is composed of peaks localized on potential minima), and thus energetically rich. Therefore while the $BEC$ wavepacket is held in the lattice it populates several bands and evolves in time according to the beat-notes ($\omega_{ij} = (H|n_i, q_0\rangle - H|n_j, q_0\rangle)/\hbar$) among the occupied Bloch states.
On the contrary, if the lattice is turned on slowly, one can adiabatically transform the dispersion curve from the free particle parabola to the band structure, transferring the BEC into the single Bloch state $|n_0, q_0\rangle$ of quantum numbers

$$n_0 = \left\lfloor \frac{p}{\hbar k} \right\rfloor \qquad \hbar q_0 = p - \hbar k \left\lfloor \frac{p}{\hbar k} \right\rfloor \tag{1.88}$$

The minimum rise time $\Delta t$ to ensure adiabaticity depends on the lattice height, but typically is of the order of a few $ms$[33].
For the turning off procedure a similar consideration applies: Bloch states $|n, q\rangle$ can be expanded in the discrete plane-wave basis $|p\rangle$ with momenta $p = q + 2m\hbar k$. This reflects the spatial periodicity of the Bloch states which implies a momentum spectrum composed of peaks separated by the momentum corresponding to the reciprocal-lattice vector $2\hbar k$. So, by adiabatically lowering the potential height one transfers

[33] Varying the Hamiltonian of the system, Bloch states (eigenfunctions) follow the change. Fulfilling adiabatic condition means that for each time every eigenstate of $H(t_0)$ is mostly mapped onto a single eigenstate of $H(t_0 + dt)$. An expression for this statement can be found in [80]

each Bloch state into a single momentum state according to 1.88, while sudden switching off gives a wavefunction with several momentum components. If one allows the condensate to fall freely as the lattice is dying, the results of the two procedures can be detected with time of flight imaging of momentum components, and take respectively the names of "band mapping" and "wave function mapping". This is particularly powerful within $BEC$ experiments, because of the extremely low momentum spreading of condensate wavefunctions, much smaller than $2\hbar k$. For example, in the Thomas-Fermi limit, the effective $rms$ width of the momentum distribution $\Delta p_i$ is connected to the condensate size $r_i \sim (1\,;\,100)\mu m$ by $\Delta p_i \simeq 1.6\frac{\hbar}{r_i}$ ([29]), leading to

$$\frac{\Delta p_i}{\hbar k} = \frac{1.6}{2\pi}\frac{\lambda}{r_i} \simeq 0.2\,;\,0.002 \tag{1.89}$$

The condensate wavefunction can thus be considered as a $\delta$-like distribution in momentum space with respect to the width of a band $2k$, which determines also the separation among the momentum components.
For comparison, the momentum spread of a thermal sample even at the critical temperature for condensation $T_c \sim (0.1\,;\,1)\mu K$ results

$$\frac{\Delta p}{\hbar k} = \frac{\sqrt{m k_b T_c}}{\hbar k} \sim 0.6\,;\,1.7 \tag{1.90}$$

In our experiment, the lattice is applied towards the elongated direction of the condensate (so that $r_i = r_y \sim 40\mu m$), leading to a ratio $\Delta p_y/(\hbar k) \sim 0.005$, while for a thermal cloud at $T_c = 0.5\mu K$ we gets $\Delta p_y/(\hbar k) > 1$. That means we cannot detect momentum components induced by a lattice, except by exploiting condensates.
By suddenly switching on and off the lattice with a waiting time $\tau$, one detects oscillations in the populations of the plane-wave components as a function of $\tau$: the so-called Bragg scattering. It is due to multi-band population obtained at rising time and function mapping at the end. During the presence of the grating in fact, the interference among the different Bloch components corresponds to an alternating sequence of squeezing of the whole wave function in space (localized in the potential minima) and momentum (when it comes back to the original shape) [94]. These two turning points correspond to maximal and minimal transfer of atoms in higher momentum states.

If one wants to explore BEC loaded in lattices for particular states of momentum/quasi-momentum, a simple and well controllable way consists in making the lattice move

instead of the cloud. This can be achieved by setting a frequency difference between the two counter-propagating beams. Proceeding as in the case for static lattice (1.86), but setting $k_2 = k_1 - \Delta\omega/c$, $\hat{e}_2 = \hat{e}_1$ and $\omega_2 = -\omega_1 + \Delta\omega$, after some mathematics and averaging therms at optical frequencies, one gets

$$I(z) = 2c\epsilon_0 E^2 \, cos^2(kz - \frac{\Delta\omega}{2}t)$$

$$U_{dip}(z) = U_0 \, cos^2\left(k\left(z - v_{\Delta\omega}t\right)\right) \tag{1.91}$$

where one has defined a lattice velocity as

$$v_{\Delta\omega} = \frac{\Delta\omega}{2k} \tag{1.92}$$

which represents the actual velocity of the lattice nodes, and so determine the quasi-momentum of the atoms in the reference frame of the lattice $q = -m\, v_{\Delta\omega}$.

The derivation presented in the above section is correct provided perfect coherence between the two radiation fields, any phase modulation resulting in an effective shaking of the periodic potential, thus cloud heating and coherence loss. Within this thesis we have employed an extended cavity diode laser to provide light beams for the lattice, that is a source with significant phase noise, but it has not turned a limitation due to the fact that we were mainly interested in short non adiabatic pulses of the Bragg scattering family.

### 1.4.3 Raman transitions

In order to drive a transition between two states with the same parity, (usually two fundamental states) one can apply either $RF/\mu-$wave using magnetic dipole coupling, or a pair of laser fields using electric dipole couplings to an intermediate state ("three-level $\Lambda$ scheme"), as sketched on fig.1.9. The former corresponds to normal Rabi oscillations, while the latter to the stimulated Raman transition (SRT). In this section basic characteristics of SRT are treated, showing that actually also this case can be reduced to an effective two levels system driven by optical Boch equations. On the contrary, next section is devoted to some important feature not completely explicable with the Bloch sphere model.

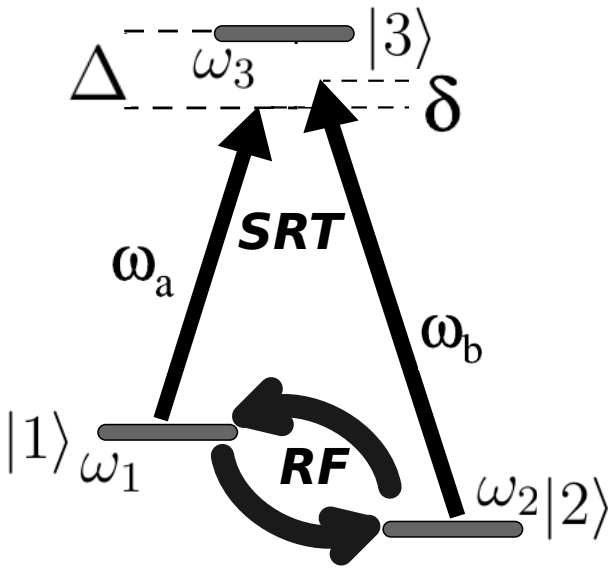


Figure 1.9: General scheme for the coupling of two states with the same parity. Two ways are possible: magnetic dipole transitions or two-photon Raman transition. The latter involves a third (excited) state, but for sufficiently large one-photon detuning it can be reduced to an effective two-level scheme. Actually the presence of the third state allows some particular feature not reproducible with a real two-level scheme, which can be quite interesting (see section 1.4.4)

The general model of a three levels atom in $\Lambda$ configuration is a central subject of this thesis: both *EIT* and optical lattice effects can be described within this model. $\Lambda$ configuration means that just one excited state is considered, connected by electric dipole transitions with two fundamental states, which in turn have no direct radiative transitions between them. This is a familiar situation with alkali atoms, where the ground state is split into hyperfine manifolds with same parity, and bright optical dipole resonances (including the famous D-lines) connect all of them with excited states.

Taking the figure as reference, we write

$$H = \sum_{j=1}^{3} \hbar\omega_j |j\rangle\langle j| + V^a cos(\omega_a t) + V^b cos(\omega_b t) \tag{1.93}$$

$V_i$ being some harmonic perturbation. Once the Hamiltonian operator defined, one can follow the standard procedure based on Heisenberg equation for the density matrix. In this case however it turns out to be quite complicated, while a solution for the evolution of amplitude probabilities is easily accessible. So, we start this way, turning on density matrix and Bloch sphere representation after some step.
Imposing the general form of the wave function with slowly varying components in the time dependent Schrödinger equation

$$|\Psi\rangle = e^{-i\omega_1 t}a_1(t)|1\rangle + e^{-i\omega_2 t}a_2(t)|2\rangle + e^{-i\omega_3 t}a_3(t)|3\rangle \qquad i\hbar\frac{\partial}{\partial t}|\Psi\rangle = H|\Psi\rangle \tag{1.94}$$

a system of equations for $\dot{a}_j$ is obtained [34]

$$\begin{cases} i\dot{a}_1 = \frac{1}{2}\Omega_a^* e^{i\Delta t}a_3 \\ i\dot{a}_2 = \frac{1}{2}\Omega_b^* e^{i(\Delta+\delta)t}a_3 \\ i\dot{a}_3 = \frac{1}{2}\Omega_a e^{-i\Delta t}a_1 + \frac{1}{2}\Omega_b e^{-i(\Delta+\delta)t}a_2 \end{cases} \tag{1.96}$$

where we have defined the Rabi frequencies $\Omega_a = \langle 3|\frac{V^a}{2}|1\rangle$, $\Omega_b = \langle 3|\frac{V^b}{2}|2\rangle$, and the detunings $\Delta = \omega_a - (\omega_3 - \omega_1)$ and $\delta = \omega_b - (\omega_3 - \omega_2) - \Delta = (\omega_b - \omega_a) - (\omega_1 - \omega_2)$.
The statements on interaction terms $\langle j|V^i|j\rangle = \langle 1|V^i|2\rangle = 0$ are imposed by hypotheses[35], while $\langle 2|V^a|3\rangle = \langle 1|V^b|3\rangle = 0$ have to be fulfilled choosing the right transitions or/and exploiting other selection rules.
To simplify and solve the system, one can point out the fact that in the equation for $\dot{a}_3$ the amplitudes $a_1$ and $a_2$ contribute almost as constant factors, due to the presence of much faster exponential factors[36]. This way an expression for $a_3(t)$ is

[34] for 1.94 one gets

$$i\hbar\sum_{j=1}^{3}(-i\omega_j a_j + \dot{a}_j)e^{-i\omega_j t} =$$

$$= \hbar\sum_{k=1}^{3}\omega_j a_j e^{-i\omega_j t} + \sum_{k=1}^{3}\left((e^{i(\omega_a-\omega_k)t} + e^{-i(\omega_a+\omega_k)t})\frac{V^a}{2} + (e^{i(\omega_b-\omega_k)t} + e^{-i(\omega_b+\omega_k)t})\frac{V^b}{2}\right)|k\rangle \tag{1.95}$$

and saving just slowly varying terms (the ones with non optical pulsation) after applied both sides inner product with $(e^{i\omega_j t}\langle j|)$, it results, e.g. for $(e^{i\omega_1 t}\langle a_1|)$, $i\dot{a}_1 = \langle 1|\frac{V^a}{2}|3\rangle e^{i[\omega_a-(\omega_3-\omega_1)]t}$

[35] $\langle j|V^i|j\rangle = 0$ is correct for electric dipole ($\Delta m = \pm 1$) transitions in systems with inversion symmetry, that is eigenfunctions with defined parity (as for atoms not under static electric field)

[36] Let's write an expression for small variations, it takes the form
$\partial\dot{a}_3 = \Omega_a e^{-i\Delta t}(\partial a_1 + i\Delta\, a_1\partial t) + ..$(the same for $a_2$)... So, the requirement in the text can be interpreted as $a_i\,\Delta \gg \dot{a}_i$ that is given in Raman configuration ($\Delta \gg$ transition linewidth)

easily calculated and can be put in equations for $\dot{a}_1$ and $\dot{a}_2$ (this approximation is the adiabatic elimination)

$$\begin{cases} \dot{a}_1 = \frac{|\Omega_a|^2}{\Delta}\, a_1 + e^{-i\delta\, t} \frac{\Omega_a^* \Omega_b}{\Delta+\delta}\, a_2 \\ \dot{a}_2 = \frac{|\Omega_b|^2}{\Delta+\delta}\, a_2 + e^{i\delta\, t} \frac{\Omega_a \Omega_b^*}{\Delta}\, a_1 \end{cases} \tag{1.97}$$

Let's rewrite the equations with replacements

$$\delta\omega_1 = |\Omega_a|^2/\Delta \qquad \delta\omega_2 = |\Omega_b|^2/\Delta \qquad \Omega_R = \Omega_a \Omega_b^*/\Delta \tag{1.98}$$

while assuming $\quad \delta \ll \Delta \quad (\Rightarrow\ \Delta + \delta \sim \Delta)$

$$\begin{cases} \dot{a}_1 = \delta\omega_1\, a_1 + e^{-i\delta\, t}\, \Omega_R^*\, a_2 \\ \dot{a}_2 = \delta\omega_2\, a_2 + e^{i\delta\, t}\, \Omega_R\, a_1 \end{cases} \tag{1.99}$$

We may identify $\delta\omega_1$ and $\delta\omega_2$ as the energy shifts due to the couplings $\Omega_a$ and $\Omega_b$, respectively. As a consequence, the resonance frequency of the Raman transition is shifted to $\omega_0 = \omega_2 + \delta\omega_2 - (\omega_1 + \delta\omega_1)$.
We may also identify $e^{-i\delta\, t}\, \Omega_R$ as the Rabi frequency for the stimulated Raman transition between the $|1\rangle$ and $|2\rangle$ states.
Turning to density matrix picture, that is manipulating the equations to write expression for $(a_1^* a_2 = \rho_{12})$ and $(a_2^* a_2 - a_1^* a_1 = \rho_{22} - \rho_{11})$

$$\frac{d}{dt}\rho_{12} = -i(\delta\omega_2 - \delta\omega_1)\rho_{12} + ie^{-i\delta\, t}\, \Omega_R(\rho_{22} - \rho_{11})$$

$$\frac{d}{dt}(\rho_{22} - \rho_{11}) = 2i\left(e^{i\delta\, t}\, \Omega_R^*\, \rho_{12} - e^{i\delta\, t}\, \Omega_R\, \rho_{21}^*\right) \tag{1.100}$$

one finds that this system is identical[37] to 1.29 (two level atom interacting with a radiation field in the semi-classical limit), and so the results for Rabi oscillation and Bloch vector representation apply. This allows to obtain the expression for the population in state $|2\rangle$

$$|a_2(t)|^2 = \frac{4|\Omega_R|^2}{\Delta\omega^2 + 4|\Omega_R|^2}\ sin^2\left(\sqrt{|\Omega_R|^2 + \frac{\Delta\omega^2}{4}}\ t\right) \tag{1.101}$$

[37] differences in exchange terms are related to rotating wave approximation, already applied here

where $\Delta\omega = \delta - (\delta\omega_2 - \delta\omega_1)$ is the actual two photon detuning (beams' intensity dependent). Hence, for Raman transitions, we have a transfer efficiency that depends on detuning as

$$|a_2|^2_{max} = \frac{1}{1 + \frac{\Delta\omega^2}{4|\Omega_R|^2}} \sim 1 - \left(\frac{\Delta\omega}{2|\Omega_R|}\right)^2 \tag{1.102}$$

The energy shifts $\delta\omega_1$ and $\delta\omega_2$ are due to the off-resonant electric dipole coupling between the ground and the excited state, called ac Stark shift. It is the same effect responsible for dipolar forces (notice that expression for $\delta\omega_i$ is equal to 1.85). In analogy with $\Omega_R$ it can be interpreted as a stimulated Raman amplitude probability for a transition with the same initial and final state. This point of view offers also an alternative explication of Bragg peaks in momentum distribution that one can get in an atomic wave function loaded in a lattice. The two counter-propagating beams can be seen as couplers for Raman transitions between momentum states separated by $\Delta p = 2\hbar k$, that is the amount of momentum transferred by absorption from one beam and stimulated emission into the other.

In the case of a static lattice, transitions in opposite directions are degenerate and slightly out of resonance, the conservation of energy is not possible. The absorbed and the emitted photons carry the same energy ($\hbar kc$), while the atom gains (or looses) two photon recoil energy ($2\hbar^2k^2/m$). This means that one gets Rabi oscillations without complete transfer of population (but only $1 - (\frac{\hbar^2k^2}{m|\Omega_R|})^2$) and accelerated Rabi frequency $\sqrt{\Omega_R^2 + (\hbar^2k^2/m)^2}$. Atoms are split in two counter-propagating lobes (with $\pm 2\hbar k/m$ velocity) and then back in the original cloud. If are increase the intensity of the beams, more detuned transitions get non vanishing probability, and one can see $\pm 4\hbar k/m$ lobes, and so on[38].

In the case of a moving lattice (laser beams with a difference in frequency $\Delta\omega$), the degeneracy is removed and one transition goes closer to resonance, which is fulfilled for $\hbar\Delta\omega = 2\frac{\hbar^2k^2}{m}$. There, one gets complete population transfer and Rabi frequency $= \Omega_R$. This condition corresponds to set atoms in a state on the boundary of the Brillouin zone (remind 1.92)

$$\hbar\delta\omega = 2\frac{\hbar^2k^2}{m} \;\Rightarrow\; \hbar k = m\frac{\Delta\omega}{2k} = m\, v_{\Delta\omega} = q \tag{1.103}$$

so that this resonance is connected to the phenomenon of Boch oscillations.

[38]Band theory interprets this as population of a higher number of bands by a stronger potentials

We may say that two photons transitions in optical lattices play the role of phonons in crystals: atoms can exchange energy quanta of $2\hbar kc$ only whit the lattice (by transfer of a photon from one beam to the other).

Detection of Rabi oscillations allows an indirect measurement of the dipolar potential realized with the beams, and is the usual tool for calibration of lattice heights. Comparing 1.85 and 1.98, and taking into account that in anti-nodes one gets $2 \times E$ amplitude

$$\Omega_R \xrightarrow{a=b} \frac{|\Omega_a|^2}{\Delta} \qquad U_{max} \xrightarrow{\Omega_{max}=2\Omega_a} 4\hbar\frac{|\Omega_a|^2}{\Delta} = 4\hbar\Omega_R \tag{1.104}$$

In general the excited state $|3\rangle$ has a finite lifetime. This spontaneous emission can drive atoms either out of the $\Lambda$-scheme (with loss of atom number), or back in ground states ($|1\rangle$ *or* $|2\rangle$), as spontaneous Raman transition, that in turn entails a loss of coherence in the sample. This rate can be reduced by having a large $\Delta\omega$ at the expense of correspondingly larger intensity to keep the Rabi frequency constant.

### 1.4.4 Beyond the Bloch sphere representation: CPT and STIRAP

In this section we show two features related to Raman type interaction which are not possible to describe within the Boch sphere representation: coherent population trapping ($CPT$) and stimulated Raman adiabatic passage ($STIRAP$). Both of them have been exploited in my thesis work.

Let's first consider a standard two levels scheme with a resonant coupling field of Rabi frequency $|\Omega_1|e^{i\varphi}$. After a $\frac{\pi}{2}$ pulse, the Bloch vector is in the $(1,2)plane$; if we apply a second pulse with phase in quadrature with respect to the first one ($|\Omega_2|e^{i(\varphi+\pi/2)}$), independently of its amplitude, it will not have any effect on the sample due to coaxiality of the two pseudo-spin vectors: we can say that atoms are prepared in a "dark state" for this perturbation.
In a three levels $\Lambda$ configuration, this particular state can be reached without applying preparation pulses, by just holding the field for a sufficiently long time. Actually the presence of the excited state, with its incoherent scattering term (spontaneous

emission), allows atoms to leave the collective coherent state to reach random superpositions of ground levels. All of these states keep on following precession around the perturbation vector, the only way to escape coupling being to fall in the superposition giving the dark state. Hence, as a net result, atoms tend to accumulate there. The phenomenon takes the name of $CPT$, the state being not only dark for the electromagnetic perturbation, but even continuously restored by this field.
The general expression for the dark state $|D\rangle$ reads

$$|D\rangle = \frac{\Omega_b|1\rangle - \Omega_a|2\rangle}{\sqrt{\Omega_1^2 + \Omega_2^2}} \tag{1.105}$$

where we have kept the meaning of the symbols as in previous sections. In 1.105 one can recognize the key point of the uncoupling mechanism: it is based on destructive interference between the excitation amplitude probabilities from the two components of the wave function. This is also the fundamental feature giving the electromagnetically induced transparency effect ($EIT$), which is a central concept for this thesis and the central argument of the next section. A complete review on properties of the trapped states can be found in [4]. The time scale on which a population-trapped state may be established depends on the initial state of the sample: in the case of a mixture of $|1\rangle$ and $|2\rangle$, the process takes several radiative decay times $\Gamma_3$, whatever the value of $\Omega_a/\Omega_b$ is (basically, it needs a number of passages through the excited state); in the case of population accumulated just in one state (e.g., $|2\rangle$), and field excitation biased in favor of the other dipole transition ($\Omega_a/\Omega_b \gg 1$), the dark state is reached in a time scale given by the longest between $1/\Omega_a$ and $\Gamma_3/\Omega_a^2$ ([48]). The second configuration is the one in which $EIT$ effect takes place.
The mechanism we have presented is valid with continuous laser beams, but not for short pulses of light, when there is not enough time for random formation of the right superposition. Actually there is a way to initiate the coherence between the ground states with the correct phase and to maintain that phase thereafter: it takes the name of $STIRAP$ (stimulated Raman adiabatic passage).
Here one field is switched on before the other one, so that the eigenvector of the trapped state is initially set to single state occupation (let's say: $\Omega_a(t = 0) \neq 0$ and $|D(t = 0)\rangle = |2\rangle$). The field $\Omega_a$ couples the two empty states, thus leaving the population of state $|2\rangle$ unchanged. Due to the field $\Omega_a$, by turning on the second beam ($\Omega_b$), the populated state $|2\rangle$ is coupled to a state which is a superposition of $|1\rangle$ and $|3\rangle$. If the relative variation of the two fields (that is the variation of their

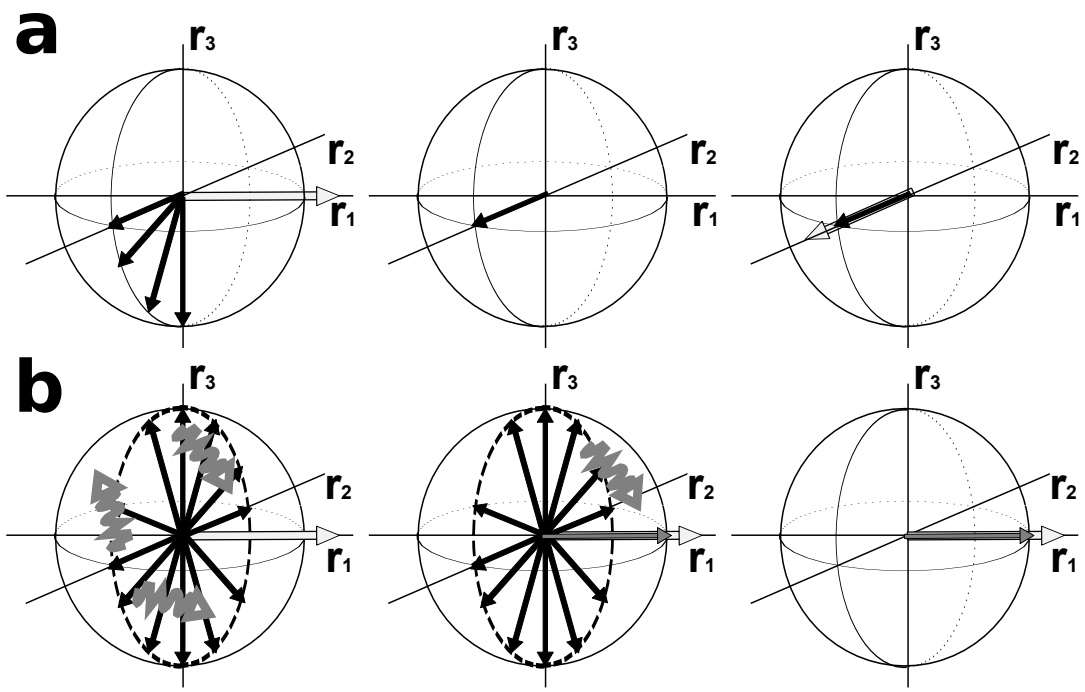


Figure 1.10: Dark states representation in the Bloch sphere:
**a** - In the case of a real two photon system, the only way to produce a dark state is by coherent manipulation (see text).
**b** - In a effective two level system related to a Raman transition, the presence of the third (excited) level allows, by means of the residual incoherent scattering, the spontaneous creation of the quantum superposition of states decoupled from the exciting fields (dark state).

ratio $\Omega_a/\Omega_b$) is sufficiently slow, the system can follow the evolution of the dark state, remaining substantially uncoupled to the field excitation [90],[109]. That is, even if the decay rate of the excited state $|3\rangle$ strongly exceeds the Rabi frequencies $\Omega_a, \Omega_b$, for slowly varying envelopes, or matched pulses, the population of this state is almost zero all the time, suppressing incoherent scattering due to spontaneous emission.

A rigorous treatment of the three levels system ([9]) shows that in presence of the two electromagnetic fields the eigenstates of the total Hamiltonian are (considering only at the atomic part) three linear combinations of the bare states, one of them being a superposition of the two ground states only: it is the dark state. The treatment allows also to determine, under the standard form for adiabatic passages in time

dependent Hamiltonian ([80])[39], a "scale" discriminant for the definition of slowly varying envelopes. In the case of $STIRAP$ the slowly varying condition is fulfilled if

$$\left| \frac{\dot{\Omega}_b \Omega_a - \Omega_b \dot{\Omega}_a}{\Omega_a^2 + \Omega_b^2} \right| \ll \sqrt{\Omega_a^2 + \Omega_b^2} \tag{1.107}$$

$STIRAP$ can provide almost perfect transfer of populations from state $|2\rangle$ to state $|1\rangle$. After the procedure described above, by smoothly decreasing $\Omega_a$ while keeping $\Omega_b$, the dark state adiabatically tends to state $|1\rangle$. Standard implementation uses for $\Omega_a$ and $\Omega_b$ two similar or equal pulses, adding some carefully determined delay to the second one. This transfer procedure can be very efficient and rapid, with the appropriate Rabi frequencies. Insufficient coupling by the coherent radiation fields may prevent the atomic state from adiabatically following the evolution of the trapped state $|D\rangle$, and loss of population due to non-adiabatic transfer to the states containing a non-zero projection on state $|3\rangle$ may occur [9].

From 1.105 we see the dark state composition is determined by the ratio of the two Rabi frequencies involved in the two photons transition. Therefore, while the perturbation vector is fixed in the $(1,2) - plane$ (for resonant light) whatever the intensities of the two fields are, the vector representing the dark state (defined by the ratio of this intensities) can show any population imbalance and get any direction between the poles $(0, 0, \pm N/2)$ of the Bloch sphere. As a consequence, for any case in which the two Rabi frequencies are not perfectly balanced, we can not say that the trapped state does not undergo precession around the perturbation because they are collinear, and the Bloch sphere representation fails to describe the phenomenon.

From 1.105 one can also understand that the dark state is sensitive to the complex amplitude of the fields, that is, it does not depend only on the intensities ratio, but on the relative phase between the two fields. This is one of the features making $EIT$ interesting for quantum memories, as described in the next chapter.

[39] to be followed adiabatically one eigenstate has to change in a way that its variation maintains projections on the other eigenstates smaller than the difference between the corresponding (energy) eigenvalues:

$$\langle \psi_j | (|\psi_i(t + \Delta t)\rangle - |\psi_i(t)\rangle) \ll \Delta t \, (E_j - E_i)/\hbar \qquad \forall j \neq i \tag{1.106}$$

# Chapter 2

# $EIT$-based memories

In this section I recall the concepts that are the key points for quantum memories protocols based on electromagnetically induced transparency ($EIT$). We will see first that under $EIT$ condition it is possible to drastically reduce the group velocity of a traveling pulse (up to seven orders of magnitude [50]). This allows for extreme spatial compression of its envelope, while at the same time it avoids incoherent scattering and absorption by the medium. This makes possible to gather, at least for a while, microseconds long pulses (of kilometric length) within small size samples (from hundreds of $\mu m$ to few $cm$). We will then see that in this configuration there is a linear and coherent (hence reversible) exchange of fluctuations between the field of interest and the collective state of the sample ([24]). Last, we will see how, with the right dynamics, it is possible to stop the pulse within the sample, and let it move on after an "on demand" time delay. These three characteristics are sufficient to provide a quantum memory protocol, that is a memory able to reproduce the input pulse in a second time without added noise and saving its statistical properties. Finally a comparison of advantages and disadvantages of different experimental systems is reported.

Electromagnetically induced transparency is a phenomenon based on interference between optical paths, thus involving more than one transition sharing at least one level. Different three-levels configurations have been the object of studies, as ladder, $V$ and $\Lambda$ structures (see [37] for a general review and comparison among them). The last one has proven more robustness against almost every experimental mismatches with theoretical assumptions, and moreover it contains a fundamental ingredient for

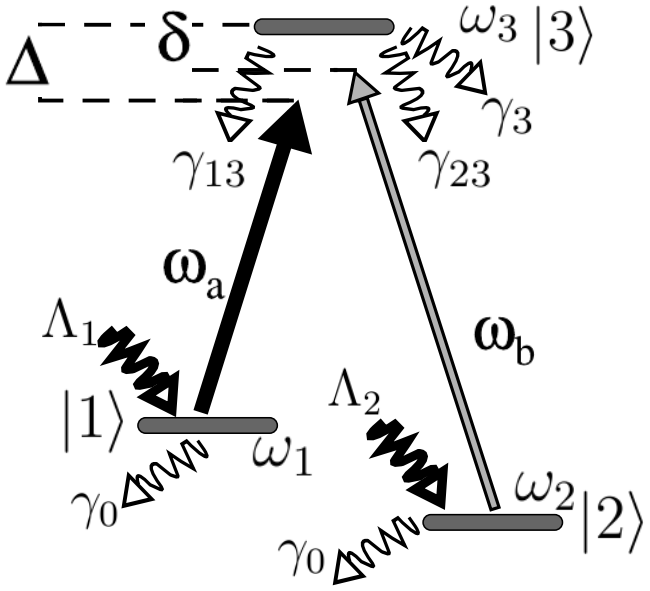


Figure 2.1: Atomic three-level scheme in $\Lambda$ configuration, with the configuration of fields necessary to reproduce the eletromagnetically induced transparency effect: the strong field, named control field (black arrow), and the probe field, named signal field (gray arrow). Notation are in agreement with the text and univocally defined throughout the part 1 of the manuscript. At the beginning of the second part, a general change of name is performed, in order to match the common notation of the references. All the decay terms are presented, together the repumping terms ($\Lambda_i$).

memories: the two uncoupled states are ground states, thus almost stable on the time scale of other variables of the system. This is the configuration considered in our models and implemented in the experiments. It is included in the general model described in section 2.4.3, with a specificity determined by two particular conditions:

- limited one-photon detunings;
- large power imbalance between the two fields, with the strongest one in a coherent state.

The possibility of storage will be indeed for the weak field. Basically, from the mean values point of view, one can look at the atomic sample plus the strong field as an isolated system probed by the weak field. On the other hand, for small fluctuations,

the atomic state strongly depends on the statistical properties of the weak field, while it is almost insensitive to those of the strong field[1].

Following the pioneering work of A. Dantan ([24], [23]), this time we use Heisenberg equation for the density matrix to determine the equation describing the atom-field interaction.

$$\frac{\partial}{\partial t}\hat{\rho} = \frac{i}{\hbar}[\rho,\, \hat{H}] + \frac{\partial}{\partial t}\rho|_{decay} \tag{2.1}$$

The Heisenberg-Langevin equations give indeed direct access to expressions for coherence terms we are interested in. The calculation is provided for two traveling waves, which is the natural case for memories protocols. Definitions and notations follow 2.1 and match that of 1.9; for notation on atomic variables we follow sec 2, just adding components for the third state. For the decay terms we consider:

$\Gamma = (\gamma_{13} + \gamma_{23} + \gamma_3)$ - total decay rate for the excited state $|3\rangle$, that is the natural linewidth for transitions $|j\rangle \to |3\rangle$, with $(j = 1, 2)$. It is composed of channels towards the two ground states ($\gamma_{j3}$) and to other states ($\gamma_3$);

$\gamma_0$ - loss of atoms from the ground states $|1\rangle$ and $|2\rangle$;

$\Gamma_e = \frac{1}{2}(\Gamma+\gamma_0) \sim \Gamma/2$ and $\Gamma_{12}$ - respectively, decay rates of optical coherences $\rho_{j3}$ and "Raman" coherence $\rho_{12}$;

due to the possibility for the atoms to escape the $\Lambda$ system (given by $\gamma_3$, $\gamma_0$), it is necessary to have source terms: $\Lambda_j$ represent repumping rates to $|1\rangle$ and $|2\rangle$.
$A_a$ and $A_b$ are the fields amplitudes acting on $(|1\rangle \to |3\rangle)$ and $(|2\rangle \to |3\rangle)$ transitions, with

$$\begin{cases} \Delta = \omega_a - (\omega_3 - \omega_1) & \text{one photon detuning for field } A_a \\ \delta = (\omega_b - \omega_a) - (\omega_1 - \omega_2) & \text{two photon detuning} \end{cases} \tag{2.2}$$

To build the Hamiltonian operator for an atomic sample crossed by traveling waves one has to define spatial distributions for both atoms and fields. We consider a volume of section $S$ and length $L$ (in the $z$ direction) as region of interaction, within which the fields can be considered as transversaly invariant. For the two modes it holds

$$E_x(z,t) = \mathcal{E}_x \left(A_x(z,t)e^{i(k_x z - \omega_x t)} + A_x^\dagger(z,t)e^{-i(k_x z - \omega_x t)}\right) \quad x = a, b \tag{2.3}$$

[1]for coherent states, fluctuations are always the same, independently from the amplitude of the coherent state. So, they have high impact on weak states while become negligible in stronger ones

where $\mathcal{E}_x = \sqrt{\frac{\hbar\omega_x}{2\epsilon_0 SL}}$ and $A_x$ is the slowly varying envelope, as shown in sec. 2.1 . For the atomic variables, it is possible to use collective operators with continuous spatial dependence (in this case the direction of light propagation $z$) $\{\rho_{ij}(z,t)\}$; for details on the validity limits for this formalism see [33].
Considering "ad hoc" slowly varying components also for these atomic variables[2]

$$\sigma_{13} = \rho_{13} e^{-i(k_a z - (\omega_3 - \omega_1)t)} \qquad \sigma_{23} = \rho_{23} e^{-i(k_b z - (\omega_3 - \omega_2)t)} \qquad \sigma_{21} = \rho_{21} e^{i((k_a - k_b)z - (\omega_1 - \omega_2)t)} \tag{2.4}$$

one gets a simple form for the electric dipole type interaction Hamiltonian (with RWA)

$$H_{int} = -\hbar \frac{N}{L} \int dz \, \left[ g_a \, e^{-i\Delta t} A_a(z,t) \sigma_{13}^{\dagger}(z,t) + g_b \, e^{-i(\Delta+\delta)t} A_b(z,t) \sigma_{23}(z,t) + \, c.c. \right] \tag{2.5}$$

$g_a = \frac{\mu_{13}\mathcal{E}_a}{\hbar}$ being the coupling constant between the field $A_a$ and the coherence $\sigma_{13}$, with $\mu_{13}$ electric dipole (similarly $g_b$ for $A_b$ and $\sigma_{23}$ ). To account for the atomic part, we can add the Hamiltonian in the standard form $(H_{at} = \hbar \sum_{i=1}^{3} \omega_i \, \rho_{ii})$ .
The total hamiltonian ($H_{at}$ + $H_{int}$) leads to the system of equations (with non-hermitian contributions added)

$$\begin{cases} \frac{\partial}{\partial t}\rho_{11} = -\gamma_0 \rho_{11} + \gamma_{13}\rho_{33} + \Lambda_1 + i g_a A_a^{\dagger} \sigma_{13} - i g_a A_a \sigma_{13}^{\dagger} + f_{11} \\ \frac{\partial}{\partial t}\rho_{22} = -\gamma_0 \rho_{22} + \gamma_{23}\rho_{33} + \Lambda_2 + i g_b A_b^{\dagger} \sigma_{23} - i g_b A_b \sigma_{13}^{\dagger} + f_{22} \\ \frac{\partial}{\partial t}\rho_{33} = -\Gamma \rho_{33} - (i g_a A_a^{\dagger} \sigma_{13} - i g_a A_a \sigma_{13}^{\dagger}) - (i g_b A_b^{\dagger} \sigma_{23} - i g_b A_b \sigma_{23}^{\dagger}) + f_{33} \\ \frac{\partial}{\partial t}\sigma_{13} = -\left(\Gamma_e - i\Delta\right) \sigma_{13} + i g_a A_a (\rho_{11} - \rho_{33}) + i g_b A_b \sigma_{21}^{\dagger} + f_{13} \\ \frac{\partial}{\partial t}\sigma_{23} = -\left(\Gamma_e - i(\Delta + \delta)\right) \sigma_{23} + i g_b A_b (\rho_{22} - \rho_{33}) + i g_a A_a \sigma_{21} + f_{23} \\ \frac{\partial}{\partial t}\sigma_{21} = -(\Gamma_{12} - i\delta)\sigma_{21} + i g_a A_a^{\dagger} \sigma_{23} - i g_b A_b \sigma_{13}^{\dagger} + f_{21} \end{cases} \tag{2.6}$$

where the $f_{ij}$ are the Langevin forces that can be evaluated using the quantum regression theorem [113, 19].
In the following paragraphs the weak field is identified with $A_b$ (transition $|2\rangle \rightarrow |3\rangle$).

[2] that is uniform density with a field-like spatial phase modulation, plus temporal phase evolution due to energy differences among the eigenstates

## 2.1 Non-linear susceptibility in electromagnetically induced transparency

The system 2.6 is the most general one that can be considered for three level atoms in $\Lambda$ configuration, and it is presented in [23] for several experimental schemes. We are here interested in determining the response of the sample to a weak field, while considering it in its steady-state limit in presence of the strong field. As already noticed, due to the low density of the atomic system, the complex susceptibility is simply proportional to the single-atom polarizability[3] $\alpha$, so that

$$\chi(\Delta,\delta) = \frac{n_0}{\epsilon_0}\,\alpha(\Delta,\delta) = n_0 \frac{|\mu_{23}|^2}{\hbar\,\epsilon_0\,\Omega_b}\,\sigma_{23}(\Delta,\delta) \tag{2.7}$$

where $n_0$ is the density of atoms, and in the last expression we have introduced the Rabi frequency $\Omega_b = \mu_{23}\mathcal{E}_b\langle A_b\rangle/\hbar$.
Thanks to the very weak mean value of the field $A_b$, it is possible to calculate the expression for the coherence $\sigma_{23}$ by perturbative steps. At zeroth order, one can assume that the whole sample is in state $|2\rangle$, so that $\rho_{11} = \rho_{33} = 0$, $\rho_{22} = 1$, and that the weak field is absent ($A_b = 0$). In this way the three equations for the coherence terms under stationary condition can be written as

$$\begin{cases} 0 = -\left(\Gamma_e - i\Delta\right)\sigma_{13}^{(0)} \\ 0 = -\left(\Gamma_e - i(\Delta+\delta)\right)\sigma_{23}^{(0)} + i\Omega_a\sigma_{21}^{(0)} \\ 0 = -(\Gamma_{21} - i\delta)\sigma_{21}^{(0)} + i\Omega_a^*\sigma_{23}^{(0)} \end{cases} \tag{2.8}$$

and we obtain in particular $\sigma_{13}^{(0)} = 0$ from the first equation. At first order in $\Omega_b$ one gets a closed system for $\sigma_{23}$ and $\sigma_{21}$ and it is possible to write $\sigma_{23}^{(1)}$ as a function of the field variables (linear in $\Omega_b$)

$$\sigma_{23}^{(1)} = i\Omega_b \frac{\Gamma_{21} - i\delta}{(\Gamma_{21} - i\delta)(\Gamma_e - i(\Delta+\delta)) + |\Omega_a|^2} \tag{2.9}$$

The linear susceptibility $\chi$ for the weak field $A_b$ can be written as

$$\chi(\Delta,\delta) = \frac{n_0\,\mu_{23}^2}{\hbar\,\epsilon_0} \frac{i(\Gamma_{21} - i\delta)}{(\Gamma_{21} - i\delta)(\Gamma_e - i(\Delta+\delta)) + |\Omega_a|^2} \tag{2.10}$$

[3] $\alpha(\Delta,\delta)\mathcal{E}_b\,\langle A_b\rangle = \mu_{23}\,\sigma_{23}(\Delta,\delta)$

As shown in sec 2.2, dispersion and absorption of the medium are described respectively by the real and imaginary parts of the susceptibility. In 2.10 one can recognize the main signature of $EIT$, that is the cancellation of $\chi$ for exact two photon detuning $\chi \xrightarrow{\delta \to 0} 0$ even in the proximity of an atomic resonance, provided that the Raman coherence decay rate is negligible with respect to the Rabi frequency of the strong field[4] $\Gamma_{21} \ll |\Omega_a|$. On both sides of the transparency region ($\delta \neq 0$), the imaginary part of the susceptibility exhibits absorptive peaks: these correspond to Autler-Townes doublet [43, 105] (when the separation is large enough, i.e., $\Omega_a > \Gamma_e$). Their position can be calculated by searching the poles of the real part in the denominator of 2.10

$$-\delta^2 - \Delta\,\delta + \Gamma_{21}\Gamma_e + |\Omega_a|^2 = 0 \tag{2.12}$$

$$\delta_{peak} = \frac{1}{2}\left(-\Delta \pm \sqrt{\Delta^2 + 4(|\Omega_a|^2 + \Gamma_{21}\Gamma_e)}\right) \sim \frac{1}{2}\left(-\Delta \pm \sqrt{\Delta^2 + 4|\Omega_a|^2}\right)$$

where the approximated form holds in case of negligible $\Gamma_{21}$. For perfect one photon resonance $\Delta = 0$, the shape of the absorption assumes a symmetric form, with maxima centered at $\delta_{peak} \sim \pm|\Omega_a|$. This double peak is expected according to the dressed state model for two levels atoms immersed in an electromagnetic field near resonance [22, 105].The interesting point is that, by addressing the atomic system on another transition sharing the excited state with the first one, as we do here with $A_b$, one finds a region between the two absorptive peaks where the transition probability drops to zero. It is the result of the interference between the amplitude probabilities for the two possible transitions, which have opposite sign due to the sharing of the same electric dipole matrix element with opposite detuning. For $\Delta = 0$, due to identical amplitude and opposite phase for the two transition probabilities, the absorption structure of the atomic medium becomes symmetric (see fig2.2.a), with the transparency peak centered at $\Delta = 0$ ($\delta = 0$). Observing the transmission profile through the sample

$$t = \frac{|A_b(L)|^2}{|A_b(0)|^2} = e^{-k_b L\, Im(\chi(\Delta,\delta))} \tag{2.13}$$

where $L$ is the sample length, one can determine a width $\Delta_{tr}$ for the transparency window. The expression for the imaginary part of the susceptibility can be obtained

[4] A simplified version of 2.10, where we set $\Gamma_{21} = 0$, can take the form

$$\chi(\Delta,\delta) = \frac{n_0\,\mu_{23}^2}{\hbar\,\epsilon_0}\frac{\delta}{\delta(\Delta+\delta) + |\Omega_a|^2 - i\delta\Gamma_e} = \frac{n_0\,\mu_{23}^2}{\hbar\,\epsilon_0}\frac{\delta(|\Omega_a|^2 - \delta(\delta+\Delta)) + + i\delta^2\Gamma_e}{(|\Omega_a|^2 - \delta(\delta+\Delta))^2 + (\delta\Gamma_e)^2} \tag{2.11}$$

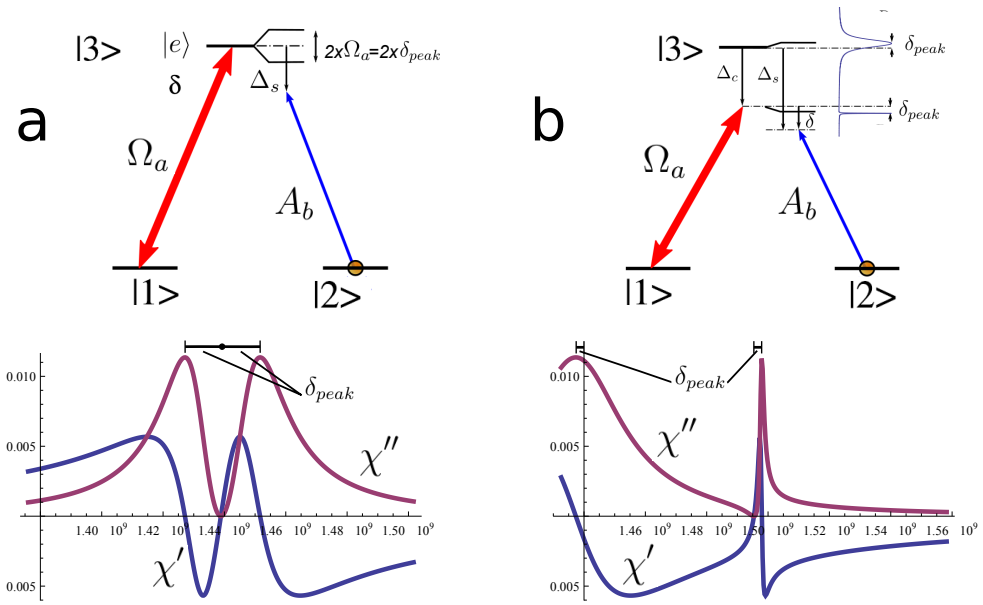


Figure 2.2: Absoption (red) and dispersion (blue) seen by the probe beam $A_b$ when the medium is illuminated by the strong field $A_a$, as a function of the two-photon detuning $\delta$. In **a** the strong field is resonant with the atomic transition, in **b** it is slightly out of resonance ($\Delta \sim \Gamma_e$). For the two-photon resonance condition the transparency is complete in both cases. In the upper part of the figure, the representation in form of dressed states of the same phenomenon is reported. For increasing one-photon detunings ($\Delta \neq 0$), one peak approaches the one-photon resonance and takes the form of the simple atomic absorption, while the other approaches the two-photon resonance eventually becoming a two-photon Raman transition peak.

from 2.11, and considering $\Delta = 0,\ \Gamma_{21} \sim 0,\ \Gamma_e \times \delta \ll |\Omega_a|^2$, one gets

$$t \sim e^{-k_b L \frac{n_0 \mu_{23}^2}{\hbar \epsilon_0} \frac{\Gamma_e}{|\Omega_a|^4} \delta^2} = e^{-\frac{\delta^2}{\Delta_{tr}^2}} \tag{2.14}$$

where we have defined $\frac{1}{\sqrt{OD}} \frac{|\Omega_a|^2}{\Gamma_e} = \Delta_{tr}$, with $OD = k_b L \frac{n_0 \mu_{23}^2}{\hbar \epsilon_0 \Gamma_e} = \frac{3}{4\pi} n_0 \lambda_b^2 L$ optical depth of the sample.

Out of resonance, even breaking the symmetry condition, the situation is similar: indeed, for increasing $|\Delta|$, one of the dressed states gets a larger width and moves closer to the atomic resonance (eventually matching the atomic transition), while the other one turns into a narrow peak, moving closer to the two photon resonance

(far from resonance it becomes the Raman transition), but transparency still exists and remains all the way fixed at the two-photon resonance (this point keeping the condition of complete destructive interference between the transition amplitude probabilities). To calculate the positions of the absorptive peaks, one can consider an approximate expression of 2.12 under condition $|\Delta| \gg |\Omega_a|$

$$\delta_{peak} = \frac{1}{2}(\Delta \pm \Delta) \pm \frac{|\Omega_a|^2}{\Delta} \tag{2.15}$$

which shows as the two peaks are shifted from $\Delta = 0$ and $\delta = 0$ by $\frac{|\Omega_a|^2}{\Delta}$ in opposite directions.

On the other hand, the real part of the susceptibility, responsible for the dispersion characteristics of the medium, is also zero at two photon detuning $\delta = 0$, while showing in the vicinity a linear slope proportional to $1/|\Omega_a|^2$

$$\chi'(\delta) = \frac{n_0 \, |\mu_{23}|^2}{\hbar \, \epsilon_0} \frac{\delta}{|\Omega_a|^2} \tag{2.16}$$

These absorptive and dispersive characteristics are kept for every one photon detuning, only limited in range by the condition $|\Omega_a|^2/\Delta \gg \delta$ .
Summarizing, both at resonance and out of resonance, there is a frequency interval where the medium is characterized by a steep linear monotonously increasing dispersion ($\chi' \propto \delta/|\Omega_a|^2$) together with a weak absorption ($\chi'' \sim 0$).
From sec. 2.2.2 we know that a positive derivative of the real part of the susceptibility $\chi'$ corresponds to a decrease of the group velocity:

$$v_g \sim \frac{c}{1 + \frac{\omega}{2}\frac{d}{d\omega}\chi'} \sim \frac{c\epsilon_0\hbar}{n_0|\mu_{23}|^2}|\Omega_a|^2 = \frac{L}{OD}\frac{|\Omega_a|^2}{\Gamma_e} \tag{2.17}$$

the last two expressions are valid in the limit of large velocity reduction ($v_g \ll c$).
Therefore, sending into the medium a pulse with the spectrum centered in this band, named $EIT$ window, one gets at the exit a pulse of almost the same energy but arriving later with respect to passage in vacuum, and the resulting delay $\Delta t$ is equal to

$$\Delta t = L\left(\frac{1}{v_g} - \frac{1}{c}\right) \sim \frac{L}{v_g} = \frac{\Gamma_e}{|\Omega_a|^2} \, OD \tag{2.18}$$

Again, the approximate form is valid in case of $v_g \ll c$.

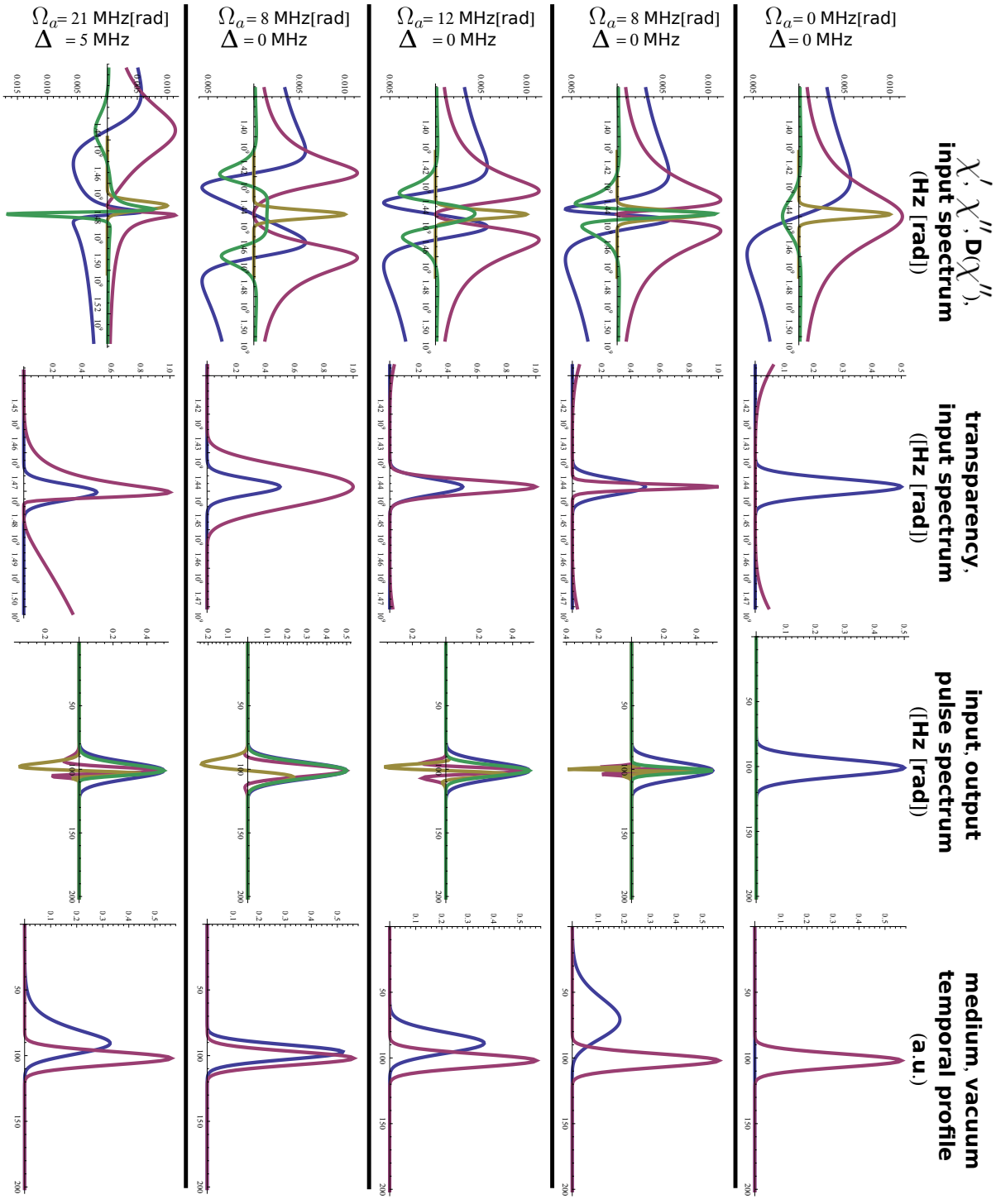


Figure 2.3: Propagation of a pulse in a medium under electromagnetically induced transparency. See the note 5 for description.

As it could have been expected, by comparing the expressions for the delay 2.18 and for the transparency width 2.14, one finds that large delay times imply a narrow transparency window, which in turn requires long pulses in order to hold a narrow spectrum and thus avoid incoherent absorption. Hence there is an upper bound for the ratio between the achievable delay time $\Delta t$ and the initial pulse length $\tau$ of a photon wavepacket, which is give by $\Delta t/\tau = \sqrt{OD}$. The optical depth is thus a figure of merit for a memory system: the larger it is, the better the system is suited for a coherent storage[5].

These characteristics are deduced neglecting the coherence decay rate between the two ground states $\Gamma_{21}$. Recalling 2.10, and imposing however $\Gamma_{21} \ll \Gamma_e$ (which is a basic requirement to get better memory results than with a simple two level transition), we can see that the decoherence rate doesn't affect much the positions of the resonances just calculated above. On the contrary, it is strongly detrimental for the "Q-factor" of the peaks. The transparency effect is obtained as an effect of the coherence accumulated between the two ground states via the two coherent fields addressing the same excited state. Therefore the natural consequence of the finite lifetime for this coherence is the broadening and reduction of the resonances. This is particularly severe for the Raman peak, which is mainly due to the coherent two-photon interaction: for $\Gamma_{21} = \Gamma_e/10$ it is already half of its ideal value (calculated for $\Gamma_{21} = 0$). The peaks close to the atomic resonance shows stronger robustness, due to the one-photon component, and save the shape even for $\Gamma_{21} \geq \Gamma_e$. Also the main features of $EIT$, transparency and linear dispersion, suffer severe dechoerence: the perfect transmission is rapidly lost and the dispersion slope decreases rapidly. For $\Gamma_{21} \gg \Gamma_e$ the coherent behavior disappears and one finds the normal profiles of a simple one photon transition.

[5]Caption of fig2.3. In the first column, the real $\chi'$ (blue) and the imaginary $\chi''$ (red) parts of the susceptibility are reported, together with the derivative of the real part $\chi'$ (dark green). We repost also the spectrum of the probe pulse (yellow) we want to evaluate the propagation throughout the medium. In the second column, the absorption profile, as obtained by a frequency scanned monochromatic probing field, is reported (red) together with the spectrum of the entering pulse as in the previous graph (blue). In the third column, the spectra of the probe pulse before entering (blue) and after exiting the medium are compared. The color code for the spectrum after the passage is: real part (red), imaginary part(yellow), absolute amplitude (dark green). In the forth column the temporal profile of the transmitted pulse (blue) is reported, together with the original profile(red).

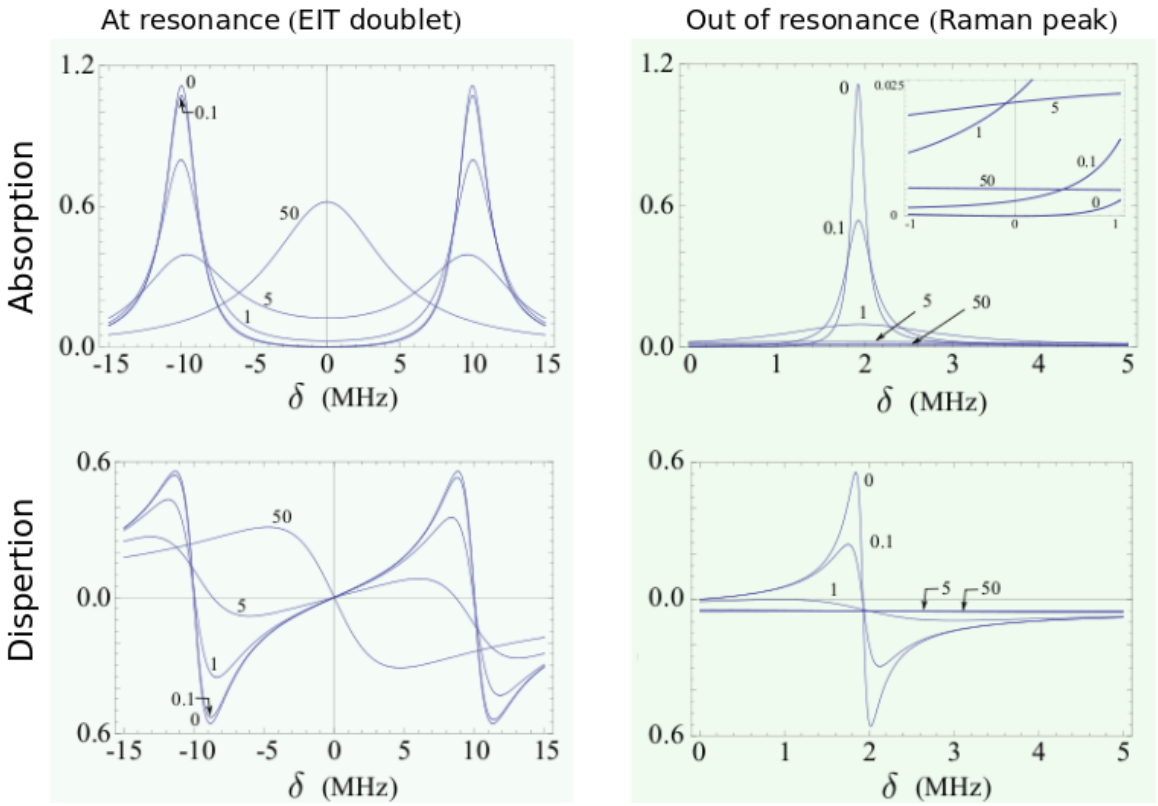


Figure 2.4: Effect of the relaxation rates of the coherences between the gound levels in cases:
(**a**) resonant EIT (left); (**b**) Raman configuration (right).
The x-axis corresponds to the two-photon detuning $\delta$ ($= \Delta_s$ in the case of perfect $EIT$, $\Delta_c = 0$). The y-axis corresponds to the real part (dispersion) and imaginary (absorption) of the linear susceptibility. Each plotted curve is indexed by the value of $\Gamma_{21}$, given in $MHz$, set in the simulation in order to obtain the curve. The figure inserted in the top right corner gives a zoom of the Raman absorption in the vicinity of the two-photon resonance.

## 2.2 Transfer of statistical properties

By considering the system 2.6 for small fluctuations operators (see section 2.1.1), it is possible to calculate how the weak field variables modify those of the atomic sample. The weak field variables enter as linear terms in the expressions for the transverse components of the fictitious spin representing the collective atomic state. A similar dependency is found in expressions for the field variables in terms of the atomic variables, so that we can say $EIT$ provides a coherent interface between atoms and fields.

To describe the interaction, besides the system 2.6, we need an expression for the propagation of the field within the sample. The evolution of the Heisenberg operator corresponding to the quantum field can be described in slowly varying amplitude approximation by the propagation equation

$$\left(\frac{\partial}{\partial t} + c\frac{\partial}{\partial z}\right) \hat{A}_b(z,t) = i g_b \, n_0 \, \hat{\sigma}_{23}(z,t) \tag{2.19}$$

which is the quantum version of 1.49.

As before, we consider $\langle A_b \rangle \sim 0$ and the whole sample pumped in state $|2\rangle$[6]. In the classical limit, imposing perfect one photon resonance for both $A_a$ and $A_b$ (i.e. $\Delta = \delta = 0$), the linearized expressions for the coherence terms of the density matrix and the wave propagation read

$$\begin{cases} \left(\frac{\partial}{\partial t} + c\frac{\partial}{\partial z}\right) \delta A_b = i g_b \, n_0 \, \delta\sigma_{23} \\ \frac{\partial}{\partial t}\sigma_{23} = -\Gamma_e \, \delta\sigma_{23} + i g_b \, \delta A_b + i\Omega_a \, \delta\sigma_{12} + f_{23} \\ \frac{\partial}{\partial t}\sigma_{21} = -\Gamma_{21} \, \delta\sigma_{21} + i\Omega_a^* \, \delta\sigma_{23} + f_{21} \end{cases} \tag{2.20}$$

We know from the above discussion that $\langle \sigma_{13} \rangle$ is zero.

Similar equations hold for the conjugate quantities, and so it is possible to combine them in order to get expressions for quadratures of the field ($X_b = A_b^* + A_b$ and $Y_b = i(A_b^* - A_b)$). Correspondingly, the atomic variables can be reorganized in terms of transverse components of the fictitious atomic collective spin (components $r_1$ and

[6]The intensity scale to define the weakness for $A_b$ is given by the requirement that populations have to be all negligible except $\rho_{22}$. It is therefore sufficient that $|A_b| \ll |A_a|$ and $|\Omega_b| \ll \Gamma_e/\sqrt{2}$ (to avoid saturation of the dipole transition)

$r_2$ of the collective Bloch vector) for each transition:

$$j_x = \frac{\sigma_{21} + \sigma_{21}^\dagger}{2} \quad j_y = i\frac{\sigma_{21}^\dagger - \sigma_{21}}{2} \qquad \sigma_x = \frac{\sigma_{23} + \sigma_{23}^\dagger}{2} \quad \sigma_y = i\frac{\sigma_{23}^\dagger - \sigma_{23}}{2} \tag{2.21}$$

After Fourier transform, $\sigma_{x/y}$ can be eliminated leaving expressions concerning just the field quadratures and the Raman coherence $j_{x/y}$

$$\begin{cases} \frac{\partial}{\partial z}\,\delta X_b(z,\omega) = \frac{1}{c}\left(i\omega - \frac{g_b^2 n_0(\Gamma_{21}-i\omega)}{(\Gamma_e-i\omega)(\Gamma_{21}-i\omega)+|\Omega_a|^2}\right)\,\delta X_b \;+\; F_{X_2}(z,\omega) \\ \delta j_x(z,\omega) = \frac{1}{2}\frac{g_b\Omega_a^*}{(\Gamma_e-i\omega)(\Gamma_{21}-i\omega)+|\Omega_a|^2}\,\delta X_b(z,\omega) \;+\; F_{j_x}(z,\omega) \end{cases} \tag{2.22}$$

with analogue equations for $Y_b$ and $j_y$ ($F_{X_b}$, $F_{J_x}$ are the resulting forms for the Langevin forces). Thus we find that in case of $\langle A_b\rangle \sim 0$, the fluctuations of the electromagnetic field $A_b$ are linearly coupled to the transverse components of the collective spin.

This can be qualitatively demonstrated also by looking to the dark state expression 1.105 in the limit case of $\Omega_b \sim 0$, by exploiting the decomposition into mean value and small variations ($\Omega_b = 0 + \delta\Omega_b$)

$$|D\rangle \sim -|2\rangle + \frac{\delta\Omega_b}{\Omega_a}|1\rangle \tag{2.23}$$

where we find again that the $\vec{R}$ projection on the $(1,2)$ plane shows a linear dependence on $\delta\Omega_b$.

I have kept the Langevin forces terms in equations 2.22 because in a rigorous calculation ([24],[23]) they are involved in the process of exchange of fluctuations between the field and the atomic sample. Therefore, exploiting a method for switching on and off the exchange channel, one can transfer (map) states of the light in the atomic spin state, and, by stopping the exchange at the right moment, leave them in the sample. Reopening the channel in a second time with no signal input, one can transfer the atomic state into the ground state while releasing the excitation on the outgoing field. Since the set of equations for the weak (signal) field is linear and there is almost no absorption in the medium, the above classical calculations remain true in the quantum case and such a switching mechanism would allow the storage and retrieval of any weak quantum state of light without destroying its quantum properties.

## 2.3 Storage procedure

The above sections have shown that the group velocity reduction is a linear process which preserves the quantum state of the slow light pulse. Therefore, a non-absorbing medium with a slow group velocity is a temporary storage device, with a memorization time given by the achievable delay. However, such a system has only limited storage capabilities, due to the constraint on the delay-to-pulse-length ratio (which cannot exceed the square root of the optical depth, as shown in section 2.5.1). This limitation originates from the fact that a small group velocity is associated with a narrow spectral acceptance window of $EIT$ and hence larger delay times require larger initial pulse length.

The key idea to get a real memory is to convert the excitations composing the signal pulse ($\hat{A}_b$) in "at rest" internal state excitations of the atomic sample. This can be realized by smoothly turning off the other beam ($\hat{A}_a$) while the pulse is within the medium, exploiting a kind of $STIRAP$ procedure as that for complete population transfer (see section 2.4.4). Due to this driving role, the strong field $\hat{A}_a$ takes the name of "control". If the signal field is much weaker than the control, the latter maintains a velocity closed to $c$, so that its decreasing profile can reach and overcome the whole envelope of the signal before it leaves the sample. Moreover, if the photons present in the pulse to be stored are much less than the atoms of the sample, the signal pulse is completely depleted before having moved the Bloch vector much from the initial position $\vec{R} = (0, 0, -1)$, and the linear relations among atomic and field variables 2.22 keep on holding throughout the whole dynamics. This means the final collective vector shows small components on the $(1, 2) - plane$ determined by amplitude and phase of the pulse[7], while its "halo" maps the statistical features of the field. Once transfered to the Raman coherence, the excitations cannot be incoherently dissipated by any allowed transition. Therefore they can survive for an arbitrary long time (limited by the decay rate of the coherence). Actually the energy of the signal pulse is mostly not accumulated in the medium, but passed to the control field, which acts like a reservoir (both in writing and reading phases). The internal state of the atomic sample keeps only a small amount of energy[8] where the information on signal

[7] both quantities defined respect to the control beam's ones

[8] which can either be in more that in less respect to the initial state, depending on which state between $|1\rangle$ and $|2\rangle$ is less energetic

amplitude and phase is contained.
To regenerate the signal pulse within a reading phase of the memory, it is sufficient to turn the control field back on. Control field excitations transform the Raman coherence back into the optical one related to the signal field: the pulse is indeed produced as a kind of superfluorescent emission. The control beam intensity is responsible for the rate of construction of the optical coherence ([72]), which, after formation, is quickly converted in field excitations, so, to map back the state of the light, a symmetric slope with respect to the writing stage has to be implemented. This superfluorescent emission shows a number of particular features: its direction of propagation is determined (it is the same as the input pulse), and it takes place even if the ensemble is much wider and dispersed than a fraction of wavelength. This is possible due to the constructive phase the first (random directed) excitations find on the "right way", which has been prepared by the input beam during the writing phase.[9] In fact, the loss of this phase path is usually the cause of the memory lifetime limit [123], [124].

A nice picture has been introduced since 2000 by Fleischhauer and coworkers ([33, 34], [41]), in which the physics of the state-preserving slow light propagation in $EIT$ is associated with the existence of quasi-particles named dark-state polaritons. A dark-state polariton is a mixture of electromagnetic and collective atomic excitations, which corresponds to the uncoupled eigenstate of the whole quantized matter-field system (see section 2.2.4). It can explains all the features of both the atomic and the signal field states (dark states, group velocity, adiabatic following) separately analyzed just above.
These polaritons are defined as solutions of the propagation equation for slowly varying envelopes (2.19) under particular conditions of adiabaticity (which finally match them for general adiabatic following as showed section 2.2.4 (1.107)). Coming back to the system of equations for the atomic density matrix elements 2.6, and holding the same approximations as them carrying to 2.8, except for steady state limit, one

[9] the direction of the restored light is determined by a phase matching condition between the fields. During the writing procedure, control and signal fields induce in the medium a coherence with wave vector $\vec{k}_{atoms} = \vec{k}_b - \vec{k}_a$, thus producing a spatial grating. During the reading procedure, interaction of the control beam with this grating restore the signal field, which propagates in the direction determined by the phase matching condition $\vec{k}'_b = \vec{k}_{atoms} + \vec{k}_a = \vec{k}_b$ (the last equality valid if the atomic coherence can be considered as frozen during the storage time)

gets[10]

$$\begin{cases} \frac{\partial}{\partial t}\sigma_{23} = -\Gamma_e \sigma_{23} + i\Omega_a \sigma_{21} + i g_b \hat{A}_b \\ \frac{\partial}{\partial t}\sigma_{21} = i\Omega_a^* \sigma_{23} \\ \left(\frac{\partial}{\partial t} + c\frac{\partial}{\partial z}\right)\, \hat{A}_b = i g_b\, n_0\, \hat{\sigma}_{23} \end{cases} \tag{2.24}$$

After some mathematics and adiabatic approximation[11], the propagation equation reads

$$\left(\frac{\partial}{\partial t} + c\frac{\partial}{\partial z}\right)\, \hat{A}_b = -\frac{g_b^2\, n_0}{\Omega_a^*}\frac{\partial}{\partial t}\left(\frac{\hat{A}_b}{\Omega_a}\right) \tag{2.27}$$

For constant $\Omega_a$, the term on the right side of the equation just leads to a variation of the group velocity ($v_g \to c/(1 + \frac{g_b^2 N}{|\Omega_a|^2)})$ for the quantum field $\hat{A}_b$. In the general case of varying $\Omega_a$, the additional term proportional to $(\dot{\Omega}_a/\Omega_a)$ describes reversible changes in quantum amplitudes due to stimulated Raman scattering.
Equation 2.27 gets simple solutions in the form of a new quantum field defined as

$$\begin{cases} \Psi = cos\theta\, \hat{A}_b - sin\theta\, \sqrt{n_0}\, \sigma_{21} \\ cos\theta = \frac{\Omega_a}{\sqrt{|\Omega_a|^2 + g_b^2\, n_0}} \qquad sin\theta = \frac{g_b\sqrt{n_0}}{\sqrt{|\Omega_a|^2 + g_b^2\, n_0}} \end{cases} \tag{2.28}$$

for which the propagation equation reduces to $\left(\frac{\partial}{\partial t} + c\, cos^2\theta \frac{\partial}{\partial z}\right)\, \Psi = 0$. It is the dark state polarition. The mixing angle $\theta$ between the atomic and the field components is governed by the atomic density and the strength of the control field, and determines

[10] $\Gamma_{21}$ is considered as neglectable for simplicity

[11] the second equation holds $\sigma_{23} = (-\frac{i}{\Omega_a^*}\frac{\partial}{\partial t})\sigma_{21}$, which applied to the first equation gives an expression containing just $\sigma_{21}$ and fields variables $\Omega_a,\ \hat{A}_b$

$$\sigma_{21} = -\frac{i}{\Omega_a}\left(\Gamma_e + \frac{\partial}{\partial t}\right)\left(-\frac{i}{\Omega_a^*}\frac{\partial}{\partial t}\right)\sigma_{21} - g_b\frac{\hat{A}_b}{\Omega_a} \tag{2.25}$$

It is possible to show ([33]) that adding an adiabatic condition on control field envelope variation such as that for general adiabatic passage 1.107, at the first order one can neglect all the terms but the last one, leading to the simple form $\sigma_{21} \sim -g_b\hat{A}_b/\Omega_a$.
Thus in the perturbative and adiabatic limit, it is possible to get a form of the propagation equation containing just fields variable

$$\left(\frac{\partial}{\partial t} + c\frac{\partial}{\partial z}\right)\, \hat{A}_b(z,t) = i g_b\, n_0 \left(-\frac{i}{\Omega_a^*}\frac{\partial}{\partial t}\right)\left(-g_b\frac{\hat{A}_b}{\Omega_a}\right) \tag{2.26}$$

which is equal the one reported in the text

the propagation velocity $v_g$. The storage procedure is thus obtained as a dynamic rotation of this mixing angle, leading to an adiabatic passage from a pure photon-like to a pure spin-wave polariton thereby decelerating the initial photon wavepacket to a full stop. During the adiabatic slowing the spectrum of the pulse becomes narrower in proportion to the group velocity, which essentially eliminates the limitations on initial spectral width or pulse length and very large ratios of storage time to initial pulse length can be achieved. The regeneration of the signal pulse comes out reversing the rotation of $\theta$ at a later time. Hence in this contest the memory procedure is seen as an extension of $EIT$ to a dynamic group-velocity reduction via adiabatic following of the fields amplitude ratio.

Other groups have pointed out the interpretation of the storage phenomenon as a limit case of slow light is somehow misleading, the crucial aspect being the construction of the dark state for the couple of field states $\Omega_a$, $\hat{A}_b$ ([79], [72], [71]). The dark state can in fact survive after fields extinction, and produce a pulse of signal field during the reading phase as a consequence of the collapse to the now dark state (all atoms on state $|2\rangle$). The abrupt switching of the control field leads to the incoherent absorption of the free field part of the dark polariton, only the bound part, i.e. the Raman coherence, getting stored. However, the ratio between the free and bound parts of the polariton being determined by the control field intensity, almost perfect storage is possible in case of strongly reduced group velocity for the signal pulse at the moment of the switching. As a proof they implemented protocols able to store pulses strongly not respecting the adiabatic condition [72], [125], [71].

## 2.4 Effects of inhomogeneous broadening

Up to now we showed the effects of a medium on the propagation of a pulse representing the ensemble just as a factor $N$ multiplying the susceptivity of the single atom. This assumption presupposes identical properties for the whole sample. When it is not the case, as for inhomogeneous broadening, the ultimate medium susceptivity has to be calculated by adding all the different expressions weighted by the relative populations as shown in 2.31, where $f(\Delta_D)$ represents the population of atoms with the resonance moved of $\Delta_D$ from the reference value. Usual cases of inhomogeneous broadening are solid state structures, where the vicinity of other atoms and the presence of impurities effectively changes the eigenstates and thus the resonant frequencies in a almost random but constant way; and Doppler broadened gases, for which the inhomogeneity is given by the frequency shift $\Delta_D$ of the field seen by the moving atoms and dependent on the velocity ($\vec{v}$) in the direction of propagation of the light ($\vec{k}$)

$$\Delta_D = -\vec{k} \cdot \vec{v} \tag{2.29}$$

$\Delta_D$ is defined in terms of pulsation.
The population for different detuning follows the distribution in velocity classes, which at thermal equilibrium takes a Gaussian shape of width determined by the temperature of the sample ($T$)

$$f(\Delta_D) = \frac{1}{\sqrt{2\pi\Gamma_D^2}}\, e^{-\frac{\Delta_D^2}{2\Gamma_D^2}} \qquad \Gamma_D = \sqrt{\frac{k_B\, T}{\lambda^2 m}} \tag{2.30}$$

Due to the fact that the frequency of the light seen by atoms with different velocities is not the same, in general, in presence of two beams, any velocity class reads different two-photon detuning $\delta$. It is trivial to understand that this aspect makes any collective $EIT$ effect impossible, because it requires an identical $\delta$ for all the one-photon detunings (for the simple three level model $\delta = 0$). Actually, for close signal and control fields frequencies (as it is the case for hyperfine splitting), by carefully superimposing the two beams one gets almost the same one-photon detuning for both fields, thus keeping the two-photon detuning fixed. This geometrical condition is a necessary prerequisite for $EIT$ in warm atoms.

So, to determine the susceptibility seen by the weak field $A_b$ crossing the warm

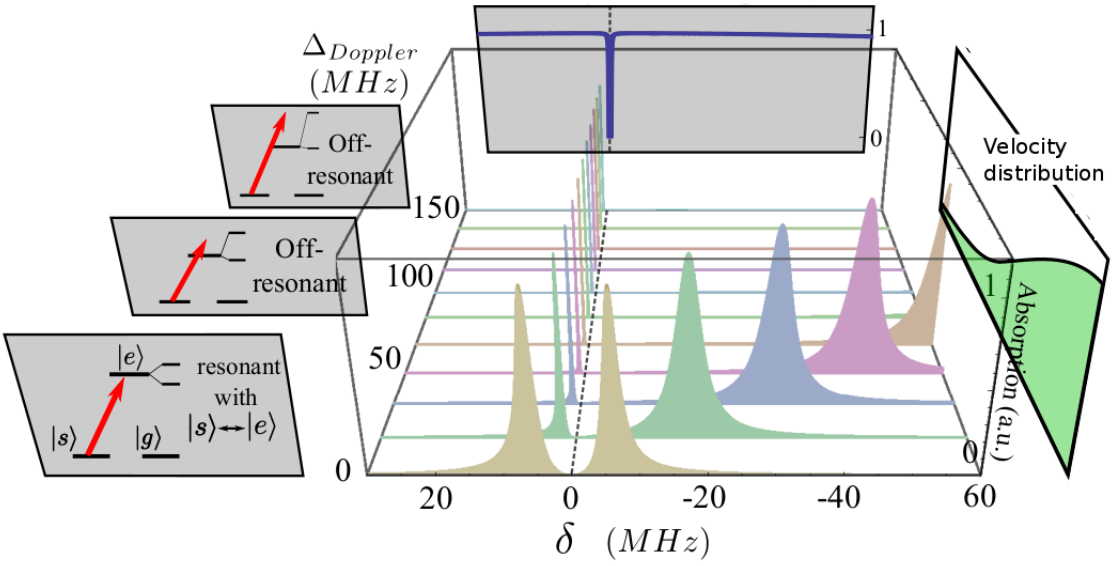


Figure 2.5: *EIT* features in a three-level system in $\Lambda$ configuration. Probe absorptions profiles are displayed for atoms with different velocities as a function of the two-photon detuning $\delta$ given by the Doppler effect. For the zero velocity classes, the one-photon resonance condition $\Delta = 0$ is fulfilled and the absorption profile matches that of fig2.2.a . For the other velocity classes, the Doppler effect induces an effective one-photon detuning $\Delta \neq 0$, and the absorption profiles are similar to that of fig2.2.b, with a narrow peak that gets closer and closer to the two-photon resonance for increasing $\Delta$ values. The AC Stark shift induced by the excited level, however, prevents it from reaching the exact resonance, which hence remains the point of maximal induced transparency. The integrated absorption is obtained for a Gaussian velocity distribution of $160\,MHz$ half-width (thermal distribution for Cesium at $300\,K$). The control Rabi frequency is $\Omega_a = 2.3\,\Gamma_e$ , where $\Gamma_e$ is the natural linewidth. [104].

atomic sample, one has to calculate the expression

$$\tilde{\chi}(\Delta, \delta) = \int \chi(\Delta + \Delta_D, \delta)\ f(\Delta_D)\ d\Delta_D \tag{2.31}$$

The contribution from the different velocity classes is reported in fig.2.5 for atoms of increasing velocity in the direction opposite to that of propagation of light. The effect of the susceptibility is shown under the aspect of transmission profile $t$, defined as in 2.13. When the one-photon detuning increases, one can recognize the upper absorption maximum of the $EIT$ window transforming into a Raman absorption peak and approaching the $\delta = 0$ limit. However, we know from theoretical treatment that it never gets that position: the net effect of Doppler broadening is a reduction of the $EIT$ window width. In terms of dispersion, as found above, the gradient in $\delta = 0$ of the real part of $\chi$ maintains the same value for every one-photon detuning, with a reduction of the width of the transparency region around $\delta = 0$ with zero curvature (2.16). Hence, the Doppler broadening reduces the transparency window and the region of linear dispersion (in which there is no distortion of the pulse), but substantially preserves the main features of the $EIT$. An analytic description of the phenomenon, based on simplifying assumption, can be found in [62].

### 2.4.1 Advantages and disadvantages of different experimental set-ups

*Warm atoms* contained in evacuated cells are for sure the simplest set-up to implement, the preparation stage limited to some optical pumping procedure. Moreover the number of available atoms is generally very high (billions). Fundamental problems with this medium are the imperfect control of the population distribution, which cannot be oriented as precisely as with cold samples, and the relatively short time of flight across the laser beams, which finally determines the coherence life time (hundreds of *microseconds*). With these samples it is usually more complicated to achieve an optimal homogeneity of magnetic field, the medium size being an order of magnitude greater than in other cases. Moreover atoms lost at some point can reenter the interaction region providing dechoerence effects. However, when it is possible, using a buffer gases one can reduce the impact of all these negative aspects, at least for the part due to the fast velocity. More than one order of magnitude can be gained in time of flight [10], [89].

*Free falling clouds from MOT* provide large numbers of atoms (hundreds of millions in regular cases, but *MOT* up to tens of billions are possible in particular cases), spatially compressed respect to warm samples (*millimeters*). Population can be almost perfectly oriented, by filtering procedures with ad hoc light flashes, and lost atoms cannot enter the interaction region at a second time (this is valid for all cold samples hereafter) (see e.g. [18]). Limiting aspects of this sample are the time interval one has to wait in free falling condition before the strong quadrupole (hence strongly inhomogeneous) magnetic field responsible for the *MOT* formation can be completely switched off (*milliseconds*), and, most important, the intrinsically not avoidable temporal evolution of the system. Due to the untrapped condition, the cloud both expands and falls, preventing long time interrogation protocols.
*Ultra-cold trapped samples*, Both optical and magnetic traps provide almost perfectly oriented, high density samples (tens to hundreds of *micrometers* is the regular extension for these traps). The number of atoms is generally one or two order of magnitude lower than in the case of a free falling cloud from a *MOT*, but with respect to the former case, here one handles a system with almost no time evolution.
Magnetic harmonic potentials are the simpler tool to provide in order to trap the sample, optical traps needing for strong far off resonance laser light. On the other hand magnetic trapping intrinsically shows a small amount of magnetic inhomogeneity, which can be neutralized only by addressing the so called clock transitions ([115]). This issue further limits the exploitable number of internal states, already reduced to the low field seeking ones.
Optical traps can instead provide almost the same potential for all the sub-levels of the ground state (either considering the two hyperfine sub-levels). Moreover, and it can be a crucial aspect, a small trapped sample is always hard to address with an additional laser beam, as in the case of memory experiments. By using an optical trap the trapping beam can be used as a reference for setting the right direction and beam size for an additional beam in order to maximize the coupling of the latter with the sample, as demonstrated for example by the group of M.Mitchel [68]. Optical potentials, in the form of lattices, can also be exploited to reduce the spatial degrees of freedom of the atoms, preventing loss of coherence due to position change during the storage time, as in [124].

# Chapter 3

# Matter-waves interferometry

In this chapter I recall the general main features of interferometers based on atomic wave-functions, then focusing on the specific case of a multi-state interferometer able to overcome the standard two-state sensitivity that we experimentally demonstrate the validity (for the experimental results see chapter 7).
Matter-wave interferometry is a powerful tool for high-precision measurements of both internal quantities, such as quantum properties of atoms and many-body phenomena, and external stress, as gravity, and accelerations. Moreover, the fact atoms are massive particles allows their exploitation as devices capable of detecting the force fields present in the occupied place.
The standard way atom interferometry is performed is by interrogating free falling samples [14]: the atomic ensembles are cooled down until ultra-low temperatures to ensure long coherence times, but "high" densities (and condensation too) are avoided, in order to minimize decoherence due to interparticle interaction. The technique is nowadays well handled, and the achieved interferometric sensitivity often reaches the boundary limit constituted by the atomic shot noise. The use of $BECs$ remains however a tempting idea. The principal reason for the interest in exploiting degenerate samples lies in the fact they are macroscopic objects, therefore easily observable, but their behavior is completely dominated by their wave nature: we can say they represents the matter analogue of the optical laser, thus providing the maximum coherence allowed by quantum mechanics.
Today the obstacle constituted by interactions is avoidable by exploiting interaction tuning techniques, and so the interest in $BEC$ based interferometers is renewed. The

full arbitrary control of the interparticle interactions opens indeed new possibilities in the field of quantum computation protocols with degenerate samples. In this framework, coherent storage of non classical state of light can be exploited as a preparation stage for non classical collective atomic state. The detection of the relative phase between the two field exploited for a two-photon Raman transition by means of atomic interferometry, presented in section 7.3.2, is conceived in this light.

Our apparatus allows only for a limited control over the interactions between atoms, however, the improvement we demonstrate can be considered as a proof of principle for a technique which is, due to its simplicity, applicable in a wide variety of devices.
of quantum computation based on atomic degenerate samples

In the classical limit the sensitivity of an interferometer, defined as the smallest signal that can be resolved, is determined by the slope of the interferometric signal and the measurement noise. The best achievable sensitivity of a conventional 2-path interferometer is determined by the shot noise and hence scales as $1/\sqrt{N}$ with the number of atoms $N$.The specific properties of atoms open two ways for overcoming this natural limit: on the one hand, nonlinear atom-atom interactions can be exploited to produce an entangled input state. This way, with a collective non-local measurement at the output, one can reduce the phase-measurement error of, e.g., a Ramsey interferometer ([45]). The best possible outcome in a lossless system is the sensitivity of $1/N$, known as the Heisenberg limit [39]. On the other hand, the intrinsic richness of both external and internal degrees of freedom, makes it relatively simple to improve the interferometer sensitivity by increasing the number of paths $M$, as for example in [117, 118]. It can be shown in fact that as a general aspect the sensitivity scales with the number of the involved paths $M$. Of course, it is paid by a decrease in the average number of atoms per path and hence results in a lower signal-to noise ratio. Finally, the sensitivity improves with the number of paths if the scaling of slope with $M$ exceeds the $\sqrt{M}$ scaling of the shot noise.

Our proposal for a multi-path interferometer is based on the energy separation among the internal states of the atoms, so that, we will rather name it multi-state than multi-path. The multi-state functionality is achieved by coherent manipulation of $BECs$ in different Zeeman states of the same hyperfine level by means of radio-

frequency (RF) and static magnetic fields.

## 3.1 Theoretical model

The general protocol on which atomic interferometry is based consists in a Ramsey-like procedure: two almost resonant pulses of well defined area (i.e. able to change the atomic state) are applied to the sample one after the other, and then the output of the interferometer is read by means of a measurement of population distribution among the involved states. In analogy with interferometers for light, we can say the radiation pulses act like beam splitters, the first one able to send a part of the initial matter wave in each path, the second one providing a remixing operation of the channels. The output is the whole population distribution resulting from interference among the wave-fuction components, so that we can actually speak in terms of Mach-Zender interferometry.
In the case of a two-path system, the physical mechanism on which the interferometer relies is quite simple and easy to understand with the help of the Bloch sphere representation in slowly varying approximation. Referring to formalism of section 2.2.3, we can summarize the whole procedure as a couple of $\pi/2$ pulses applied in succession on a sample initially in the collective ground state (corresponding to a collective Bloch vector $\vec{R}$ oriented along the negative "3" direction). The first pulse of radiation defines the phase reference of the system, and so we can give it, for simplicity, the "1" axis direction. After its application, the Bloch vector $\vec{R}$ is thus aligned along with the "2" axis. If the frequency of the radiation is perfectly equal to the energy difference between the two states, in the time interval separating the two pulses $\vec{R}$ holds the position. This means that application of a second pulse with the same phase as the first one ends up in an overall effect similar to that obtained for a single $\pi$ pulse, with all the atoms transferred to the initially unpopulated state ($\vec{R}$ towards positive "3" direction). If on the contrary the radiation is detuned with respect to the atomic resonance, after the first pulse $\vec{R}$ rotates in the $(1,2) - plane$ with an angular velocity equal to the detuning, thus accumulating an angle respect to axis "2". It interacts hence with the second pulse with a modified phase, which results in a reduced overall effect with respect to the resonant case. For a phase shift equal to $\pi$, it gets completely canceled due to a perfectly opposite effect of the two pulses, corresponding to total population back in the initial state.

Ramsey spectroscopy resolved in frequency domain is obtained by repetition of the sequence for a fixed "interrogation" time $T_d$ (the time interval separating the two pulses) while scanning the frequency of the radiation. The result is a fringe structure in the population transfer, with an absolute maximum for perfect resonance and local maxima every time the accumulated phase matches a multiple of[1] $(2\pi)$. The peak value of state transfer decreases with detuning as expected for coherent interaction. For longer interrogation time the fringes get narrower and closer, with an enhancement of the attainable sensitivity: this is the motivation for the quest of as longer as possible coherence durations.
The capability as a sensor comes from the fact that any external perturbation modifying somehow the atomic wave-functions during the interrogation time results in a modification of the obtained fringes.
Ramsey spectroscopy can be exploited in a simpler way, in which the frequency of the radiation is maintained fixed and the sequence is repeated while moving the relative phase between the two pulses. The theoretical treatment is similar to the previous one, only that here it is the second pulse instead of $\vec{R}$ varying direction in the $(1,2) - plane$. In this case the sensitivity is defined by the slope in the population distribution variation as a function of the relative phase, and does not depend on the interrogation time. Our experimental realization follows this scheme, which results to be simpler to perform with respect to the original one. However, switching to the other scheme is just a mere technical issue, as it is shown in chapter 7.

For multi-path interferometry it is not possible to have an easy representation of the system, and a more rigorous mathematical approach is required. In general, the whole evolution of the collective atomic state can be mathematically represented by a transfer matrix $J$ that acts on the atom state wave-function $\Psi(t) = (\Psi_1(t), \Psi_2(t), \ldots, \Psi_M(t))^T$ where $M$ represents the path of the atomic interferometer. The transfer matrix $J$ connects the initial $\Psi_{\text{in}}$ and final $\Psi_{\text{out}}$ states, $\Psi_{\text{out}} = J\,\Psi_{\text{in}}$. It is composed of the matrix $R$ that corresponds to a coupling Rabi pulse and the operator $P$ that describes evolution of the states between the pulses,

$$J = RPR \tag{3.1}$$

[1] that is $|T_d \times \Delta\omega| = n \times 2\pi, \quad \forall n\mathcal{N}$, with $\Delta\omega$ detuning of the radiation

The matrix $P$ contains the elements which generate the interference among the components after the second pulse. In the normal case it is simply a diagonal matrix that adds a phase $\phi_j$ to each state during the delay $\tau$ between the two coupling pulses. The matrix $R$ is derived by solving the time dependent Schrödinger equation for $M$ atomic states

$$i\hbar\frac{d\Psi(t)}{dt} = H\Psi(t) \tag{3.2}$$

where the Hamiltonian $H$ is obtained by the reduction of a general Hamiltonian with coupling off-diagonal terms.

### 3.1.1 The case of three-diagonal coupling

The multi-path (multi-state) atomic interferometer we have experimentally realized with our degenerate sample of $^{87}Rb$ is based on a coherent coupling among the sublevels constituting the Zeeman manifold of the hyperfine level $F = 2\rangle$ $(M = 5)$. The multiple transitions are achieved by means of a single RF magnetic field resonant with the Larmor frequency $\omega_L$ induced by the static field of the trap. Hence the transfer is possible just between neighboring sub-levels, and the manifold shows a constant energetic spacing equal to $\Delta E = \hbar\ \omega_L$. Under these conditions, the matrix $P$ is given by $P_{jk} = \delta_{jk}\ e^{-i(j-1)\omega_L\ T_d}$, while the matrix $R$ is obtained by a three-diagonal Hamiltonian that retains only the neighboring-level-coupling terms

$$H = \begin{pmatrix} 0 & \Omega/2 & & & \\ \Omega/2 & \Delta_1 & \Omega/2 & & \\ & \ddots & \ddots & \ddots & \\ & & \Omega/2 & \Delta_{M-2} & \Omega/2 \\ & & & \Omega/2 & \Delta_{M-1} \end{pmatrix}, \tag{3.3}$$

where $\Omega$ is the Rabi frequency of the RF pulses, while the detuning $\Delta_j$ are given by $\Delta_j = j \cdot \Delta = j(\omega_L - \omega)$ ($\omega$ frequency of the radiation).
To solve this system we refer to the solution of a general multi-level atom in the presence of multiple coupling among the states, given in [36]. The resulting wave function can be expressed in the form $\Psi_R = R\Psi_{\rm in}$, where

$$\begin{aligned} R_{j,k}(\tau,\Omega,M) &= e^{-(j-1)\omega\tau}\frac{2}{M+1}\sum_{l=1}^{M} e^{-i\Omega\tau\cos\frac{\pi l}{M+1}} \\ &\quad \times \sin\frac{\pi jl}{M+1}\sin\frac{\pi kl}{M+1}\,. \end{aligned} \tag{3.4}$$

By simple matrix multiplication we can find the interferometer transfer matrix $J$

$$J_{j,k} = \sum_{l=1}^{M} R_{j,l} R_{l,k} e^{-i(l-1)\Delta E \ T_d/\hbar} \,. \tag{3.5}$$

The output of the interferometer is then calculated by the application of the transfer matrix to the input state vector

$$|\Psi_{\mathrm{out},j}(T_d, \tau, \Omega, M)|^2 = \left| \sum_{k=1}^{M} J_{j,k} \Psi_k^{\mathrm{in}} \right|^2 \tag{3.6}$$

The output signal depends on the delay $T_d$ between the two Rabi pulses, their duration $\tau$ and Rabi frequency $\Omega$ and the number of interferometer paths $M$. In the expression for the transfer function it is possible to recognize the form describing the transmission of a Fabry-Perot cavity, here as limiting the calculations to a finite (equal to $M$) number of reflections on the mirrors. The effect of an increase in the number of paths (states) is thus evident. The interferometer output has the form of a finite Fourier series whose terms correspond to the multiples of the energy separation $\omega_L$ between adjacent Zeeman states. Coherent coupling of the Zeeman manifold leads indeed to the generation of high-harmonic output signals which corresponds a sharpening of the interferometric fringes and hence an enhancement of the resolution. In this sense, an increase in the number of states $M$ leads to an increase in the number and order of the harmonics in Eq. (3.5).

It is interesting to note that for a number of states larger than 3 the eigenfrequencies of the Hamiltonian $H$ are incommensurate to each other making the Rabi coupling quasiperiodic. Indeed, while for a 2-state interferometer the optimal sensitivity of 0.5 rad$^{-1}$ can be analytically calculated for a $\Omega\tau = \pi/2$ pulse, for our 5-state interferometer the optimization of the sensitivity remains nontrivial (simulations lead to the optimal performances of 0.82 rad$^{-1}$ for $\Omega\tau = \pi 3/\sqrt{5}$).

# Part II

# Experimental work on $EIT$-based memories

In the first chapter of this part of the manuscript I will present our characterization of the $EIT$ effect on the $D2$ line of a Doppler broadened $^{133}Cs$ vapor. It shows particular features with respect to the simple behavior illustrated in section 2.5 due to the vicinity of the sub-levels of the excited hyperfine manifold, whose spacing is comparable to the Doppler width at room temperature ($T = 300K \rightarrow \Gamma_D \sim 180\ MHz$). The experimental results, showing lower than expected induced transparency and memory efficiency (see below), led our group to elaborate a more complex general theoretical model ([83]) which has proven its ability to faithfully describe the sample response. In particular it is able to explain the weakness of the measured $EIT$ effect, and to suggest a way to improve it. The proposal has then been experimentally demonstrated ([104]).

The generalization of the three levels $\Lambda$ scheme to a more realistic multi level configuration has been a subject of interest since the early studies of Harris ([120],[119]). Most of times, atoms have a hyperfine structure yielding manifolds of states too close to be neglected in calculations for atom-light quasi-resonant interaction. However most theoretical works focused on the deformation of the $EIT$ induced by a second excited state in the case of homogeneous media (as cold atoms), that is without considering inhomogeneous broadening. The predicted features were small deviations from maximal transparency and linear dispersion (as in [25]) . In a number of experiments, both on ultra-cold atoms (as [58], [50]) and warm $Rb$ atoms exploiting the $D1$ line (as [76], [97]), the detected small deviations from the three level model, such as non perfect transparency or temporal spreading of the pulse, could be explained in the frame of these simple extensions. However the $D1$ line excited manifold (at least in $Rb$ and $Cs$ atoms) shows a spacing larger then the Doppler broadening, thus ensuring a qualitatively similar susceptibility expression for the whole velocity distribution, which is not the case for the $D2$ line.
Actually, the fact that the $D2$ line presents additional problems had already been showed in experiments on coherent population trapping ([110]), where the fringe contrast attainable in Ramsey-like interferometry was a factor 5 smaller in the $D2$ line than on the $D1$ line. Moreover, deformed and reduced transparency windows as in our case had been detected on the $D2$ line of a $Rb$ vapor cell ([122]) by the group of M.O.Scully in 2002. Thus, in hindsight, the presence of additional problems concerning $EIT$ on the $D2$ line is not surprising. However, to our knowledge, no extensive

theoretical work has been published on the subject, so that our efforts have resulted in a clearer understanding of $EIT$ in inhomogeneously broadened multilevel system.

In the second chapter I will show the experimental work we carried out in Firenze about the same subject with a magnetically trapped ultra-cold sample of $^{87}Rb$. This part includes first a characterization of the $EIT$ effect on the $D2$ line; second a direct verification of the theoretical model [83], by simulating the Doppler effect for different velocity classes adjusting the one photon detuning $\Delta$; third a measurement of the group velocity $v_g$ and time delay attainable in the usual three level configuration (atoms collected in state $|2,+2\rangle$); finally an estimation of the time delay, coherence decay rate and memory efficiency, attainable in an optimal configuration (atoms in $|1,-1\rangle$)[2].

To ensure uniformity of terminology throughout the whole part and with the referenced articles , I rename all the quantities entering the system as:

$$\begin{cases} |1\rangle \to |s\rangle \qquad |2\rangle \to |g\rangle \qquad |3\rangle \to |e_2\rangle \\ \Gamma_e \to \gamma_{e_2 g}\ (=\gamma_{e_2 s}) \qquad \Gamma_{21} \to \gamma_{sg} \qquad \Delta \to \Delta_c \qquad (\Delta+\delta) \to \Delta_s \\ \Omega_a \to \Omega^c_{e_2 s}\ \text{“control field”} \qquad \Omega_b \to \Omega^s_{e_2 g}\ \text{“signal field”} \end{cases} \tag{3.7}$$

[2]issues related to starting with different initial states will be explained in there

# Chapter 4

# Memory experiments exploiting D2 line in warm $^{133}Cs$ atoms

The memory experiment described in this section was already working when I joined the group, the first evidence of quantum storage of coherent states was just obtained before my arrival [21]. However, there was a lot of open questions to analyze in order to enhance the efficiency of the process. Basically, if the low efficiency ($10^{-2}$ in number of photons for a storage time of 10 $\mu s$) could be possibly justified by the rather small optical depth of the sample, on the other hand there was no clear explanation for the decay time observed for the Zeeman coherence, evaluated to be on the order of $10\,\mu s$, while $T_2 < T_1$ was measured at least of one order of magnitude larger. A key point has been the understanding of the reasons for the low level of transparency we were able to reach ($< 35\%$, [91]) in comparison to results from the literature obtained with similar systems (see for example [31], [97]), which showed substantial agreement with theoretical predictions.
Our work can be summarized in three main directions: minimization of the leakage of light during the storage time; optimized choice of the sample; research of optimal one and two photon detunings.

## 4.1 The memory set-up

The atomic medium we used is a sample of cesium vapor in homogeneous magnetic field environment, and the dipolar transition exploited for the $\Lambda$ configuration is the D2 line component between the levels $(6S_{1/2}\,,\, F = 3)$ and $(6P_{3/2}\,,\, F = 2)$ . By choosing control and signal beams with opposite $\sigma$ polarizations, one gets a nearly exact $\Lambda$ atomic scheme (see inset of fig.4.1) with $|g\rangle \equiv |3, \pm 3\rangle$, $|s\rangle \equiv |3, \pm 1\rangle$ and $|e_2\rangle \equiv |2', \pm 2\rangle$. The $EIT$ scheme is thus based on a Zeeman coherence, so that the response of the medium can be optimized acting on the magnetic field. The response of the medium can be finely optimized for storage of the pulse by matching the $EIT$ window with its frequency spectrum. This way indeed the transparency window width can be minimized, with a gain in spatial compression of the envelope to store[1]. $\sigma$-type optical pumping provides a good orientation of the sample, collecting the population in the maximal $|m_F|$, so that the choice for $|g\rangle$ is constrained to $|m_F| = 3$. The pumping should work better by choosing $F = 4$, but in that case we would address the weakest of the transitions to the excited hyperfine multiplet ($F = 4 \rightarrow F' = 3$), while from $F = 3$ we exploit the strongest one.
The experimental set-up is shown in 4.1. The cesium vapor is contained in a $3\,cm$ long cell with a paraffin coating that suppresses ground state relaxation caused by collisions with the walls. It is placed in a longitudinal magnetic field produced by a stack of coils and protected from external perturbation by a shield made of three layers of $\mu$-metal. The homogeneity is better than $1/500$, which corresponds to less than $10\,mG$ over a magnetic field $B_0$ set to $B_0 \sim 3.5\,G$. The optical pumping is provided by two diode lasers with the same polarization as the control field, acting respectively on the transitions $F = 4 \rightarrow F' = 4$ and $F = 3 \rightarrow F' = 3$: the first one is necessary to repopulate state $F = 3$ (the atoms naturally tend to decay to states not coupled by the light), the latter one is used to optimize the pumping made by the control beam by emptying the state $|F = 3, m_F = \pm 2\rangle$ not coupled by the control beam. For control and signal beams a stabilized Titanium-Sapphire (Ti:Sa) source is exploited, which ensures light with a linewidth of $100\,kHz$. The signal is a single sideband field frequency shifted by $\Omega$ from the laser frequency by a set of two electro-optical modulators. Two photon resonance is fulfilled when $\Omega$ is equal

[1]The optical depth being too low to get the pulse completely contained within the medium even for a while, any gain in compression is a gain in efficiency for the memory

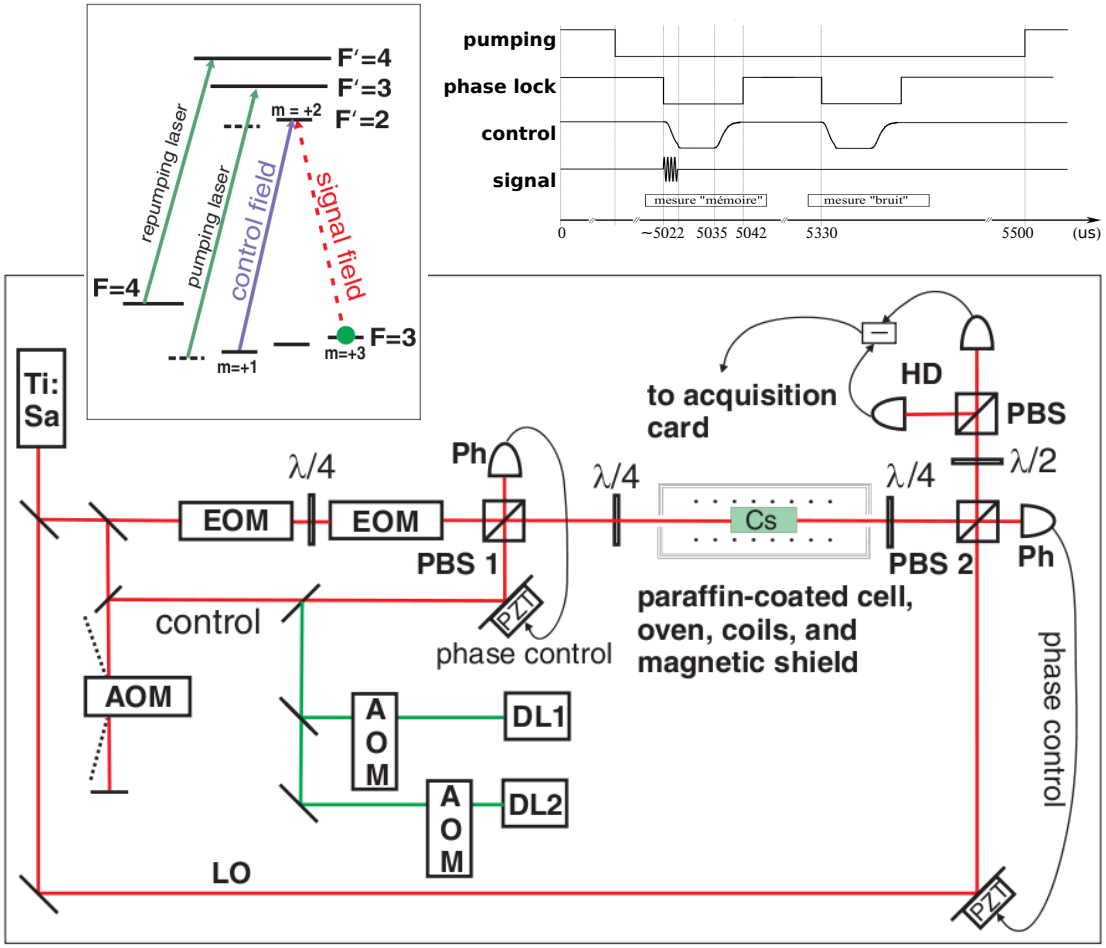


Figure 4.1: Experimental set-up. $DL1$ and $DL2$ : pumping and repumping diode lasers. $HD$ : homodyne detection. $Ph$: photodiode. $EOM$: electro-optical modulator. $AOM$: acousto-optical modulator. $PBS$ : polarizing beam splitter. The control field intensity is controlled by an $AOM$ in double pass configuration in the zeroth order (1:200 extinction). Left inset: atomic levels involved in the experimental procedure, with arrows indicating the transition addressed by each beam exploited in the experiment. Right inset: complete experimental sequence, including the second writing/reading sequence without signal, used for subtracting the effect of the control field leakage on the output of the homodyne detection.

to twice the Larmor frequency $\Omega_L$ induced by the magnetic bias field (that is twice the energy shift between successive Zeeman sub-levels). The sideband is a very weak coherent field, with a power on the order of a fraction of $nW$ ($\sim 10^7$ photons per $second$)[2], an adjustable frequency detuning and a polarization perpendicular to that of the $\sim 5\ mW$ carrier beam (see [20] for details).This configuration is a powerful tool, indeed the two fields (signal and carrier) can be separated easily with a polarizing beam splitter ($PBS1$ in fig.4.1), while the same beam splitter can also provide a superposition of the signal and the control beams (on one output of the $PBS_1$), and a measure of their relative phase (on the second output), by detection of the interference between the carrier and a portion of the control field. Due to the fact that carrier and control beams come from the same parent beam, they are coherent and have the same frequency, hence, by setting to zero the voltage corresponding to the nullification of the interference term, one gets directly an error signal exploitable for phase lock.

The light going out of the cell is mixed with a local oscillator and analyzed using a homodyne detection, after eliminating the control beam with a polarizing beam-splitter ($PBS_2$ in fig.4.1). Similarly to what was done for the carrier beam, the local oscillator phase is locked to the one of the control beam after $PBS_2$. So, finally, we can keep constant the relative phase of all the beams we are interested in (namely: control, signal, local oscillator), and statistical properties can be studied directly by confrontation of measured values for a number of repetitions.

In the experimental sequence, shown in fig.4.1(top-right panel), the atoms are first optically pumped for $6\,ms$ into the $m_F = +3$ sub-level[3], with a $\sim 90\%$ efficiency. After a dark period of $0.5\,ms$, a $(1.6 - 3.2)\,\mu s$ long signal pulse is sent into the cell for the writing procedure. The control field is then switched off for $(4 - 40)\,\mu s$, and finally turned on again. The homodyne detection output is registered for the whole sequence without interruption, from few $\mu s$ before the signal pulse to few $\mu s$ after the arrival of the regenerated field (see fig4.2). A Fourier transform is performed numerically by multiplying the signal with a sine or a cosine function of frequency $\Omega$ and integrating over a time $t_m = n\,2\pi/\Omega$, with $n = 2$ to 4. This yields sets of measured values of the quadrature operators $\hat{X}$ and $\hat{Y}$ of the outgoing field. Averaging over

[2]intensity for which one gets amplitude mean value of the order of the uncertainty spreading $\langle \hat{X}_I \rangle \sim \sqrt{\Delta^2(\hat{X}_{\Omega;\Delta t=1.5\mu s})}$ (integration over two arches; $\Omega = 2\pi \times 1.25\,MHz$)

[3]this case we set control field $\sigma_+$ and signal field $\sigma_-$ polarized

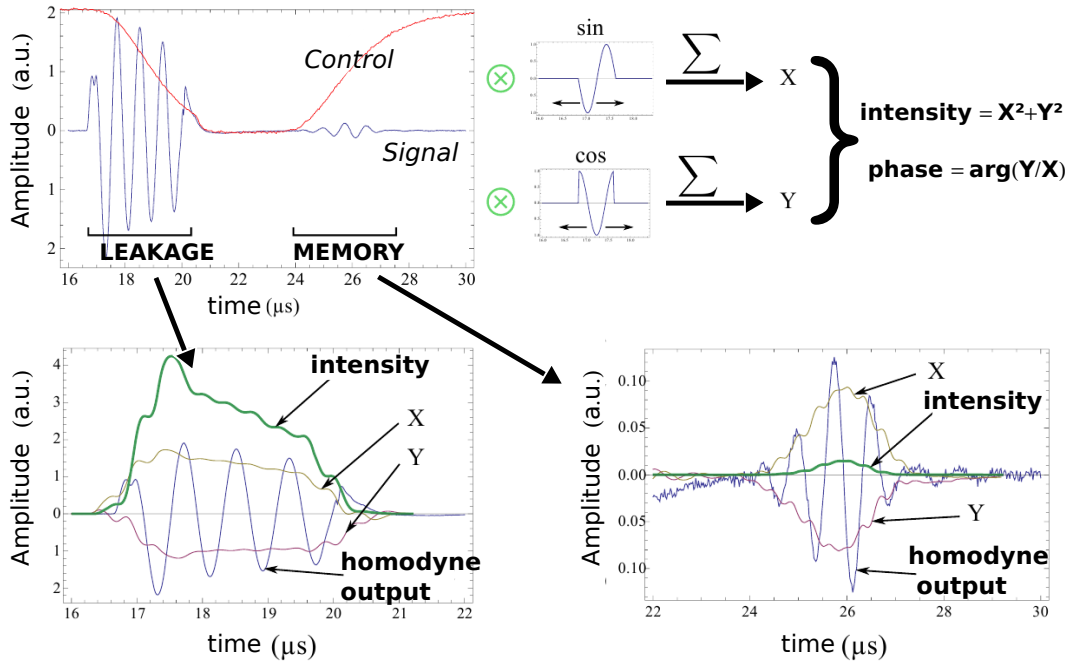


Figure 4.2: Homodyne detection output: raw data and output of the demodulation procedure. In the upper panel a typical curve of the photocurrent acquired for a repetition of the memory experiment is reported, together with the temporal intensity profile of the control field. The figure describes the demodulation operation which leads to the data points reported in fig4.3.a . The curve related to a sample of the experiment is divided in segments of temporal length equal to an integer multiple of the inverse of the frequency of demodulation. The segments are independently multiplied point by point for the profiles correspondent to a sine function and a cosine function, and then averaged. This operation provides access to the quadratures X and Y as well as to the field strength, each segment corresponding to a measure of these quantities (a point in fig4.3.a). In the lower panels an example of the operation of demodulation is reported for both the signal leakage (the part of the signal pulse that escapes the medium) and the retrieved pulse. In these figure all the profiles are represented by continuous curves to facilitate the understanding.

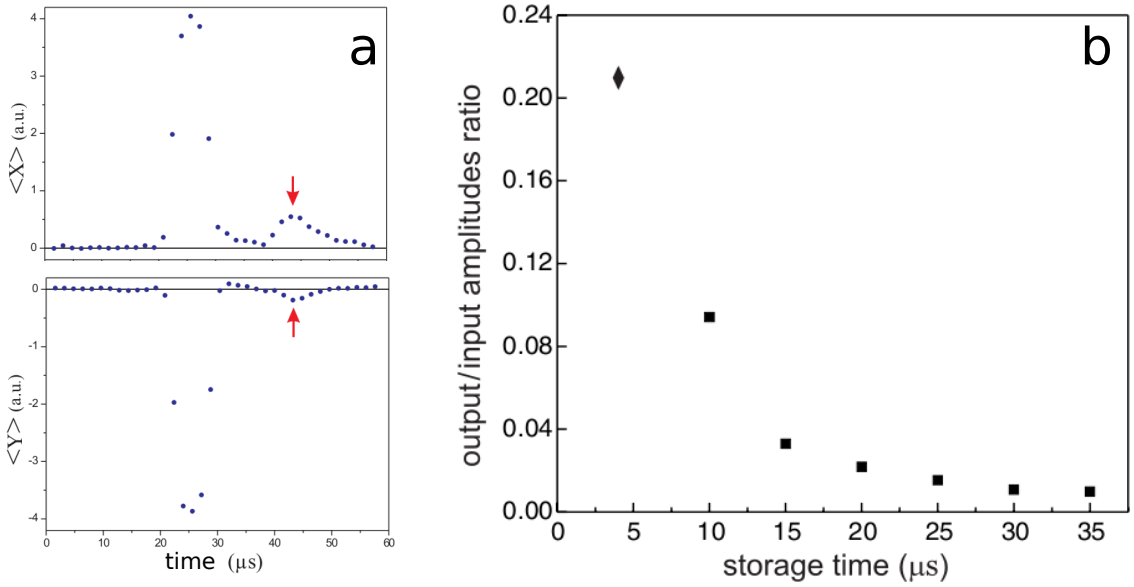


Figure 4.3: **a** - Time-dependent mean values of the two quadratures, measured from a typical 2000-sequence run for an input pulse of duration $5\,\mu s$. The red arrow indicates the retrieved pulse.
**b** - Ratio of the amplitudes of the input and output states, as a function of the storage time. The squares correspond to a signal pulse duration of $6.4\mu\,s$ with a control field power of $10\,mW$; the result indicated by the diamond is instead obtained for a pulse of $1.6\,\mu$ and a control power of $140\,mW$. The $1/e^2$ diameter of the beams was set to $14\,cm$. The decay rate of the memory efficiency is estimated in $\sim 10\,\mu s$. [21].

2000 realizations of the experiment gives the quantum mean values $\langle\hat{X}\rangle$ and $\langle\hat{Y}\rangle$ and variances $\Delta^2(\hat{X}) = \langle\hat{X}^2\rangle - \langle\hat{X}\rangle^2$ and $\Delta^2(\hat{Y})$. Typical traces for mean values are shown in fig4.3.a, for a storage time of about $15\,\mu s$. The first peak corresponds to the leakage of the signal field, the second one to the retrieved signal, for the "in-phase" (X) quadrature (up) and for the "out-of-phase" (Y) quadrature (down). The retrieved signal decreases rapidly with the storage time, with a time constant $\tau \sim 10\,\mu s$ (fig4.3.b), due to the fast spin decoherence processes in the ground state that we will investigate. The noise curves fig4.4 corresponding to the mean values discussed above are obtained by calculating the variances from the same data set. Because of

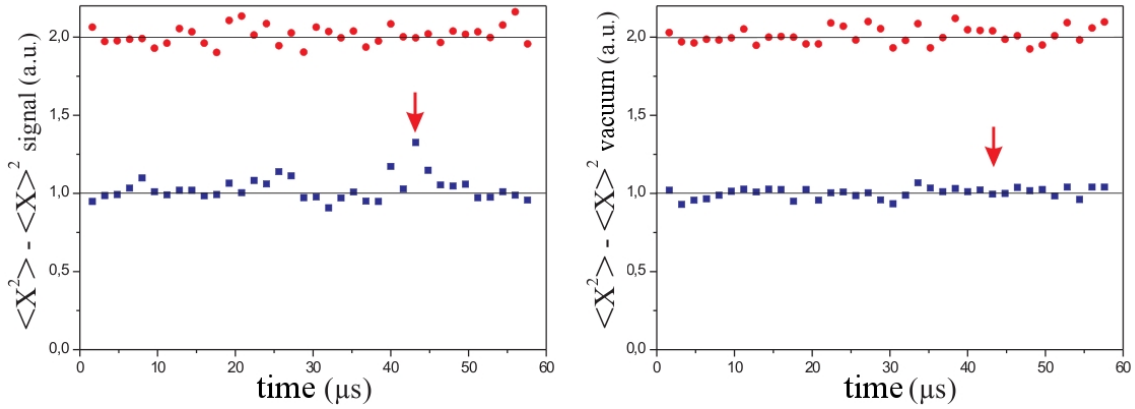


Figure 4.4: Variance of one quadrature in the presence of a signal pulse (left) and without the emission of any signal (right) obtained by comparison of the homodyne detection output of 2000 repetitions of the memory sequence. During transient intervals, the control field contains Fourier components which enter the integration band of the demodulation (lower curves, the arrows indicate the switching on transient). The additional noise can be removed by subtracting, each repetition, the variance obtained in the absence of signal pulse (upper curves).

the small difference in frequency between the control and the signal fields, the small leak of control entering the signal channel leads to additional features in the noise curves. Although it has been designed with a smooth shape, during transient intervals the control field still contains Fourier components around $\Omega/2\pi \sim 1.25\,MHz$, thus entering the integration band of the demodulation (see fig4.4, lower curve in the left panel). To get rid of this spurious effect, which is in some way systematic, the transients are measured independently a second time, after each sequence, with no signal field, and the corresponding data are subtracted point to point from the data taken with a signal field. For the noise, this procedure is equivalent to a 50/50 beam-splitter on the analyzed beam and adds one unit of shot noise to the noise measured without subtraction, yielding the upper curve in fig4.4. Here we can see there are no differences across the detection period.
This memory set-up has been evaluated in terms of fidelity and positioning in the $T-V$ diagram ([55]) during the PhD work of J. Ortalo ([92], [91]), showing a behavior on the edge between classical and quantum devices.

### 4.1.1 Leakage of optical beams during the storage time

The system as prepared by J.Cviklinski and J.Ortalo is optimized from the optical point of view, but it does not optimize the lifetime the atomic coherence. First of all, the control beam is shuttered by an $AOM$ used on the zero order to ensure that no additional noise is added by the $AOM$. The beam is turned off when deviated by the acousto-optic modulator, while it is present when the $AOM$ is off. This way however it cannot be extinguished completely and so a small amount of control light is always entering the atomic sample. By using a double pass configuration (cat's eye scheme) and a diaphragm on the way between the $AOM$ and the retroreflecting mirror, it is possible to get attenuations as small as $\sim 1/200$. So, considering a control power of the order of the saturation intensity $I_s$, during the storage time we have a leakage of the order of $I_s/200$.
Moreover, the generation of the signal pulse as an orthogonally polarized single sideband of a stronger carrier allows the achievement of a phase lock of signal and control beams in a simple and elegant way, but it involves a leakage of the carrier of the order of $\sim 10\ \mu W \sim I_s/3000$ with indeterminate polarization into the atoms.
With a simple model, described in the thesis of M.Scherman ([103]), we have evaluated the effects of these leakages on the memory efficiency. We found that with the above order of magnitude the atomic coherence is destroyed in a few tens of *microseconds* time[4].

[4]In the model we look at the evolution of a coherence with no direct relaxation terms ($\sigma_{21}$) subjected to an Hamiltonian concerning just a dipolar coupling ($\Omega$) between one of the states forming the coherence with a third one ($\rho_{33}$) open to incoherent scattering ($\Gamma$). Considering the system for slowly varying envelope within the RWA, we pose the initial value of $\sigma_{21} = \sigma_0 \neq 0$, while the Hamiltonian looks like $\hat{H}/\hbar = \Omega(|1\rangle\langle 3| + |3\rangle\langle 1|)$. The Heisenberg equations for the density matrix elements read

$$\begin{cases} \dot{\sigma}_{21} = i\Omega\sigma_{31} \\ \dot{\sigma}_{31} = i\Omega\sigma_{21} - \Gamma\sigma_{31} \end{cases} \tag{4.1}$$

By solving for $\sigma_{21}$ one find that in case $\Omega \ll \Gamma$, that is for incoming intensities $I$ much lower than saturation intensity $I_s$, the coherence evolves like a simple exponential decay

$$\sigma_{21} \sim \sigma_0\, e^{-\frac{t}{\tau}} \qquad \text{with } \tau = \frac{\Gamma}{2\Omega^2} = \frac{1}{\Gamma}\frac{I_s}{I} \sim 5 * 10^{-6}\,\mu s \tag{4.2}$$

The final numerical evaluation refers to our experimental case. A more accurate calculation will evaluate the Rabi frequencies for each leakage by considering the particular transition addressed by it. For detail [103]

To verify this estimations we have modified the set-up imposing to both control and signal-carrier beams a double passage into $AOM$s used on the first order of diffraction. This way an extinction up to $10^{-5}$ is ensured, while the possibility of varying the diffracted frequency independently for the two beams is added. Actually, as reported in [103] we have not registered an improvement either in the overall classical efficiency of the memory or in the Zeeman coherence lifetime. The fast decay we registered has thus a different origin, which is not explained up to now. However the modification of the set-up has proved very useful for $EIT$ characterization, as shown below.

## 4.2 Characterization of atomic samples

Having verified that there was no optical destruction of a previously created Raman coherence, we carried forward the search of explanation for the low level of coherence in our atomic sample.
Due to Doppler broadening, we were convinced that the choice of the one photon detuning could not be the solution, so we moved on the characterization of a number of different samples, in order to understand the relations among the different parameters we measured. A sample was defined by determining :
attainable optical depth $OD$ and orientation[5] $p$, orientation decay rate $T_1$, Raman coherence decay rate $T_2$, $EIT$ spectroscopy.
The samples included both paraffin coated and buffer gas filled cells (2 and 10 $torr$ of $Ne$). These are the two ways to circumvent the orientation destroying impacts against the walls: in the first case the detrimental effect of each impact is reduced; in the second one, the motion of atoms is converted from ballistic to Brownian-like, strongly reducing the rate of collision against the walls. The buffer gas filled cells were considered particularly promising due to the increase of the flying time of the atoms through the beams.
The result of this systematic characterization didn't provide a solution to our problem: for every sample indeed, the evaluated parameters could not explain the poor $EIT$ effect obtained. In particular, we were not able to see induced transparency at all with buffer gas filled cell, even if the $T_1$ and $T_2$ were still sufficiently long (e.g. respectively 10 $ms$ and 100 $\mu s$ for the 2 $torr$ cell). In the following I summarize the measurements' methods, showing some example of the obtained results, which lead us to understand the cause of the $EIT$ impairment with respect to the simple theoretical prediction (next section).

[5]the optical depth is defined as $OD = ln(1/\alpha)$, while the parameter describing the orientation of the sample as $p = \frac{\alpha_+ - \alpha_-}{\alpha_+ + \alpha_-}$; $\alpha_i$ staying for the transmission of the $\sigma_i$ polarization. The measurements are performed with light resonant with the atomic transition $|F = 3\rangle|F' = 2\rangle$, that is the transition exploited for the $\Lambda$ scheme

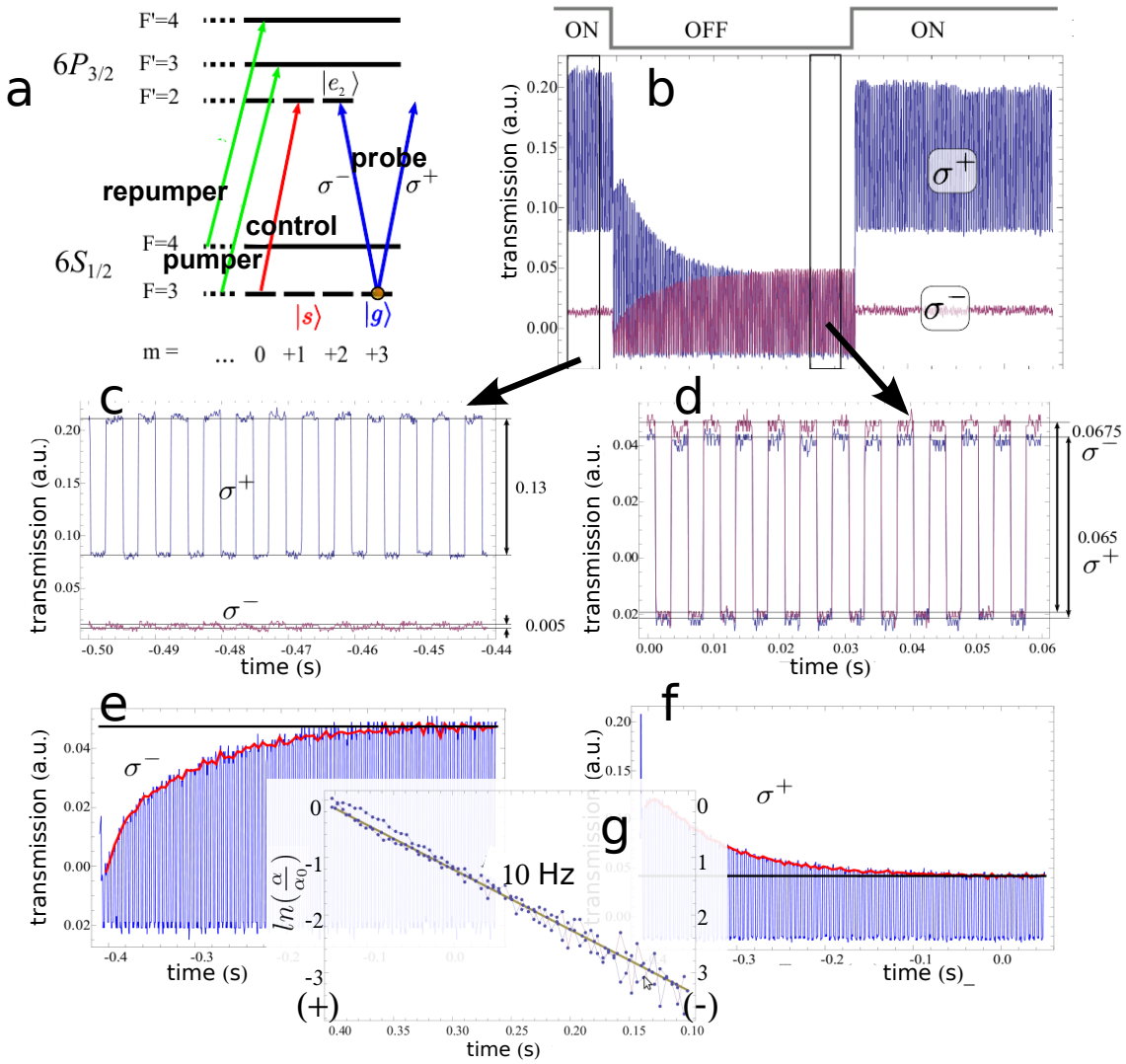


Figure 4.5: Measurement of the atomic orientation.

**a** - atomic transition involved in the experiment;

**b** - variation of the optical depth for the two opposite $\sigma$ polarizations of the probe due to the switching of the optical pumping responsible for the orientation of the sample;

**c** and **d** - stationary optical depth under optical pumping and without any pumping;

**e** and **f** - transient regime following the switching off of the optical pumping for , respectively, the $\sigma_-$ and the $\sigma_+$ polarizations of the probe;

**g** - Evaluation of the orientation decay rate $T_1$ (population life time).

### 4.2.1 Determination of $OD$, $p$, $T_1$

The optical depth $OD_-$, the orientation $p$ and the orientation decay rate $T_1$ were evaluated with a single experimental procedure[6], which is presented fig.4.5. The system was oriented by optical pumping as in the memory experiment (fig.4.5.a), and probed by a linearly polarized weak beam (about 100 $nW$ with a waist of a few $millimeters$) resonant with the transition $|2\rangle \rightarrow |3\rangle$ and propagating in the same direction as the signal field. This way one has simultaneous access to the optical depth seen by the two orthogonal polarizations $\sigma_+$ and $\sigma_-$, which are detectable separately by using a quarter wave-plate and a polarizing beam-splitter. If all the atoms are in the sublevels $|3,+2\rangle$ and $|3,+3\rangle$, the $\sigma_+$ component of the probe is not absorbed, while the $\sigma_-$ component can be absorbed. Since optical pumping can accumulate atoms in the states with maximum orientation, such a result for absorption means that almost all the atoms are in $|3,+3\rangle$.
The experimental sequence is made of a series of optical pumping and free evolution time intervals of 1 $s$, in a way that the orientation decay rate becomes directly detectable by monitoring the evolution of the optical depth for the two polarizations $\sigma_-$ and $\sigma_+$ when the pumping is off. The leakage of the pumping beams produces an offset in the detectors for the probe, due to the weakness of the probe. This problem was solved by modulating the probe with a square shape (we checked that $200Hz$ frequency was sufficient to have enough time resolution). In fig4.5.b one of these sequences is reported; it is the measurement realized on the paraffin coated cell which was used in the experiments reported in the next section. In the stationary regime with optical pumping, one finds $OD_- > 3$ and $p > 0.9$ (fig. 4.5.c); while during the off period (fig.4.5.d), the stationary regime corresponds to $p \sim 0$ (as expected[7]) and $OD \sim 0.75$. In fig4.5.e/f, the free evolution of the two transmissions $OD_i$ is reported: they show exponential relaxation toward the stationary value (fig.4.5.g), the time constant of this decay corresponding to the orientation decay rate $T_1$, here equal to 100 $ms$. Considering the mean velocity for cesium atoms at room temperature $\sim 10^2$ $m/s$ and the dimension of the cell in the transverse plane ($\sim 10^{-2}$ $m$), this result shows that the orientation is preserved for around $10^3$ impacts, which means

[6] due to the low optical depth of the sample, which allowed a direct measure of the transmission of resonant light

[7] the small amount of imbalance between the two components, giving $p = 0.025$, was due to an imperfect determination of the polarization of the probe light

that the paraffin coating is properly working.

### 4.2.2 Determination of $T_2$

To evaluate the Zeeman coherence decay rate $T_2$ for our samples we exploited a magneto-optical resonance technique as proposed and implemented in [63]. This method relies on the Faraday rotation effect produced on a slightly out of resonance ($\sim 1\ GHz$ in our case) linearly polarized beam by an oriented sample. Due to the different dispersion seen by the two $\sigma$ components of the beam, the linear polarization exiting the sample is rotated respect to the initial one by an angle proportional to the collective atomic orientation in the direction of propagation of the light. Evaluation of this rotation is accomplished by sending the beam into a polarizing beam-splitter set in a way to split the power in equal parts for the initial polarization, and looking at the difference between the output of the two photodiodes receiving the light. By measuring the Faraday effect induced by the sample on a beam propagating orthogonally to the direction of quantization, one can monitor the evolution of the coherences between the sub-levels of the atomic system. Due to non degeneracy of the sub-levels, the coherences have a phase rotating with an angular velocity equal to the frequency difference between neighboring states, that is the Larmor pulsation $\Omega_L$. This corresponds to the Larmor precession of the collective transverse orientation around the bias magnetic field defining the quantization axis, so that the Faraday effect shows harmonic oscillations at the same frequency $\Omega_L$ (following the projection of the collective orientation on the direction of propagation of the light). The amplitude of the rotation can be evaluated by demodulating the differential output with a double phase lock in amplifier.
Here transitions between the Zeeman sub-levels are excited by a $RF$ magnetic field of variable frequency: when the harmonic signal approaches the Larmor pulsation, the transfer is efficient and induces the formation of large coherences, hence a large rotation for the polarization of the light. By scanning the frequency of the $RF$ field, one detects resonances with a Lorentzian shape proportional to the inverse lifetime of the coherences. The width of these Faraday peaks corresponds to the coherence

decay rates, which are the quantities we are looking for[8]. Following [63] and [91], the expression for the output of the double phase lock in amplifier reads

$$signal \propto \left| \sum_{m=-F}^{F-1} (F(F+1) - (m(m+1)) \frac{\rho_{m+1,m+1} - \rho_{m,m}}{\Gamma_{m,m+1} + i((\omega_{m+1} - \omega_m) - \omega_{RF})} \right| \quad (4.3)$$

where $F$ stays for the hyperfine ground state ($F = 3$ in our case), while the $\Gamma_{m,m+1}$ is the decay rate for the specific coherence $|m_F\rangle \leftrightarrow |m_F + 1\rangle$, related to $T_2$ as $T_2^{m,m+1} = 1/\Gamma_{m,m+1}$. In our case both the quadratic Zeeman shift and the differences among $\Gamma_{m,m+1}$ are much smaller than their mean values (for any sample $> 1\ kHz$), and so 4.3 can be reduced to

$$signal \propto \left| \sum_{m=-F}^{F-1} (F(F+1) - (m(m+1)) \frac{\rho_{m+1,m+1} - \rho_{m,m}}{\Gamma + i(\Omega_L - \omega_{RF})} \right| \quad (4.4)$$

and $T_2 = 1/\Gamma = 1/\gamma_{sg}$.
The measurement was already implemented by J.Cviklinski during his PhD thesis ([20]), so we just had to use it for the new samples.
In our case the measurement gave an optimistic estimation of the parameter because from the side of the set-up we only have access to less than half of the volume of the cells, thus not accounting for all the inhomogeneities present in the samples. However, the concerned volume constituting a substantial part of the studied cell, the real value could not be order of magnitude different from what measured.

To simplify the characterization procedure of a sample, we elaborated a technique to estimate the decay rate $T_1$ using the set-up for the measurement of $T_2$. Looking at 4.4, one can see the signal is proportional to the population imbalance. Actually, in order to make measurements as described in fig.4.6.a, an optical pumping similar to the one for the memory experiment was applied. Similarly to measurements described in fig.4.5, we tried to detect the decay of the amplitude of the Faraday effect (at fixed $RF$ frequency) after switching the pumping light. A direct detection was not possible, because it needed an integration time in the lock-in amplifier for which the output signal was too noisy. The samples have always shown rather long coherence

[8] Actually we are interested in the decay rate for coherences between not adjacent states ($|\Delta m_F| = 2$), while this technique gives access to coherences related to $|\Delta m_F| = 1$. However it is assumed the two are very similar [63]

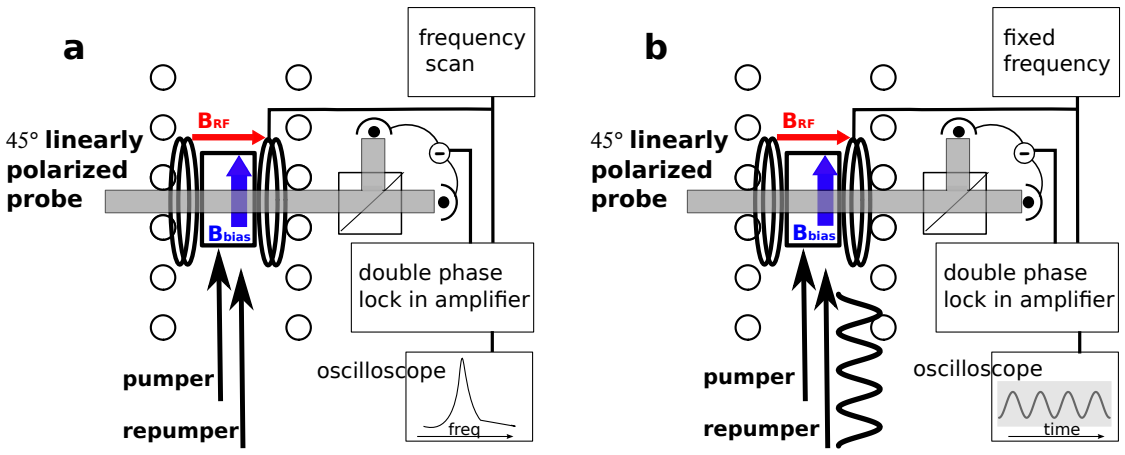


Figure 4.6: **a** - Experimental scheme for the determination of the Zeeman coherence decay rate $T_2$ by means of a magneto-optic resonance technique ([63]).
**b** - Variation of the experimental procedure in order to evaluate the orientation decay rate $T_1$ by means of the same set-up as for the determination of $T_2$. The $RF$ magnetic field for the magneto-optical resonance has a fixed frequency. The power of the optical pumping laser responsible for the orientation of the sample is modulated. $T_1$ is determined from the evaluation of the "transfer function" relating the modulation of the light to the amplitude modulation of the oscillations of the detected Faraday rotation.

duration, with values ranging from $\sim 400\,\mu s$ for paraffin coated to $\sim 150\,\mu s$ for the $2\,torr$ Ne filled cells; for the latter the data are shown in fig.4.7.a . However, by applying a harmonic amplitude modulation over a "bias" pumping for which the orientation was not saturated, and demodulating the output of the lock-in amplifier at the same frequency, it was possible to obtain the Faraday rotation contribution (provided integration was performed on a sufficiently long time). Considering that $T_1$ acts on the system limiting the velocity at which the population distribution can be modified, we estimated its value as the first cut-off frequency we got in the oscillation of the amplitude of the Faraday effect under the modulation of the intensity of the pumping lasers. The measure of $T_1$ obtained with this technique is reported in fig.4.6.b for the 2 $torr$ Ne filled cell. Abscissa represent the frequencies at which the intensity of the repumping light was modulated, while in the ordinate the amplitude of the oscillation of the Faraday effect amplitude is reported. We checked carefully the

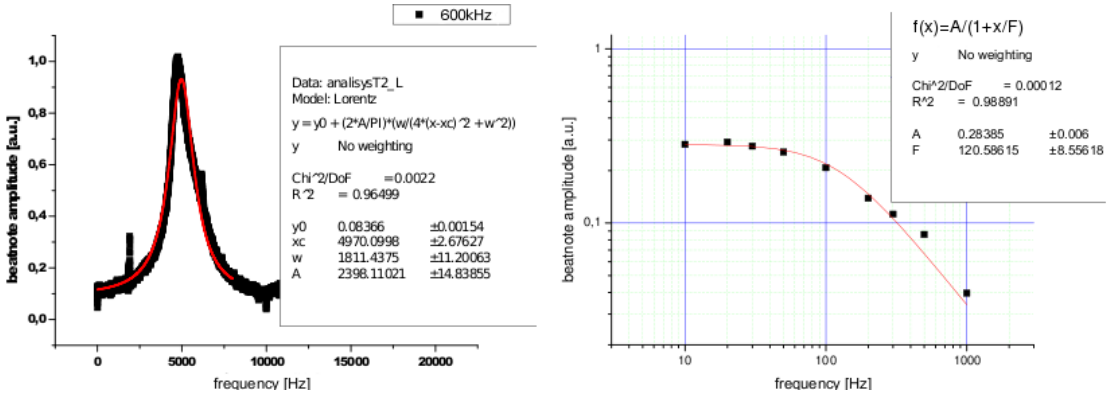


Figure 4.7: Results of the measurements of $T_2$ and $T_1$ for the sample with $2\,torr$ of $Ne$ buffer gas obtained with the two techniques illustrated in fig4.6.
**a** - magneto-optic resonance detection performed on a magnetic bias field giving a Zeeman shift $\sim 600\,Hz$. The FWHM of the resonance is $\sim 1800\,Hz$, which corresponds a $T_2 = 170\,\mu s$.
**b** - The amplitude modulation of the oscillating Faraday rotation shows a cut-off frequency at $\sim 100\,Hz$, which corresponds a $T_1 \sim 1.7\,ms$.

following invalidation issues: a too strong $RF$ coupling can shorten the orientation lifetime; and a too long integration time in the lock-in amplifier can create an artificial pole limiting the response of the atoms.

### 4.2.3 $EIT$ characterization

Since from our early measurements, $EIT$ on the $D2$ line showed an unexpected variety of forms and peak values, as can be seen in fig.4.8, with a constant feature: the weakness of the phenomenon. To understand the mechanism responsible for the weakness of the coherent collective effect, we made a detailed study of the transparency characteristics in a number of configurations.
For every set of parameters we scanned the probe over the whole Doppler distribution, maintaining however the finest frequency resolution as possible. This way we obtained informations on the whole velocity distribution and details relative to the shape of the transparency peak from the same curve. The measurement procedure required a frequency scan of the probe light on the scale of one $GHz$ without mode

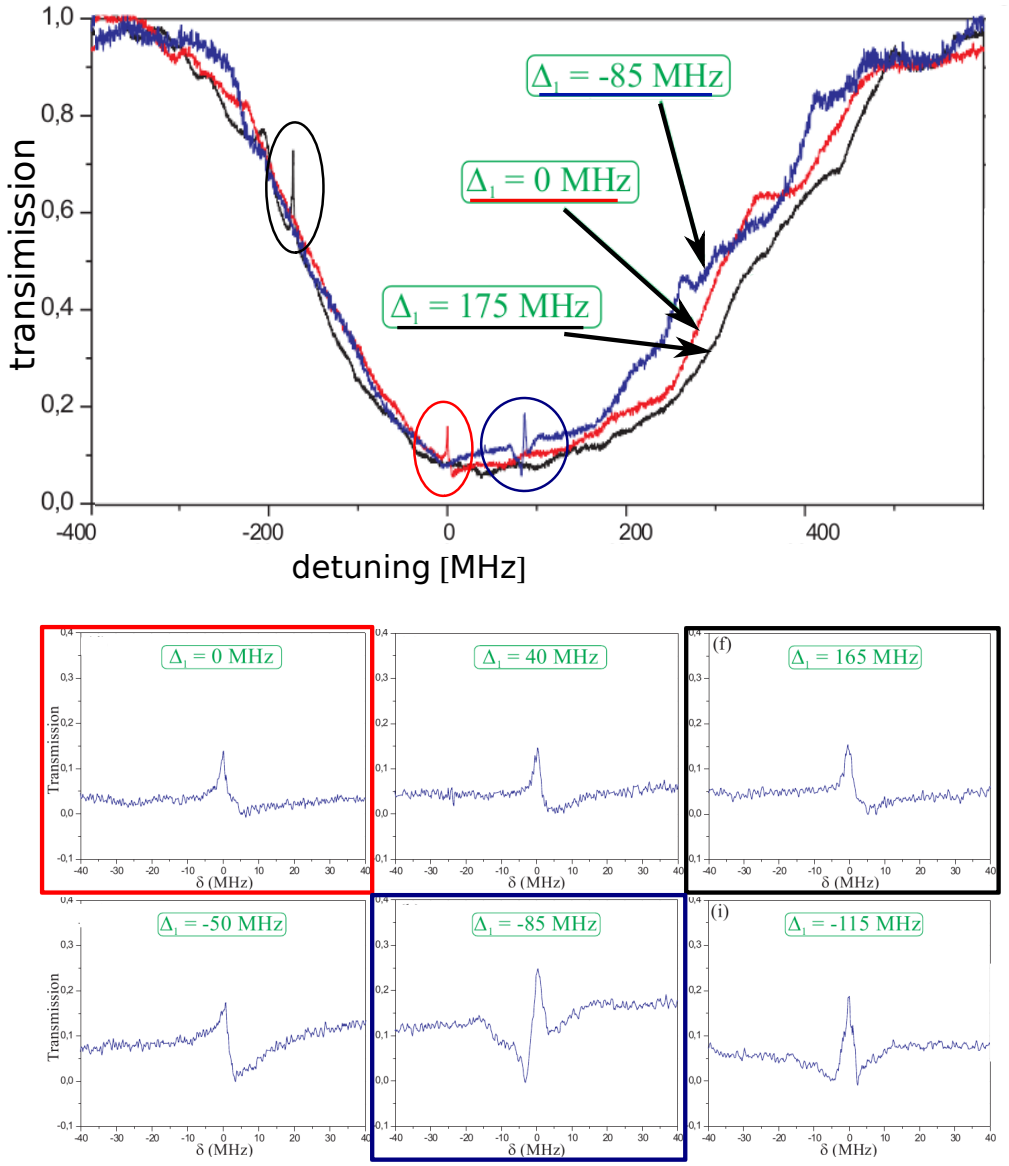


Figure 4.8: *EIT* spectroscopy in $^{133}Cs$ vapor. Absorption profiles obtained by scanning the probe frequency over the whole Doppler width is reported for three different one-photon detuning of the control field $\Delta_c = 2\pi \times (0\,/\,-85\,/\,+175)\,Hz$. Both the whole velocity distribution and the *EIT* peak show a dependence on $\Delta$ (see the text).

hopping. We had hence to provide light from an additional laser, the scan range been too wide to be obtained from an $AOM$. For this aim we exploited an external cavity grating stabilized diode laser, which was able to provide such a scan by acting with a linear voltage ramp on the piezoelectric positioner of the grating. Some examples of the obtained profiles are reported in fig.4.8, with a zoom of the same curves centered on the transparency peak shown in the lower part of the figure. This procedure allow to keep a direct connection between the transparency shapes and the velocity distribution responsible for such a collective response, which has been of some help for the understanding of the system. The set-up for these measurements corresponded to that of fig.4.15 (without the beams named depumper). In particular, the use of a Glan polarizer ensured extinction of the powerful control field up to $10^{-4}$, leaving the possibility of detect a probe field as weak as tens of $microwatt$[9]. Interpretation of the obtained curves was quite complicated because the optical pumping stage was very sensitive to even small changes of power of any involved beam, which caused large variations of the optical depth. A lot of measurements were performed to characterize the system. Fig.4.9 shows a set of such measurements. The upper panels show the height and the width of the induced transparency as a function of the control field power (for zero one photon detuning). The lower panels show the dependence of the transparency height on, respectively, the one photon detuning of the control field (keeping constant powers) [left], and the intensity of the repumper light (control beam held at resonance) [right]. Other parameters are reported in the caption of the figure.
From the data we can conclude that:

- the height and the width of the induced transparency increase with the power of the control beam (as expected from theory). Actually, for high power, we find a saturation of the window, which remains of unclear origin;

- the height of the transparency, in case of red detuned control field ($\Delta_c < 0$), increases with the detuning from the atomic resonance(s);

- the height of the transparency rapidly drop down for increasing repumper power.

[9] a careful optimization of the set-up allowed a better exploitation of the Glan polarizer, reaching extinctions of the order of $10^{-6}$, so that even weaker probe could be used (e.g. just $150\,nW$ in [104])

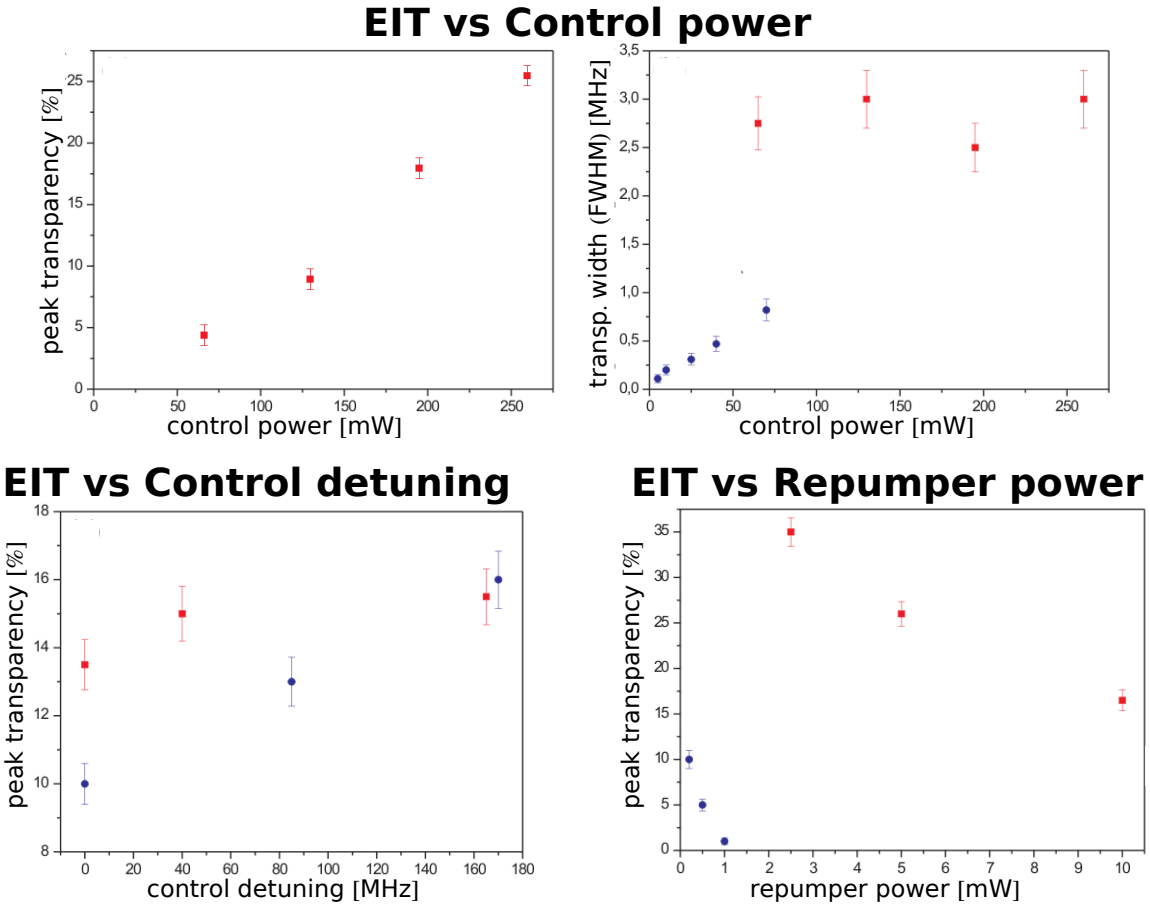


Figure 4.9: $EIT$ characterization for a paraffin coated $^{133}Cs$ cell:
TOP - height and width of the transparency as a function of the control power;
BOTTOM left - height of the transparency as a function of the one photon detuning;
BOTTOM right - height of the transparency as a function of the repumper power.
Beams' diameter is held to $1\,cm$ for all cases. Red points correspond to measures with the following parameters (when not scanned): signal, control, repumper and pumper power respectively equal to $10\,\mu W$, $195\,mW$ ($\Omega^c_{e_2s} = 6.1\,MHz$), $10\,mW$, $4\,mW$; one photon detuning $\Delta_c = 0$.
Blue points correspond to measurements obtained for the following parameters (when not scanned): signal, control, repumper and pumper power respectively equal to $300\,\mu W$, $10\,mW$ ($\Omega^c_{e_2s} = 1.4\,MHz$), $0.2\,mW$, $0.1\,mW$; $\Delta_c = 0$.

- the shape of the transparency window results strongly dependent on the one-photon detuning of the control field. At resonance, it gets an asymmetric profile: the blue side shows a steeper trend, which ends with a small absorption peak that exceeds the value in case of no $EIT$ effect. For blue detuning, this aspect is enhanced up to get a dispersion-like profile. For red detuning instead, the form of the window tends progressively to the expected shape. The three cases can be recognized in the curves of fig4.8.

- also the Doppler profile depends on the one-photon detuning of the control field. In particular, moving from red to blue detuning, we detect a reduction of the width of the profile on the high frequencies side ($\Delta_s > 0$), while the low frequency side ($\Delta_s < 0$) does not show appreciable modification. This can be seen in the curves of fig4.8.

The interpretation of this behavior is the subject of the next sections.

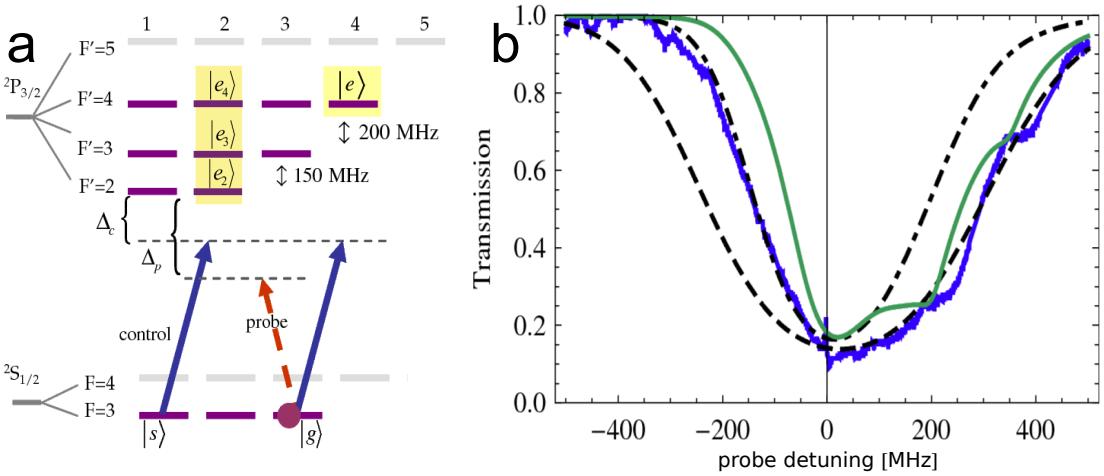


Figure 4.10: **a** - The six-level scheme considered in the general model [83] able to account for the *EIT* peak reduction in the $D2$ line of alkali atoms. Levels $e_{2,3,4}$ are addressed by the control field from the ground state $|s\rangle$, while the state $|e\rangle$ is addressed from $|g\rangle$, which hence, is no more a perfect dark state for the control field in Doppler broadened media. **b** - The absorption profiles describing the distribution of velocities in the medium do not fit any Gaussian distribution. In particular, while the blue detuned side matches the profile calculated for a sample at $T = 310\,K$ (as expected), the red detuned one follows the distribution obtained for a sample at $T = 100\,K$ (dashed lines). The green curve is the absorption profile corresponding to a velocity selective optical pumping shaped distribution.

## 4.3 *EIT* in multiple excited levels $\Lambda$ scheme

The systematic characterization of a number of samples lead us to look for an explanation of the low induced transparency in the properties of the atomic structure.

This has been possible by means of a model containing the contribution to the susceptibility of all the sub-levels of the $D2$ manifold. The theoretical work carried out by O.Mishina in collaboration with us during her post-doc in our group, allowed the elaboration of a model which is able to give a complete description of the experimental observations [83]. The main properties of this model are summarized in the next section. Fig.4.10.a highlights the levels of the atomic system which have to be

considered in the scheme.

### 4.3.1 Theoretical model

To show the main features due to the multiple excited level structure of the $D2$ line it is not necessary to consider the whole system presented in fig.4.10.a . It is enough to take into account a second excited level able to sustain a $\Lambda$ type interaction (we denote it $|e_3\rangle$). For the sake of clarity we will limit the treatment to this case.
For the analytical treatment, we proceed as in sec.2.5 with the simple model for three levels: the system of equations 2.6 is still valid[10], we need to add the terms accounting for the second excited state ($\sigma_{e_3e_3} = \rho_{e_3e_3},\ \sigma_{e_3i}$), which are easily derivable from those written for $|e_2\rangle$.
We still assume $\Omega^c \gg \Omega^s$, and zero value for the zero order solution for the optical coherences involving state $|g\rangle$ and for all populations, except for $\sigma^{(0)}_{gg} = 1$ (that is: $\sigma^{(0)}_{ii} = 0 \quad \forall\ i \neq g;\ \ \sigma^{(0)}_{se_k} = 0 \quad k = 2, 3$). At first order in the signal field $\Omega^s$, the equations for the non diagonal density matrix elements are

$$\begin{cases} \frac{\partial}{\partial t}\sigma^{(1)}_{e_kg} = -\left(\gamma_{e_kg} - i(\Delta_s - \omega_{e_2e_k})\right)\sigma^{(1)}_{e_kg} + i\Omega^s_{e_2g}\ \sigma^{(0)}_{gg} + i\Omega^c_{e_2s}\ \sigma^{(1)}_{sg} \qquad (k = 2, 3) \\ \frac{\partial}{\partial t}\sigma^{(1)}_{sg} = -(\gamma_{sg} - i\delta)\sigma^{(1)}_{sg} + i\Omega^c_{e_2s}\ \sigma^{(1)}_{e_2g} + i\Omega^c_{e_3s}\ \sigma^{(1)}_{e_3g} \end{cases} \tag{4.5}$$

The coherence between the two excited states is considered negligible because both states are almost not populated.
To calculate the linear susceptibility for the signal field $\Omega^s$, we determine expressions for the $\sigma_{e_ks}$ from the steady state solution of the system 4.5

$$\begin{cases} \sigma^{(1)}_{e_2g} = -\frac{\Omega^s_{e_2g}}{\Delta_{e_2g}}\left(1 + \frac{|\Omega^c_{e_2s}|^2}{\Delta_{sg}\Delta_{e_2g}}\right) - \frac{\Omega^c_{e_2s}\ \Omega^c_{e_3s}\ \Omega^s_{e_3g}}{\Delta_{sg}\ \Delta_{e_2g}\ \Delta_{e_3g}} \\ \sigma^{(1)}_{e_3g} = -\frac{\Omega^s_{e_3g}}{\Delta_{e_3g}}\left(1 + \frac{|\Omega^c_{e_3s}|^2}{\Delta_{sg}\Delta_{e_3g}}\right) - \frac{\Omega^c_{e_3s}\ \Omega^c_{e_2s}\ \Omega^s_{e_2g}}{\Delta_{sg}\ \Delta_{e_2g}\ \Delta_{e_2g}} \end{cases} \tag{4.6}$$

where we have used the notations

$$\begin{cases} \Delta_{e_kg} = i\gamma_{e_kg} + (\Delta_s - \omega_{e_2e_k}) \\ \Delta_{sg} = i\gamma_{sg} + \delta - \frac{|\Omega^c_{e_2s}|^2}{\Delta_{e_2g}} - \frac{|\Omega^c_{e_3s}|^2}{\Delta_{e_3g}} \end{cases} \tag{4.7}$$

[10] with the change of notation as reported in 3.7 and considering that the system of equation is already in the rotating frame and under RWA

With a multiple excited states atomic structure, the susceptibility is obtained by adding the contributions from all the optical coherences related to the transitions addressed by the field

$$\chi = \frac{n_0}{\epsilon_0} \sum_k \frac{\mu_{ge_k}}{E_s} \sigma_{e_k g} = \frac{n_0 \hbar}{\epsilon_0 \, |E_2|^2} \sum_k \Omega^s_{ge_k} \, \sigma_{e_k g} \tag{4.8}$$

so one gets the expression

$$\frac{\epsilon_0 |E_s|^2}{n_0 \hbar} \chi = - \underbrace{\frac{|\Omega^s_{e_2 g}|^2}{\Delta_{e_2 g}} \left( 1 + \frac{|\Omega^c_{e_2 s}|^2}{\Delta_{sg} \Delta_{e_2 g}} \right)}_{\chi^{three\ levels}_{e_2}} - \underbrace{\frac{|\Omega^s_{e_3 g}|^2}{\Delta_{e_3 g}} \left( 1 + \frac{|\Omega^c_{e_3 s}|^2}{\Delta_{sg} \Delta_{e_3 g}} \right)}_{\chi^{three\ levels}_{e_3}} - \frac{1}{\Delta_{sg}} \frac{\Omega^c_{e_2 s} \Omega^s_{g e_2}}{\Delta_{e_2 g}} \frac{\Omega^c_{e_3 s} \Omega^s_{g e_3}}{\Delta_{e_3 g}} \tag{4.9}$$

Here we recognize the contribution of each $\Lambda$ scheme considered individually, and there is a third term, which contains quantities related to the different $\Lambda$ structures, and represents the effects of the interference between the two possible paths (via $|e_2\rangle$ or $|e_3\rangle$). The third term is strongly dependent on detunings and polarizations of the addressing light: its sign (and thus its constructive or destructive contribution to the overall susceptibility) depends in fact on the signs of the involved Rabi frequencies (ultimately on Clebsh-Gordan coefficients) and of the detunings from the two resonances. The expression for the susceptibility can be rewritten to show the interference character of the response

$$\frac{\epsilon_0 |E_s|^2}{n_0 \hbar} \chi = - \sum_k \left( \frac{|\Omega^s_{e_k g}|^2}{\Delta_{e_2 g}} \right) - \frac{1}{\Delta_{sg}} \left( \sum_k \frac{\Omega^c_{e_k s} \Omega^s_{g e_k}}{\Delta_{e_k g}} \right)^2 \qquad k = 2, 3 \tag{4.10}$$

The first term account for the susceptibility encountered by the probe field in the absence of control light, while the second one account for the two-photon effects.

### Effects on the resonances

As expected, the expression for the susceptibility 4.10 shows three poles (which, for far from resonance control field correspond to the two one-photon atomic resonances and to the two-photon Raman resonance). One can see, however, that in general the presence of the second excited state modifies the response of the medium over a wide range of frequencies. The two-photon contributions have an overall factor $\frac{1}{\Delta_{sg}}$ in which, according to definition 4.7, variables of the Zeeman coherence ($\delta$ and $\gamma_{sg}$) add

to terms related to the control field ($\propto 1/\Delta_{e_k g}$). With respect to the result obtained in the case of a single excited state one has to consider the contribution related to the state $|e_3\rangle$: the real part of $1/\Delta_{e_k g}$

$$Re\left(\frac{1}{i\gamma_{e_k g} + (\Delta_s - \omega_{e_1 e_k})}\right) = (\Delta_s - \omega_{e_2 e_3})\frac{|\Omega^c_{e_2 s}|^2}{\gamma^2_{e_k g} + (\Delta_s - \omega_{e_2 e_3})^2} \tag{4.11}$$

modifies the two photon resonance condition (for large one photon detuning it becomes a standard AC Stark shift).
On the other hand the imaginary part contributes to the decay rate of the coherence

$$Im\left(\frac{1}{\Delta_{e_k g}}\right) = \gamma_{e_k g}\frac{|\Omega^2_{e_2 s}|^2}{\gamma^2_{e_k g} + (\Delta_s - \omega_{e_2 e_3})^2} \tag{4.12}$$

Its form, in the far from resonance limit, approaches the expression for the scattering rate of a non resonant light beam as calculated for far from resonance dipole potentials in section 2.4.2 (1.84). This term accounts thus for the contribution to the decay of the Raman coherence given by the non resonant scattering due to the presence of the second excited state.
An evaluation of the position of the $EIT$ transparency window becomes simple in the case the energy difference between the two excited states can be considered much larger than the decay rates and the control field Rabi frequency ($\omega_{e_2 e_3} \gg \gamma_{e_k g},\ \gamma_{sg},\ \Omega^c_{e_k s}$):

- **In vicinity of a one photon resonance -** (corresponding to $\omega_{e_2 e_3} \gg \Delta_s$) one can consider only the first term in eq.4.9. Further simplification comes by assuming $\gamma_{sg} \sim 0$: this way only the real part of $\chi$ remains non negligible at first order in $1/\omega_{e_2 e_3}$, and it can be approximated as

$$\chi \propto \delta + \frac{|\Omega^2_{e_2 s}|^2}{\Delta_s - \omega_{e_2 e_3}} + i\ o((1/\omega_{e_2 e_3})^2) \tag{4.13}$$

  For a control field perfectly on resonance $\Delta_c = 0$ ($\rightarrow \delta = \Delta_s$), we find thus the dispersion ($\chi'$) crosses the zero value for a two-photon detuning $\delta^{4\,levels}_{EIT}$ equal to

$$\delta^{4\,levels}_{EIT} \sim -\frac{|\Omega^c_{e_3 s}|^2}{\omega_{e_2 e_3}} \tag{4.14}$$

  Using detuning definitions 2.2 and 3.7, we find that the second excited level shifts the transparency window away from itself; the same result is obtained in

proximity of $|e_3\rangle$, in which case it is the level $|e_2\rangle$ pushes the transparency away.

- **Far from resonance -** if the one photon detunings are much larger than the decay rates ($|\Delta_s| \gg \gamma_{e_2g}$, $|\Delta_s - \omega_{e_2e_3}| \gg \gamma_{e_3g}$), we can consider the terms $\Delta_{e_kg}$ far from resonance, so that the Raman absorption peak can be determined by looking at the real part of $\Delta_{sg}$ only

$$Re(\Delta_{sg}) = \delta - \frac{\Delta_s|\Omega^c_{e_2s}|^2}{\gamma^2_{e_2g} + \Delta^2_s} - \frac{(\Delta_s - \omega_{e_2e_3})|\Omega^c_{e_3s}|^2}{\gamma^2_{e_3g} + (\Delta_s - \omega_{e_2e_3})^2} = 0 \tag{4.15}$$

  Assuming $\delta \ll \Delta_i \rightarrow (\Delta_s \sim \Delta_c)$, which is immediately verified in this configuration, one finds that equation 4.15 is verified for a two-photon detuning $\delta^{4\,levels}_{Raman}$ equal to

$$\delta^{4\,levels}_{Raman} = \frac{|\Omega^c_{e_2s}|^2}{\Delta_c} + \frac{|\Omega^c_{e_3s}|^2}{\Delta_c - \omega_{e_2e_3}} \tag{4.16}$$

  Hence the Raman absorption peak is shifted from the bare two photon resonance by the AC Stark effects related to the two excited states. The shift $\delta^{4\,levels}_{Raman}$ gets the same sign if the control field is red or blue detuned respect to both transitions ($\Delta_c < 0$ or $\Delta_c > \omega_{e_2e_3}$), while the two components have opposite signs if it is between the two resonances. Actually, in this frequency range, $\delta^{4\,levels}_{Raman}$ moves continuously from one side to the other of the two photon resonance, the crossing point being determined by the relative strength of the dipole matrix elements on which the two transitions rest.

This feature is clearly shown in fig.4.11. Here the transparency effect induced by a control field is reported for increasing one-photon $\Delta_c$ blue detunings. The probe frequency scan is centered on the two photon resonance: it is evident that the point of maximal transparency for $\Delta_c = 0$ corresponds to absorption peaks for some one-photon detunings $\Delta_c \neq 0$. This is not the case for red detunings, where the absence of other excited states leaves the susceptibility similar to the case of the simple three levels scheme (fig2.5).
It is clear that this feature can explain the weakness of the $EIT$ encountered in our experimental work with Doppler broadened samples.
The simplified 4-level model given here enables to identify the velocity classes most responsible of the detrimental contributions. It is sufficient to determine the one

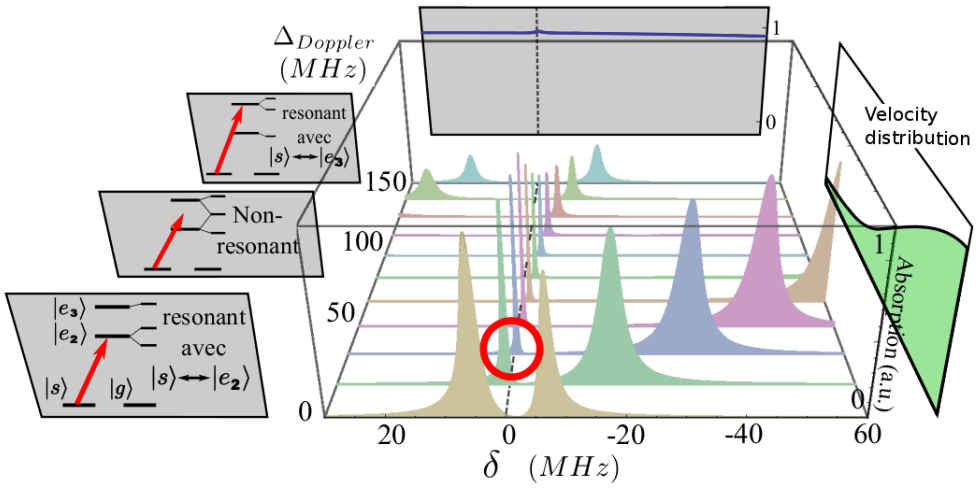


Figure 4.11: EIT features in a multi-level system (two excited states). As in fig2.5, probe absorptions are displayed for atoms with different velocities as a function of the two-photon detuning $\delta$ given by the Doppler detunings. In this case the Raman peak is moved by the AC Stark shift induced by the second excited level until crossing the center of the transparency for the zero velocity class, leading to a vanishing overall transparency. The dotted line indicates the center of the EIT window for atoms of the zero velocity class. The integrated absorption is obtained for a Gaussian velocity distribution of 160 $MHz$ half-width (thermal distribution for Cesium at 300 $K$). The control Rabi frequency is $\Omega^c_{e_2 s} = 2.3\gamma_{e_2 g}$ , where $\gamma_{e_2 g}$ is the natural linewidth. Image taken from [104].

photon detuning $\Delta_c = \Delta_c^{detr}$ for which the Raman absorption peak (4.16) falls at the center of the $EIT$ window obtained for resonant control field (4.14): the detrimental velocity classes have a Doppler effect $\bar{\Delta}_D = \Delta_c^{detr}$. So, setting $\delta_{Raman}^{4\,levels} = \delta_{EIT}^{4\,levels}$ , one gets

$$\frac{|\Omega^c_{e_2 s}|^2}{\Delta_c} + \frac{|\Omega^c_{e_3 s}|^2}{\Delta_c - \omega_{e_2 e_3}} = -\frac{|\Omega^c_{e_3 s}|^2}{\omega_{e_2 e_3}} \tag{4.17}$$

This equation is of the second order in $\Delta_c$, and has two solutions that do not depend on the control field intensity:

$$\Delta_c^{detr} = \frac{\omega_{e_2 e_3}}{2} \frac{|\Omega^c_{e_2 s}|^2}{|\Omega^c_{e_3 s}|^2} \left( -1 \pm \sqrt{1 + 4 \frac{|\Omega^c_{e_3 s}|^2}{|\Omega^c_{e_2 s}|^2}} \right) \tag{4.18}$$

One obtains two solutions, $\Delta_{c+}^{detr} > 0$ (blue detuned) and $\Delta_{c-}^{detr} < 0$ (red detuned), with values determined by the relative strength of the involved dipole elements. Reminding that for $\Delta_c = 0$ the transparency window position is $\delta_{EIT}^{4\,levels} < 0$, one sees the solutions correspond to the two cases:
($\Delta_{c-}^{detr}$) the two AC Stark effects add to get the value of $\delta_{EIT}^{4\,levels}$;
($\Delta_{c+}^{detr}$) the AC Stark effect of the upper level is strong enough to push down the Raman absorption peak towards the transparency window for zero velocity atoms.

A general model able to describe all aspects of the linear susceptibility in a multiple excited states atomic structure, as that of the $^{133}Cs$ $D2$ line, is presented in the publication [83] of our group. It is based on a Hamiltonian including all the 6 levels shown in fig4.10.a . In the paper, the expression for the susceptibility seen by the signal field has a form similar to eq.4.10 (with index $k$ going up to 4 to include the level $|e_4\rangle = |4', +2\rangle$), with the addition of terms accounting for interaction between states $|g\rangle$ and $|e\rangle = |4', +4\rangle$ due to the control field. I will not report this study, because it involves more complicated calculations without adding new qualitative elements to the physical phenomena respect to what is possible to show with 2 excited states. Moreover, for our experimental case ($^{133}Cs$ $D2$ line at room temperature), the addition of levels $e_4\rangle$ and $|e\rangle$ does not modify significantly the susceptibility seen by the signal[11].

Simulations as shown in fig.4.11, which are obtained by evaluating the imaginary part of the susceptibility 4.10, can be performed with a set of parameters matching those of our experimental configuration[12], in a way to give informations immediately applicable in the experiment.

### 4.3.2 Experimental verification of the model

To evaluate the response of a warm atomic medium we need to calculate the function $\chi(\Delta_c+\Delta_D,\, \delta)$ with the Gaussian velocity distribution $f(\Delta_D)$ corresponding to cesium atoms at $T = 300K$ (2.31). In fig4.12 the results in terms of transmission $t$ (2.13)

[11] it should not be the case with other elements, as $K$, $Na$, $^{85}Rb$

[12] identifying the ground states with $|g\rangle \equiv |3, +3\rangle$, $|s\rangle \equiv |3, +1\rangle$; and the excited states ($D2$ line: $^2P_{3/2}$) with $|e_2\rangle \equiv |2', +2\rangle$, $|e_3\rangle \equiv |3', +2\rangle$. All the parameters can be taken or calculated from data reported in [111]

are reported for different temperatures $T = (1\,/\,4\,/\,100)\,K$ (up-down) and control field powers $\Omega^c_{e_2 s} = (0.1\,/\,10) \times \gamma_{e_2 g}$ (left-right). For comparison, the same simulation for the case of a three-level system is also reported (red dashed lines). Surprisingly the model is more pessimistic than the experiment, in fact it predicts complete destruction of the transparency window even for low temperatures ($T \sim 100\ K$) and high control Rabi frequency, while experimental results for $T = 300\,K$ (as the ones reported in fig.4.8) still show some induced transparency. Therefore, we can say our model allows the understanding of the weakness of the $EIT$ effect; we now discuss the fact that there is still some transparency.

Since early studies, we had observed no perfect Gaussian velocity distributions, suggesting some reshaping mechanism changing the populations of the velocity classes. Finally we understood it was this asymmetric Doppler distribution, due to an effective velocity selective optical pumping, which depopulated the detrimental velocity classes, allowing us to get some $EIT$ effect[13].

The induced deformation was clearly detected in the long range $EIT$ spectroscopy, as it can be seen in the figures reported in fig4.10.b and fig4.8. In particular, from fig4.8 one can note that the Doppler shape shows dependency on the control field detuning[14], with velocity classes moving in the same direction as the light progressively depopulated for positive $\Delta_c$; in fig4.10.b, we see that it is impossible to fit the measured absorption profiles with a symmetric Gaussian distribution, even for temperature different from $T = 300\ K$: while the blue detuned side is substantially in agreement with the curve for $T = 310\ K$ ($\Gamma_D \sim 160\ MHz$), to approach the red detuned side one have to reduce drastically the temperature down to $T = 115\ K$ (correspondent to $\Gamma_D \sim 100\ MHz$). These features can be understood with the help of fig.4.13.a. As mentioned at the beginning of this section, the mainly populated ground state $|g\rangle = |F = 3, m_F = +3\rangle$ is a dark state for the control field, if considering just the transition ($F = 3 \rightarrow F' = 2$). However, atoms can be non resonantly

[13]This is possible, in spite of the collisions with the walls. Actually, taking into account the power of the control beam (of the order of the saturation intensity), an optical pumping transient (even $\sim 100\ MHz$ out of resonance) takes a time at least one order of magnitude shorter than the beam crossing time and the time between two successive impact with the walls ($\sim 100\ \mu s$). So, due to the continuous regime used in the $EIT$ spectroscopy, even if the shocks destroy any reshaped distribution, the system is maintained of equilibrium, showing asymmetric Doppler profile. Actually similar features had already been recognized in 2005 on D2 line based $EIT$ on rubidium [16]

[14]and it shows even stronger dependence on intensity (not reported here)

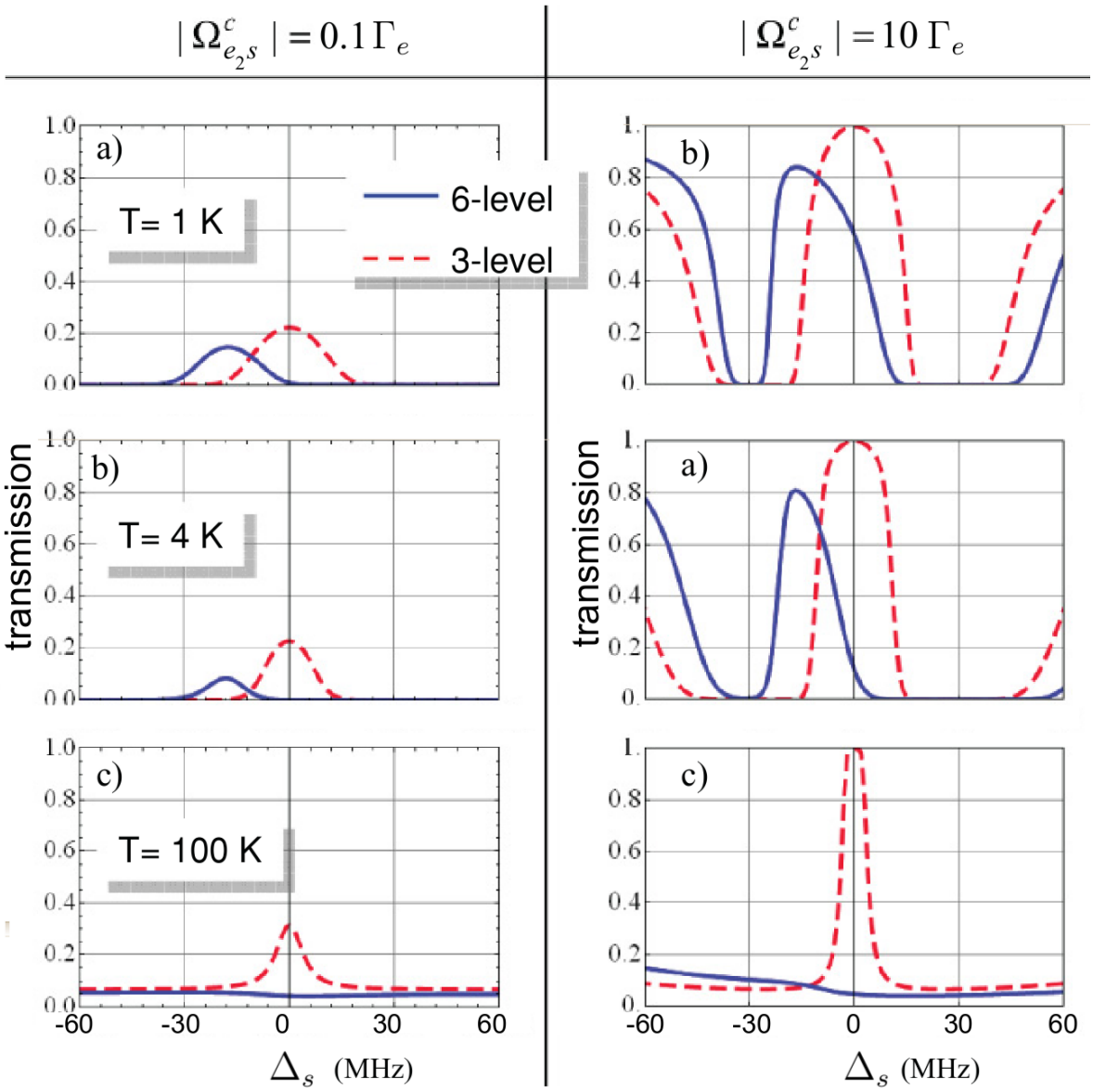


Figure 4.12: (Color online) Signal field transmittance $t$ for a Doppler-broadened $D2$ line for $^{133}Cs$ vapor for control Rabi frequency $\Omega^c_{e_2 g} = 0.1\gamma_{e_2 g} = 2\pi \times 0.52\,MHz$ (left) and $\Omega^c_{e_2 g} = 10\gamma_{e_2 g} = 2\pi \times 52\,MHz$ (right). In both cases, large inhomogeneous broadening leads to the total disappearance of the transparency peak. Note that the reduced transmittance in the three-level model for small Rabi frequency is due to a reduced ratio between this frequency and the decoherence rate, taken equal to $\gamma_{sg} = 0.0001\gamma_{e_2 g}$ in all the simulations. [83].

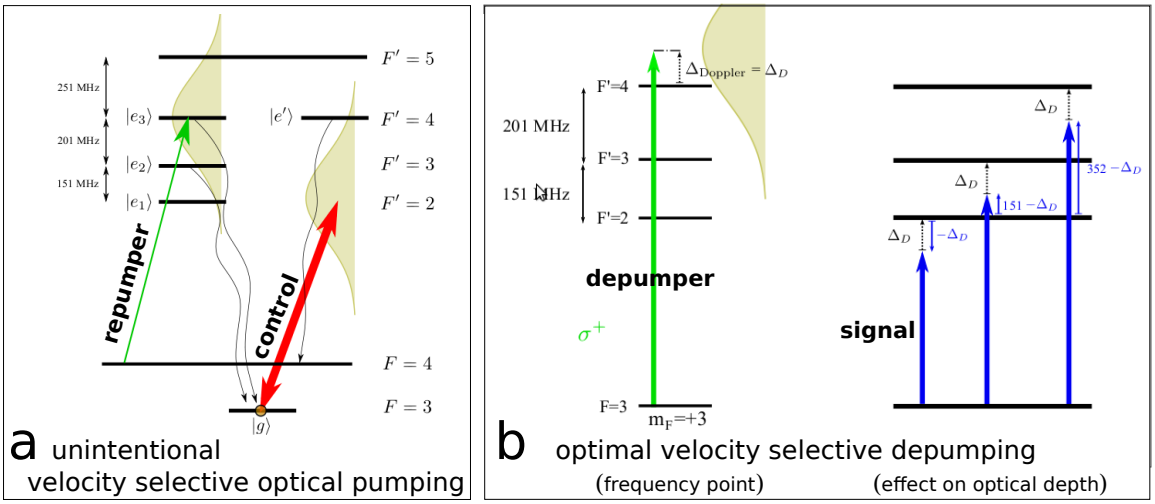


Figure 4.13: **a** - Velocity selective optical pumping induced by the fields configuration set to orient the sample on the extreme state $|F = 3, m_F = +3\rangle$. The profiles plotted in the background of the figure describe a Gaussian velocity distribution of width $\Gamma_D = 2\pi \times 160\, MHz[rad]$, which corresponds to the Doppler broadening for a thermal distribution at $T = 310\, K$. The profiles give an indication of all the frequencies that are seen by the different velocity classes present in the medium. The zig-zag arrows represent the incoherent scattering which participates to the optical pumping. **b** - Overview of the intentional depumping procedure. Left: most efficiently depumped velocity class $\Delta_{Doppler}$ for a depumper beam detuned of $\Delta_D$ from resonance ($\Delta_{Doppler} = \Delta_D$); right: visualization of the holes in the absorption profile seen by the probe beam in the case of an efficient velocity selective depumping stage. Three holes appear, centered at one-photon detunings: $\Delta_s = 2\pi \times (-\Delta_D, 151 - \Delta_D, 352 - \Delta_D) MHz[rad]$.

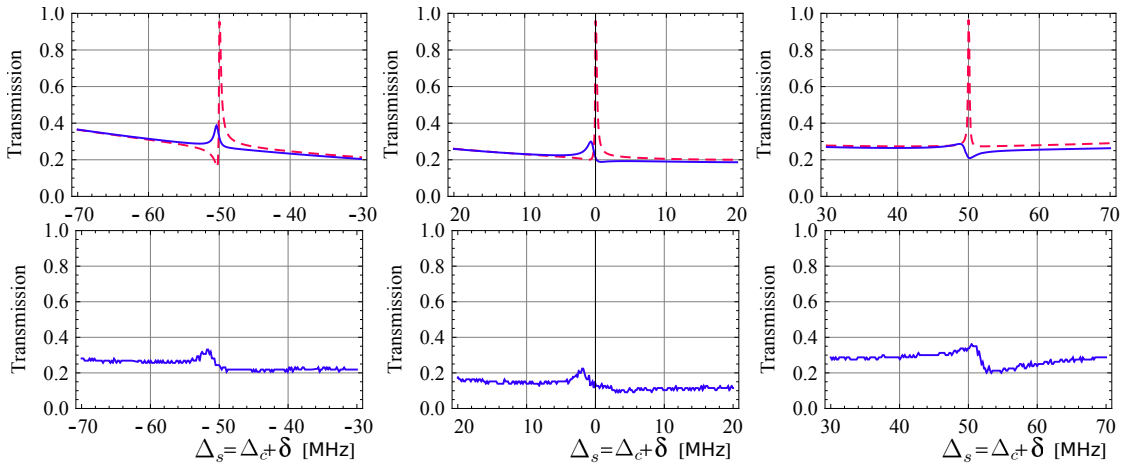


Figure 4.14: Comparison between model predictions and experimental measurements: the model [83] is able to describe also the details of the shape of the $EIT$ peak. Here the simulation is compared to the experimentally detected profile for three value of the control field one-photon detuning $\Delta_c = 2\pi \times (-50, 0, 50) MHz$.

excited to level $|e\rangle = |F' = 4, m_F = +4\rangle$, from which decay to both hyperfine ground states ($F = 3$, $F = 4$) is allowed. To maintain a population in $F = 3$ one have to add a repumping field exciting atoms from $F = 4$ to a level which can decay on $F = 3$. The important point is that this "exchange" of atoms between $F = 3$ and $F = 4$ by means of the light beams is not accomplished on the same velocity classes: while the repumper efficiently sends back to $F = 3$ the atoms with low velocities in the direction of the light ($\Delta_D \sim 0$), the control preferentially throws out $F = 3$ the atoms with large blue detuning (atoms running against the light with high velocity, $\Delta_D \gg 0$). This results in a reduction of the population of the blue detuned velocity classes, among which are the detrimental ones for $EIT$. This description is also in agreement with the experimental evidence of a decrease in the transparency for high power repumper beam (fig4.9). The repumper enhances the velocities classes close to zero that it can efficiently send back to $F = 3$, hence counteracting the optical pumping done by the control field.

Our efforts to model the velocity selective optical pumping did not give fully satisfactory results, as can be seen fig4.10.b . However, by imposing in the model the

Doppler distributions detected experimentally, the simulations for the resulting susceptibility $\tilde{\chi}(\Delta_c, \delta)$ show an excellent agreement with the detected $EIT$ peaks, for a wide range of settings. Some examples are reported in fig4.14.

Once understood why the experimental results could be better than the theoretical estimation, we tried to improve the $EIT$ effect (and thus the memory performances) by enhancing the depopulation of the detrimental velocity classes. With an ad hoc one-photon detuned "depumper" beam (with $\Delta_{dep} = -\bar{\Delta}_D$ respect to transition $|3, +3\rangle \rightarrow |4', +4\rangle$), it is possible to redirect atoms from the detrimental velocity classes into states $F = 4$ with maximal efficiency. The principle of this depumping is illustrated in fig.4.13.b, with the optimal depumper blue detuned (instead of red detuned) because depumping light travels oppositely to the other beams (see text below and fig4.15).

The experimental verification of this proposal has been achieved after my departure, so I just show the technical solutions (fig4.15) I contributed to implement during the phase of construction, and the main results obtained by my colleague M. Scherman (fig4.16), which was published in ref.[104]. Both figures are taken from this publication. Details on the subject can be found in [83] and in the thesis of M. Scherman [103]. It was not obvious to add one or two depumping beams of similar frequency and same polarization as the control field. Indeed one can not exploit birefringent elements as $PBS$ and the use of a partial reflecting mirror is required. This means a net loss of the available light power. The set-up already had of a succession of two partial reflecting mirrors to get alignment of control, pumping and repumping light (fig.4.1), which actually prevented us from exploring the whole range of optical power suitable for the systematic characterization of the $EIT$ (fig.4.9) effect. The addition of other elements of the same kind on the way of control field was thus impossible. However, perfect alignment is not a stringent requirement for optical pumping, even with room temperature samples: the incoherent single photon interaction does not depend much on Doppler detuning, so it is sufficient to achieve overlap with the other beams in the cell. By exploiting the large optical aperture available entering the rear face of the $\mu$-metal shield, we could illuminate the cell with others beams from the opposite direction without adding new mixing elements.With parameters corresponding to our experimental configuration, expression 4.17 gives

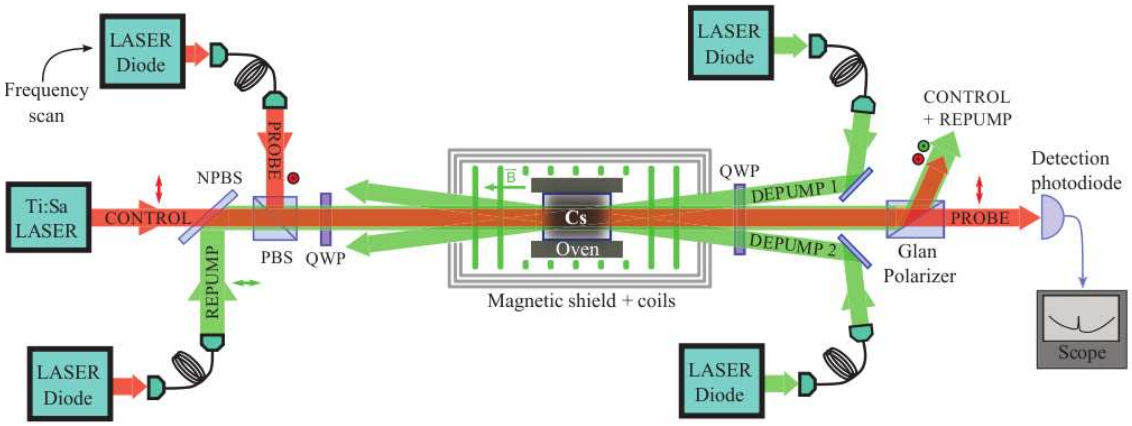


Figure 4.15: Set-up for the characterization of the $EIT$ effect. The transmittance of a cesium vapor is probed by scanning the frequency of a weak $\sigma$-polarized probe field. The strong $\sigma_+$-polarized control field is kept on resonance with the $|s\rangle \rightarrow |e_2\rangle$ transition. A repumper beam enables to efficiently prepare the atoms in the $|g\rangle$ ground state. In the configuration designed for the recovery of the transparency, two $\sigma_+$-polarized depumpers beams are added. They can be used to burn holes in the velocity distribution in order to exclude atoms with specific Doppler shifts from the interaction process. $PBS$ and $NPBS$ : polarizing and non-polarizing beam splitter, $QWP$ : /4 plate. [104].

$\Delta_D = 48\ MHz$ for the velocity class introducing the largest absorptive contribution within the $EIT$ window[15] (circled in fig4.11). The green curve in fig4.16.a shows the best $EIT$ enhancement obtained with a single depumper beam: the agreement with the theoretical estimation is very good, the maximal transparency corresponding to a detuning of $\sim -45\ MHz$. Adding a second depumper beam (red curve in fig4.16), we could even verify the minor effects induced by depopulation of other velocity classes. In both cases the frequency of the depumper(s) was empirically scanned over the Doppler distribution looking for maxima of the induced effect.

[15]with a full model calculation [83], taking into account the whole hyperfine structure of cesium and the variation of the height of the Raman absorption resonance with Doppler detuning, we found that in our case the atomic velocity classes to be removed for optimal $EIT$ recovery correspond to Doppler detunings $\bar{\Delta}_D = 35 - 45\ MHz$, thus consistent with the simplified calculation

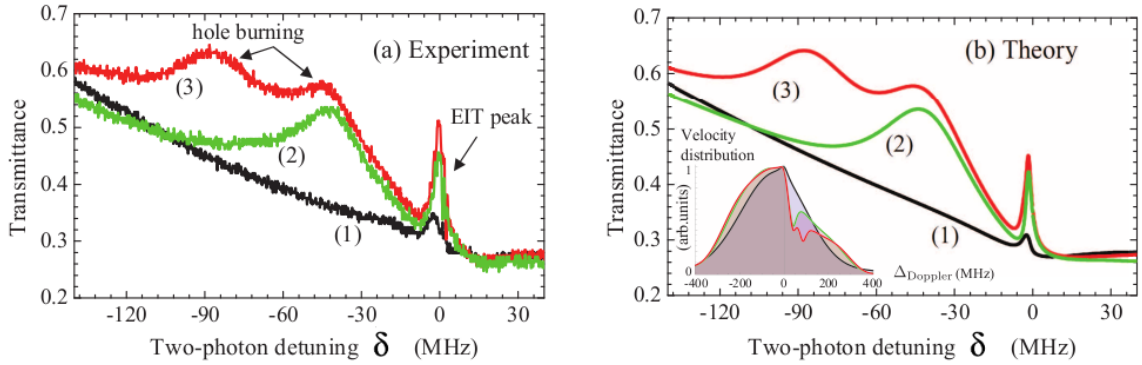


Figure 4.16: Transparency enhancement by reshaping of the velocity distribution.
**a** - Transmission of the probe field as a function of the two-photon detuning $\delta = \Delta_s$ (control field held at resonance $\Delta_c = 0$). Curve (1): without depumping beams; Curve (2): one depumping beam with $\Delta_D = 40\,MHz$; Curve (3): two depumping beams with $\Delta_D = 40\,MHz$ and $85\,MHz$. The transmission is normalized to the transmission for large detunings. Beams powers are $6\,mW$ for the depumpers; $(4.5\,/\,5.5,\,/\,7.5)\,mW$ for the repumper without depump/with one depumps/with two depumps.
**b** - Theoretical predictions calculated from [83] for $\Omega^c_{e_2s} = 2.3\gamma_{e_2g}$, corresponding to the experimental value ($\gamma_{e_2g} = 2\pi \times 5.2\,MHz$). We include the ground state decoherence due to the dephasing between control and probe lasers experimentally estimated to be $\gamma_{sg} = 0.077\gamma_{e_2g}$. This value corresponds to twice the linewidth of these independent lasers. The inset gives the velocity distribution extracted from the data and used for the model. [104].

In fig4.16.b we show the *EIT* effect calculated with the velocity distribution detected experimentally. The transparency is enhanced by a factor 2.7 in the case of a single depumping beam, and 3.4 for two beams. Due to the fact that the hole(s) in the velocity distribution is produced by the light on a *microseconds* time scale while it is destroyed by collisions in hundreds of *microseconds*[16] , it is reasonable to try an optimization of the memory performance by modifying the preparation stage with

[16]rough estimations obtained by considering:
resonant light of intensity closed to the saturation value, for the first time scale;
time between successive impacts against the walls for cesium atoms at room temperature in centimetric cell, for the second one.

this method (the reshaped Doppler broadening should be in fact almost stable within the storage time scale ($\sim 10\,\mu s$)). The simulation of fig4.16 has been thus used to predict the delay and storage efficiency attainable with this medium. Due to the good agreement of the simulation with the experiment for the imaginary part of the susceptibility, we assumed it was valid for the real part too, and we used it to calculate the propagation of a pulse through such a medium.The enhancement of $EIT$ results in an increase of the time delay by a factor of 13 (which together with the transmission determines the memory efficiency). The experimental verification of this improvement has not been realized until now.
Even if the expected memory efficiency is still too low for applications ($\sim 2\%$ in terms of photons), the technique shows the ability to enhance the characteristics of the medium under examination by a factor of 10.

# Chapter 5

# $EIT$ on D2 line of magnetically trapped ultra-cold $^{87}Rb$ clouds

In this chapter I present our investigation of $EIT$, carried on in cold atomic samples, with the set-up in Firenze. For the sake of continuity in the exposition I will first show the experimental results, referring to the next chapter for set-up description and characterization.

Cold samples are an ideal medium for studying $EIT$ effects. Indeed, the reduced (almost negligible) Doppler effect allows the exploitation of the intrinsic sharpness of atomic dipole transitions: all the atoms see light at the same frequency and it not necessary to average on a velocity distribution. Even simulations and rough estimations are simpler to perform, since the overall susceptibility of the medium matches the expression 4.10 for given values of $(\Delta_c, \delta)$. Moreover, the low mean velocity of the ensemble involves low rates of spatial mixing, and it allows trapping in non dissipative way (without laser cooling, but exploiting only magnetic or dipole potentials). Both aspects enhance the coherence of the system, the first one allowing the conservation of the imprinted spin wave for longer times[1], the second one preventing decoherence and deorientation induced by collisions against the walls. Magnetic trapping, due to its internal state selectivity, provides also a sort of continuous cleanup of the sample, pushing away atoms in wrong internal states. Moreover, in this environment the

[1] complete mixing of the sample is however unavoidable on time scale longer than milliseconds without lattice-like sub-confinement

probability of recovering in the interaction region an atom lost in a previous moment, which is one of the factors carrying decoherence in warm atoms experiments, is almost null.

To implement experiments based on coherence properties with magnetically trapped samples can appear somehow meaningless, since the magnetic inhomogeneity often results to be the leading term in coherence decay rate. Even with ultra-cold samples at *microkelvin* temperature, the variations of the magnetic field responsible for the localization of the cloud are on the scale of hundreds of *kilohertz* (corresponding to few *milligauss*)[2], leading to coherence times of the order of the *microsecond*. However, among the trappable internal states, one can find couples of "clock states" ([106, 84]), i.e., couples which can play the role of ground states for a Raman transition and which show equal first order Zeeman shift. Exploiting these states, coherence can gain three orders of magnitude in life time, reaching the already interesting *millisecond* scale. For atoms with maximal total angular momentum $F$ equal to 2 (including $^{87}Rb$), the magnetically trappable clock states ($|F = 1, m_F = -1\rangle$; $|F = 2, m_F = +1\rangle$) are particularly useful, because the first of them is a maximal orientation sub-level, and so population can be efficiently squeezed in it by an optical pumping procedure (following the terminology of the theoretical sections, we may say that it can almost perfectly play the role of state $|g\rangle$). Moreover, between the two limits behavior for low and high field values (Zeeman an Paschen-Back limits), the differential shift between the two states shows a minimum, that is a stationary point. Therefore, by setting the magnetic field bias at this value, coherence time can be further enhanced. In the case of $^{87}Rb$, this "magic" point is placed at $|\bar{B}| \simeq 3.2\ G$, which is a value easy to reach and maintain with low magnetic noise. Actually, carefully prepared samples of magnetically trapped rubidium atoms have proven to be suitable for Ramsey spectroscopy attaining sensitivity at the *hertz* scale ([47]). Moreover, coherence time up to more than one *second* has been directly measured in an atom chip set-up ([115]). The three level $\Lambda$ scheme constituted by states $[|F = 1, m_F = -1\rangle \equiv |g\rangle$; $|F' = i, m_F = 0\rangle \equiv |e_2\rangle$; $|F = 2, m_F = +1\rangle \equiv |s\rangle]$ (with $i = 1, 2$) is thus suitable for memory experiments, as proven by Hau's group ([72]). In this case the Raman transition requires opposite $\sigma$ polarized light beams, which can be provided by circularly polarized beams propagating almost along the direction of magnetization of

[2]the mean potential seen by the atoms is equal to $\langle V\rangle/\hbar \sim \frac{k_B T}{2\hbar} \sim 0.7 \times 10^{11} \times T[Hz/K]$

the sample. In this way they are also easily separable with, e.g., a polarizing beam splitter.

The atom chip we have built during my permanence in Firenze is able to produce a $^{87}$Rb condensate of $N \sim 40 \times 10^3$ atoms, confined by a magnetic trap within a cigar shaped volume of dimensions ($2\,\mu m \times 2\,\mu m \times 35\,\mu m$). Moreover, until last months, we were able to trap just the strongest low-field seeking state $|F = 2, m_F = +2\rangle$, which is not one of the trappable clock states.
The available degenerate sample was indeed not good for memory experiments for the following reasons:

- the internal state of the atoms is not one of the clock states;
- the spatial transversal dimensions of the cloud is too small to allow good coupling with an external beam;
- the number of atoms is too low to ensure a thick optical depth.

For planning experiments involving coherent storage, the requirement on the initial state is unavoidable, as Raman coherences involving $|F = 2, m_F = +2\rangle$ can not survive more than few *microseconds* (due to non-zero first order differential Zeeman shift between the considered ground states) . On the contrary, degeneracy of the sample is not a necessary characteristic to provide long lived coherence, and stopping evaporative cooling at higher temperature allows both to save a larger number of atoms and to provide a wider transversal section. Within a certain limit, substantial change in atom number and dimensions can be obtained at small expense in terms of inhomogeneity. In this context, we decided to divide the experimental activity in two parts: while working on the set-up to reach a good trapping stage for state $|g\rangle \equiv |F = 1, m_F = -1\rangle$, we carried out a characterization of the system by implementing $EIT$ spectroscopy (for which long coherence time is not required) with an optimized thermal cloud of atoms in state $|g\rangle \equiv |F = 2, m_F = +2\rangle$. The latter is the subject of this section.
On one hand, this work allowed us to verify the functionality of the developed set-up for the memory experiment. On the other hand, by matching the experimental results with a numerical simulation of the atomic medium, we got reliable estimations for the memory performances in the ideal sample in state $|g\rangle \equiv |F = 1, m_F = -1\rangle$.

As a first stage we have developed a modified experimental procedure in order to produce a thermal cloud with geometrical characteristics adapted to the memory experiment. For this purpose indeed one needs on one hand an optical depth as large as possible (it can be enhanced by squeezing the aspect ratio of the cloud on the direction of propagation of the light), but, at the same time, a not too small transversal section, in order to ensure a complete coverage of the signal field on the transversal plane.
The best sample we have been able to generate consists in a thermal cloud with the following characteristics:

$$\begin{cases} \text{number of atoms} \quad N \sim 10^7 \\ \text{temperature} \quad T \sim 22\,\mu K \\ \text{spatial extent} \quad \sim (50\,\mu m \times 50\,\mu m \times 220\,\mu m) \\ \text{distance from chip surface} \sim 250\ \mu m \end{cases} \tag{5.1}$$

Details on the preparation procedure are reported in section 10.2 . The elongated direction is on the plane parallel to the chip and correspond to the magnetization axis. This involves that light for spectroscopy can cross the sample exploiting the maximal optical depth without hitting the massive structure. This sample ensures sufficiently high optical depth $OD$ and still low inhomogeneity induced decoherence rate (for both Doppler $\Gamma_{s,D}$ and Zeeman $\Gamma_{s,Z}$ contributions), while the transversal extent is large enough to cover the waist of the beam that we can easily obtain (minimal waist $\sim 30\,\mu m$, see section 8.1 )[3]. A sketch of the experimental configuration is reported in fig.5.1, together with the data describing the profile of the control beam around the position of minimal waist. These measures are obtained by directly imaging the transversal profile of the interrogation beams on the plane of the sample. We have access to these profiles by means of the imaging set-up sharing the optical path with the interrogation beams (see section 8.1).

[3]for focal distance of $20\,cm$ one can easily prepare a beam size smaller than $30\,\mu m$; we decided to keep this limit by considering the increasing difficulty of overlapping smaller objects, and in order to maintain a reasonable distance to the divergence limitation given by the presence of the chip (a beam with minimal waist of $w_0 \sim 40\,\mu m$, at a distance of half the chip extent ($\sim 10\,m$) from that point, shows a waist of $w(10\,mm) \sim 90\,\mu m$, thus almost three times the distance from the chip)

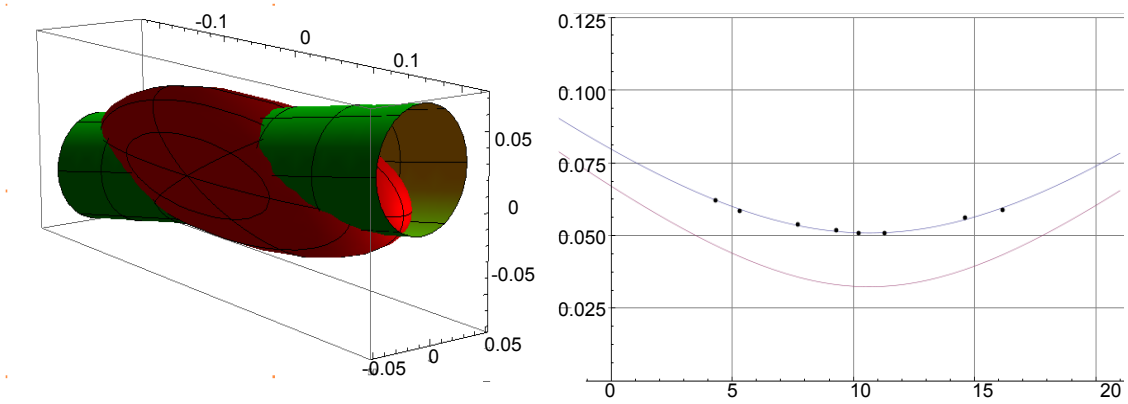


Figure 5.1: On the left a qualitative representation of the geometrical configuration in which the experiments of $EIT$ take place is reported. Both the axis of the ellipsoid representing the atomic cloud and the transversal section of the cylinder representing the light field are set equal to estimated value. In the right side the measurement of the longitudinal profile of the control beam is reported. This measures are obtained by directly imaging the light beam with the imaging set-up which use the same optical path (see section 7.1). The measurements related to different point along the propagation directionare obtained by changing the distance from the chip of the lens focusing the light on the atoms.

We can summarize the properties of our sample as follows[4]

$$\begin{cases} OD \sim \frac{3}{4\pi}\lambda^2 \frac{N}{S} \sim 180 \\ \Gamma_{s,D} \sim \frac{\langle v \rangle}{c}\omega \sim \sqrt{\frac{k_B}{m_{^{87}Rb}}T}\frac{\omega}{c} \sim 2\pi \times 60\, kHz \\ \Gamma_{s,Z} \sim \frac{k_B\, T}{2\hbar} \sim 1\, MHz \xrightarrow{\text{for clock states}} \sim 1\, kHz \quad (\text{for } |\bar{B}| \neq 3.2\, G) \end{cases} \tag{5.2}$$

The difficulty in trapping state $|F = 1, m_F = -1\rangle$ is due mostly to its weaker sensibility to magnetic field (for the same magnetic field, it feels half the potential with

[4]we have used the notation: $\lambda$ - light wavelength; $S$ - cross section of the cloud (assumed circular); $\langle v \rangle$ - mean velocity of the atoms; $c$ - light velocity in vacuum; $k_B$ - Boltzmann constant; $m_{^{87}Rb}$ - mass of a $^{87}Rb$ atom; $2\pi\hbar$ - Plank constant. Actually the evaluation of an optical depth can change even by an order of magnitude due to the specific addressed transition (as it will be shown below), the value reported here remaining a rough indicator

respect to state $|F = 2, m_F = +2\rangle$). Therefore we argue that once improved the current generators and the current controllers, we will be able to get similar clouds for atoms in the clock state. In this perspective, for bias magnetic field matching the magic value ($|\bar{B}| = 3.2\,G$), the decoherence rate $\Gamma_{s,Z}$ would allow storage times longer than one *millisecond*. Such a time scale is of the same order of the maximal quantum memory storage time reported in the literature, attained until now just for single photons ([124],[123]).

Condensation in state $|F = 1, m_F = -1\rangle$ has been recently obtained, producing a degenerate sample with a number of atoms simile to that obtained for $|F = 2, m_F = +2\rangle$; optimization of the thermal cloud in this state, $EIT$ characterization, and then memory experiments, are the next programmed steps in the laboratory activity.

For simplicity we refer in the chapter to the Rabi frequency related to the transition $|g\rangle \equiv |F = 2, m_F = +2\rangle \rightarrow |e_2\rangle \equiv |F' = 1, m_F = +1\rangle$ as $\Omega^c_{F'=1}$, and to the decay rate of the excited states (which we consider of the same entity for both $|e_2\rangle \equiv |F' = 1, m_F = +1\rangle$ and $|e_3\rangle \equiv |F' = 2, m_F = +1\rangle$) as $\Gamma_e$ ($= \gamma_{e_2 g} = \gamma_{e_3 g}$).

## 5.1 $EIT$ effect characterization in a thermal cloud at $T = 22\mu K$

To perform spectroscopy as in the previous section with a ultra-cold trapped sample requires quite different devices. The fundamental problem is that the number of atoms is limited, and once lost for some reason (e.g. incoherent scattering) they are not recoverable until the successive cooling stage. It is not possible to provide continuous repopulation as in the case of warm atoms, and so the sample have to be carefully protected and the resonant interaction has to be limited to the minimal strength. The $EIT$ measurements are realized with the set-up and the procedure prepared for storage experiments (see fig7.4 and 7.3 for reference, and section 8.1 for motivations). Control and signal field are thus copropagating beams with opposite polarization. The exploited $\Lambda$ scheme is constituted by the states $[|F = 2, m_F = +2\rangle \equiv |g\rangle$; $|F' = i, m_F = +1\rangle \equiv |e\rangle$; $|F = 1, m_F = 0\rangle \equiv |g\rangle]$ (with $i = 1, 2$). The two beams are merged on a beam splitter before the cell and take opposite $\sigma$ polarization crossing a quarter-wave plate. After interacting with the sample, the two fields are separated with a second beam splitter after another quarter-wave plate. To minimize the effect of the almost resonant signal field, we have kept it as weak as necessary to ensure a small damage of the cloud during the measure sequence (few *nanowatts*). It is detected as beat note with a few *megahertz* detuned local oscillator ($\Delta\nu = 5\,MHz$ in the reported measures). This technique allows the detection of such weak fields just with the help of some *milliwatts* of local oscillator.

The spectroscopy is performed in a discrete way, as a series of control, signal and local oscillator synchronized pulses. While the control field maintains all the time the same one photon detuning $\Delta_c$, signal and local oscillator change frequency with regular steps at each pulse, keeping the beat note at fixed pulsation. With few *nanowatts* pulses of length $\Delta t = 4\,\mu s$, we are able to construct a signal composed of hundreds of pulses of almost resonant light without spoiling the sample more than 10%[5]. Pulsing the local oscillator has been proven necessary, since its back reflection on the photodiodes destroys completely the sample in few *milliseconds*. It is indeed

[5]the key question is to send on the cloud a total number of resonant photons smaller than the number of atoms. In our case we send $200 \times 1\,nW \times 4\,\mu s\,/(\hbar\,\omega) \sim 2 \times 10^7$ photons, which is slightly greater than the number of trapped atoms. However the spectroscopy is still valid, due to the fact that most of the times the pulses are not perfectly resonant, thus causing a smaller damage

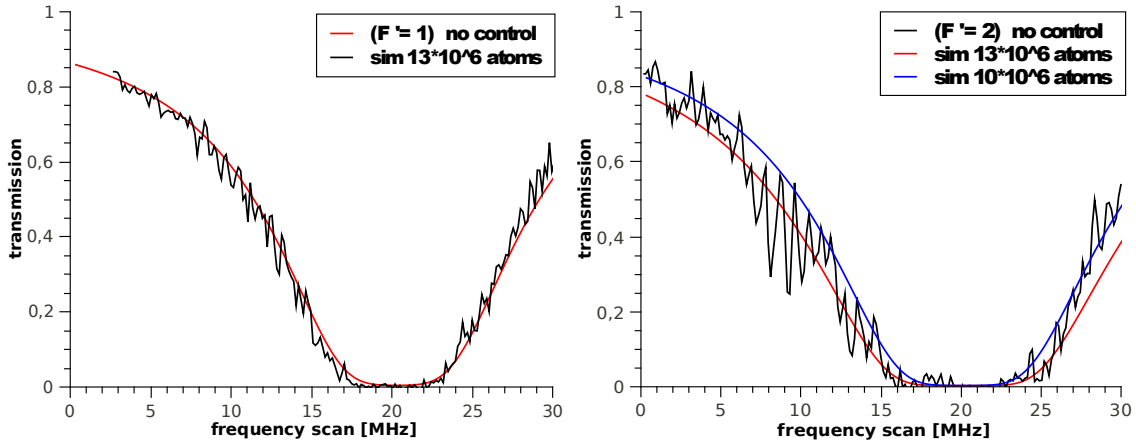


Figure 5.2: Absorption profiles, obtained with the technique described in this section, for a scan of the probe frequency around the $|F = 2\rangle \rightarrow |F' = 1\rangle$ (**a**) and $|F = 2\rangle \rightarrow |F' = 2\rangle$ (**b**). The measurements are performed in the absence of any control field, so that the detected absorptions are due to the simple atomic resonances. The result of a simulation performed exploiting the expressions of the model [83] is also reported. The simulations for the two transitions match the experimental profiles for almost the same number of atoms ($\sim 13 \times 10^6$). We detect a stronger absorption when addressing the $F' = 2$ excited state. This is in agreement with the specific dipole matrix elements involved in the interaction with the $\sigma_-$ polarized signal field, which show a relative amplitude equal to $\sqrt{5/3}$.

a powerful beam ($P_{l.o.} \sim 6\,mW$) almost at resonance with the atoms, and to save the cloud during experiments we had to carefully shield this beam all the way to the photodiodes. The beat note is recorded just within a $4\,\mu s$ time window triggered by the same electric TTL signal driving the pulse production; then the series of segments are numerically demodulated in order to evaluate the amplitude of the beat note (which is proportional to the amplitude of the transmitted signal) for each single pulse. The sequence of the obtained amplitudes provides the absorption profile of the medium in the frequency band covered by the scan. In fig.5.2 two examples of the complete spectroscopy signal are reported. In this case the control beam was absent, and the absorption profiles correspond to simple one photon resonances for light crossing the transitions $|F = 2, m_F = 2\rangle \rightarrow |F' = 1, m_F = +1\rangle$ (left side) and

$|F = 2, m_F = 2\rangle \rightarrow |F' = 2, m_F = +1\rangle$ (right side). The frequency scan is realized as a sequence of two hundreds pulses separated by $\delta\nu = 150\,kHz$, thus covering a band of $\Delta\nu = 200 \times \delta\nu = 30\,MHz$. All the measurements reported in this section are obtained in this configuration.
Some result of the $EIT$ characterization in the vicinity of the $|F' = 1, m_F = 0\rangle$ excited state are reported fig.5.3 and fig5.4. In the first figure is shown a sequence of measurements obtained for different values of the intensity of the control beam ($\propto |\Omega^c_{F'=1}|^2$), in condition of both one-photon and two-photon resonance ($\Delta_c = \delta = \Delta_s = 0$). In fig5.4, instead, I report the profiles obtained by varying the control one-photon detuning $\Delta_c$ for a fixed Rabi frequency $\Omega^c_{F'=1} = 0.9\,\Gamma_e$. By means of these data we have checked the validity of the theoretical expressions for $EIT$ and Raman absorption peaks position as obtained from the simple three level $\Lambda$ scheme (2.12 and 2.15); one example for both cases analyzed on the right side of each figure.

Focusing on the measurements at resonance measures (fig5.3), we have verified the correspondence between the applied Rabi frequency $\Omega^c_{F'=1}$ and the displacement of the $EIT$ absorption peaks displacement from the bare one photon resonance (2.12). Moreover, the effects induced by the presence of the second excited state ($F' = 2, m_F = +1\rangle$) are clearly visible in the asymmetric shape of the transparency window. On the other hand, we have not detected the AC Stark shift, which should progressively move the peak of the transparency towards lower frequencies (right side) for a more intense control field (as predicted by 4.14). The latter aspect remains to be clarified, because, at least for the measurements at high Rabi frequencies ($> \Gamma_e$), the shift should attain amplitudes of the order of one *megahertz*, thus well above the sensitivity of the detection ($30\,MHz\,/200 = 150\,kHz$)[6].
In the case of the one-photon detuning series instead (fig5.4), the induced shift is of the order of $100\,kHz$ (measurements performed for a Rabi frequency of $\Omega^c_{F'=1} = 0.9\,\Gamma_e$), thus not resolved by our system. The detunings considered here are too small to rigorously apply the expression 2.15 in order to determine the position of the absorptive Raman peak. However, at least for the case of greater detuning ($\Delta_c = 2\pi \times 15\,MHz$)

$$\delta_{peak} \sim \frac{|\Omega^c_{F'=1}|^2}{\Delta_c} \sim 2\pi \frac{0.8\;\Gamma_e^2}{15\,MHz} \sim 2\pi \times 1.95\,MHz \tag{5.3}$$

[6]For Rabi frequency $\Omega^c_{F'=1} = 3\,\Gamma_e \rightarrow \Omega^c_{F'=2} = 2.3\,\Gamma_e$ the induced shift evaluated following 4.14 results $\delta_{EIT} \sim -\frac{|\Omega^c_{F'=2}|^2}{\omega_{F'=1,F'=2}} \sim -\frac{(2.3\Gamma_e)^2}{2\pi \times 156\,MHz[rad]} \sim 2\pi \times 1.3\,MHz[rad] \quad (\Gamma_e = 2\pi \times 6.06\,MHz[rad])$

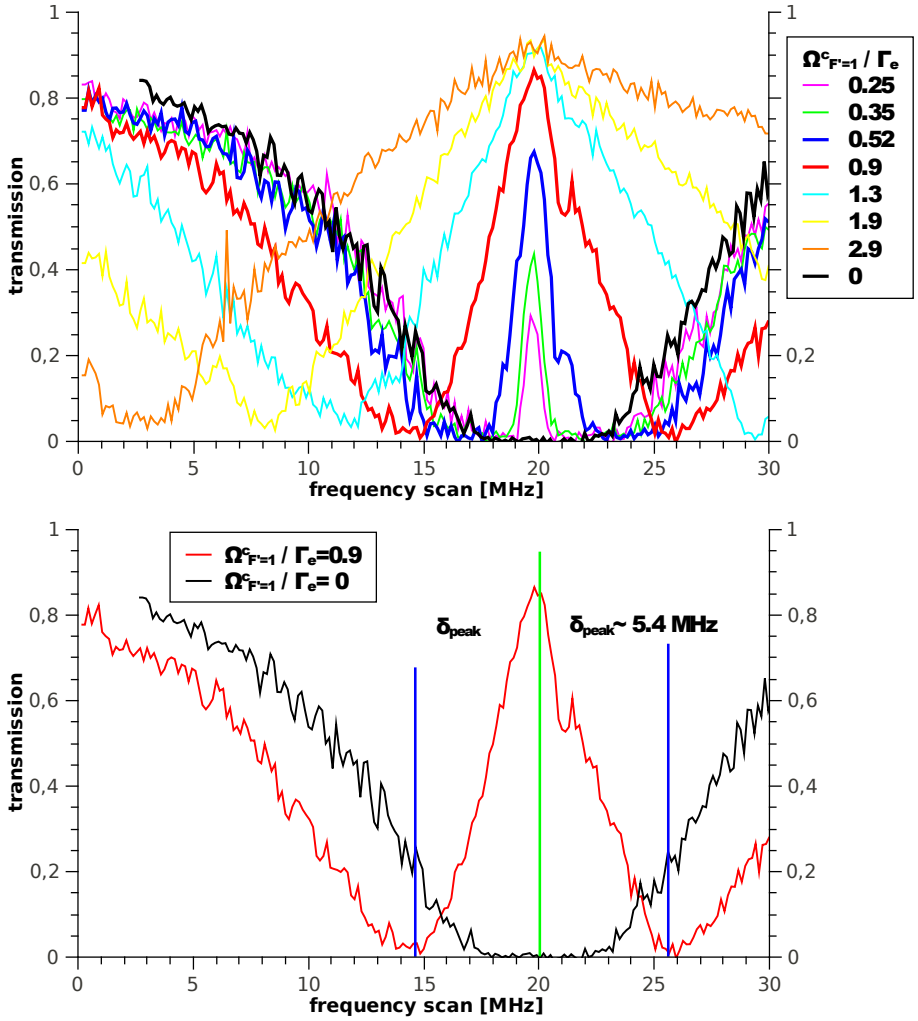


Figure 5.3: Absorption profiles for a scan of the probe light frequency around the atomic resonance $|F = 2\rangle \rightarrow |F' = 1\rangle$ in presence of one-photon resonant control field. The profiles relative to an increasing control Rabi frequency are reported. The formation of the induced transparency is evident. In the lower panel, one specific case ($\Omega^c_{F'=1} = 0.9\,\Gamma_e$) is considered with more attention, and a rough verification of the expression 2.12 for the position of the absorption peaks with respect to the center of the induced transparency is given ($\delta^{peak} = \Omega^c_{F'=1} = 0.9\,\Gamma_e$).
The V-like shape shown by the induced transparency profiles is a feature reproducible just by simulations accounting for inhomogeneous broadening, such as those of fig4.12. Actually this is the case, due to the presence of the magnetic trapping potential and the exploitation of two ground states with first order differential Zeeman shift.

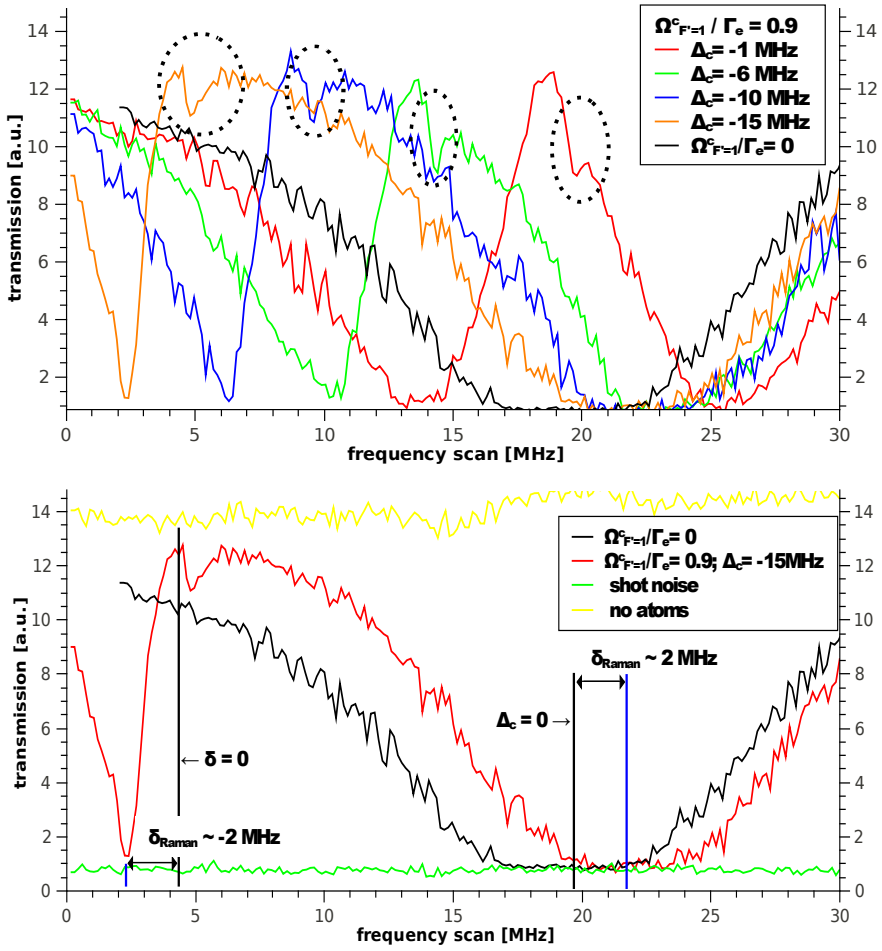


Figure 5.4: Absorption profiles for a scan of the probe light frequency around the atomic resonance $|F = 2\rangle \rightarrow |F = 1\rangle$ in presence of a control field with variable one-photon detuning $\Delta_c \geq 0$. The detuning is obtained by changing the frequency of the control field $AOM$ driver. In the sequence it is possible to recognize the two peaks approaching, respectively the profile of the simple atomic absorption (right) and the narrow shape of a Raman resonance (left). In the lower panel, a rough verification of the expression 2.15 for the position of the absorption peaks for far of resonance interaction is performed for the most detuned case ($\Delta_c = 2\pi \times 15\, MHz[rad]$). In the upper panel, dotted circles highlight the small peaks due to the beat note between the local oscillator and the leakage of the control carrier which survives the filtering action of the cavity (for details see section for 7.3).

and the measured value of $\sim 2\,MHz$ almost matches the predicted one.
In fig5.4 I have also highlighted the small peaks that can be seen in the proximity of the two-photon resonance for each value of the one-photon detuning. This small peak is actually the result of the beat note between the local oscillator and the small leakage of control field carrier which survives the filtering action of the cavity and enters the homodyne detection path. Details about this issue are reported in section 8.3, together with the description of a technical solution to reduce its detrimental effect down to a negligible level in the framework of memory experiments.

For an efficient interpretation of the data, the transmission profiles have been renormalized in order to express the transmittance of the medium. To perform this calibration, we have acquired a number of spectroscopic sequences in the absence of signal (to evaluate the background noise), and in the absence of atoms (to evaluate the output amplitude corresponding to perfect transmission). An example of such curves is reported in the right panel of fig5.4. The normalized profiles are obtained dividing the data taken in presence of atoms by the perfect transmission curve, after subtraction of the background noise (in quadrature) from both of them. If no excess noise is present, the background noise have to match the shot noise of the detection. We have indeed detected a linear dependence of its amplitude with respect to the local oscillator power, as predicted for standard quantum limit fluctuations. Moreover, the measured noise, if evaluated in terms of power spectrum by confrontation with the mean output value obtained for a given signal power, results very close to the predicted shot noise limit for the chosen band of integration ($2.5\,MHz$) of the beat note. These considerations let us assess that the detection system has the necessary sensitivity to measure pulses whose amplitude gives a contribution to the demodulated output of the same order of the shot noise summed over the whole integration band.

Exploiting this high sensitivity, we could perform the spectroscopy with pulses up to an order of magnitude weaker than the ones used in the measures of fig5.3 and 5.3, thus reducing almost to zero the induced loss of atoms. Due to the small damage produced on the cloud even with a , we preferred to get a higher signal-to-noise ratio.

## 5.2 Delay measurement

Once carefully determined the position of the one- and two-photon resonances ($\Delta_c = 0$ and $\delta = 0$) with the help of the measurements reported in fig5.3, we tried to detect the delay induced by the low group velocity attainable with this sample. Actually the detection procedure is such that it is immediate to switch from spectroscopy-like measurements to temporal profiles detection. While for spectroscopy each segment is demodulated all together, giving the average amplitude value to be confronted with the ones obtained for other segments, here we divide each segment in shorter sub-intervals, which are separately demodulated. In this way we have access to the modulation of the envelope within the temporal window defined by the segment. The detection technique resembles the one employed in the experiment in Paris, with the series of points relative to the single segment holding the same meaning of the points of fig4.3.a . In the case reported in fig.5.5, for simplicity, we left unchanged the temporal interval of beat note detection ($\Delta t = 4\,\mu s$), while providing independent demodulation on sub-intervals of duration $\delta t = 0.4\,\mu s$. The temporal profile of the pulses was shortened until getting smaller than $\Delta t$ (approximatively Gaussian profiles of standard deviation $\sigma_t \sim 0.5\,\mu s$), and centered on the detection window. In this way each segment contains the whole envelope, and comparing the results for different configurations we can directly explore the variation of delay and absorption. By providing the same experimental sequence used for the spectroscopy, but maintaining fixed the frequency of all the beams, we are able to ensure a two hundreds set of measurements of the same output pulse profile for a given configuration with a single experimental realization of the cold cloud. Each curve of fig.5.5 is actually the average over such a statistical ensemble.
The temporal resolution in these measurements is quite low ($\delta t = 0.4\,\mu s$), because we simply used here the same beat note frequency as in spectroscopy experiments ($5\,MHz$). In this context the time resolution is in fact limited by the period of oscillation of the interferential signal, the minimal achievable value corresponding to an average over two arcs of demodulation (here $\delta t = 2/5 \times 10^{-6}\,s = 0.4\,\mu s$). Actually the set-up is able to detect beat notes at frequencies up to $20\,MHz$, thus ensuring temporal resolution down to $\delta t = 0.1\,\mu s$.

In the figure 5.5 the delayed profiles obtained for different control field Rabi fre-

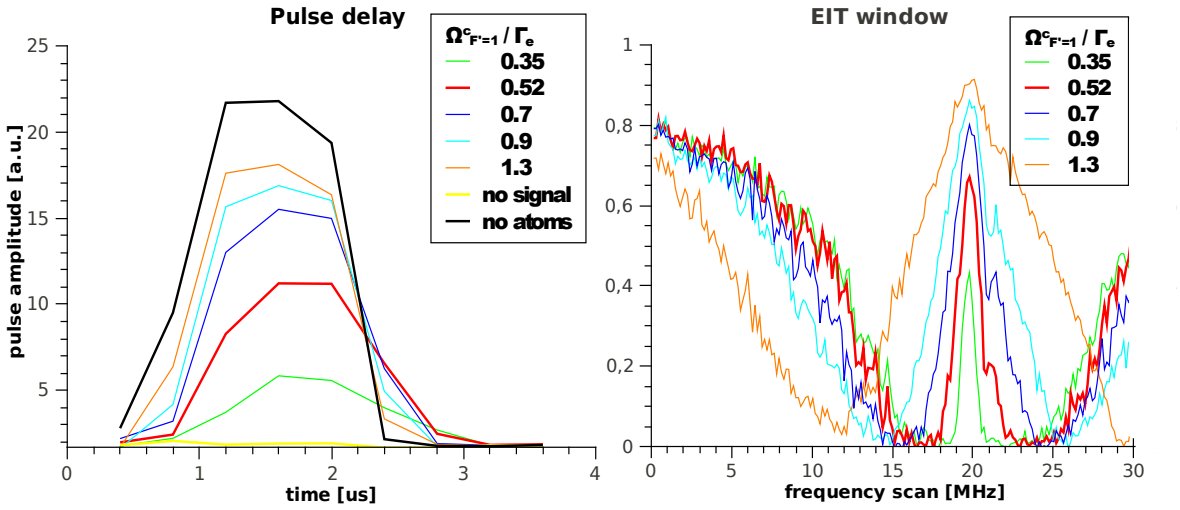


Figure 5.5: Delayed profiles for different control Rabi frequencies, based on a $\Lambda$ scheme as reported in 7.1.c . The black curve serves as a reference, it is the pulse profile obtained in the absence of atoms. On the right the $EIT$ spectroscopy signals obtained with the same control Rabi frequencies are reported (colors indicate curves for a given value of the Rabi frequency). The attained delay is low, due to the high decay rate of the hyperfine coherence. Indeed, when approaching control Rabi frequencies able to induce a large delay, the incoherent absorption has already destroyed the pulse.

quencies are reported, together with a reference profile got in the absence of trapped atoms (black line). On the right side, one can see the $EIT$ spectroscopy curves corresponding to the imposed values of control power[7]. The carrier frequency of the pulses was set almost at the center of the $EIT$ window.
The differential delay between two pulses is calculated evaluating the temporal position of the center of gravity for the two profiles. The attainable delay $\Delta t$ with respect to the case without atoms results quite small, the maximal value obtained for $\Omega^c_{F'=1} = 2\pi \times 3.1\, MHz[rad] = 0.52\,\Gamma_e$ still less than half a *microsecond* (red curve). We remark that it corresponds however to a group velocity of $v_g \sim 700\, m/s$, with a reduction of more than 5 orders of magnitude with respect to the velocity in vacuum. The motivation for this low level of delay is mainly due to the high decay rate characterizing the Raman coherence between states $|F = 2, m_F = +2\rangle$ and

[7]the same color code is used in both graphs to indicate the selected value of $\Omega^c_{F'=1}$

$|F = 1, m_F = 0\rangle$ ($\gamma_{sg} \sim 1\,MHz \sim \Gamma_e/6$, as mentioned above), which allows a low and thin transparency window, thus imposing "high" $\Omega^c_{F'=1}$ values in order to get a substantial transmission of the pulse.
The delay attained by a pulse with respect to the case without atoms ($\Delta t$) gives an indication about the storage capabilities of the medium. However, a better parameter for assessing the quality of a system as memory device is obtained calculating the portion of area in the envelope of the retarded pulse that is not shared with the reference pulse, and normalizing the obtained value to the total area of the initial pulse. Such a parameter, calculated for the intensity profiles (thus in terms of number of photons), is named here as "$m$". Its range spans in principle from zero to one. The case $m = 0$ is obtained either for no group velocity reduction (corresponding to a negligible portion of pulse present at any moment within the medium) or to complete incoherent absorption of the pulse during passage. Both issues prevent any storage.
A value of $m$ close to unity is obtained instead for an envelope exiting the medium with the same area it entered and showing a negligible overlap with the reference output (temporal profile obtained in absence of atoms). This result corresponds to a pulse completely contained in the medium at the same time without appreciable absorption during the passage: in this case the entire signal excitation can be in principle mapped on the atomic coherence.
In general $m$ indicate the maximal portion of the pulse contained in the medium at the same time.

In parallel with the experimental work, I elaborated a simple code to simulate the pulse modification due to passage through an atomic ensemble. In the program, the input pulse temporal envelope is first discrete Fourier transformed, in order to get a limited set of spectral components. Hence the effect of the crossed medium is added by simply multiplying each spectral component by the corresponding factor[8] $e^{-ik\,L\,\chi(\omega)/2}$ (see equation 1.40). To evaluate $\chi(\omega)$ for each frequency component of the discrete spectrum, the code calculates the set of exact values by exploiting a form of the expression 4.10 with parameters referred to the configuration we want to simulate[9]. Finally the output temporal envelope of the pulse is determined by inverse

[8] $k$ being the wavevector of the carrier mode, $L$ the sample length, while $\omega/(2\pi)$ represents the frequency of the spectral component

[9] Actually this is a very delicate passage, the final result showing sharp dependence on almost all

Fourier transforming the modified discrete spectrum. All the susceptibility profiles presented in the text, such as the explicative ones of fig.2.3, are obtained with this code. To determine absorption profiles as the ones detected with our experimental spectroscopies (e.g. fig.5.3) one simply needs to graph the expression for the transmission $t$ as defined in 2.13. The simulated absorption profiles reported in fig5.2, fig5.6.d, fig5.7 and fig5.8 are the results of such a calculation.

By a careful comparison between experimentally detected profiles and simulation results, we have been able to precisely determine the fundamental parameters governing the susceptibility of the medium, which in turn has led us to obtain impressive matching between predictions and experimental data in a wide range of control field power (fig5.6)[10] and one photon detuning (5.7).

The only feature the simulation does not forecast is the "V"-like shape shown by the transparency window, which on the contrary is a persistent characteristic in our detection. This is because the "homogeneous" parameter $\gamma_{sg}$ cannot represent completely the effects of an inhomogeneous broadening such as that induced by the trapping potential. For any value imposed to $\gamma_{sg}$ in fact, the transmission profile keeps a "U"-like shape. On the other hand, we recognize a similar aspect in the profiles of fig4.12, relative to Doppler (inhomogeneous) broadened media. So finally we can associate the "V" shape to media presenting some kind of inhomogeneity in the transition. To verify this hypothesis we should calculate a mean susceptibility as in the case of warm

---

the involved parameters

[10]Caption of fig5.6. Detailed comparison between the delayed profiles experimentally detected (left) and the results of the simulations based on a fixed set of parameters (right). From the simulated profiles we have calculated the set of parameters describing the quality of the induced transparency, namely, the delay time $\Delta t$, the $m$ parameter (discussed earlier in this section), and the overall transmission of the medium, defined as the ratio between the areas of the output and input pulses (to be expressed in terms of number of photons, the area is calculated integrating the square of the detected profile, which is otherwise proportional to the amplitude of the field (it is obtained as amplitude of a beat note)). $\Delta t$, defined as the difference of the barycenters of the two envelopes, is evaluated also from the experimental data. The maximal detected delay reaches $\Delta t \sim 0.35\,\mu s$, which corresponds to a group velocity in the medium of $\sim 700\,m/s$. In **d** the spectroscopy signals obtained for the Rabi frequencies used in the delay experiment are compared to the results of simulations with the same set of parameters giving the time profiles (a,b,c). To match the variation of the transparency peak, actually, we had to assume a slight one-photon detuning of the signal field of $\sim 0.5\,MHz$ (**e**). In **f** we have thus evaluated the maximal retardation attainable if the pulse were exactly at the center of the transparency.

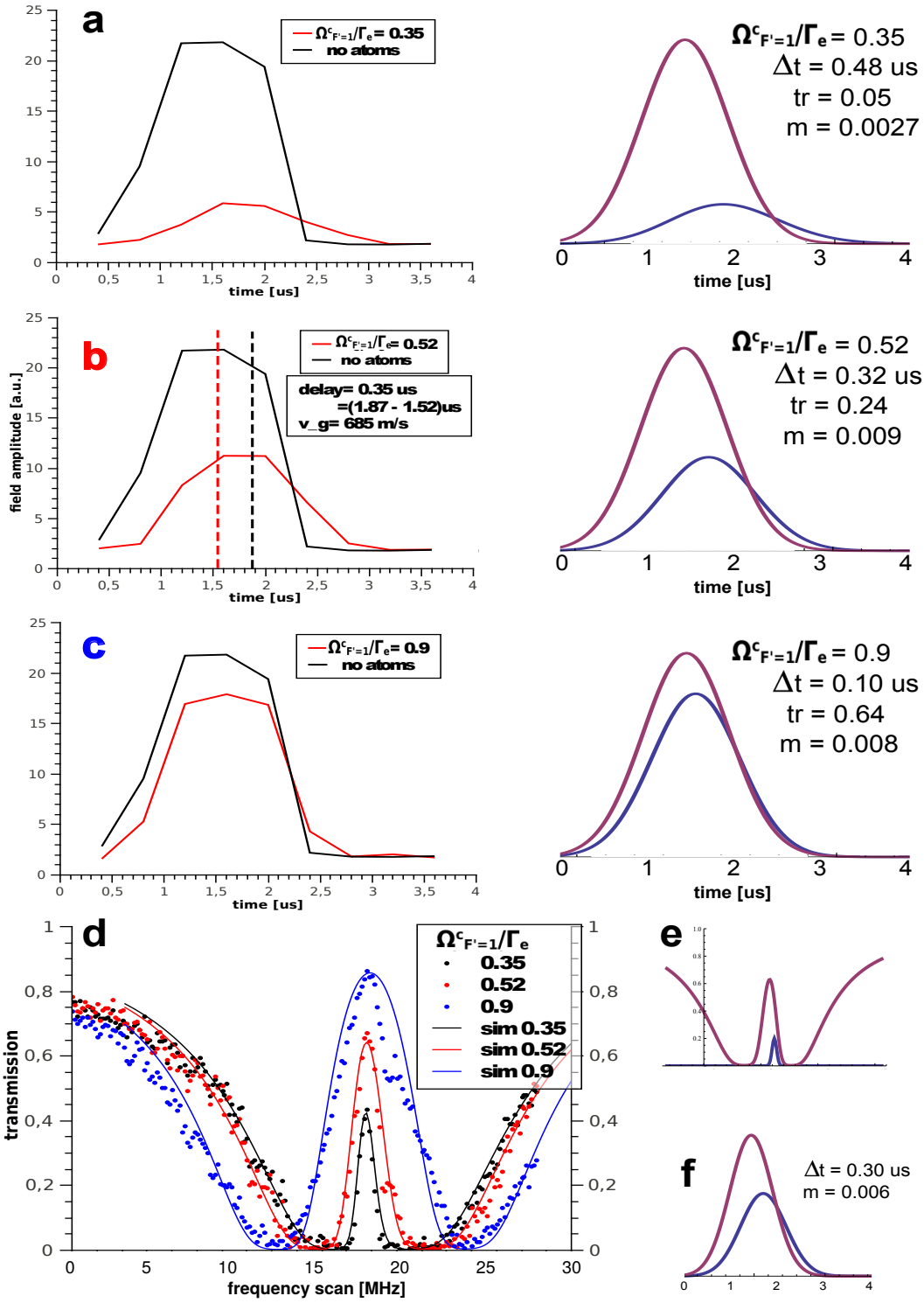


Figure 5.6: See note 10 for caption

atoms. However, due to the small amount of broadening, it is not necessary in order to get satisfactory representations of the response of the cloud, as it can be seen fig5.6.d .

Even after this calibration procedure, we were not able to reproduce the delayed pulses as well as it is reported in fig5.6.a/b/c. We revealed in particular a deviation on the amplitude of the output envelope, with a less steep dependence on th intensity of the control field with respect to the experimental results. Since transparency profiles are almost perfectly simulated in a wide range of control power, we have deduced that the discrepancy is related to a non-perfectly null one-photon detuning for the signal carrier ($\Delta_s \neq 0$). If the carrier is not centered on the window, the transmission depends also on the transparency width, thus showing a steeper trend as a function of the control Rabi frequency. Setting $\Delta_s = 0.5\,MHz$ (which corresponds to a position of the spectral envelope shown in fig5.6.e) we have got a really nice simulation of the delayed pulse for every configuration experimentally explored (such as the ones of fig5.6.a/b/c). For a non perfectly centered spectrum, the capacity of the medium is not completely exploited: as additional data, we calculated the delay attainable for a centered pulse, the result reported in fig5.6.e .

**Calibration of the parameters of the simulation**

The single atom susceptibility, taking as reference the general expression given by 4.10 and 4.7, is defined by the following parameters[11]:

- the one photon detuning of the control field $\Delta_c$;
- the Rabi frequency of the control field $\Omega^c_{F'=1} \propto P_c/S_c$
  (determined by its power $P_c$ and its transversal section on the atoms $S_c$);
- the Raman coherence decay rate $\gamma_{sg}$;
- the number of atoms $N$ that determines the optical depth encountered by the signal field $OD \propto N/S_a = n_0\ L$ (with $S_a$ transversal section of the cloud, $n_0$ number density and $L$ sample dimension along the direction of propagation of the light).

[11] we do not consider here the parameters related to the specific transitions involved, as the optical decay rate $\Gamma_e$, the energy spacing among the levels, and the dipole matrix elements, which are taken as constants of the system, set to the values indicated in [112]

The last parameter is the simplest to evaluate: its value is determined by simply matching spectroscopic signals and simulations for zero control field Rabi frequency (as reported in fig.5.2). As a matter of fact, the number of atoms $N$ in the trap is quite well known through normal resonant imaging procedures ($N \sim 8 \times 10^6$): what have to be optimized is hence the cloud transversal size $S_a$. Its effective value results to be $S_a \sim \pi \times (42\,\mu m)^2$, slightly smaller than what directly estimated by resonant imaging ($\pi \times (55\,\mu m)^2$). This is somehow expected due to the representation of the cloud as a cylinder rather than an ellipsoid in the computer program. The validity of the assessment for ($N/S_a = n_0\ L$) is strengthened by the good estimation we get for absorption profiles around the other excited state ($|F' = 2, m_F = +1\rangle$) without changing any parameter but the dipole matrix element.

The calibration of the Rabi frequency $\Omega_c$ is obtained by evaluating the position of the $EIT$ absorptive peaks respect to the center of the resonance (fig5.3). Following 4.14 we see that in the case of $\Delta_c \sim 0$ the induced frequency splitting directly equals the amplitude of $\Omega^c_{F'=1}$. With this indirect measurement technique for $\Omega^c_{F'=1}$, we even realized that the beam size at the level of the cloud is slightly smaller with respect to what directly measured ($S_c \sim 45\,\mu m$ instead of $\sim 50\,\mu m$ as derived from fig5.1). The actual Rabi frequency exceeds in fact the detected value for a beam size of $50\,\mu m$.

The one photon detuning $\Delta_c$ is determined by looking at the position of the transparency for low intensity control field, as in the profile obtained for $\Omega^c_{F'=1} = 0.25\,\Gamma_e$ (pink line) in fig5.3. For the reported set of measurements we realized that it was almost but not perfectly zero , the correct value being $\Delta_c \sim 1\,MHz$ .

Once defined all the other parameters, we can set the Raman coherence decay rate $\gamma_{sg}$ in order to match the simulated transmission profiles with the ones measured with the spectroscopy

## 5.3 A real verification of Mishina model

In the previous section we have proven that the transmission profiles obtained with spectroscopic technique on our could sample are very close to the theoretical zero temperature profiles resulting from simulations. As a consequence, we can now experimentally open what is usually a sort of "closed box" in case of warm atoms: we can look indeed at the specific response of single velocity classes by simulating the Doppler shift through a suitable one photon detuning $\Delta_c$. This is possible due to the fact that the result obtained for a certain $\Delta_c$ corresponds (at the first order) to the response given by the velocity class $v = 2\pi\ c\frac{\Delta_c}{\omega}$ under one photon resonance condition[12].

In fig5.7 I report a series of curves that verifies our model [83]. The measurements correspond to transmission profiles around the two-photon resonance $\delta = 0$ for $\Delta_c$ scanned from zero to $160\,MHz$, that is moving the control field from one-photon resonance with $|F' = 1, m_F = +1\rangle$ to one-photon resonance with $|F' = 2, m_F = +1\rangle$. The simulations (curves on the right) are able to reproduce very closely the experimental data, and a slight difference can be noticed just for measurements close to the upper resonance. This is probably due to the bad quality of the frequency stabilization for the laser, as it can be seen even in fig.5.2: the lock apparatus has in fact been designed to work around resonance with $|F' = 1, m_F = 0\rangle$. On one hand, an instability in the involved light field results in a higher effective Raman decoherence rate; on the other hand, an even thin frequency modulation results in a spectroscopic signal averaged over a certain band.

The main result of the experiment is clearly evident: increasing the one-photon detuning $\Delta_c$, the upper frequency edge of the $EIT$ window for the transition $|F' =, m_F = +1\rangle$ is transformed into a Raman peak which gets closer and closer to the two-photon resonance until it changes side, and eventually becomes the lower frequency edge of the induced transparency for the level $|F' = 2, m_F = +1\rangle$. As described in section 3.1.4, this is actually the main process responsible for the cancellation of the induced transparency in case of $\Lambda$ scheme based on an excited state manifold spaced less than the inhomogeneous broadening of the medium.

One can notice that the crossing point is next to the upper resonance, contrary to the

[12] we follow the convention that the positive velocities correspond to atoms moving towards the incoming light

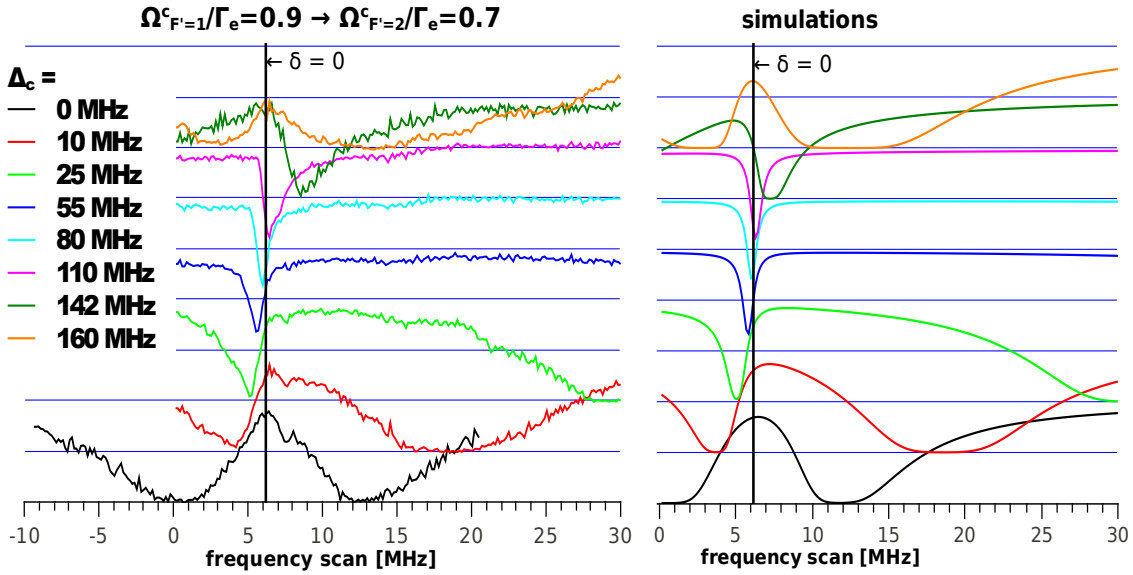


Figure 5.7: *EIT* spectroscopy signals like those reported in fig5.3 and fig5.4 are recorded here for a one-photon detuning of the control field passing from one-photon resonance condition with the transition $|F = 2 \rightarrow |F' = 1\rangle$ to one-photon resonance condition with the transition $|F = 2 \rightarrow |F' = 2\rangle$. The two-photon detuning $\delta$ is kept at the center of the scanned band. The migration of the Raman peak from one side to the other with respect to $\delta = 0$ (marked by the black line) is evident and takes place for $80\,MHz < \Delta_c < 110\,MHz$. On the right panel simulations with a fixed set of parameters are reported.

prediction for Cesium (fig4.11, [104, 83]). This is due to the relative strength of the involved transitions: the zero crossing point is indeed determined by the annihilation of the opposite AC Stark shift contributions induced by the two levels (2.15), which takes place for a detuning able to balance the difference between the amplitudes of the resonant Rabi frequencies (i.e., between the Clebsch-Gordan coefficients).
For the double $\Lambda$ scheme based on $^{133}Cs$ levels ($|s\rangle \equiv |F = 3, m_F = +1\rangle$; $|g\rangle \equiv |F = 3, m_F = +3\rangle$; $|e_2\rangle \equiv |F = 2, m_F = +2\rangle$; $|e_3\rangle \equiv |F = 3, m_F = +2\rangle$), the control field is more strongly coupled to the $|e_3\rangle$ than to the lower state $|e_2\rangle$. In the case of $^{87}Rb$, for a $\Lambda$ scheme based on levels ($|s\rangle \equiv |F = 1, m_F = 0\rangle$; $|g\rangle \equiv |F = 2, m_F = +2\rangle$; $|e_2\rangle \equiv |F = 1, m_F = +1\rangle$; $|e_3\rangle \equiv |F = 2, m_F = +1\rangle$), one gets the opposite situation.

The general expression for the crossing point one-photon detuning reads:

$$\frac{|\Omega^c_{e_2 s}|^2}{\Delta_c} = -\frac{|\Omega^c_{e_3 s}|^2}{\Delta_c - \omega_{e_2 e_3}} \quad \Rightarrow \quad \Delta_c = \frac{\omega_{e_2 e_3}}{1 + \frac{|\Omega^c_{e_3 s}|^2}{|\Omega^c_{e_2 s}|^2}} \tag{5.4}$$

which corresponds[13], in the case of $^{133}Cs$, to $\Delta_c \sim 20\, MHz$; on the other hand, in the present case of $^{87}Rb$, it reads $\Delta_c \sim 100\, MHz$. The prediction is thus in agreement with the experimental results, from which we can say the passage from blue to red two-photon detuning occurs for a one-photon detuning contained within the values $\Delta_c = 80\, MHz$ and $\Delta_c = 110\, MHz$.

[13] taking Clebsch-Gordan coefficients from [111],[112], we get:
for Cesium $|\Omega^c_{e_3 s}|^2/|\Omega^c_{e_2 s}|^2 = \frac{5}{32}/\frac{1}{42} = 105/16 \sim 6.5$, $\omega_{e_2 e_3} = 151\, MHz$
for Rubidium $|\Omega^c_{e_3 s}|^2/|\Omega^c_{e_2 s}|^2 = \frac{1}{8}/\frac{5}{24} = 3/5 = 0.6$, $\omega_{e_2 e_3} = 157\, MHz$

## 5.4 Limits of the system and perspectives

When we planed to exploit the Firenze apparatus for a memory experiment we realized that it presents a number of intrinsic limiting aspects which could prevent us from getting good efficiency.
An open question was constituted by the level of matching between the cloud and the signal beam which can be regularly attained day by day. This is a not trivial technical question due to the small transversal section ($\sim \pi\ (50\,\mu m)^2$) of both objects. Actually we can act only on optical elements (lenses or mirrors) at least $20\,cm$ from the cloud, without any accurate indication about the direction to follow (as it is instead the case for dipole trapped samples). Another issue was the effect of the non negligible angle (evaluated to be about $8^o$) between the propagation and the magnetization axes, which induces to a non perfectly determined polarization of the light with respect to the atomic orientation. This aspect could even be catastrophic due to the large power imbalance characterizing the involved fields: a signal at the shot noise level ($\sim 10\,pW$)[14] results up to 5 order of magnitude weaker than the control field able to induce transparency ($\sim 1\,\mu W$), thus even a few percentage of the latter interacting with the populated state would prevent any coherent interaction.
Besides these geometrical questions, we wondered on the effect of the magnetic noise of the trap that we could clearly detect while producing the condensate. We know the energy of the trap bottom oscillates with a modulation depth of $\sim 1\ kHz$, but we have not details on its characteristic frequencies.

After the preliminary results reported in this section, however, we are convinced that the system is able to provide significant storage times and quantum efficiency. We have indeed to interpret them considering that the exploited $\Lambda$ scheme is characterized by a very high coherence decay rate. Using the calibration of the model obtained with our data, we can estimate the results attainable by working with the $\Lambda$ scheme based on the clock transition. In fig5.8 I present some estimations of delay for such a configuration. For a control field Rabi frequency $\Omega^c_{F'=1} = 0.3\,\Gamma_e$ the predicted delay attains $\Delta t = 1.8\,\mu s$, while for the parameter related to the memory efficiency we get $m = 0.44$. The simulations look hence very promising, considering also that we

[14] shot noise level defined for an integration band of $10\,MHz$ at an optical wavelength of $\lambda = 800\,nm$

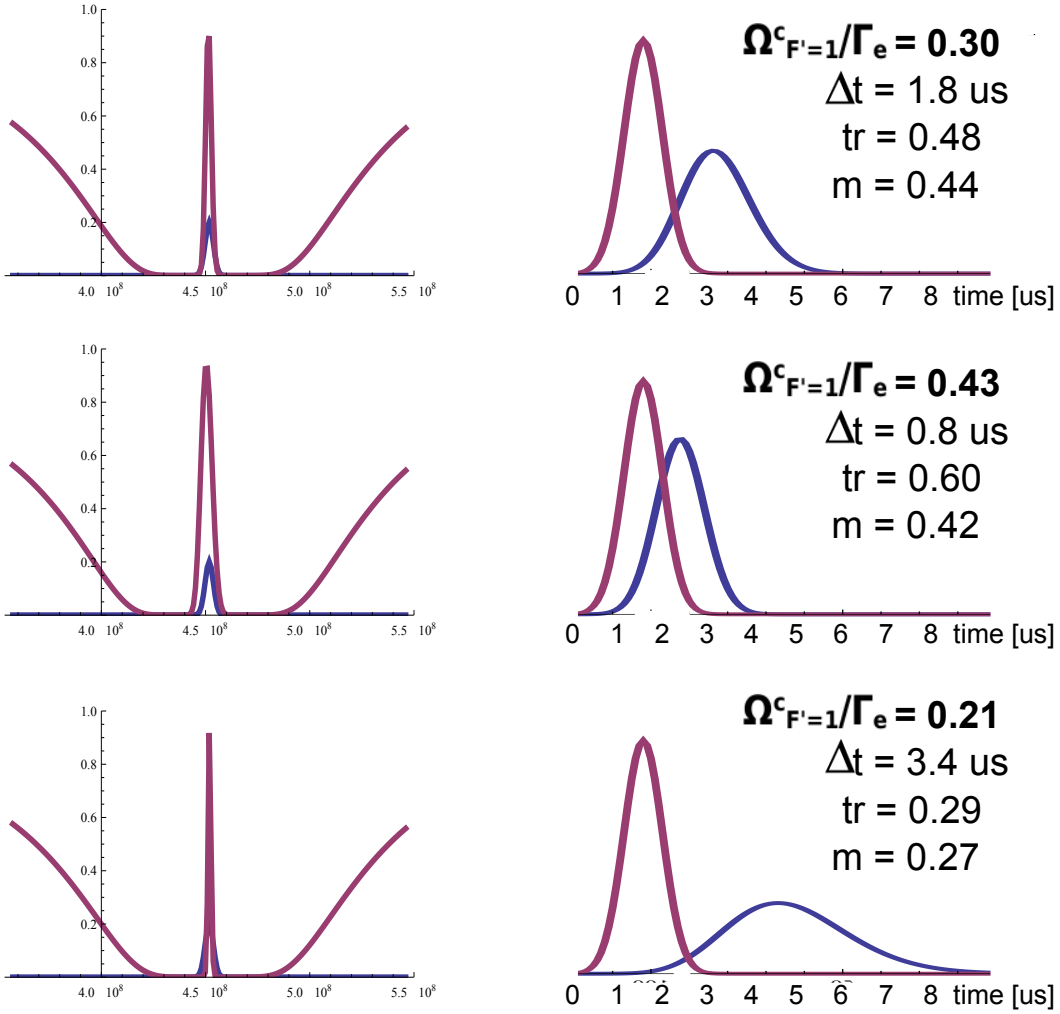


Figure 5.8: Estimation of the attainable time delay $\Delta t$ and parameter $m$ by working with the $\Lambda$ scheme based on the clock transition $|F = 1, m_F = -1\rangle \rightarrow |F = 2, m_F = +1\rangle$. The simulation gives a quite good prediction for two main reasons: the transition addressed by the signal field ($|F = 1, m_F = -1\rangle \rightarrow |F' = 1, m_F = 0\rangle$) is mediated by a larger dipole matrix element with respect to the case experimentally explored ($|F = 2, m_F = +2\rangle \rightarrow |F' = 1, m_F = +1\rangle$), thus resulting in a higher effective optical depth (about four time higher). Moreover, the coherence decay rate $\gamma_{sg}$ can be assumed to be lower by 1/1000 with respect to the value found by the calibration procedure for the investigated case (we set 1/500 in this simulations). This low rate of dechoerence allows a substantial transmission of the signal pulse for lower values of the control Rabi frequency with respect to the experimentally explored case, which corresponds to lower group velocities.

have taken into account the possibility of a less efficient trapping procedure (by setting the number of atoms to 75% of the value we have for state $|F = 2, m_F = +2\rangle$), and a weaker confinement ($S_a \sim \pi\ (50\,\mu m)^2$ instead of $S_a \sim \pi\ (42\,\mu m)^2$). The impressive improvement respect to the explored $\Lambda$ scheme is mainly due to the combination of two factors: the reduction of the Raman coherence decay rate $\gamma_{sg}$ by a factor 1/1000 with respect to the value determined within the calibration procedure, and the larger dipole matrix element corresponding to the transition addressed by the signal field, which is almost twice the value $|g\rangle \equiv |F = 2, m_F = +2\rangle$[15]. The smaller $\gamma_{sg}$ allows to keep a substantial transmission even for lower control Rabi frequency respect to the present case, hence leaving the possibility of exploiting sharper dispersion profiles. For example, the better $m$ reported in the figure is obtained for a Rabi frequency which induces a very low transparency in the configuration used for the measurements. On the other hand, the expression for the susceptibility is proportional to the square of the involved dipole matrix element, thus in the second case its profile gets an overall magnification by a factor $\sim 4$ with respect to the first case. The attained coupling with the sample is thus quite satisfactory, and it turns out not too hard to reach day by day.

On the other side, concerning the spurious components of the control light, we can manage to render them harmless by keeping them far from resonance with respect to the atomic transitions. How to get this condition is explained in the next section.

Concerning the magnetic noise, since its amplitude is of the same order of magnitude of the trapping potential, we conclude that it will not reduce too much the potentialities of the system, which should further improve by approaching the magic bias magnetic field value.

[15] the corresponding Clebsh-Gordan is $\sqrt{5/24}$ instead of $\sqrt{1/20}$

# Part III

# Atomic interferometry

# Chapter 6

# Multistate matter waves interferometry

The unprecedented measurement precision of the atomic interferometers justifies the building of complex and bulky apparatuses such as atom fountains for local gravity measurements [95]. At the same time, applications outside the laboratory depend on the compactness and robustness of interferometric setups. Therefore, further enhancement of sensitivity and reduction of complexity are crucial conditions for success and widening of their applications.

Here we report our demonstration of a multi-path interferometer relying on the internal degree of freedom constituted by the orientation manifold of an hyperfine ground state. The multi-state functionality is achieved by means of a resonant RF magnetic field, which is able to coherently couple the Zeeman sub-levels. The complete coherence of the atom transfer guarantees a visibility of nearly unity. In addition our interferometer does not require neither alignment nor high resolution imaging, due to non local evaluation of the collective occupancy of the internal state manifold. Applications of the proposed interferometer are based on different responses of the Zeeman states to external fields, like the measurement of the local magnetic field amplitude (which is directly mapped into the periodicity of the fringes), or measurements of parameters of light-atom interactions. Due to the simultaneous measurement of multiple state populations, the interferometer should be capable of multi-parameter sensing. This concept is well known in photonics where it is employed in interrogation schemes with fiber gratings. However this possibility has to be further theoretically

explored.

In the first section of this chapter I present the technical realization of such an interferometer that we implemented in a set-up fully merged with the atom chip apparatus for condensation. In the second section, the experimental results verifying the properties of the interferometer are reported. In the third section I show our demonstration of detection of effects induced by external optical fields.

Our realization of an internal state atom interferometer is a proof of principle for a technique easily implementable in other set-up explicitly developed for interferometry. However, what we have realized presents a lot of limiting aspects which reduce its direct effective utility.
The main limiting element in our set-up is indeed the trapping potential: being of the magnetic type it is state sensitive and can not hold all the orientation sub-levels populated by the coupling pulses. In our experiments the interrogation time is thus limited by the time the high field seeking states need to escape the trap or to get a velocity large enough that the spatial phase modulation has a wavelength shorter than the sample size. Both events reduce the possibility of seeing interference among the wave-functions envelopes for the different internal states. In general however, this problem can be simply overcome by using a dipole rather than magnetic trap.

Several multi-path matter-wave interferometers have been based on the property of optical lattices [1, 30], Raman laser pulses [108] and individual laser pulses [56] to cause a controlled atom recoil. While they offer numerous advantages such as a large number of paths, easy control of the relative phase accumulation rate, and compatibility with techniques for control of atom-atom interactions, these interferometers rely on the spatial separation of paths and hence cannot be realized in a trap. Moreover the use of optical fields makes the system highly sensible to instabilities related to alignment, which can affect also the visibility of the interferometric signal.

The integration of the interferometer with an atom chip offers several technical advantages. The vicinity of the conducting structures to the sample allows for both fast switching and large field gradient. The first point is of particular importance for time-domain interferometers in which the signal is constructed from a series of measurements at different time delays. On the other hand a high magnetic gradient facilitates spatial separation of the Zeeman states, which allows collective measure-

ments of the populations by means of a simple resonant imaging.

## 6.1 Atom chip based set-up

As described in the theoretical section, the interferometer is realized by measuring the interferential term in the population distribution obtained after application of a couple of pulses of a resonant perturbation able to mix the wave-functions of the states. In our case, the initial state is the result of the procedure to Bose condense on the atom chip, that is, a pure, low field seeking $|F = 2, m_F = +2\rangle$ state. The sequence of operations that allows us attaining the condensation is briefly described in section 9.2, while for details on this subject we refer to Herrera's thesis [54].
At the bottom of the trap the atoms experience a magnetic field of $B_0 \approx 1$ G, which constitutes the bias field giving the spacing among the states of the Zeeman manifold. The resonant RF field is thus set at about $\omega_{RF} = 2\pi \times 700\ kHz$ ($= m_F g_F \mu_0 |B|$), where $m_F$ and $g_F$ are respectively the spin and Landé numbers and $\mu_0$ is the Bohr magneton. The measurement is accomplished by detecting the fringes in the population distribution obtained by varying the phase of the second pulse with respect to the reference given by the first pulse.

The RF coupling is produced by exploiting as antenna one of the U-wires positioned immediately behind the chip surface (fig.6.1). The proximity of this conductor to the sample allows to generate high Rabi frequencies just applying the output of a function generator, in our case an *Agilent* 33250*A*. This kind of generator can provide wave pulses synchronized with a reference external trigger signal, emitting a predetermined number of periods with phase locked to the triggering front. Therefore, to achieve the modulation of the relative phase one simply needs to apply the two pulses with a controllable time delay between them: changing the delay until a Larmor period ($T_L = 2\pi/\omega_L = 2\pi/\omega_{RF}$), the phase of the second pulse spans on a complete interval modulus $2\pi$. Recalling the Bloch representation as in the theoretical section (4.1), we may say that the vector describing the second pulse gets a complete turn on the $(1, 2) - plane$. This technique was already used in [82].
The pulse length $\tau$ has been fixed to 25 oscillations ($\sim 36\,\mu s$), ensuring that the pulse bandwidth cover the $10\,kHz$ mean field energy spread of the atoms in our $BEC$. The time delay between the pulses is controlled in $100\,ns$ steps with $5\,ns$ precision, thus resolving the fringe period in about 14 points. The second pulse maps the relative

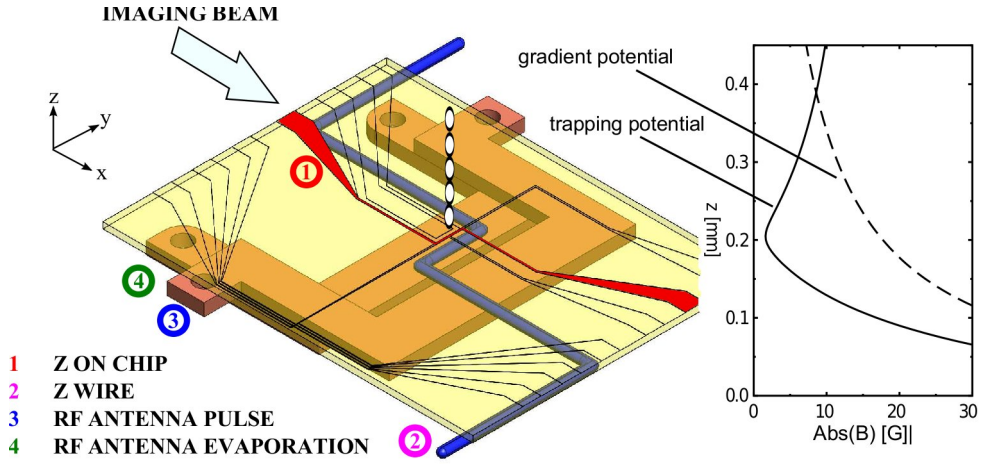


Figure 6.1: The atom-chip apparatus with the available tools for magnetic manipulation of the sample.
The micrometer z-wire which provides the magnetic trapping (1) is highlighted in red. Blue indicates instead the millimeter Z-wire (2) responsible for the ancillary magnetic trap (see chapter 9). Number (3) and (4) indicate the two U-wires used as RF antennas. The plot on the right shows z-wire induced magnetic potential obtained with bias (z-trap) and without bias (Stern-Gerlach gradient). Image taken from [96]

phases accumulated between different states during the delay into a population distribution at the output of the interferometer. The induced coherences among the states evolve with frequencies equal to multiples of the energy separation between the adjacent levels $\omega_L$, yielding the interference signals rich in harmonics, which corresponds (as shown in section 4.1) to a sharpening of the fringes profile.
Finally, in order to determine the population of each output state, they are spatially separated by applying of the Stern-Gerlach method followed by a free-fall expansion, and then imaged. The field gradient is obtained by switching off the external bias field and letting the atoms move in the field of the chip z-wire. Both trap and gradient fields are sketched in fig.6.1.
We leave the current on for $100\,\mu s$, which is sufficient to give the internal components a differential velocity higher than the mean field induced expansion. The result is an imaging of well separated clouds, as shown in fig.6.2 for a free falling time of $10\,ms$. These images are obtained with a 7.5×-magnifying absorption imaging system and

a $CCD$ camera ($SIS1 - s285, Theta - System$). Each measurement destroys the coherent sample, so that a new $BEC$ has to be created every time.
The passage from the trap to the gradient stage is obtained with an, in principle, abrupt change which should prejudice the correct evaluation of the orientation distribution. The directions of the field in the two cases are indeed orthogonal[1], and so the switching procedure involves a rotation of the quantization axis. According to what described in the theoretical section about adiabatic change, population should be remixed by this operation. What actually happens is a smooth rotation of the axis, due to the $\sim 100\,\mu s$ time scale, imposed by the inductive load of the coils, which characterizes the switching of the bias field. This time scale is slow enough to prevent loss of orientation ($\omega_L = 2\pi \times 700\,kHz \gg \frac{\pi}{2}/(100\,\mu s)$). From the data we deduce that the change of magnetic field direction does not cause more than 15% of the atoms to change their magnetic sub-level.

The Ramsey-like interferometry is performed here by exploring the result obtained by varying the relative phase between the two RF pulses. As shown in the theoretical section 4.1, this method provides a lower sensitivity with respect to the original Ramsey spectroscopy. Switching to the "powerful method" is however a simple issue: to get a conservation of the relative phase between the twin pulses, we can exploit the low phase noise characterizing the *Agilent* $33250A$ function generator, by using it to produce a continuous wave at the needed RF frequency and shaping the pulses with a voltage controlled attenuator inserted before the antenna.

## 6.2 Interferometry

I present here our experimental results on the characterization of the interferometer. The validity of the proposal is demonstrated by measuring narrower fringes related to the population distribution with respect to both the experimental ([82]) and theoretical results where just two states are exploited. Although the detected slope for the 5-state interferometer is 1.26 times steeper than that of the ideal 2-state interferometer, the sensitivity of the latter is still unsurpassed. In a correct calculus of the sensitivity, in fact, one have to "weight" the resolution of the measuring technique

[1] the trap bias field is aligned along the y axis, while the wire produces a field on the plane orthogonal to the wire axis itself ($(x, z) - plane$)

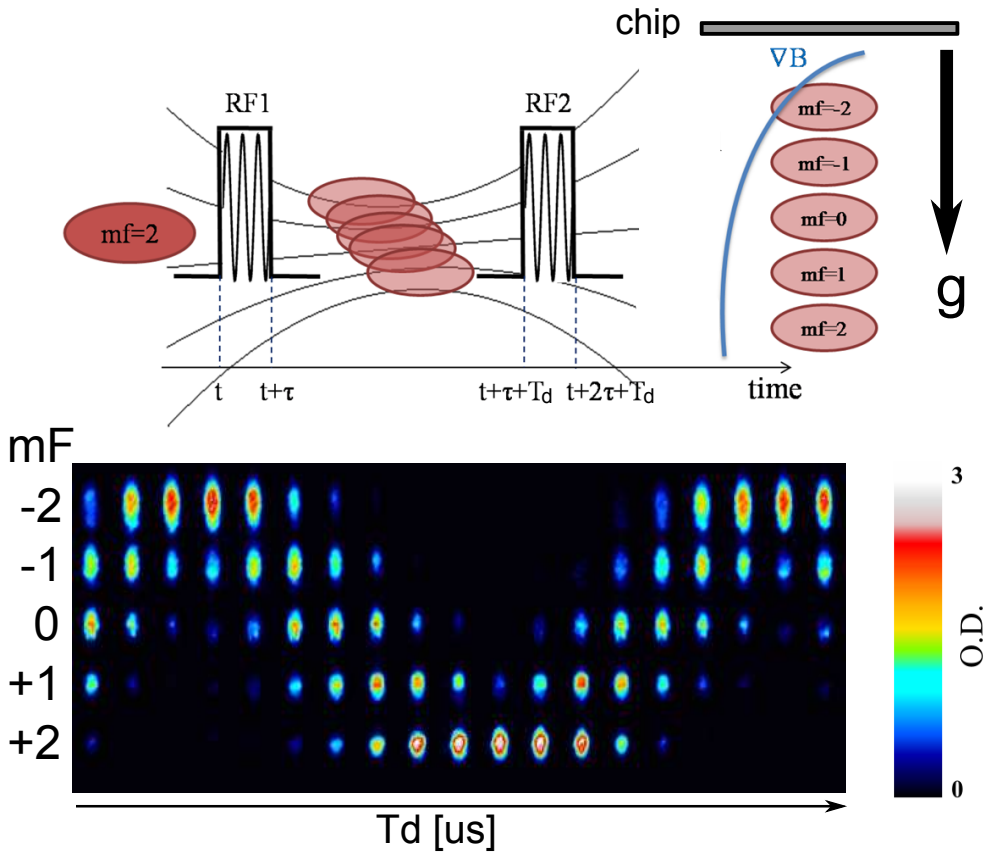


Figure 6.2: Upper panel: experimental sequence for the implementation of the RF multi-state atomic interferometer. Lower panel: raw absorption images of the interferometer output for different time delays $T_d$ between the two Rabi pulses. The pulse'area is set to $\Omega\,\tau = 3.3\pi$ . Black corresponds to the lowest atom density, white to the highest one. The $m_F = +2$ state corresponds to the bottom row of atom clouds, the $m_F = -2$ state to the top row.

with the uncertainty of the detection. In our case, the reduction of the signal-to-noise ratio due to the splitting of the same amount of atoms on a higher number of states (evaluated in $\sqrt{5}/\sqrt{2} \sim 1.58$), is bigger than the improvement in the slope of the fringes $\sim 1.26$, and thus the sensitivity results of smaller entity. Our interferometer is however a proof of principle for the employed technique, and moreover it remains competitive for all applications that primarily require fringe narrowing.

In fig6.3 the characteristic output signals of the interferometer are reported for different values of Rabi frequencies; they are derived from raw absorption images like the ones shown in fig.6.2. The atom number in each state is divided by the total atom number, in order to be independent from the measurement-to-measurement fluctuations of the number of condensed atoms. The measurements have been repeated at least three times at each point, showing a statistical error on the population ratio measurement of the order of 5%.
Due to the number of involved states which is higher than three, the theoretical model predicts a quasi-periodic "Rabi flopping". Indeed, differently from the classic 2-state system, the determination of the pulse area which corresponds the maximal sensitivity for the interferometer is not trivial. On the other hand, performing simulation based on the equations 3.5, 3.6, we have seen that the quasi-periodicity is responsible for very similar sensitivities in spite of very different $(\Omega\tau)$ products. This consideration led us perform a complete scan of the available $(\Omega\tau)$ product $(< 4.5)$, while looking for the interferometer output with the sharpest fringes (fig.6.3 shows some of these measurements). The dependence of the interferometer signal on the degree of population scattering in the available manifold can be understood from a comparison of fig.6.4.a and fig.6.3 . Fig.6.4.a shows the measured and calculated population transfer between all five Zeeman states obtained by applying a single Rabi pulse; from this graph we have calibrated the coupling strength $(\Omega\tau)$ in terms of population transfer. From the figures we deduce that well defined narrow interferometric fringes (with enhanced sensitivity) are related to pulses that populate most of the Zeeman states. This result is in agreement with the qualitative idea, deduced from equation 3.5, that the output signal gets steeper when it contains high harmonics of the fundamental frequency $\omega_L$, which add contributes with fast temporal dynamics. The best result is obtained for a Rabi pulse of area $\Omega\ \tau = 3.3\pi$ (central graph in fig.6.3), which corresponds to a fringe slope evaluated in $(0.63 \pm 0.09)[rad]^{-1}$, thus larger than the $0.5\,[rad]^{-1}$ slope of an ideal 2-state interferometer.

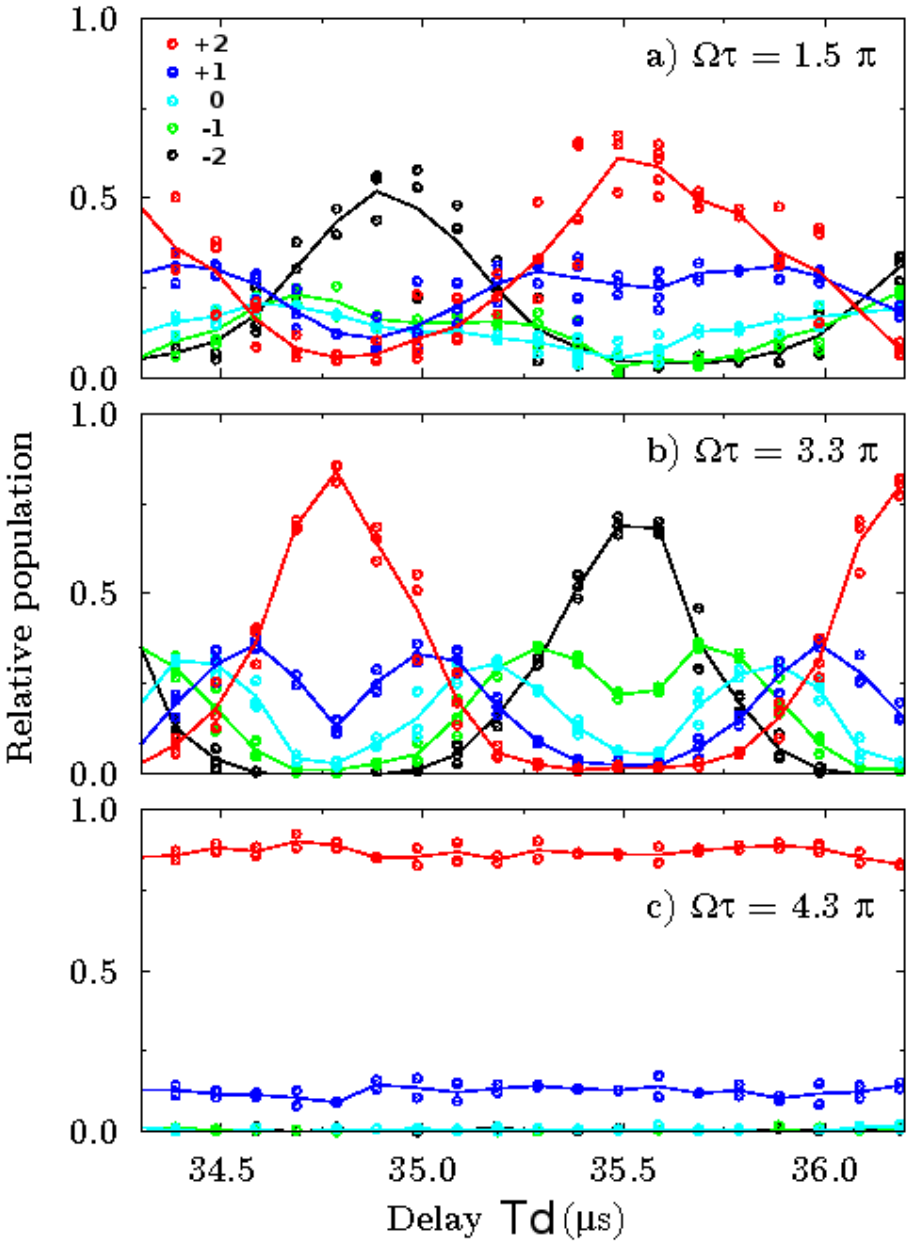


Figure 6.3: State populations at the output of the interferometer obtained from the absorption images by integration and normalization to the number of atoms in all states. The results are shown for RF-pulse areas of a) $1.5\pi$, b) $3.3\pi$, c) $4.3\pi$.
The best result (fringe narrowing) is obtained for a couple of Rabi pulses of area $\Omega\tau = 3.3\pi$. In this case the output distribution corresponding to the application of a single pulse fills all the states of the manifold (see fig6.4).

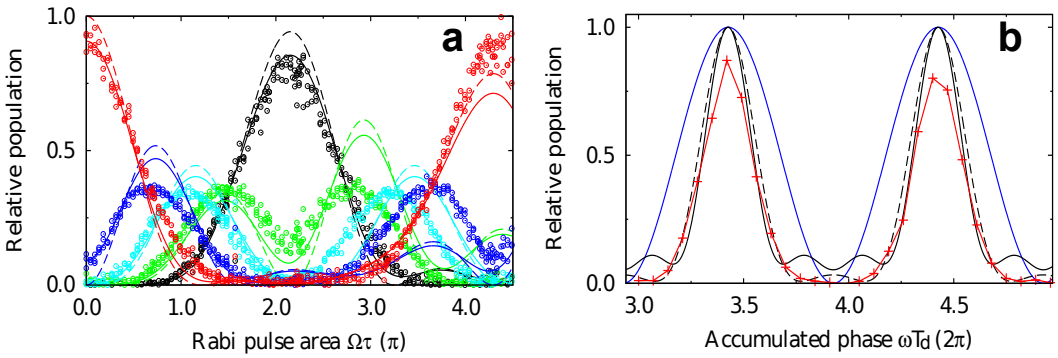


Figure 6.4: **a** - Rabi pulse population transfer between $m_F = 2$ (red), $m_F = 1$ (dark blue), $m_F = 0$ (light blue), $m_F = -1$ (green) and $m_F = -2$ (black) states as a function of the pulse area. Circles - experimental data, solid/dashed line - theoretical result for the experimental/ideal initial conditions.
**b** - Interferometric signals for the mF = 2 state. Red solid line is the best experimental signal obtained for $\Omega\,\tau = 3.3\pi$ . Black lines show theoretical results for the corresponding (solid, $\Omega\,\tau = 3.3\pi$) and optimal (dashed, $\Omega\,\tau = 3/\sqrt{5}\,\pi$) 5-state interferometer. For comparison, the optimal 2-state interferometer is also shown (blue). The realized 5-state interferometer has 1.75 times higher resolution than the ideal 2-state interferometer and approaches the resolution of the best 5-state one.

On the contrary, a Rabi pulse that populates only the highest or the lowest Zeeman states (with $\Omega\tau$ around 0, $2.1\,\pi$ or $4.2\,\pi$) yields interferometric fringes with low visibility that approaches zero in the case of the nearly complete population cycle. The attained almost zero visibility confirms that the whole procedure (RF coupling and Stern-Gerlach separation) does not alter incoherently the state populations by more than 15% and allows for a very good reproducibility of the state readout.

The performance of the interferometer in terms of resolution (slope of the fringe) and sensitivity is evaluated through a comparison with an ideal 2-state interferometer (fig.6.4.b). The measured signal shows higher resolution ($0.63\,[rad]^{-1}$) than the ideal 2-path interferometer ($0.5\,[rad]^{-1}$), and compares well with the theoretical result obtained for the same ($\Omega\,\tau$) product (simulations indicate that the optimal performance is $0.82\,[rad]^{-1}$). Indeed, with a visibility close to 1 it would surpass the theoretical

prediction of sensitivity for the ideal 2-path[2]. Since it has good but not perfect visibility, it does not gain in resolution as much as it looses in signal-to noise-ratio due to the addition of paths, and the resulting sensitivity remains lower than the ideal 2-path case.

A remarkable feature of our interferometer is that the enhancement of resolution is achieved without reduction in visibility. However, as anticipated, we have detected an exponential decay with the half-maximum time constant of $100\,\mu s$, mostly due to the additional phases accumulated during the motion of the condensates in the magnetic field [82]. Different Zeeman states experience indeed different potentials in the same magnetic field. The condensates created by the first Rabi pulse move hence towards their respective minimum of potentials, undergoing different accelerations which make them accumulate individual spatial phase modulations, eventually responsible for the wash out of the collective interference. Moreover, the differential motion undergone by the components reduces the initial total overlap until the complete separation of the envelopes, which corresponds to zero contrast. We notice, however, that for evolution times below 50 $\mu s$ no significant contribution to the phase evolution comes from the differential motion. Realizing the interferometer with a thermal cloud instead of the condensate we have proven indeed that the decay is not related to interparticle interaction [30], the decay showing shorter time scale in this new case. Details on the subject can be found in Herrera thesis [54] and in [96].

[2]as mentioned at the beginning of this section, the sensitivity is proportional to the ratio between resolution and signal-to-noise ratio, hence in this case we get: $0.82/0.5 \times \sqrt{2}/\sqrt{5} \sim 1.64 \times 1/1.58 > 1$

## 6.3 Detection of external fields

As stated at the beginning of the previous section, the interferometer can be used as sensor for external perturbations inducing different responses on the Zeeman manifold. If such a signal is applied during the delay time between the pulses, it contributes to the relative phases accumulated between the states causing a shift in the fringe positions at the output. Since the Zeeman components, for the first few hundreds of *microseconds*, are spatially overlapped, the interferometer can detect just state-sensitive perturbations, but on the other side, it is able to perform a really localized measure.
Here I report on two verifications of the capabilities of the interferometer as a sensor for optical field. In the first experiment we have illuminated the atomic sample with an out-of-resonance pulse of light during the waiting time between the two pulses. We have clearly detected the fringe shift induced by the AC Stark shift. In the second experiment we have replaced the first RF pulse with an optical Raman pulse able to produce the same coupling within the Zeeman manifold. We have then verified the mapping of the relative phase between the two optical fields into the population distribution at the output of the interferometer.

### 6.3.1 AC Stark shift detection

In fig.6.5 (up-right corner) the experimental sequence is qualitatively explained. It is based on the simple procedure for the calibration of the interferometer. By illuminating the atomic sample with a non resonant light during the interrogation time, the atoms undergo a variation of their energy eigenvalue induced by the AC Stark shift without suffering incoherent scattering. For isotropic light, this effect is of the same entity for each sub-level orientation, thus it is not able to modify the evolution of the atomic coherences (which relies on the energy difference among the states) and its effect is not detected by the interferometer. If on the contrary the light has well defined polarization, the AC Stark shift is different for each component, its entity defined by the dipole matrix element correspondent to the specific addressed transition. E.g., for $\sigma_-$ polarization, as shown in the bottom part of fig.6.5 (left: conceptual scheme; right: experimental results), it turns out an induced energy displacement which is progressively enhanced going towards negative orientations, characterized by a constant increase for successive sub-levels. Between the maximally negative ori-

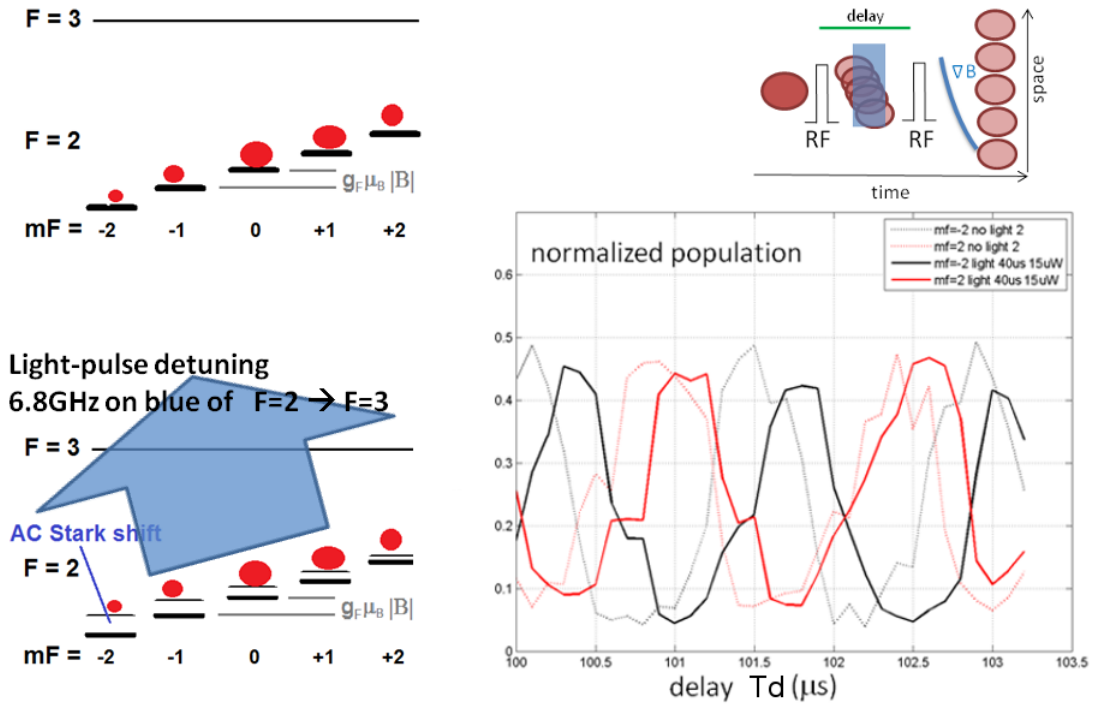


Figure 6.5: By means of a differential AC Stark shift, a $\sigma_-$ polarized far from resonance beam induces changes of the energy eigenvalues of the atomic orientation states which are progressively larger going towards negative orientations, characterized by a constant increase for successive sub-levels. This is equivalent to a change in the modulus of the magnetic bias field inducing the Zeeman splitting. The effect of the illumination is therefore detectable as a shift of the population distribution fringes. Left: schematic representation of the induced AC Stark shift; bottom-right, experimental results; top-right, experimental sequence.

ented state $|F = 2, m_F = -2\rangle$, and its opposite $|F = 2, m_F = +2\rangle$, the shift gets a difference by a factor[3] of 3.
In fig6.5 (down-right corner) the interferential fringes obtained in presence of the light pulse are superposed to those obtained in case of no illumination. The detection is referred to a $\sigma_-$ polarized pulse of intensity $I = 0.25\, W/cm^2$ and duration $\Delta t = 40\, \mu s$, whose frequency was set to a detuning of $\Delta = 6.835\, GHz$ to the blue (of the $D2$ line). In this case the theoretical AC Stark shift for the $|F = 2, m_F = -2\rangle$ attains a value of about $2\pi \times 45\, kHz$, which corresponds to a step between successive sub-levels of $\sim 2\pi \times 4\, kHz$. After integration over $\Delta t = 40\, \mu s$, the accumulated phase should hence differ from the trivial case by about one *radiant*, which is in agreement with the detected displacement.
The inter-pulse delay is set to a value as small as possible to ensure maximal visibility. Even if it is set to $100\, \mu s$ (larger than the usual $50\, \mu s$ due to the durations of the pulses and some extra waiting time[4]), the fringes are well resolved and the shift is evident. We have obtained the opposite effect in case of $\sigma_+$ polarization and in case of red detuned light.

### 6.3.2 Reading the phase of a two-photon Raman excitation

In this experiment the first of the two RF pulses used to demonstrate the atom interferometer is replaced by a light pulse capable of coupling the states of the Zeeman manifold in a similar way. This procedure is made possible by means of a velocity insensitive (no-momentum transferring) two-photon Raman transition, realized by sending on the cloud two copropagating pulses differing both in frequency and in polarization.
A variation of the relative phase between the two components of the radiation pulse has no effect on the resulting distribution of populations, but inprints a different initial phase to the coherences. The additional phases ($\Delta\phi_i$, $i = 1...M$) are equivalent

[3] A calculation of the overall AC Stark shift for each sub-level, obtained by adding the effect induced by all the addressable excited states, gives a relative strength $|\Omega|^2/\Delta \propto \frac{1}{12}(6; 5; 4; 3; 2)$, where $\Omega$ represents the resonant Rabi frequency, $\Delta$ the detuning from resonance, and inside the brackets we span from $m_F = -2$ to $m_F = +2$.

[4] total time $\sim 100\, \mu s \sim (36 + 12 + 40 + 12) \mu s$ (the total time indicates the delay between the trigger of the two $RF$ pulses):
$RF$ pulses duration $\sim 36\, \mu s$; light pulse duration $\sim 40\, \mu s$; waiting time $\sim 12\ \mu s$ each

to the result of a temporal evolution ($\Delta\phi_{i+1} - \Delta\phi_i = \Delta\phi$), and thus the variation of the relative phase is equivalent to a change in the timing of the illumination. A fringe-like modulation in the final distribution of populations is hence predicted in dependence of the phase, similarly to what has been detected for varying delay time in the case of two RF pulses.

To determine the phase imposed to the sample by means of the Raman pulse in the modified procedure for the interferometer, in each realization of the experiment the beat note signal obtained by detecting the Raman pulse light outgoing the cell is recorded. The phase read by demodulating this signal is indeed almost univocally associated to the phase seen by the atoms: this is because the kilometric differential wavelength related to a couple of beams separated in frequency by just $400\,kHz$, is much longer that the few tens of centimeters separating the detector from the cell, thus making fluctuations usually responsible for phase spikes or drift completely negligible (see fig.6.8).

The relative phase of the two fields composing the Raman pulse is left free to evolve, so that due to of mechanical, thermal, and electronic fluctuations and drifts, it spans randomly much more than a whole $2\pi$ interval. By just adding the results of the interferometer for a sufficiently high number of repetitions it is hence possible to get a complete statistics concerning the dependence of the population distribution on the relative phase.
The graphs of fig.6.6 are obtained after a binning operation guided by the detected phases: the $2\pi$ range has been divided in a convenient number of segments (in such a way to have more than three measurements for each segment), and the population distributions related to the same segment have been added to determine a mean distribution associated to the specific phase value.
It is evident from the graphs that the output of the interferometer is able to indicate the relative phase of the two fields which have crossed the sample. The main feature of the interferometer, that is the narrowing of the interferometric fringes, is still present. The three graphs are referred to different time delays between the Raman and the RF pulses. Exploiting this degree of freedom it is possible to move the maximal slope of the fringe from a phase region to another one, as expected from the results obtained with the simple RF interferometer (fig6.3). The visibility results to be reduced with

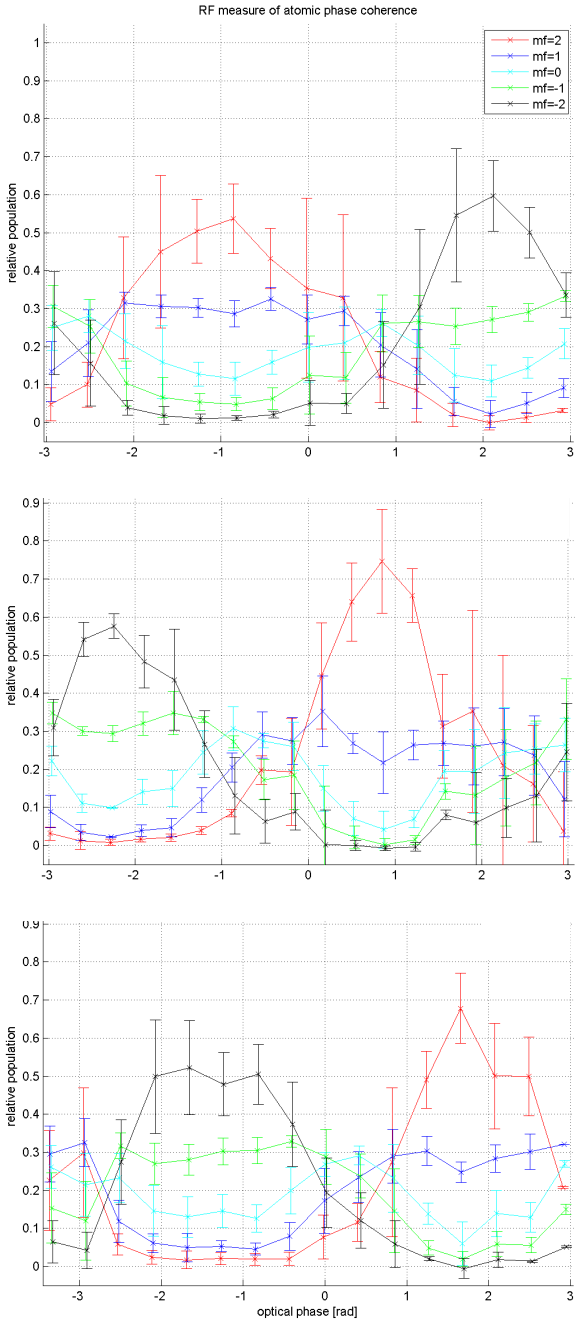


Figure 6.6: Results of the experimental procedure for different delay time between the Raman and the RF pulses. A displacement of the fringes is evident; it corresponds to the periodicity of the Zeeman coherence. By changing the delay between the two pulses it is possible to exploit the maximal resolution on the phase region of interest.

respect to that case, probably due to some residual incoherent scattering induced by the light. The maximal slope is determined as $\sim 0.5\,[rad]^{-1}$, equal to the ideal case for a two-path interferometer. However the fringes seem to undergo a more complex dynamics respect to a simple shift, including a sort of quality factor modulation for the peaks. This is evident comparing the first and the second graphs of fig6.6. However further verifications have to be performed to check the presence of a more complex behavior of the system, together with the implementation of simulations based on equations 3.6, 3.5.

**Stability of measurement**

In fig6.7 are reported temporal series obtained with a Stern-Gerlach analysis performed at different stage of the interferometer procedure. On the left-up corner, a series of results for the initial state is presented. We can say that the stability of the critical stage represented by the release from the trap is good enough, since the initial state shows fluctuation in population distribution of the order of $\pm 5\%$ about the mean distribution with 85% of the atoms in state $|F = 2, m_F = +2\rangle$. Similar statistic is reported for the state realized after a single pulse, both of RF and Raman light (upper and lower corner on the right of fig6.7, respectively). Also in this case it is evident that fluctuations are limited to 5% of the total number of atoms. Due to the constant presence in the initial state of a non-null component in state $|F = 2, m_F = +1\rangle$, we have tested the presence of coherence between these two population components before addressing the manifold with coherent fields. To obtain such a verification, we have performed the experimental procedure as for the detection of the phase of a Raman pulse (inset of fig6.8), but without the application of the second pulse (RF pulse). The result is reported in fig6.7 (bottom-left corner). The measurement does not show any phase dependence, and thus we deduce that the mechanism displacing a part of the sample from state $|F = 2, m_F = +2\rangle$ to state $|F = 2, m_F = +1\rangle$ during the release from the trap is incoherent (in case of condensates, it means that the coherence presents each time a random phase).

**Experimental implementation**

The Raman pulse able to replace the $RF$ is formed by two spectral components separated in frequency as the Zeeman shift for adjacent sub-levels, and whose polar-

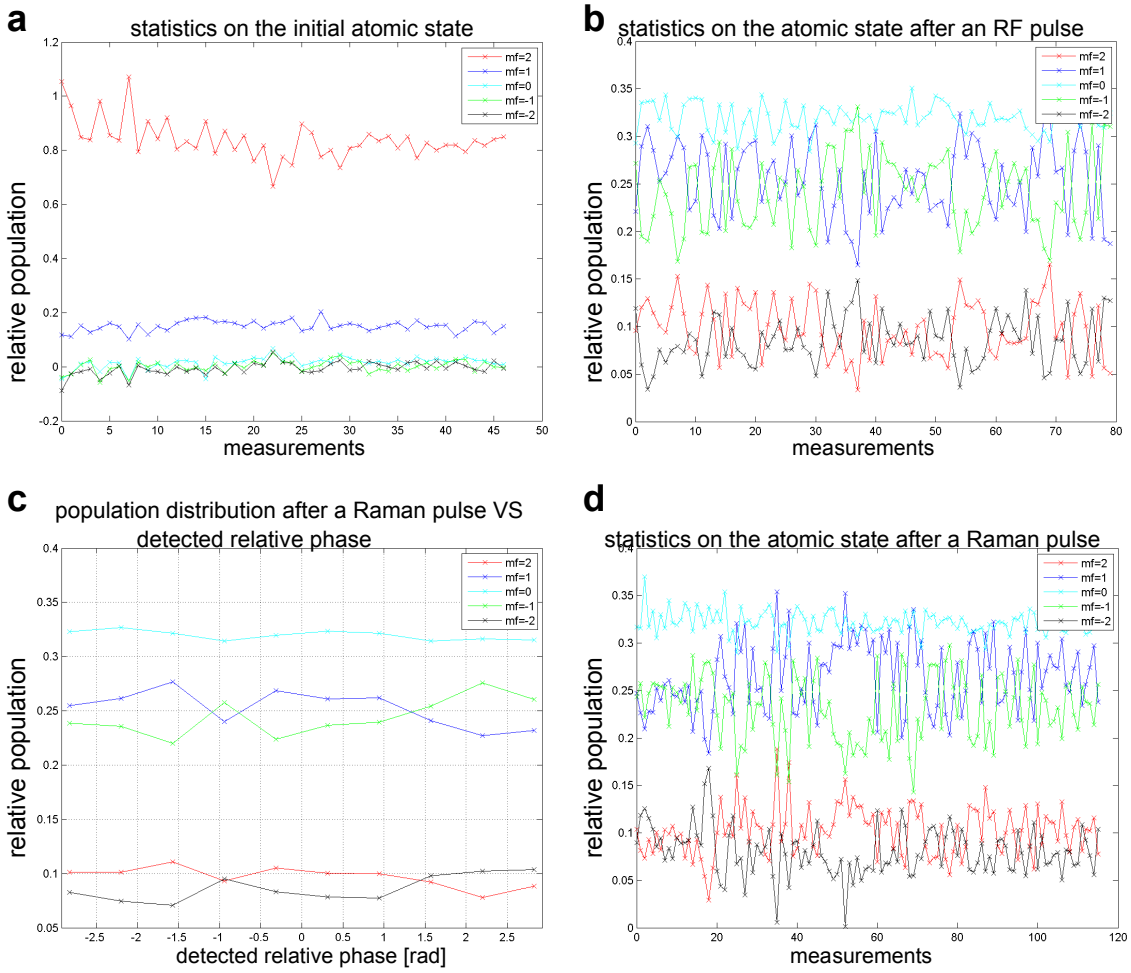


Figure 6.7: (**a**,**b**,**d**) - Temporal series of the Stern-Gerlach analysis performed at different stages of the interferometer procedure. Every stage of the experimental procedure gives a population distribution defined with an uncertainty of $\sim 5\%$.
**c** - Due to the constant presence in the initial state of a component in state $|F = 2, m_F = +1\rangle$, we have tested the presence of coherence between the two population components by performing the binning operation on Stern-Gerlach analysis realized after the application of just the Raman light pulse. The result is reported in the bottom-left panel. The measured population distribution does not show any dependency on the phase of the Raman pulses.

izations are set respectively to $\sigma$ and $\pi$ (see fig7.1.b). The set-up to perform such transition is represented in fig6.8.
The polarization of an electromagnetic field is determined with respect to the direction of magnetization of the atomic sample: $\pi$ polarization corresponds to a field showing electric field vector linearly polarized along this axis, which requires wave propagation on the orthogonal plane. On the other hand, a $\sigma$ polarization is defined, in terms of electric field, as a vector of constant amplitude rotating on the orthogonal plane, so that a field can be $\sigma$ polarized only if propagating along the magnetization axis. Actually $\sigma$ polarization can be obtained even for propagation on the orthogonal plane, provided the electric field is linearly polarized along the third direction. In this way indeed the field does not match any vector of the proper base for the oriented sample, but it is seen by the atoms as the sum of two fields with the same amplitude and opposite $\sigma$ polarizations. The only inconvenient of this configuration is that one looses half of the available field power, which goes on the polarization mode not involved in the two-photon transition.
Exploiting this possibility, the two fields required for the transition can be provided by means of collinear beams with orthogonal linear polarizations. Due to the equi-spaced differential AC Stark shift between successive sub-levels, this configuration of fields is actually equally resonant with all the successive couples of adjacent Zeeman sub-levels, thus perfectly replicating the effect of a pulse of radiofrequency. Copropagating beams limit indeed the momentum transferred to the atoms to the negligible amount induced by the difference in frequency between them, i.e., $p = \hbar(k_1 - k_2) = \hbar\frac{\Delta\omega}{c} \sim 10^{-36}\, kg\frac{m}{s}$, and so the conservation of the total energy and total momentum are always fulfilled in the same way, whatever is the number of transitions occurred.
The choice of the polarization for the two fields is here almost arbitrary since the coupled states belong to the same hyperfine level[5]. On the contrary, when coupling the two hyperfine ground levels, a suitable choice can significantly reduce the residual incoherent scattering due to the presence of other states. This aspect will be carefully analyzed in section 8.1 .
The resulting configuration is based hence on beams propagating in a direction orthogonal to the magnetization axis, so that it does not match the set-up for *EIT*

[5]This statement has been verified by comparing the results obtained for pulses with exchanged polarizations

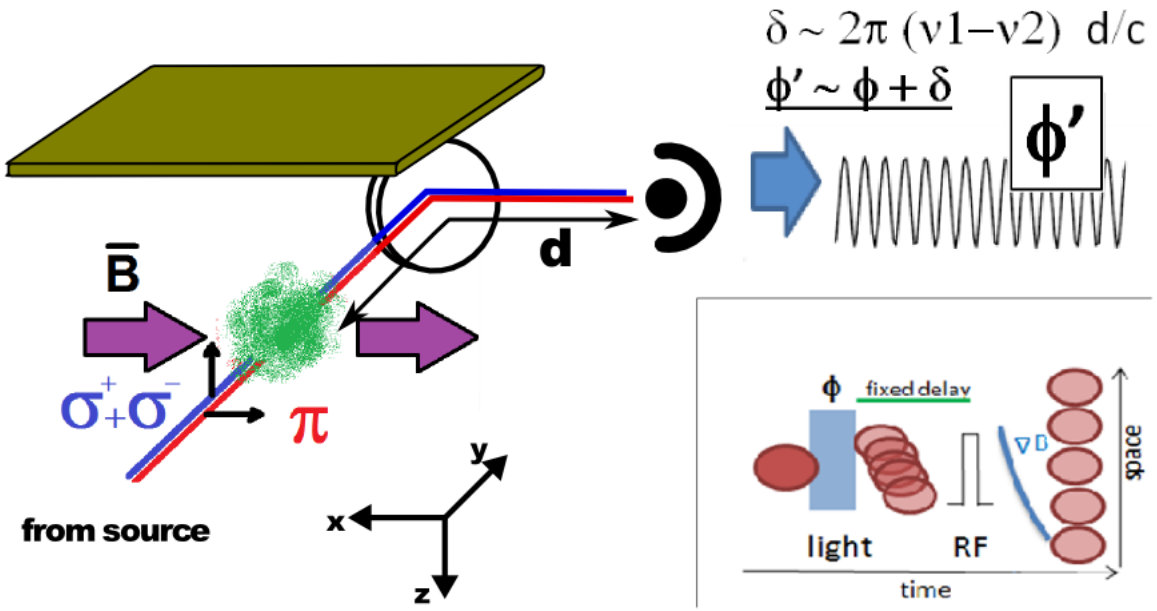


Figure 6.8: Experimental realization of the detection of the phase of a two-photon Raman excitation by means of an atomic interferometry technique. The sample is released from the trap and left in free falling regime. The magnetization axis is turned by $\pi/2$ on the horizontal plane (from $y$ to $x$ direction) in order to match the two incoming linear polarizations with $\sigma + \sigma$ and $\pi$ polarizations. Due to the small distance traveled by light after the cell, the beat note phase recorded by the photodiode is always well related to the one seen by the atoms. To determine the phase applied to the sample by means of the Raman pulse, for each realization we recorded both the beat note signal and the output state of the Stern-Gerlach analysis. A binning operation guided by the detected phases allows then averaging of the results obtained for similar applied phases, in order to reveal any possible correlation between the phase of the Raman excitation and the output of the interferometer. In the inset a sketch of the experimental sequence is reported.

measurement[6]. To take advantage also in this case of the apparatus constructed for experiments on coherent storage, we have managed to turn the magnetization axis of the sample by postponing the whole sequence for interferometry after the release of the trap (keeping all the operations within the first *millisecond* of expansion, when the condensate have not yet inverted the aspect ratio and we are sure that it neither exceeds the beam size nor evades it[7]). With the switching off we get indeed almost automatically a rotation of $\pi/2$ of the orientation of the sample on the horizontal plane, the terrestrial field pointing almost in such direction[8]. The bias field responsible for the loss of degeneracy among the states of the orientation manifold is thus in this case a component (the one along the $x$ direction) of the spurious field present in the room (mostly due to the magnetic dipole of the earth); its amplitude is carefully detected by means of $RF$ spectroscopy and evaluated in $410\,kHz$ of Zeeman shift, corresponding to a magnetic field of $B_s \sim 0.58\,G$.

The calibration of the Raman pulses is provided in the same way as for the RF pulses, that is by performing Stern-Gerlach analysis after a single pulse. In this way we can carefully determine the population distribution that a particular set of parameter (amplitude-duration) is able to induce. We have checked the possibility of having a complete revolution of the distribution, finally reproducing the initial state. We find that a Raman pulse of duration $\Delta t = 20\,\mu s$ and power $[45\,\mu W\,(\pi) + 85\,\mu W\,(\sigma)]$ provides the same coupling as the RF pulse maximizing the performances of the interferometer. Considering the waist of the beam ($w_0 \sim 50\,\mu m$), these intensities provide aneffective Rabi frequency of $\sim 2\pi \times 180 kHz$ (fields intensities: $600\,mW/cm^2\,(\pi) + 1.1\,W/cm^2\,(\sigma)$). A theoretical calculation based on the

[6]in that case in fact propagation along the magnetization axis is required in order to ensure pure opposite $\sigma$ polarization for the two involved fields

[7]condensate dimensions in trap are estimated respectively in $(2\,\mu m \times 2\,\mu m \times 35\,\mu m)$. The elongated dimension almost does not change size for the whole extent of expansion times we can detects (up to $12\,\mu s$); so, before the inversion of the aspect ratio, we can ensure the cloud extent does not exceed $35\,\mu m$ in any direction. Moreover, the gravitation induced displacement relative to a free falling time of $1\,\mu s$ is contained within $10\,\mu m$. Exploiting a beam that shows on the atoms a minimal waist of $\sim 100\,\mu m$ we are thus sure that the interaction is of the same entity as for tapped samples

[8]actually there is also a small component on the vertical direction, which brings the new axis out from the horizontal plane. This component is canceled by a bias magnetic field in order to simplify the determination of the axis defining the $\pi$ polarization (= horizontal)

tabulated Clebsch-Gordan coefficients shows that the transitions ($m_F = 0 \rightarrow |mF| = 1$) are slightly better coupled by the Raman fields with respect to the transitions ($|m_F| = 2 \rightarrow |m_F| = 1$), with a proportion between the respective effective Rabi frequencies (defined following 1.98) $\sim \sqrt{3}/\sqrt{2}$, but we have not detected any effect induced by this asymmetry.

# Part IV

# Set-up for optical interrogation of ultracold samples on chip

In this section we resume all the details on the apparatus constructed for the realization of the $EIT$ spectroscopy and, in the near future, of memory experiments. I recall that the same apparatus has provided the optical beams for the experiment on the atomic interferometer reported in sections 7.3.1 and 7.3.2 .

First I present and motivate the solution adopted in the design phase of the apparatus for the realization of memory experiments with the available cold cloud.
In a second chapter I show the characterization of technical aspects of the apparatus that directly limits the time range for coherent interaction even in case of a perfectly coherent source: we have evaluated the phase fluctuations induced by both electronic and mechanical switching of the fields.
We have then checked the adaptability of the apparatus by reproducing some experiments taken from literature: Rabi flopping in a pulsed monochromatic lattice [94] and exact Rabi flopping for a closed two-level system [64],[107]. In the last chapter I report some details on the chip-based set-up for the realization of magnetically trapped ultracold Rubidium cloud, and on the procedure elaborated to obtain the condensate. It is then shown how the Stern-Gerlach analysis can be performed. Finally I report the modification to the experimental procedure which allows the realization of a suitable ultracold cloud for the memory experiments.

# Chapter 7

# Design of the apparatus

To perform $EIT$-based memory experiments with a trapped atomic cloud one has to exploit a two-photon transition able to couple two trapped levels. Moreover, in order to get a long lived coherence, the two levels have to feel the same potential (at least within some order of approximation). A spatial asynchronous evolution of the phase related to the coherence ends up indeed in a destruction of the collective response. With magnetic traps this is quite a stringent constrain, the exploited potential being internal state seeking. In the case of $^{87}Rb$ atoms, levels $|F = 2, m_F = +1\rangle$ and $|F = 1, m_F = -1\rangle$ fulfill these requirements: they are connected by a two-photon transition of opposite $\sigma$-polarized fields (see fig.7.1.d), and have equal first order Zeeman dependence.
The first requirement for the apparatus we had to build was thus the ability to produce two beams of light, both resonant with the same $^{87}Rb$ dipole transition, but from the two different hyperfine ground states (separated by $\Delta_{hyp} = 6.835\,GHz$). In addition the designed set-up had to respect two additional constraints:

- it had to fit the set-up for the production of the degenerate sample already settled and in full activity;
- it had to be exploitable in other context, e.g., to provide optical potential (such as $1D$ lattices, dipole traps).

For the $\Lambda$ scheme exploited in the preliminary studies reported in the chapter 6 (corresponding to fig7.1.c), the requirements on the light beams are the same, so that we could test the apparatus and check if it fulfills the designed targets. Once developed

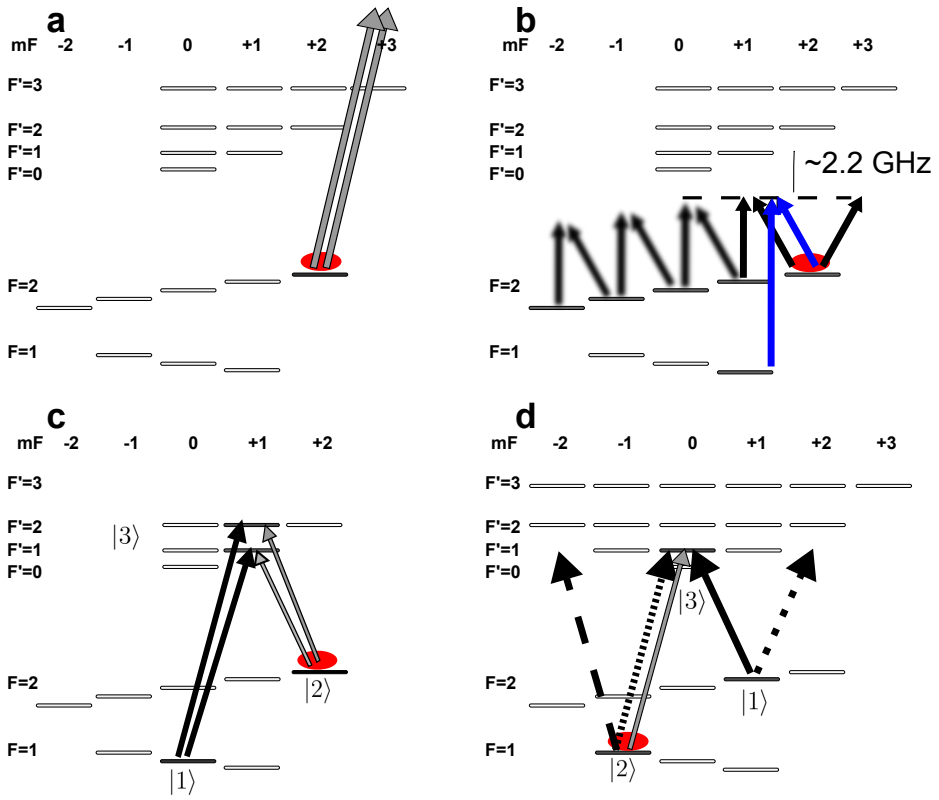


Figure 7.1: Different configurations of eletromagnetic fields used in experiment described in this thesis.**a** - out of resonance fields with equal $\sigma$ polarizations, used for momochormatic lattice and momentum state Rabi flopping (section 8.2);
**b** - out of resonance fields with $\sigma$ and $\pi$ polarizations, (black arrows) used for the coupling of the whole manifold of the $F = 2$ hyperfine state (section 6.3.2), and (blue arrows) used for hyperfine Rabi flopping (section 8.2);
**c** - *EIT* $\Lambda$ scheme exploited in the spectroscopic analisys reported in chapter 5. Control and signal fields are represented respectively by a black and a gray arrows.
**d** - optimal *EIT* scheme for the implementation of memory experiments. Color code is like in (c). Leakage components of the control field are also reported. Dotted arrow is due to the non perfectly defined polarization of the control field; dashed arrow represents the leakage of carrier surviving the filtering action of the cavity; fine dotted arrow is determined by the small portion of the previous leakage showing same polarization as the signal field. The other fields are not resonant with any atomic transition by choosing $|F' = 1\rangle$ as excited state of the $\Lambda$ scheme, while to make harmless the latter one a direct frequency shift is needed.

the technique for the production of a valid trapped cloud in state $|F = 1, m_F = -1\rangle$, the set-up should be immediately applicable for memory experiments.

In the strategic choices related to the design of the apparatus we were driven by the experience in Paris. So, for the production of the two beams which would cover the roles of control and signal fields we followed the idea to obtain them from a single laser source. In this way indeed the two fields do not show relative phase noise by default, and we have not to spend any effort on complicated phase locking systems at the prohibitive $\mu$wave frequency $\Delta_{hyp} = 6.835\,GHz$. Moreover this choice let us avoid the use of an additional laser source.
Due to the long term goal of quantum fluctuations measurement, the detection of the weak signal pulse requires a set-up like that in Paris: heterodyne detection provided with a local oscillator at a frequency close to that of the signal. The heterodyne scheme is actually the simplest way to detect a small intensity field, even in classical terms, by means of the "amplification" effect induced by the local oscillator (see section 2.1.2). So, in addition to the signal and the control field, the apparatus have to provide a third field, with frequency few *megaherts* far from the first one.
Another aspect which has reveled its importance in the experiments in Paris is the careful control of any light leakage. The question can affect either the coherence lifetime (as shown in section 5.1.1, equation 4.2), if resonant light address the sample during the storage time) or the detection stage (as shown in section 5.1, fig.4.4, if a part of the control field enters the path of the homodyne detection). We have chosen to obtain the three beams of interest (signal, control, local oscillator) from three branches separated at the beginning of the optical circuit. This choice opens a question related to long lived quantum memories. If the beams are not copropagating indeed, there is no possibility to control the relative phase drift during the experiments, each beam following a complete independent phase dynamics. The holding of the relative phases was instead an unavoidable aspect in the experiment in Paris ([21]) focused on the statistical evaluation of the quantum properties of both the original and the regenerated signal pulse. For this issue however we have elaborated a possible solution which is illustrated in section 8.1.3 .

## 7.1 Fitting the apparatus for condensation

The first technical question to solve in order to exploit the ultracold cloud for memory experiments has been how to illuminate the sample with light propagating along the longitudinal direction of its cigar shape (the $y$ axis in the Cartesian reference considered throughout the whole text). This is indeed necessity due to the coincidence between this direction and the magnetization axis. As it is shown in fig7.2.a, the axis is occupied by one of the MOT beams, so that a small angular shift is unavoidable. The apparatus presented already a free optical path constructed in order to minimize the angle with respect to the $y$ axis, and devoted to the imaging set-up (yellow beam in fig7.2). Rather than adding a new set-up for the interrogation beams, we have decided to exploit this path of the imaging system, at least in the part closer to the cell, entering and leaving it by means of two mirrors mounted on flippers. In the part preceding the cell, the imaging beam and the interrogation beams are characterized by completely different transverse profiles. While the imaging needs for an almost plane wave front, obtained in our case with a collimated beam of transversal diameter around $\sim 5\,mm$, the interrogation beams for memory experiments has to be as small as few tens of $micrometers$, a condition obtainable just by focusing the light on the plane of the sample. The problem has been solved adding a telescope on the path of the imaging beam, in such a way that it is still collimated after the second lens and further on toward the sample. The telescope is arranged so that just the second lens is on the path of the interrogation beams, therefore these beams approach the sample while focusing (see fig7.2.b).
No additional optical elements are needed instead in the part of the optical path leaving the cell. Here indeed both the interrogation beam and the "shadow" of the sample have to be collimated in order to properly continue their respective paths.

The choice of exploiting the same path occupied by an imaging set-up has proved to be really useful. Indeed, on the one hand, this imaging allowed us to look at the cloud as it is seen by the interrogation beams, providing for example the measurement reported in fig9.4. On the other hand, by directly imaging the light of the interrogation beams, it allowed us a direct evaluation of its spatial profile around the plane of the trapped sample. In this way we have obtained the measurements reported in fig5.1.b.

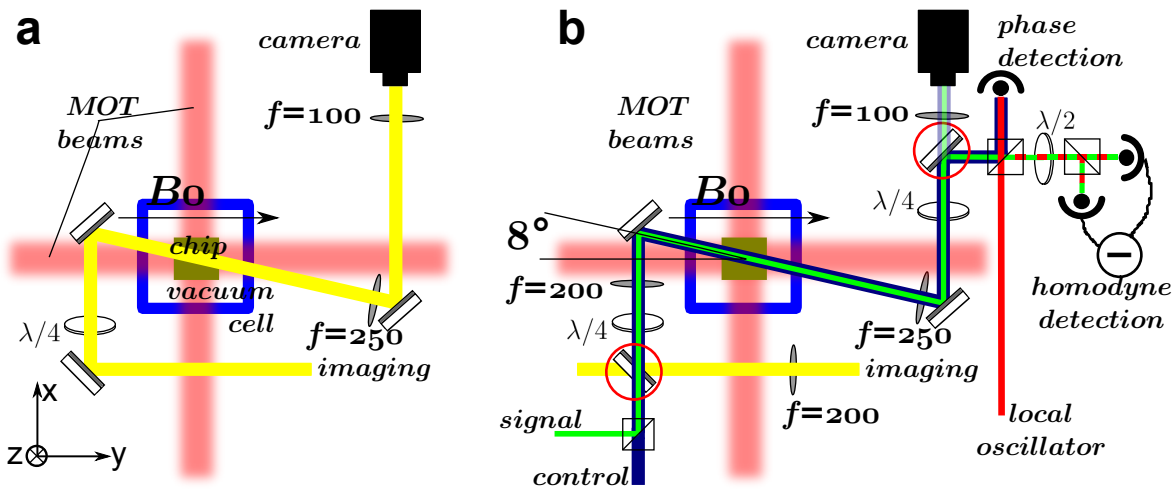


Figure 7.2: **a** - Imaging set-up settled along the $y$ axis; **b** - modification of the apparatus to exploit the same optical path for memory experiments. The red circles indicate optical elements mounted on flipper bases. To let the imaging beam keep the large collimated mode on the atoms, a lens is set on its path before the part shared with the interrogation beams. In this way the lens used to focus the interrogation beams acts on the imaging beam as the second lens of a telescope.

Moreover, the imaging has driven our work on the first stages of the difficult alignment of the signal beam for the *EIT* experiment on the thermal cloud, where both the laser beam and the sample are characterized by a transversal section $\sim 45\,\mu m$.

The lens focusing the interrogation beams on the sample has to be set at least $20\,cm$ far from the atoms, (see fig7.2). Its focal length (hence fixed to $20\,cm$) is however sufficient to reduce a collimated beam of waist $w_i \sim 1.1\,mm$ (which is the mode the beams exit the fiber collimators) down to a minimal waist of $w_0 \sim 55\,\mu m$. This transversal section is actually a good compromise for both illuminating in homogeneous way the condensate (as required for example in case of optical lattice or Raman transitions) and providing a good overlap with a thermal cloud. Moreover, the Rayleigh range for this configuration ($z_R \sim 1\,cm$) gives a confocal parameter of the order of the chip extent, allowing both for a limitation of the diffraction effects due to the presence of the metallic surface of the chip, and a longitudinal alignment almost insensible to positioning errors up to few *millimeters*. We have hence decided

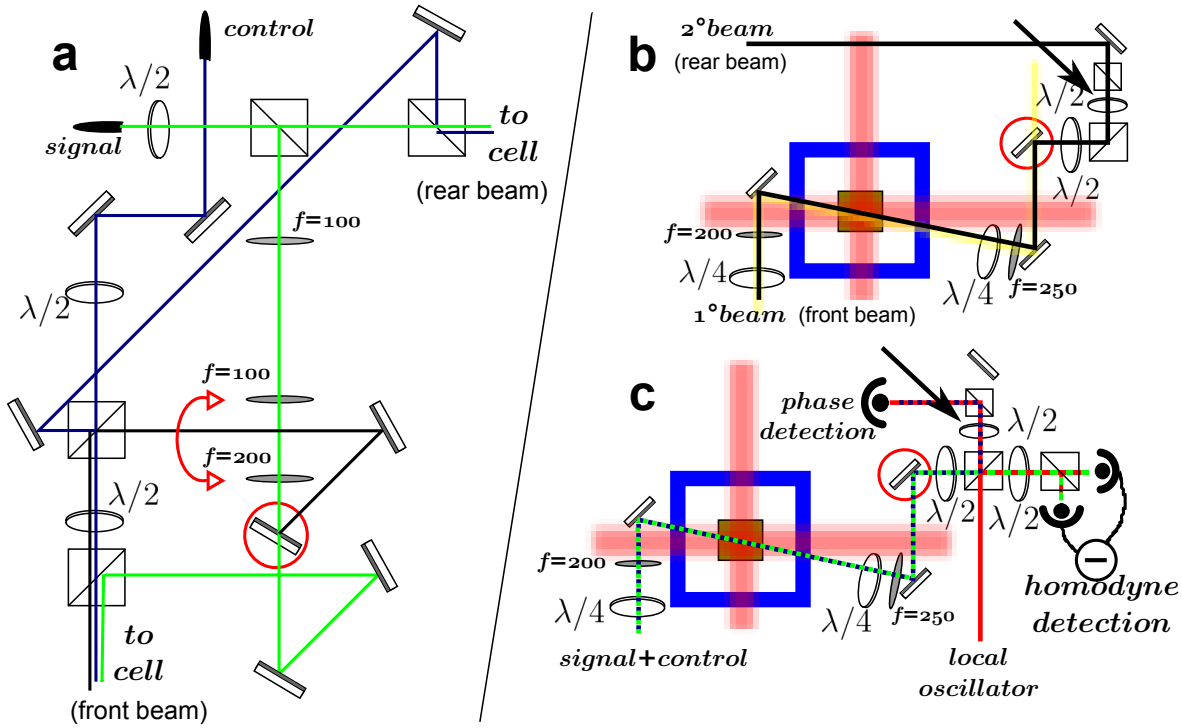


Figure 7.3: **a** - Optical circuit designed to give the possibility of overlapping the signal and the control fields in a wide range of configurations. They can separately and not exclusively enter the cell from the two directions of the $y$ axis. They can address the sample with equal or opposite polarizations. The signal field can either match the transverse profile of the control field or (but just in the front direction) show a waist larger by a factor 2 (smaller of a factor 2 on the sample). The red arrows indicate the alternative optical lenses to shape the signal beam into the two modes. The red circle indicates the mirror mounted on a flipper stage, which allows the signal beam to match the polarization of the control beam in the front direction (black line).
**b** - Optical circuit around the science cell set to perform periodical potentials.
**c** - Optical circuit around the science cell set to perform $EIT$ experiments.

not to modify the mode of the beam until the last lens in front of the cell, in order to minimize the deformations of the almost perfect Gaussian profile determined by the passage in a single mode optical fiber.

The new apparatus was requested for a good versatility, in the perspective of an utilization on a wide number of experiments besides the coherent storage of a pulse of light. For this reason, we designed an optical circuit in which the "control" and the "signal" fields can independently reach the cell from both the opposite directions along the magnetization axis. A superposition of the two fields presenting opposite as well as equal polarizations on the atoms is possible on both sides. Moreover, as needed for the memory experiment, on the front path it is possible to have the two fields with opposite polarizations and different waists (the signal has twice the diameter of the control beam ($w_s = 2 \times w_c = w_i = 1.1\,cm$), which corresponds a minimal waist with the opposite proportion $w_{0s} = w_{0c}/2 \sim 25\,\mu m$). The set-up is illustrated in fig7.3. As it can be understood from the sketch, the designed configuration of $PBS$ allows the mechanical blockade (thus perfect extinction) of each single component of each field without limiting the other paths.
Near the cell, on the "rear" face, the common optical path is organized in such a way that switching from the memory set-up to a lattice potential needs just for the rotation of a $\lambda/2$ plate (the one indicated by the arrow)[1].

[1] Actually, as it is explained in section 10.2 (which is devoted to the illustration of the preparation procedures for both the $BEC$ and the optimal thermal cloud for $EIT$), the atomic sample can be positioned at different distances from the chip for the two cases, so that, generally, in order to switch from one configuration to the other, a realignment of the interrogation beams is also required

## 7.2 Light beams generation

I have already mentioned the advantages of using a single source. However, in this case the challenge is to obtain the two frequencies from the same parent field. The separation is indeed too big for acousto-optic modulators ($AOM$), which are the simplest devices to both shift and switch laser beams. The only modulator able to reach the $\mu$waves band are resonant electro-optic modulators ($EOM$)[2]. In this case however the output beam contains the two symmetric sidebands at frequencies $+\Omega$ and $-\Omega$ with respect to the input beam frequency ($\omega$), where $\Omega$ is the modulation frequency of the $EOM$. Moreover the three spectral components fit the same spatial mode of the parent field. We have thus to provide a filter in frequency able to separate one sideband from the rest of the spectrum. This passage can be fulfilled by means of an optical Fabry-Perot resonator. For an appropriate finesse $f$ indeed, a stable lock is easily provided, while the rejection of the out-of-resonance frequencies is already high. The cavity we have exploited is characterized by a finesse $f \sim 150$, for which we measured a transmission far from the peak of about $t_{out} \sim 5 \times 10^{-4}$. The free spectral range of the cavity is $FSR \sim 5\,GHz$, which corresponds a $FWHM$ of the transmission profile $\Delta\nu_c \sim 35\,MHz$. It is much wider than the laser linewidth, which can hence be easily held on the center of the transmission peak. We have estimated (from the intensity fluctuations of the transmitted light[3]) a phase modulation induced by the cavity of the order of $\Delta\phi \sim \pi/2 \times 10^{-1}[rad]$. This modulation is however concentrated at low frequencies $\nu_n < 8 \times 10^3\,Hz$ (which is the first resonance of the piezoelectric transducer acting on the cavity length). In this range it is located also the unavoidable mechanical and thermal noise affecting the relative phase of two non-copropagating beams, and for which a correction procedure has to be provided in any case. The cavity can be locked to the frequency of the laser by means of the Pound-Drever-Hall (P-D-H) technique, exploiting the already present modulation at $\Delta_{hyp} = 6.835\,GHz$. This is actually a powerful tool since it is possible to center indifferently the transmission on the carrier or on one of the sidebands. The set-up

[2]These particular $EOM$ exploit a resonance of their crystal to get good efficiency even for frequencies at which the linear response is already dropped. The $EOM$ at our disposal is fabricated expressly to provide optimal modulation at the frequency of the $^{87}Rb$ hyperfine splitting ($\Delta_{hyp} \sim 6.8\,GHz$); the maximal efficiency is of the order of 6% for each sideband

[3]we have estimated the transmitted field phase fluctuations by evaluating the single pass dephasing $\Delta\phi$ fluctuations from the detected intensity fluctuations

composed by the $EOM$ and the cavity is thus able to provide a beam with frequency detuned with respect to the parent one by $(-6.835;\ 0;\ +6.835)\,GHz$, with an overall efficiency of $\sim 45\%$ in the case of the carrier and $\sim 3\%$ for the sidebands. In case of selection of one of the sidebands, the residual transmitted carrier has $\sim 10^{-2}$ the power of the sideband.
The beam obtained by isolating a sideband is exploited as control field. Indeed the field where we need more power is the local oscillator ($\sim 8\,mW$ to maximize the performance of the detectors), while for the control field $\sim 100\,\mu W$ are enough. A detailed report on the attainable powers for the three beams of interest can be found in the scheme in the upper part of fig7.4.
Some details on the cavity and on the P-D-H photodiode are reported in section 8.6.1.

## 7.3 Leakages

To get a long storage time an optimal switching of all the resonant optical beams is strictly necessary. This is however a well known problems in the field of cooled atomic samples, the limited available number of atoms being very sensible to the presence of even few resonant photons. In general the question is definitively solved by closing the laser source in a sort of black box, from which light escapes just within optical fibers. The fiber couplers inside the box are preceded by a mechanical shutter, which provide almost perfect extinction. We have adopted this solution, blinding in a black box our whole optical circuit for the production of the three beams of interest. The set-up is presented in fig7.4. Due to their massive nature, mechanical shutters can not reach conversion times shorter than $\sim 100\,\mu s$; moreover, the obtained temporal profile during the transition is not homogeneous on the transversal plane of the beam[4]. For this reason $AOM$ modulators are also exploited as fast (even if not perfect) switches: a diffracted beam can indeed be attenuated up to $10^{-4}$ in a time as short as $2 \times 1/\nu_{RF}$, where $\nu_{RF}$ stay for the modulation frequency of the $AOM$. The two devices used together provide optimal performances both in timing and in extinction, the normal procedure consisting in a temporal window of open shutter slightly larger than necessary, in which the real pulses are shaped by the $AOM$. We have followed this scheme throughout the whole thesis work.

To avoid as much as possible any leakage on the sample during the storage time, we have decided to produce the signal pulse in a different way with respect to the one elaborated by J.Cviklinski for the experiment in Paris. In that configuration indeed, it is almost impossible to avoid a carrier leakage, at least limited to the same time profile as the signal, yet very strong with respect to a signal of amplitude close to the detected shot noise power spectrum. Moreover it is almost at resonance with the same transition and characterized by undefined polarization. On the other hand, in our scheme we loose the simple way to realize the phase lock among the three beams, which is a fundamental issue in the protocol exploited in Paris [21, 92]. However, in the case of a hyperfine coherence based storage, this phase locking stage should take place at high frequency (almost $\Delta_{hyp}$), and hence the extreme degree of simplicity

[4]the shutters used in our apparatus, which are made of plastic material to reduce the inertial load, can switch a beam of waist $w \sim 1\,mm$ in a time of $t_c \sim 250\,\mu s$

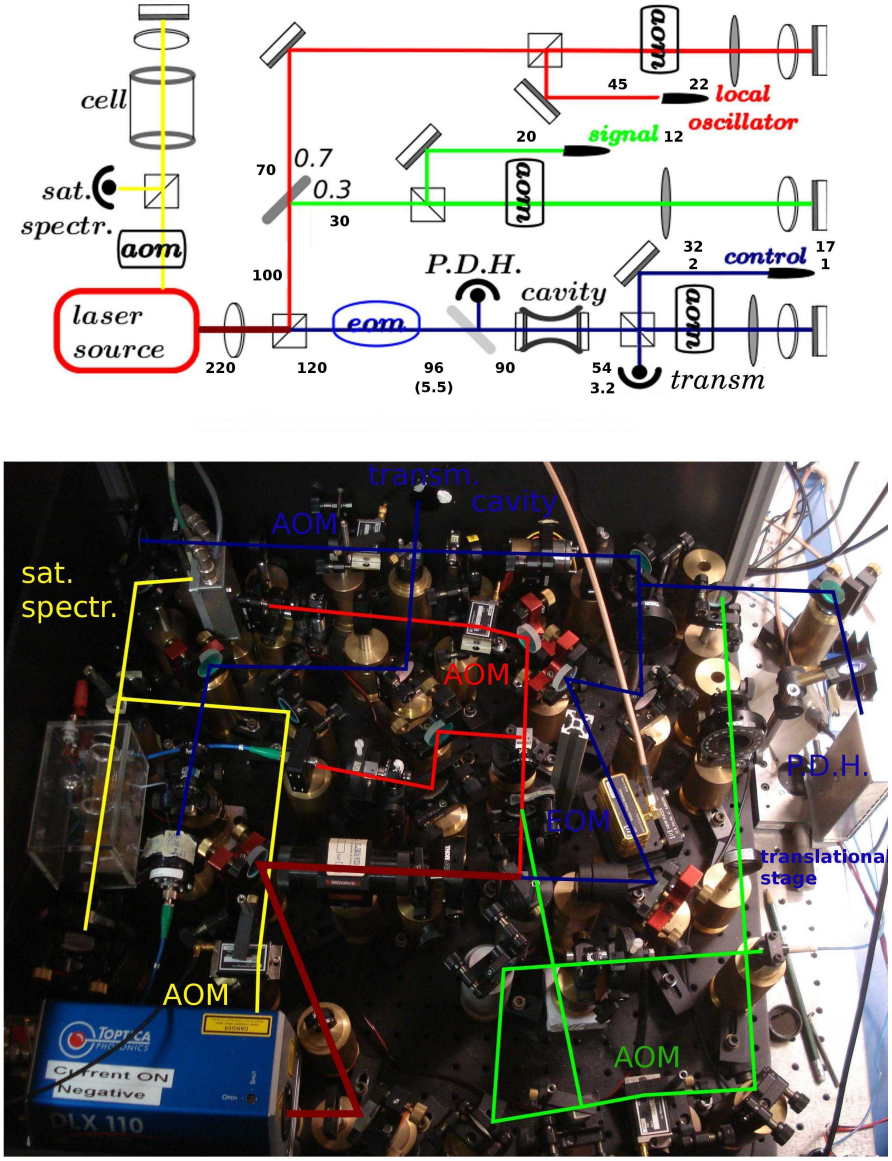


Figure 7.4: Apparatus for the production of the three fields of interest (control, signal, local oscillator). Schematic representation (upper part) and panoramic snapshot of the whole optical circuits (enclosed in the black box).
Specific colors mark the branches which end up in the different outputs (green-signal; blue-control; red-local oscillator). In the schematic representation, the typical power measured at various points of the system is reported (the two numbers in column are referred to the carrier and the sidebands). The laser provides also an auxiliary output which is exploited, by means of a saturated spectroscopy set-up (yellow line), to stabilize its frequency when set in the proximity of an atomic resonance.

present in the Paris scheme (where the two fields have the same frequency) is anyway lost[5].

As in principle the local oscillator does not need for temporal shaping, in the original project we planned to provide it by directly taking a part of the light as it exits the laser source (without involving any device up to the fiber). In this way we avoid any additional technical noise on the field.
In the other hand, to get a displacement as small as few *megahertz* as it is needed for the signal field, we have to perform a double passage on a succession of two $AOM$s set to diffract on opposite orders (scheme shown in fig7.5.b). We need to drive the two $AOM$s with two RF waves differing by half the frequency we want in the beat note with the local oscillator. To provide the two radiofrequencies, we have managed to exploit a double output $DDS$ device. As verified in section 8.2, the relative phase between the two output (which is the relevant quantity) results extremely stable. Hence, with this set-up, also the signal is almost protected from the addition of phase noise. By using the two $AOM$s on the zero order as it has been done in Paris, this set-up can also be used as switch for a squeezed vacuum beam[6] (whose storage is one of the long term possible goals of the experiment), as demonstrated in [57].
However, as mentioned in section 5.1, the reflection of the local oscillator on the homodyne detectors is sufficient to destroy the cloud in few *milliseconds*, and so we need to provide it at least with an $AOM$-type switch. Moreover the above set-up can not provide the procedure used for the spectroscopic analysis presented in chapter 5. Due to the fact that in the preliminary stages of the experiment we do not take into account quantum fluctuations, and we limit the detection to the classical amplitude of the field, there is no reason for this careful attention to the added classical noise. The apparatus has hence been modified and both beams (signal and local oscillator) undergo a cat's eye double pass scheme on a single $AOM$ (fig7.5.a). The $DDS$ is

[5]How to get a sort of phase locking among the fields (which is an unavoidable issue to perform statistical evaluations by repetition of the experiment), will be shown in the next section

[6]A squeezed vacuum field suffers drastically any loss, thus it is not possible to switch it on by diffracting it with an $AOM$, whose maximal efficiency do not surpass 85%. A simple passage through the acousto-optic crystal does not cause instead more than few percents of attenuation, and so one can use the diffraction as switching off mechanism. Again, due to limited efficiency, more than a single passage is needed to ensure a good extinction, thus determining the utility of the double $AOM$ set-up of fig7.5.b

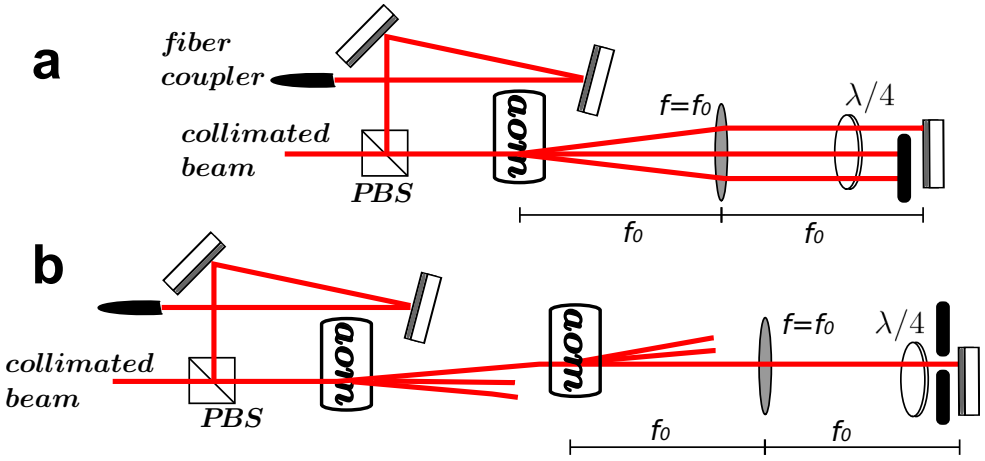


Figure 7.5: **a** - Usual cat's eye configuration. This double pass configuration make the output direction independent from the diffraction frequency, thus allowing frequency modulation without inducing amplitude modulation (in the limit of the frequency dependent efficiency of the $AOM$).
**b** - quadrupole pass configuration. It presents the same feature as the previous scheme, but in this case the induced frequency shift can be set close to zero by choosing opposite diffraction orders for the two $AOM$s (as qualitatively shown in the figure). This choice allows the elimination of the phase noise induced by the driving wave (at least at the first order) if the same wave generator is used for both $AOM$s.

still useful as it is able to provide the parallel frequency scan of the two RF needed for the $EIT$ spectroscopy (section 6.1).

To be used for quantum memories, that is, for characterizing the fluctuations of the stored coherent field pulse, the set-up will need some change. The simplest solution is to provide both beams (local oscillator and signal) of the scheme shown in fig7.5.b . This keeps also the possibility of performing the $EIT$ spectroscopy as presented in chapter 5.

To ensure an optimal extinction of the control field, after the passage through the cavity it undergoes a cat's eye double pass scheme on an $AOM$ like the other beams do. The driving RF wave of this third modulator is chosen in order to main-

tain definitively out of resonance the leakage of carrier present in the control field, which can potentially address the same transition as the signal field (with obvious detrimental consequences).
For usual control field power ($P_c \sim 3.5\,\mu W$)[7], the entity of this leakage amounts to $P_{c,leak} \sim 2\,nW$, which is a non-negligible value respect to the signal field (which attains $P_s \sim 1\,nW$ in the spectroscopy of chapter 5, and even few *picowatts* in case of weak coherent states for quantum memories testing). Its polarization is the same as that of the control field, that is the opposite $\sigma$ with respect to the signal field, but its intensity two order of magnitude greater than the latter one makes relevant the residual spurious component with a not well defined polarization. In the homodyne detection, if we set on the $AOM$ acting on the control field a frequency close to that for the other fields, it is possible to read the beat note related to the interference between the local oscillator and this leakage. After minimization of its amplitude by means of careful optimization of the wave-plates all along the optical path, we detect a beating which corresponds to a power of the order of $10\,pW$ (see fig5.4.left). The measured value is in agreement with the extinction rate expected for a polarizing beam-splitter from $CVI$ (vertical polarization transmission lower than 2 parts per thousand). However this does not mean that the atomic sample is illuminated by just such a low power of control carrier leakage with the polarization of the signal. The polarization of a field is indeed never perfectly determined, and moreover, in our case, the small angle ($\sim 8^o$) it is between the propagation axis of the light and the magnetization axis of the sample (imposed by construction constrains, see below), makes its definition even less marked[8]. To ensure a negligible detrimental effect of this leakage we can set the frequency of the $AOM$ diffracting the control field up to $20\,MHz$ far from the one set for the signal. In this way the leakage of carrier can not resonantly address any atomic transition (see fig7.1.d), and, moreover, the post-demodulation of the homodyne detection output can filter out its contribution (as explained in the last part of the section).
The mismatch of the two frequency shifts does not prevent from fulfilling the two-

[7] which corresponds to $\Omega^c \sim 0.52$ in the case of fig.5.6 and to $\Omega^c \sim 0.30$ in the case of fig.5.8

[8] To optimize the control and signal polarization we have exploited the imaging set-up which works on the same direction. We identify the configuration which correspond to $\sigma_+$ polarization as the one determining the maximal absorption of the imaging light in the case it is set resonant on the closed transition $|F = 2, m_F = +2\rangle \rightarrow |F' = 3, m_F = +3\rangle$

photon resonance condition: the frequency shift can indeed be "corrected" by changing the frequency of the $EOM$ modulation[9].

The other main issue concerning light leakages is related to the detection stage. Other experiments using cold atoms reported in literature solve the question by setting a small angle between the control and the signal fields. In this way the separation is automatically obtained on the optical path after the cell. This choice has however two consequences:

- the momentum transferred to the atoms by the two-photon transition is orders of magnitude greater than in the collinear case even for small angles $\theta$. The resulting coherence, therefore, shows a narrower spatial modulation with a wavelength that corresponds in the general case to[10]

$$\lambda_{coh} = \frac{2\pi}{|\Delta\vec{k}|} \sim 2\pi \,/\sqrt{(|\vec{k}_s| - |\vec{k}_c|\, cos(\theta))^2 \;+\; (|\vec{k}_c|\, sin(\theta))^2} \tag{7.1}$$

  For $\theta = 0$ (i.e., collinear case), it is much greater than the sample extent ($\lambda_{coh} = 2\pi c/\Delta_{hyp} \sim 4.4\, cm$), while even for $\theta = 1/30\,[rad] \sim 2^o$ it drops down to $\sim 25\,\mu m$, which corresponds to the mean distance covered in a $millisecond$ by an atom in a sample at $T = 6\,\mu K$. As a consequence any coherence is washed out by the atomic motion in a similar time;

- if the beams are not copropagating, there is no possibility to control the relative phase drift during the experiments, each beam following a complete independent phase dynamics. In experiments focused on the evaluation of the quantum properties of the regenerated pulse, instead, it is necessary to determine (in order to subtract it) the contribution to the phase of the regenerated pulse

[9] As an example, the different one-photon detunings $\Delta_c$ for the measurements presented in fig5.4 are obtained by acting just on the wave generator driving the $AOM$, while keeping a constant frequency for the $EOM$. This is manifested in the fixed displacement shown by the leakage beat note with respect to the two-photon resonance. By setting the $AOM$ like in the most detuned configuration reported in the figure ($\Delta_c = +15\, MHz$), but reducing the $EOM$ modulation frequency $\Omega$ by the same amount ($\Rightarrow \Omega' = \Omega - 15\, MHz$), we can recover the two-photon resonance leaving the small peak on the side of the spectroscopic signal, hence out of the integration band in case of memory experiments

[10] $\vec{k}_s$ and $\vec{k}_c$ represent the wave vectors of the two fields, while $\Delta\vec{k} = \vec{k}_s - \vec{k}_c$

given by the variation of the phase of the control field during the storage time. During the read out procedure the regenerated pulse emerges from the atomic cloud with a phase difference with respect to the control field given by the atomic coherence. If, during the storage time, the control field phase fluctuates randomly, the recovered signal pulse phase will have no relation with that of the original one, thus invalidating the statistical measurement of the quadratures of the field.

Using copropagating control and signal fields it is possible to use a single polarizing beam splitter to separate them as well as to mix them with the local oscillator (as illustrated in fig7.6.a). In this way all the optical paths after the sample in which the control and the signal fields are separated, they are overlapped with the local oscillator, and it is possible to use the detected variation of the relative phase between the control and the local oscillator to correct the phase attributed to the regenerated signal pulse.

In the experiment performed in Paris, the beams were copropagating and all the phases were locked together, so that this question was solved a priori. Other experiments in literature, such as [57, 2], do not need to address the issue of the phase fluctuations because the involved time scales are short enough (storage time limited to $\sim 1\,\mu s$) to ensure that all the relevant phases remain constant within the single experimental realization. This is not the case in the perspective of storage times up to the *millisecond* scale and further on. We have hence chosen a collinear configuration for the control and the signal field. To ensure no effects on the homodyne detection during the transition time for the control field, it is however sufficient to set the beat note of interest at a frequency significantly higher than the spectral components created by the switching operation. For a shutdown carried out in a *microsecond* time scale, the relevant components are almost contained within a *megaherz*. Hence, a beat note at $10\,MHz$, with a demodulation integrated over 2 arcs (which corresponds a detection band limited to the interval $(10 \pm 2.5)MHz$), is already capable to efficiently filter out any effect due to the presence of the control leakage[11], while keeping a high time resolution ($0.2\,\mu s$).

[11]The experiment in Paris suffered the leakage of the control on the path of the homodyne detection because in that case the beat note was set by construction to $1\,MHz$, hence centered on a frequency band attained by the spectral spreading induced by the switching operation

## 7.4 Phase detection

Since the experiment in Florence aims at long storage times, we designed the detection system in such a way that it is possible to recover the information on all the relative phase of interest. By setting the control field and the signal field in a copropagative configuration, it is indeed possible to correct the phase of the regenerated pulse of signal field for the contribution induced by the drifts of the control field phase. The latter can be detected like interferential signal with the local oscillator by means of a photodiode as the one exploited for the P-D-H locking technique of the cavity. The fast beat note can be demodulated using as reference the same wave generator providing the $\mu-$wave for the $EOM$. The quantity of interest is the variation of the relative phase between the beat note preceding the writing stage and the beat note following the reading stage. In both cases we can integrate the beating signal for an almost arbitrary long time [12], so that the phase can be determined with the required precision[13].

Actually, abandoning the procedure for the generation of the signal pulse elaborated by J.Cvikclinski ([21]), we have renounced to a technique which allowed the production of pulses with a fixed phase with respect to the other fields (control and local oscillator). Indeed, to perform an estimation of the statistical distribution for the quadratures of the field by means of a large number of repetitions of the same experiment, we need a method allowing the precise determination, for each single repetition, of the phase of the original pulse we are storing. Our idea is to use a method similar to the one exploited in references [57, 2] for the storage of a pulse of squeezed vacuum. Just before sending the pulse to be stored, but with the control field and the local oscillator already on, we can keep the signal field on for the time needed for a good determination of its relative phase with respect to the local oscillator. By starting the storage procedure just after this preliminary stage (within

[12] the experiment has however an intrinsic limited lifetime. Moreover we have to recall the fact that the reflection of the local oscillator on the photodiode is able to destroy the cloud in few *milliseconds* of continuous exposition

[13] The technique is able to account just for phase variation induced by the optical paths, but not for the contribution given by the phase noise of the wave generator. To ensure a good phase correction, a syntesizer of good quality has to be exploited. We can use at this purpose an *Anritzu* syntesizer, model 68017$C$

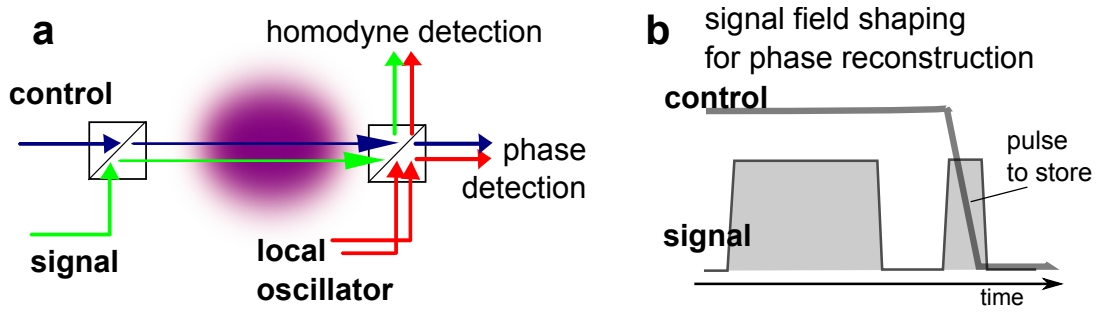


Figure 7.6: **a** - A copropagating configuration for control and signal fields allows the use of a single polarizing beam splitter to separate them as well as to mix them with the local oscillator. In this way all the optical paths after the sample in which the control and the signal fields are separated, they are overlapped with the local oscillator. One can therefore use the variation of the relative phase between the control and the local oscillator to correct the phase attributed to the regenerated signal pulse.
**b** - Experimental procedure to precisely determine the random phase of a short pulse as the ones we plane to store. If the random drift of the phase is too fast to ensure the same phase in successive repetitions of the experiment, but it is sufficiently slow to maintain the same phase during a fraction of *millisecond*, the transmission under condition of $EIT$ of a preliminary pulse immediately preceding the one to be stored can improve the knowledge of its phase by repeated measurements.

$10\,\mu s$), as shown in fig7.6.b, we can assume that the signal pulse has maintained the same phase. The presence of the control field allows the passage of the signal with no major damage to the cloud.

On the perspective of such a procedure, we have designed the entire set-up to make possible setting the beat note between signal and local oscillator at a frequency up to $20\,MHz$. In this way a demodulation integrated over two arcs gives a result (that is, a measurement of the two quadratures, and so, indirectly, of the phase) each $100\,ns$, and so we can provide up to 10 measurements of the phase for a pulse of length $\sim 1\,\mu s$. By sending a preliminary pulse of the same length, we can hence estimate the value of the phase from a statistical ensemble of 20 measurements. From general statistic theory ([114]), we know that the mean value of a normal distribution

obtained from a limited number of measurements ($n$) has itself a normal distribution with a variance $\tilde{\sigma}^2$ given by the variance of the original distribution $\sigma^2$ divided by the number of measurements ($\tilde{\sigma}^2 = \sigma^2/n$).
The non perfect determination of the phase of the pulse to be stored induces an additional contribution to the spread of the final statistical distribution measured for the regenerated pulse, which hence can no longer reach the standard quantum limit (shot noise). Since the estimation of the phase is obtained by the statistical distribution of the result of the demodulation within the single repetition, while the statistical properties of the field are evaluated by comparing the value at a given instant for the pulses of the different repetitions, the two normal distributions[14] are independent, and the final normal distribution for the variables of the regenerated field has a variance $\sigma^6_{tot}$ determined by the sum of their variances $\sigma^2_{tot} = \sigma^2 + \sigma^2/n$. In case the estimation of the phase is obtained from an ensemble of $n = 20$ measurements, therefore, the additional noise with respect to the quantum limit (defined by the variance $\sigma^2$) is evaluated in

$$\sigma^2_{tot}/\sigma^2 = 1 + 1/20 \Rightarrow \ +0.21\, dB \tag{7.2}$$

In the case of a preliminary pulse giving 30 measurements of the phase of the signal filed (corresponding to a pulse length of $\sim 3\,\mu s$), the excess noise will be reduced to $+0.1\, dB$ with respect to the shot noise.
From such considerations, we deduce that the designed procedure for the recovery of the signal pulse phase is precise enough to allow the evaluation of the statistic distribution of the regenerated pulse.

[14] the first one related to the estimation of a random variable by a finite number of measurements, the second one direct expression of the quantum mechanics uncertainty principle

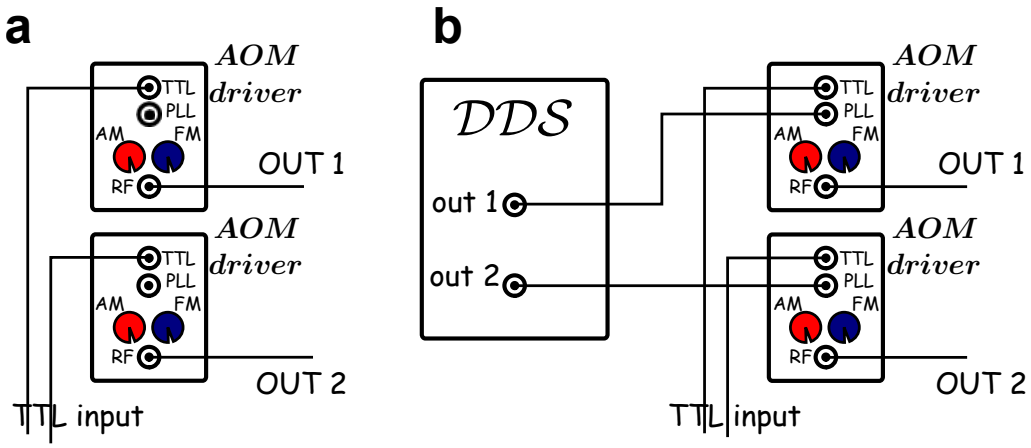


Figure 7.7: Two ways for shaping independently the two RF which drive the $AOM$s of the signal and the control fields. In the simplest way two free running homemade $AOM$-drivers are used (**a**). A better is locking their frequency to the double output $DDS$ (**b**), which in turn can not rapidly change amplitudes. In this way exploits the property of the $DDS$ to control the frequency and the phase of the waves, and the capability of the $AOM$-driver to shape the envelopes.

## 7.5 Light pulses generation

Performing a fine shaping of coherent pulses of light, as required for memory experiments, is not a trivial task. The $DDS$ able to provide the two phase-locked waves can not change continuously the amplitude of the output. On the other hand, the homemade $AOM$-drivers, which are provided of both an amplitude modulation ($am$) input and a fast switch $TTL$ *control*, can produce pulses but are single wave generators. A first solution relied on the PLL function of the $AOM$-drivers, which allowed the control of the output frequency of two independent $AOM$-drivers with the $DDS$ (see fig.7.7.b). We could thus exploit the properties of the $DDS$ to control frequency and phase of the waves, and the capability of the $AOM$-drivers to shape their envelopes. However, the PLL locking stage has demonstrated to suffer the step-like frequency changes of the $DDS$, making the set-up quite instable. Moreover, the $am$ input is limited to a conversion time (rising and falling times) slower than $2\,\mu s$, while the $TTL$ *control* can only switch the wave on and off in a transition time of $200\,ns$. Therefore, neither the signal pulse (which is conceived with a temporal

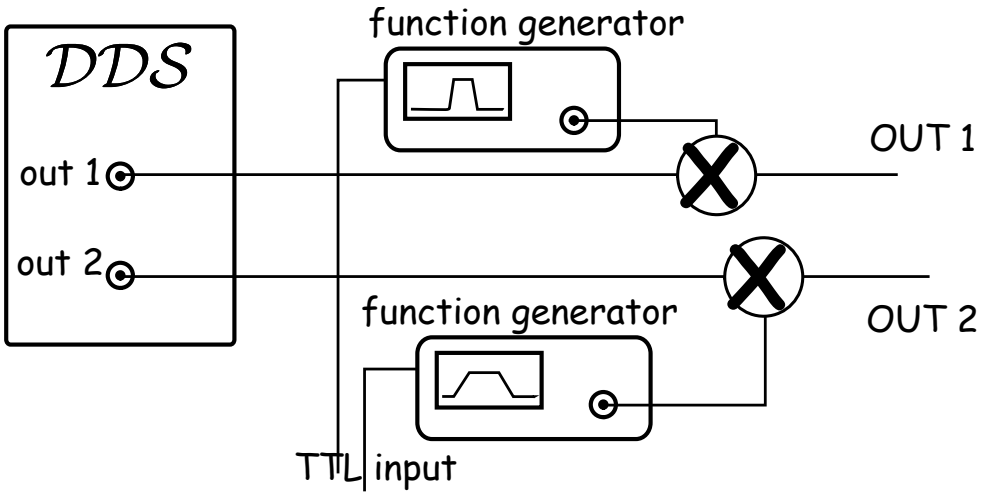


Figure 7.8: Set-up for the realization of the pulses of RF used to drive the $AOM$s diffracting the signal and the control fields. The two outputs of the $DDS$ are mixed with two DC profiles (time domain defined profiles) provided by two independent function generators. The mixing operation of a wave and a DC current gives an output signal at the same frequency of the input wave, but with an amplitude regulated by the DC current. In this way it is possible to exploit directly the properties of the $DDS$ to control frequency and phase of the waves, while adding the versatility of the function generator for shaping the envelopes.

envelope spanning one *microsecond*[15]) nor the control switch (which is conceived as sharpened on the *microsecond* scale) can be efficiently provided by this system. Actually a frequency range of operation limited to less than one *megahertz* is a common characteristic of commercial voltage controlled attenuators, so that it was not possible to modify the driver in order to produce a faster amplitude modulation. An optimal solution has been found in the use of a mixer as a "current controlled" attenuator (fig7.8). Commercial mixers have two AC channels (usually named $L.O.$ and $R.F.$) and one DC channel (named $I.F.$), and they are usually exploited to get a low frequency (down to the DC limit) signal from the frequency difference term of the mixing of two RF frequency waves. However, the same device can give on one of the AC channel the result of the mixing operation between one wave (entering the

[15]even for a group velocity $v_g = 10\,m/s$, due to the small extension of the atomic samples ($\sim 100\,\mu m$), the delay will be $\Delta t \sim 10^{-4} m\,/(10\,m/s) = 10^{-5}\,s$

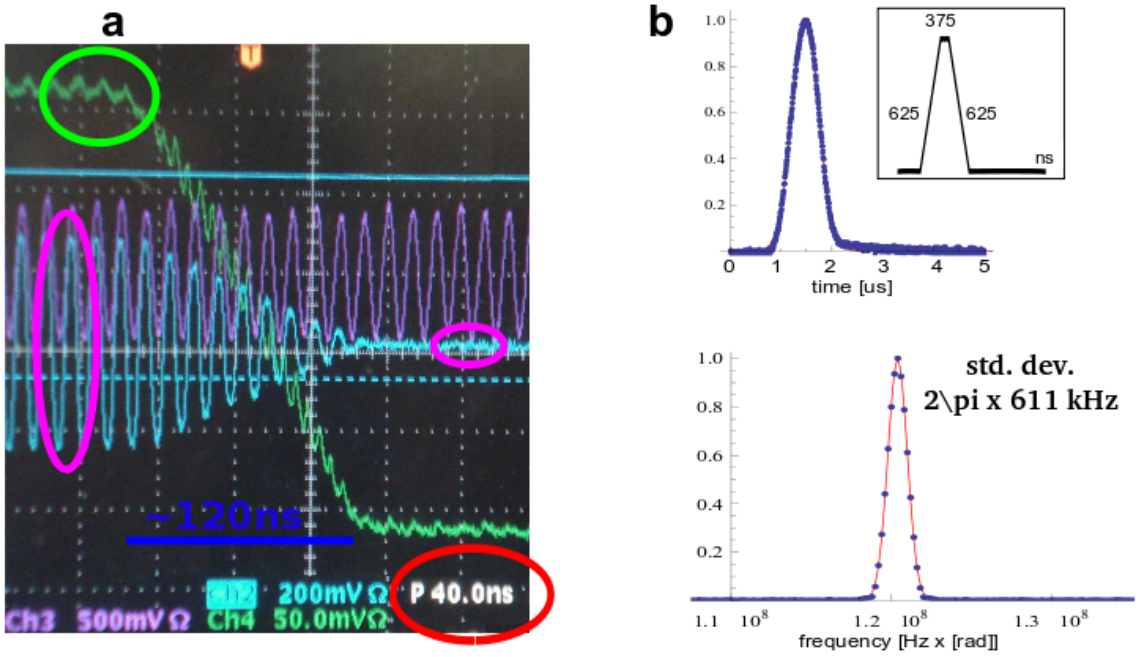


Figure 7.9: Verification of the capabilities of the set-up for the generation of the pulses. **a** - Detection of the a switching off procedure consisting in a linear falling ramp of time length $\sim 120\,ns$. The pink line is the reference wave entering the mixer; the green line is the DC profile providing the amplitude modulation; the cyan line is the output of the mixer. We can appreciate how, even on this time scale, the output envelope precisely follows the DC profile. The dynamics of the output reach the extension of $44dB$. The small modulation detected on the DC profile is induced by the signal present in the output port of the mixer (RF): it is hence proportional to the DC amplitude itself and almost disappears for a switched off output.
**b** - Example of a temporal shape optimized to produce almost Fourier limited pulses of light. The upper curve is the square root of the detected envelope , the lower curve is a discrete Fourier transform of the upper one. The spectrum profile is fitted with a Gaussian function, the result obtained for the standard deviation is $611\,kHz$. In the inset, the DC driving signal (as set on the function generator) which provides such a light pulse is reported.

other AC channel) and a DC signal entering the $I.F.$ channel. The output is a wave with the same frequency as the input one, but with an amplitude determined by the profile of the DC signal: its envelope follows exactly the amplitude of the current entering the DC channel, as it is shown for example in fig7.9.a . We may say that the operational bandwidth of such device is determined by the frequency of the input RF wave, which determines the carrier frequency of the output. In the figure it is shown the switching transient related to an input DC profile linearly dropping to zero in $\sim 100\,ns$. The RF wave envelope faithfully reproduces the dynamics of the driving DC signal even on this short time scale. The small modulation we detect on the DC driving signal is due to the non perfect isolation between the $I.F.$ channel and the $L.O.$ channel. However, the maximal attainable attenuation corresponds to a reduction of the output wave greater than $-45dB$, thus fulfilling the requirement of an effective switch off. This wide degree of freedom on shaping the envelope of an RF pulse is obtained at the expense of a reduction by $5dB$ of the RF power, this is indeed an unavoidable characteristic of passive mixer devices. By producing the profile with a function generator (an $Agilent\,33250A$ in our case), one gets access to a fully controllable manipulation of the pulse shape. As an example, we have exploited this capabilities in order to optimize the "gaussianity" of the envelope of a pulse similar to that we plane to use in the memory experiments. The better result we have obtained is reported in fig7.9.b . The discrete Fourier transform of the detected envelope[16] is very closely represented by a Gaussian shape, meaning that we have produced an almost Fourier limited pulse. This capability will be useful in the framework of experiments on light storage also for the determination of the optimal switching profile for the control field.

[16]actually, we have applied the Fourier transform to the square root of the detected profile, as the latter corresponds to the intensity envelope instead of the amplitude envelope. To get a spectral distribution shifted from the zero frequency, we have also multiplied the data for a plane wave at $\omega = 2\pi \times 20\,MHz$.

## 7.6 Technical issues

### 7.6.1 $P-D-H$ photodiode and cavity characterization

The Pound-Drever-Hall technique is a well developed since long time [27, 12] and is widely exploited in locking loop relying laser sources and Fabri-Perot cavities ([87]). The information on the position of the laser frequency with respect to the resonance of the cavity is contained in the phase acquired by the light after reflection on the first mirror of the resonator.
This phase, in the proximity of the resonance, is indeed linearly dependent on the detuning, showing an odd profile which can be used as error signal. The phase is detected by adding to the carrier frequency two equispaced sidebands (with frequencies $\omega+\Omega$ and $\omega-\Omega$) distant from the main frequency $\omega$ by more than the cavity linewidth $\Delta\omega$ $(\Omega \gg \Delta\omega)$. In this way, when the carrier is around the resonance, its reflection undergoes the phase shift induced by the interaction with the cavity, while the reflection of the two sidebands holds the asymptotic phase value associated to far from resonance light, which can be considered as a reference. The variation of the phase induced by a change either of the resonance of the cavity or of the frequency of the light is thus imprinted on the phase of the detected $\Omega$ beat note. By mixing this signal with an electric wave at the same frequency one gets a DC output which takes values around zero and is determined by the relative phase between the two waves. If the electric wave is adjusted to be in quadrature with the beating note coming from the photodiode when the laser is at resonance with the cavity (so that the DC output of the mixer is zero for perfect frequency matching), this signal can be exploited as error signal to drive a $PID$ locking stage.

In our case the electronic part of the set-up is not trivial, involving the treatment of a beat note frequency $\Omega = 6.835\,GHz$ on the $\mu-$waves region. The detection, preamplification, and demodulation stages of the signal read by the photodiode are provided by plug-in commercial elements from *minicircuits*. The electronic scheme together with the references of the chosen elements are reported in fig7.10.right . The detection is performed by a $G4176-03$ diode from $Hamamatsu$, which shows a $30\,ps$ rise and fall time. This model is constructed in a case for direct plug-in to $SMB$ standard elements, so that it can be connected to the bias-tee $(ZX85-12G+)$

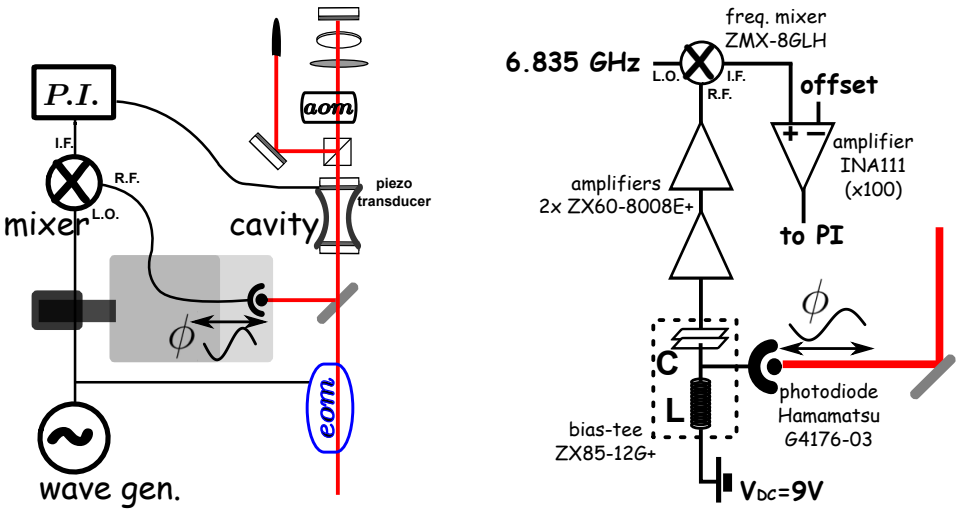


Figure 7.10: Detection stage for the beat note at $6.8\,GHz$. **a** - Representation of the scheme used to implement the P-D-H technique for locking the cavity to the frequency of the laser. A typical configuration is exploited, except for the way of providing the phase modulation. For a beat note at $\sim 6.8\,GHz$, the wavelength in air is only $\sim 4.4\,cm$, and an effective control of the phase is possible by means of a physical displacement of the photodiode.
**b** - To ensure optimum operation, all the treatments of the signal, from detection to amplification of the demodulation output, are provided by commercial elements (made by *minicircuits*) and spatially concentrated into the metallic case of the detector. In the figure the whole electronic chain is reported.

separating the DC bias from the received signal without homemade connections. The demodulation is performed by means of a simple mixer ($ZMX-8GLH$), and the DC output is then amplified with an isolated differential amplification stage exploiting a $INA111$ operational amplifier, and than sent to the homemade $PID$. The $INA111$ provides also an offset shifting as well as a decoupling between the circuit where the error signal is generated and the circuit where it is elaborated to produce the correction to be sent to the cavity.
Usually the phase of the electronic wave used to demodulate the signal coming from the detection is adjusted by modifying the length of the electronic cable connecting the generator and the mixer, a substantial phase change needing for meters of ca-

ble. In our case instead, due to the high frequency involved, the wavelength of the electronic wave within the cable is shorter than $5\,cm$, and this procedure for phase adjustment is no more simple to perform. On the other hand, such a short distance can be covered by a common translation stage, and so we have decided to exploit the propagation of the light instead of that of the electric signal as dephaser mechanism. It needs just to mount the photodiode (and its focusing lens) on a translation stage aligned with the direction of propagation of the light to be detected. By translating the photodiode from one extreme position to the other, which corresponds to $\sim 2.5\,cm$ we have evidence of the change in the relative phase by $\geq \pi$, which is enough (together with a polarity switch) to attain the optimal signal for any possible phase configuration. In fig7.10.left a representation of the P-D-H locking loop is reported, while the DC output of the mixer, after amplification and resetting of the offset, is shown in fig7.11.left for two range of the cavity length scan (cyan curve), together with the transmission of the cavity (pink curve). In the upper panel I report a small scan, $\sim 400\,MHz$, centered on the transmission peak of the carrier frequency. In the lower panel instead, the scan surpasses the free spectral range of the cavity ($FSR \sim 5\,GHz$), showing two peaks related to the even cavity modes for the carrier (the big ones), together with one peak corresponding to the odd cavity modes for the carrier and two peaks which are determined by the excited sidebands. We can see that a similar error signal is obtained in correspondence of the transmission of the sidebands, which shows inverted polarity and half amplitude with respect to that obtained for the carrier frequency, as expected from theory. The profile is however an optimal error signal in this case too.

The cavity we have exploited is characterized by a finesse $f \sim 150$, for which we measured a transmission far from the peak of about $t_{out} \sim 5 \times 10^{-4}$. The free spectral range of the cavity is $FSR \sim 5\,GHz$, which corresponds a $FWHM$ of the transmission profile $\Delta\nu_c \sim 35\,MHz$. It is much wider than the laser linewidth, which can be hence easily held on the center of the transmission peak. In order to both maximize the transmission of the frequency of interest, and minimize that for the other spectral components, the cavity has been regulated to fulfill as better as possible the confocal condition. In this way all the transverse modes are concentrated on two transmission peaks, the one related to even modes (containing in particular the $TEM_{00}$) an the one for the odd modes, set exactly in the middle of the $FSR$. This

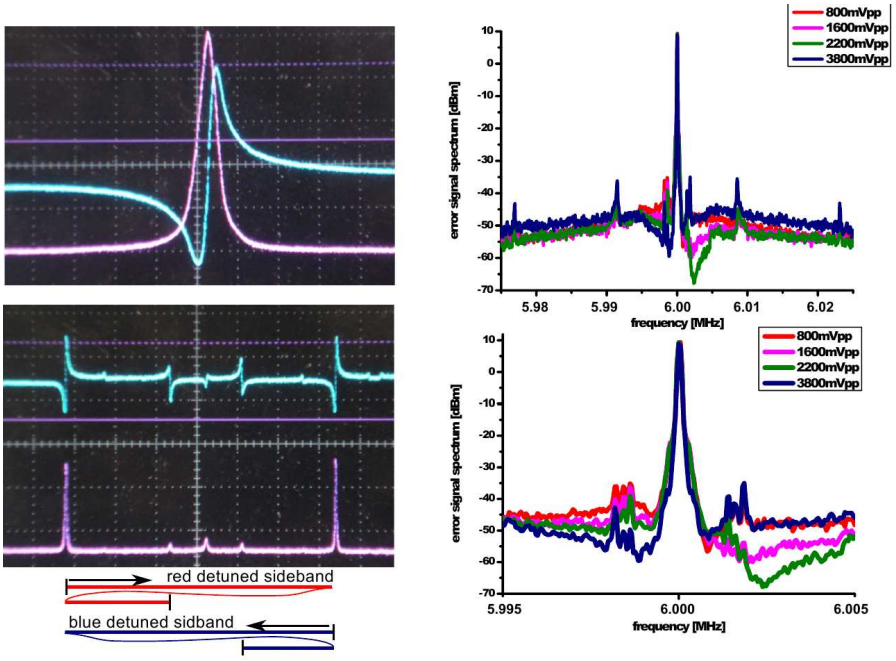


Figure 7.11: **left** - Transmission of the cavity (pink curve) and P-D-H signal for a small modulation of the length of cavity around an even modes transmission peak (upper panel); signal obtained with a larger modulation, covering more than one free spectral range (lower panel). From these images we have characterized the properties of the cavity, as the finesse $f \sim 150$, the ratio between the transmission far from resonance and the maximal transmission $\sim 5 \times 10^{(} - 4)$, and the linewidth of the transmission peak $\Delta\omega_c \sim 2\pi \times 35\, MHz$. In the lower panel, we can recognize the transmission peaks related to both the odd modes and the sidebands at $\pm 6.8\, GHz$. **b** - Finding the best lock signal for the cavity. We report here the beat note obtained as the result of the interference of the two fields diffracted by $AOM$s driven by the $DDS$, one of them then passing through the cavity (the $DDS$ is set for a frequency difference of $6\, MHz$). The different curves are related to different amplitudes of the error signal. The $FWHM$ of the beating is smaller than $200\, Hz$ in every case, the spectrum reaching $-50\, dBc$ within the first $kilohertz$. We take as best setting the amplitude related to the green curve ($2200\, mV$ peak to peak).

allows, on the one hand, the coincident transmission of all the spatial components with the same frequency; on the other hand, it "empties" the $FSR$ from secondary transmission peaks which can enhance the transmission of the spectral components that should be filtered out. In the presence of well formed and isolated transmission peaks, we get even a better shape for the error signal. Finally in fig7.11.right we show the beat note at $6\,MHz$ as obtained in section 8.1, here reported for a number of locking configuration, differing in the error signal amplitude. The beat note is the result of the detection of the interference between the two fields diffracted by $AOM$s driven by the $DDS$, one of them then passing through the cavity. The FWHM is smaller than $200\,Hz$ in every case, the beat note spectrum reaching $-50\,dBc$ for components closer than $1\,kHz$ to the central frequency.

### 7.6.2 Relative phase control by means of the $DDS$

In this section I report the measurements we have performed to understand the effective capabilities of our $DDS$. This electronic device is based on a microchip $AD\,9958$ by *Analog devices*, which is able, among a much longer list of function, to generate two phase locked RF waves (frequency range limited within the interval $0.5 - 95\,MHz$) with the possibility of defining independently for the two outputs the parameters amplitude, frequency and phase.
We were interested on the properties of the effective relative phase between the beams obtained by diffraction on two $AOM$s driven by the two output of the $DDS$. To test the real system we have registered on the oscilloscope the interferential beat note of the two beams detected on a photodiode. An evaluation of the standard amplitude and frequency noise performed for the two wave generators ($AOM$-driver and $DDS$) is reported in section 8.2.1 . Here we focus the attention on the capabilities related to the control of the relative phase; in particular we have checked the behavior of the optical beams in the temporal interval around a change of the output state. First we have checked how it behaves the relative phase when the frequency of one of the two waves is changed. The trace on the top-left panel of fig7.12 is referred to the switch from a state emitting two waves differing by $20\,kHz$ to a state emitting the same frequency on both output. Null variation of phase is required. The detected signal shows that the "new" wave begins its evolution starting from the phase accumulated in the previous history. Indeed, by switching on a non evolving relative phase state

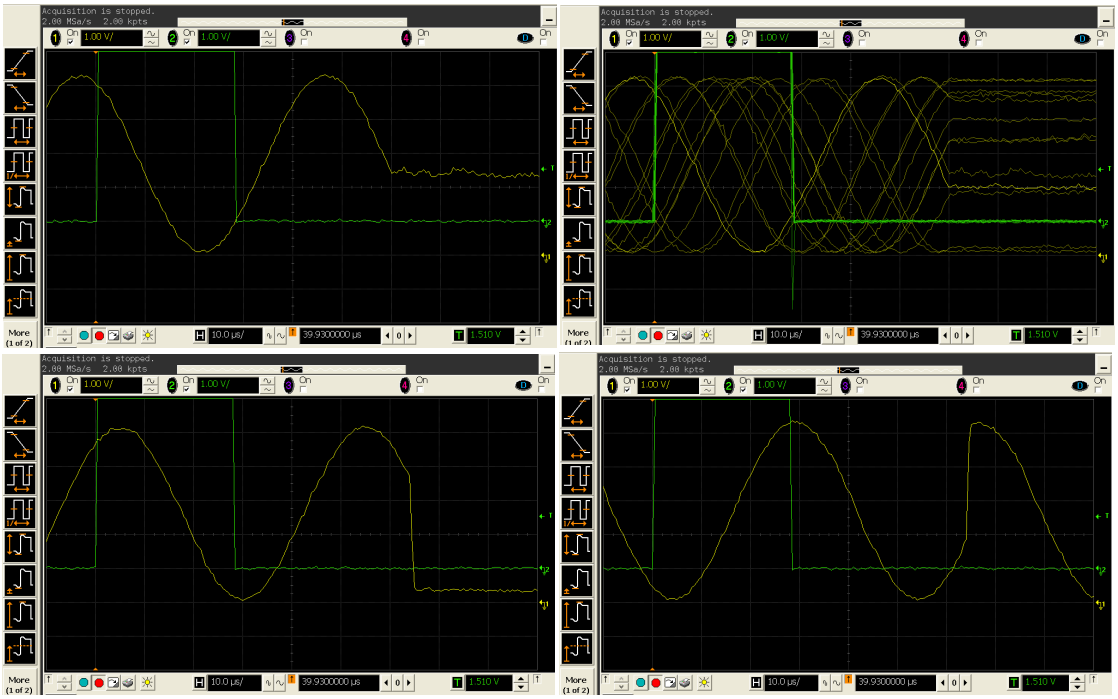

Figure 7.12: Exploring the behavior of the $DDS$. The optical beat notes reported in the figure are obtained as interference between two beams diffracted by $DDS$ driven $AOM$s. The detection is focused on the transient time corresponding to the switching operation between two states[18] in order to determine the phase reference the $DDS$ uses to define the relative phase between the two outputs when switching to a new configuration. The interference profiles show that the zero phase for the new state is set equal to the last value attained by the phase evolution related to the previous state. In the top-right panel a number of repetitions of the same switch operations are reported. The acquisition is triggered by the command sent to the $DDS$. The image shows that the jitter on the switch operation with respect to the request is smaller than $0.1\,\mu s$.

(equal frequency on both output), the beat note gets frozen on the interference point attained at the moment of the switch[19]. On the top-right panel we have checked the jitter associated to a change of state. From this rough estimation we can say that the timing of the change is stable at least on the scale of $100\,ns$. These aspects are fundamental details when a multiple pulse coherent interaction has to be performed: in this case indeed the relative phase between the successive pulses modifies the overall effect of the interaction (as in the case of the interferometer).
In the bottom part of fig7.12 we have checked the optical interference obtained when a change of the relative phase is demanded. On the left side, the request involved also a change in frequency as in the top part of the figure, while on the right side, the relative phase it is the only varied parameter. In both cases the phase has been changed by adding a $\pi/2$ offset to the previous value. The test has proven that the control on the phase of the output of the $DDS$ is transferred faithfully to the optical relative phase of the two beams.

[19]neglecting the evolution induced by the mechanical and thermal fluctuations of the optical path

# Chapter 8

# Probing the coherence of the interaction

## 8.1 Electronic and mechanical phase noise

The coherent source we have exploited for the optical interrogation of the ultra-cold cloud is a commercial grating stabilized external cavity diode laser by *Toptica*, the $DLX110$ model. It is realized following a special design, in which, differently from the usual Litthrow configuration, the output beam is transmitted by the rear face of the emitter diode. This particular geometry allows a higher stability of the beam with respect to external cavity alignment. The source is able to provide up to $P \sim 350\,mW$. The usual amplitude noise spectrum of a grating stabilized diode source drops to shot noise level for frequencies higher than $\sim 1\,MHz$, while phase noise spectrum shows components up to the *gigahertz* scale. Diode lasers are hence not indicated, at least as master laser, for experiments related to non classical states of light, because they have short coherence time with respect to other sources, as for example $Ti : Sa$ lasers. A method to get narrow lines from such active medium is phase locking them to a more stable source, as performed in the set-up realizing storage of squeezed vacuum [57, 2]. In the preliminary part of the project however, we plane to characterize the classical efficiency of the system, so that we do not need for pulsed coherent states and this laser fits our necessities. Moreover, the black box with the optical circuits for the production of the beams for the memory experiment is designed in such a way that it is possible to enter the set-up with an additional external

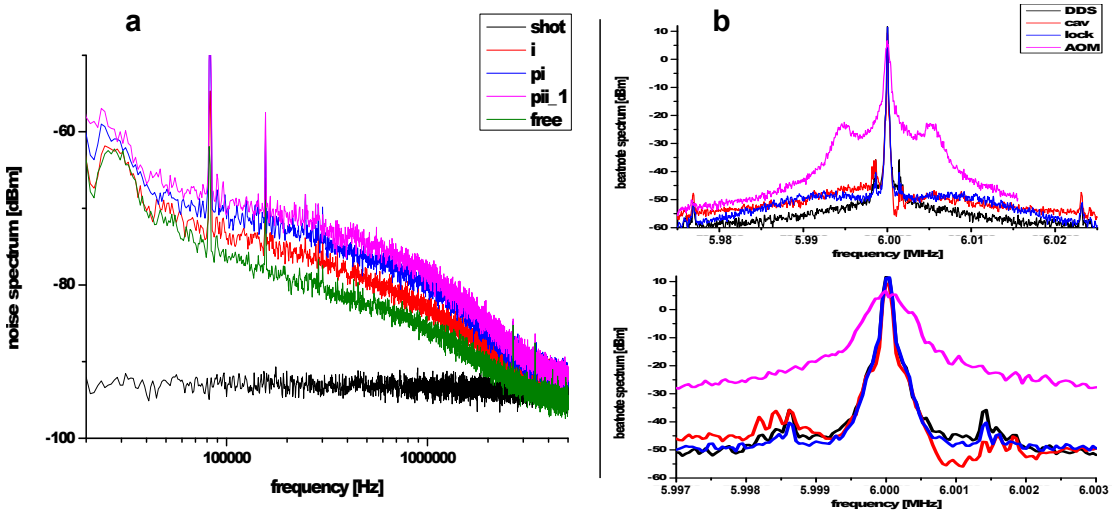


Figure 8.1: **a** - Amplitude noise as obtained by processing with a spectrum analyzer the output voltage of a fast photodiode illuminated with the light from the free running laser (green curve). The amplitude noise spectrum reaches the shot noise level at a frequency $\sim 3\,MHz$. The same evaluation is carried on the laser locked to an atomic transition. The red curve corresponds to a correction applied just to the piezotransducer acting on the grating. Blue and pink curves are obtained when a proportional correction, and a proportional plus integral correction, respectively, are sent to the current input of the diode emitter.

**b** - Quantification of the noise added by the opto-electronics components. Due to the fact that the beat note between two beams coming from the same source is insensitive to the phase noise of the source itself, the additional noise induced on the laser beams by both the active elements ($AOM$s and cavity), and the mechanical vibrations present in the laboratory can be analyzed by observing the beat note (fixed to $6\,MHz$) between two fields (of the three) produced in the black box. The main results of the analysis are the following: 1) for two fields both diffracted by $AOM$s driven by the $DDS$ (black curve) the noise spectrum is very low (attaining $-60\,dBc$ closer than $200\,Hz$ from the carrier frequency); 2) the cavity does not add appreciable spectral components.

source by means of a fiber and a flipping mirror. Therefore, the apparatus will not require any modification when a laser with a longer coherence length will be installed.

In fig8.1.a the measurement of the amplitude noise of our diode source is reported. The measurement is obtained by simply processing with a spectrum analyzer the output voltage of a fast photodiode illuminated with the light of the laser. We can see that the amplitude noise spectrum reaches the shot noise level at $\sim 3\,MHz$. This result explains the noise level detected in the spectroscopic technique described in chapter 5, in absence of the signal pulse. The detected noise amplitude is there very close to a rough estimation of the shot noise level. Actually this is due to the characteristics of the integration band adopted in the spectroscopy experiment, which was centered at $5\,MHz$ and large $\sim \pm 2.5\,MHz$, hence mostly located in a spectral region where the laser is at the quantum limit.
In the figure we also reported the amplitude noise spectrum when the laser is locked to an atomic transition via saturated absorption spectroscopy. The curves refer to different kind of feedback. The red curve corresponds to a correction applied just to the piezotrasducer acting on the grating, which is limited in frequency to $\sim 1\,kHz$. The other curves are instead the result of adding to the feedback a proportional (blue) and a proportional plus integral (pink) correction signal sent to the current.

In the framework of characterizing the temporal limits for coherent interaction with the apparatus, we have analyzed the additional noise induced on the laser beams by both the "active" elements ( $AOM$s and cavity), and the mechanical vibrations present in the laboratory[1]. We have quantified these effects by observing the beat note (fixed at $6\,MHz$) between two fields (of the three) produced in the black box. The beat note is produced on a fast photodiode and the signal is analyzed with a spectrum analyzer. The interference obtained superposing two beams coming from the same laser is insensitive to the phase noise of the source unless the two independent paths have a length differing by more than the coherence distance[2]. Therefore,

[1] In general, mechanical noise on the optics can induce a significant relative phase noise on the laser fields following different optical paths, degrading the quality of the phase-locking

[2] Actually this is what is realized in memory experiments, since the regenerated pulse carries the statistical properties of the laser light at the moment of the writing stage, while it is evaluated by a local oscillator given by the light of the laser at the reading stage time. Indeed a storage time $\tau$ of the order of a *millisecond* is equivalent to a path of $(\tau \times c \sim 3 \times 10^5\,m)$.

even if the diode source we are exploiting is characterized by a large excess of noise with respect the quantum limit, by means of two beams with paths differing of few meters it is still possible to check the contribution to the noise given by the additional elements and the differential optical paths. The results are reported in fig8.1.b . The beat note obtained with two fields both diffracted by $AOM$s driven by the $DDS$ (black curve) shows very low noise. The spectrum drop to $-60\,dBc$ at a frequency below $1\,kHz$, while the FWHM of the spread is $\sim 200\,Hz$.
By locking the laser to an atomic transition, the beat note spectrum gets some additional components up to $20\,kHz$ from the carrier frequency, however with amplitudes lower than $-60\,dBc$. These components can be related to the small frequency modulation due to the active correction of the laser, which is transformed by the differential path between the two beams in an effective fluctuating difference in frequency. The red curve in fig8.1.b is obtained when one of the beams passes through the cavity. We see that this element does not add relevant components to the noise spectrum of the beat note.
If one beam is diffracted by an $AOM$ driven by a standard homemade $AOM$-driver (pink curve), the noise spectrum results much higher than in the other cases (with a FWHM of the spread $\sim 500\,Hz$, and components up to $-30\,dBc$ up to $7\,kHz$ from the carrier), demonstrating the utility of exploiting a $DDS$ for coherent interaction issues.

The above measurements allow us the evaluation of the additional noise induced by the apparatus in stationary conditions. However, during the experimental procedures there are also moments characterized by exceptional mechanical noise induced by the conversion operation of the shutters. We have verified the effects of these events on the relative phase between the control and the signal field by detecting the zero frequency beat note between the two fields in a time interval around this temporal transient.
In fig.8.2 one can see the effect induced by the closing (left) and opening (right) operations of the massive shutter we use for switching the cooling light for the MOT. In this case a metallic material is required due to the intensity of the light beam ($\sim 0.5\,W$ concentrated on a waist of $\sim 1\,mm$), thus involving the rapid motion of a big inertial load[3]. From the interference profiles one can see that the relative phase oscillates over the whole $2\pi$ range for almost $0.5\,s$ after the occurrence of the event,

[3]with respect to the other shutter, which are in plastic

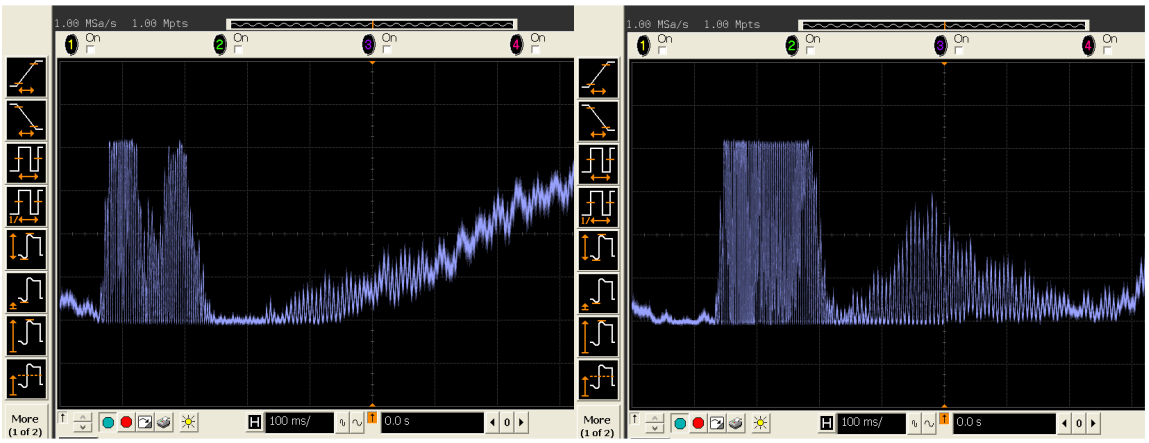


Figure 8.2: The temporal series shows dynamics of the relative phase between the two interrogation beams following a conversion operation of the massive shutter which is used to block the cooling light of the $MOT$ stage. The phase is measured by means of the detection of their interference (zero frequency beat note). The phase undergoes oscillations over more than a complete turn $(0 - 2\pi)$ for up to $0.5\,s$ after the event, both for closing (left) and opening events (right). To ensure phase consistency, the interrogation has to take place after this time interval, or it has to be limited to a duration time much shorter than the period of these oscillations ($\sim 200\,\mu s$).

so that two-field interaction with a stable phase can be performed only within two regimes: either waiting more than half a *second* after a conversion operation of this shutter, or fitting the whole interaction within a time interval much shorter than the period of the induced phase oscillation ($\sim 200\,\mu s$). In all the experiments reported in this thesis we have fulfilled the first option, which consists in waiting for half a *second* with atoms in the magnetic trap.

In fig.8.3 we report instead the fluctuations induced by the conversion of the shutters blocking the signal and the control fields themselves. In the upper-left panel it is reported the whole dynamics of the relative phase following the opening procedure (to have an exact detection we left the $AOM$ on all the time). The oscillation is smaller than $2\pi$, but it is still present up to $150\,ms$ after the event. In the upper-

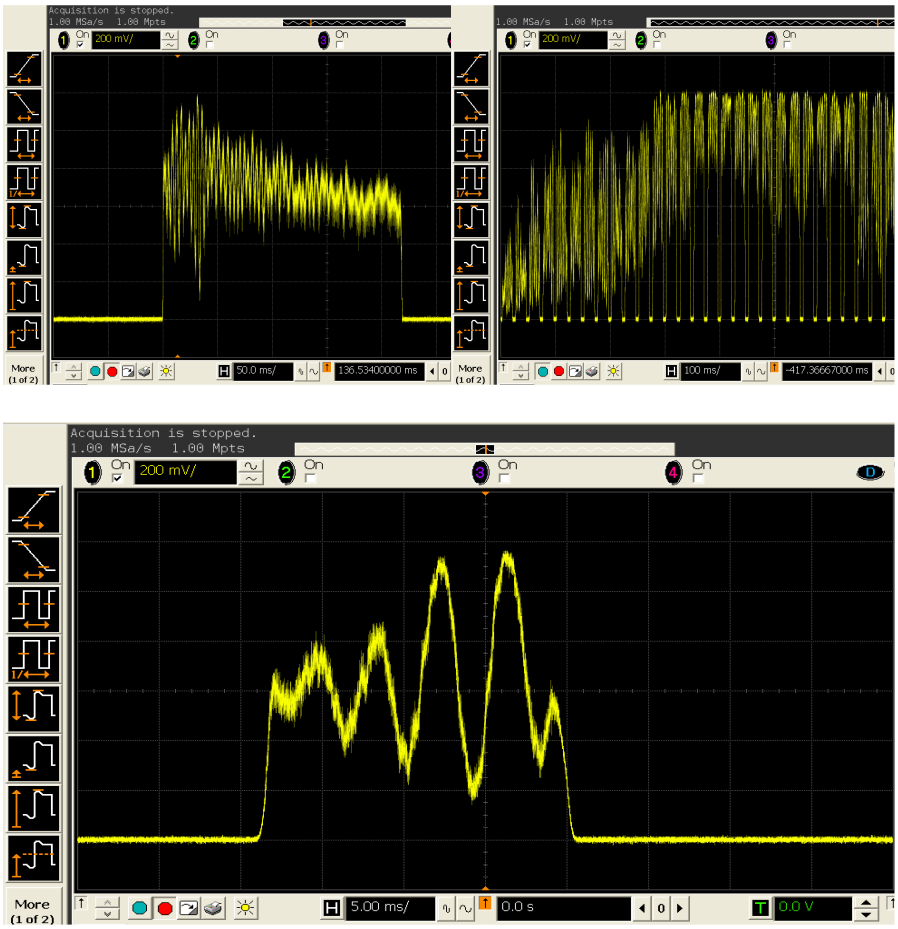


Figure 8.3: Self-induced oscillations of the relative phase between the two interrogation beams following a conversion operation of their own shutter. The relative phase, detected as in fig8.2, shows oscillations of amplitude smaller than $2\pi$, but the stability is recovered at least $150\,ms$ after the event (top-left panel). This problem prevents from performing coherent series of pulses, as those reported in the top-right panel, where a series of pulses of duration $20\,ms$, separated by $5\,ms$, is reported. However, instead of waiting for $150\,ms$ before illuminating the atoms, it is possible to recover the stability of the phase by restricting the interaction within the second *millisecond* after the starting of the opening operation (see fig8.4). This protocol exhibits particular stability due to the fact that the evolution of the phase always shows the turning point of the first, small, oscillation at this moment.

right panel it is reported the effect of the shutter on the relative phase in the context of a series of pulses. In this case we have used pulses of $\sim 20\,ms$ with a repetition time of $25\,ms$. It is evident how the mechanical action is very negative for the preservation of the relative phase between the two fields.
In the bottom panel, we report the interference profile for a single pulse like those of the upper panel. From measurements like this one we realized that the phase oscillation holds a fixed phase reference with respect to the opening front, showing always a turning point around the second *millisecond* after the opening is started. We have checked that for interaction time $\leq 1\,ms$, by centering the pulses within this time interval, the phase stability is very close to that obtained in the stationary case (that is, without opening the shutters). We will refer to this particular time setting with the expression "optimal setting".
To directly evaluate the effect of the undesired phase modulation on the coherent interaction, we have analyzed the interference detected for a series of two couples of pulses, separated by $200\,\mu s$, both producing a beat note at $20\,kHz$, but with the phase shifted by $\pi/2$ one respect to the other. The result of the characterization is reported in fig8.4. Fig8.4.a shows an example of the detected beat note, with the harmonic fit obtained separately for the first and for the second couple of pulses. In fig8.4.b the residual related to the fit on the first couple of pulses is reported, respectively from top to bottom, for the stationary case, for shuttering with a generic timing, and for the optimal setting. The reduction of the modulation depth in the last case with respect to the previous one is evident. Fig8.4.c shows the fluctuations of the effective phase difference between the two couple of pulses induced by the shuttering operation. In the case of optimal setting (red points), the spread of the detected phase shift approaches the one obtained in the stationary case (black points), while for a generic timing the spread is one order of magnitude wider.
For experiments involving short interaction times, as in the case of the interferometer, we exploited the optimal setting, which allows for a minimization of the time the shutter is open (very important when working with the degenerate sample, for which few resonant photons are sufficient to produce wide damage).

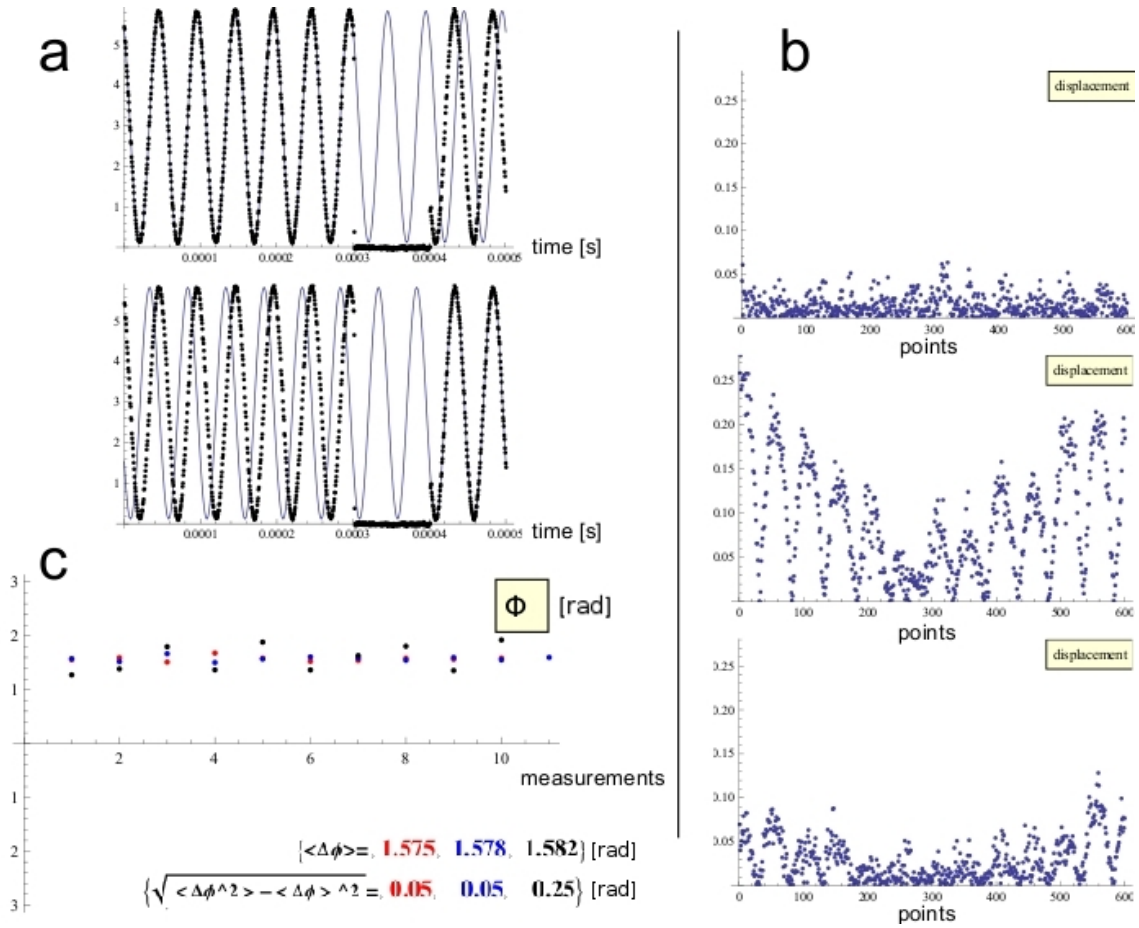


Figure 8.4: Direct evaluation of the effect of the undesired phase modulation on coherent interaction. **a** - Single shot result of the detection of a series of two couples of pulses, separated by $200\,\mu s$, both producing a beat note at $20\,kHz$, but with the phase shifted by $\pi/2$ one respect to the other. The random fluctuations of the phase are evaluated by performing two separated harmonic fits to the data related to the two couples of pulses.
**b** - Residuals related to the fit to the first beat note, for the stationary case (top), for shuttering with a generic timing (center), and for the optimal setting (bottom).
**c** - Fluctuations of the effective phase difference between the two beat notes. In the case of the optimal setting (red points), the spread of the detected phase shift approaches the one obtained in the stationary case (black points), while for a generic timing the spread is one order of magnitude wider (blue points)

## 8.2 Rabi flopping

The presence of a condensate gave us the possibility of testing the actual degree of control on the apparatus for the optical interrogation of the atomic sample. Indeed the very small momentum spread of a released degenerate sample allows a Doppler free (homogeneous) interaction for any angle difference between the exciting beams and the easy spatial separation of the components owning to different beams.
In this framework we have reproduced a number of experiments present in the literature, namely, Bragg diffraction ([94]) and Rabi flopping in a close two-level system (based both on momentum states ([64, 67]) and on internal states (hyperfine flopping with copropagating beams [107])), which have been theoretically introduced in sections 2.4.2 and 2.4.3 . The first and second phenomena refer to a fields configuration as the one reported in fig7.1.a , exploiting counterpropagating beams; while the latter is realized by a configuration corresponding to that of fig7.1.b , with copropagating beams.

In our sample[4], the momentum spreading induced on the released cloud by the mean field potential results of the same order of twice the recoil momentum induced by the absorption of a photon[5]. Components differing by a two photon recoil momentum (as the ones related to Bragg scattering) are hence directly resolved in time of flight images. This is clearly evident in fig8.5.a/b, in which we report several images of the horizontal ($y$ axis) spatial distributions of the diffracted $BEC$ atoms after interaction with standing wave pulses of different durations. Fig8.5.a shows the results obtained for a standing wave lattice, while fig8.5.b refers to the case of counterpropagating beams differing in frequency by twice the photon recoil energy ($\Delta\omega = 2\pi \times 15\, kHz[rad]$). To produce diffraction, a short pulse of a horizontal standing wave light is applied. For this task the apparatus for the production of the light for the memory experiment is used, and the optical circuit around the cell is set to perform harmonic potentials (fig.7.3.b). After an additional time of flight of $12\, ms$, the horizontal spatial distribution of the diffracted atoms are detected us-

[4] which presents quite high mean field potential (estimated in $> 1\, kHz$) due to the high frequencies of the transversal confinement of the trap $\omega_\rho \sim 2\pi \times 900\, Hz[rad]$

[5] we are considering here the case of light in proximity of the $D2$ line and atoms of Rubidium. The wavelength of the light is hence $\lambda \sim 780\, nm$, which corresponds (considering the mass of the $^{87}Rb$: $m \sim 1.4 \times 10^{-25}\, kg$) to a photon recoil velocity of $\frac{\hbar k}{m} = \frac{h}{m\lambda} \sim 6\, mm/s$.

ing a standard absorption imaging method. The hyperfine Rabi flopping reported in fig8.5.c is obtained instead with copropagating beams and the separation of the two components is realized by means of a magnetic gradient along the horizontal $y$ axis (see section 9.1). Using the zero momentum transfer configuration prevents from confusing a momentum component with a hyperfine flipped component. The parameters relative to the experiments shown in the figure are reported in the caption.

In all the Rabi flopping experiments reported here, the $BEC$ is suddenly released from the magnetic trap and is allowed to expand for $0.3\,ms$. This is necessary to get proper results in a context of non adiabatic switching of the harmonic potential. Instead, the same operation performed on a trapped condensate would lead to the destruction of the coherence in the sample due to the heating induced by the interatomic collisions, which transform the energy suddenly added by the lattice to thermal motion. Actually, in the case of the hyperfine Rabi flopping, the procedure is analogue to that performed in section 6.3.2 for the reading of the phase of a two-photon Raman transition. The short coherence time for all the performed oscillations can be attributed both to the free falling expansion condition of the cloud, and to the laser source used for the generation of the beams, which is a commercial grating stabilized external cavity diode laser ($DLX110$ from $Toptica$), characterized by a very short coherence time.

In the momentum states Rabi flopping, three different fits are realized, corresponding to the analyses performed on three different sub-set of the data. From the fits it results that the Rabi flopping gets faster for longer interaction times. This is due to the fact that a small detuning from perfect resonance becomes detectable for long interrogation times, for which the frequencies are sufficiently defined to resolve the mismatch. In the case of fig8.5.b, we have intentionally set a small two-photon detuning: the frequency difference between the two fields is set to $20\,kHz$, while the perfect resonance is fulfilled by setting $\Delta\omega \sim 2\pi \times 15\,kHz[rad]$. The detuning from resonance is hence about $2\pi \times 5\,kHz[rad]$, which is in agreement both with the evidence that the atomic system "detects" the displacement for interaction times of the order of $200\,\mu s$ and longer, and with the entity of the change of the effective Rabi frequency between short and long interrogation times. Actually, calculating the expression $\omega_2 = \sqrt{\omega_1^2 + \Delta^2}$ for $\Delta$, and replacing $\omega_i$ with the two values obtained from

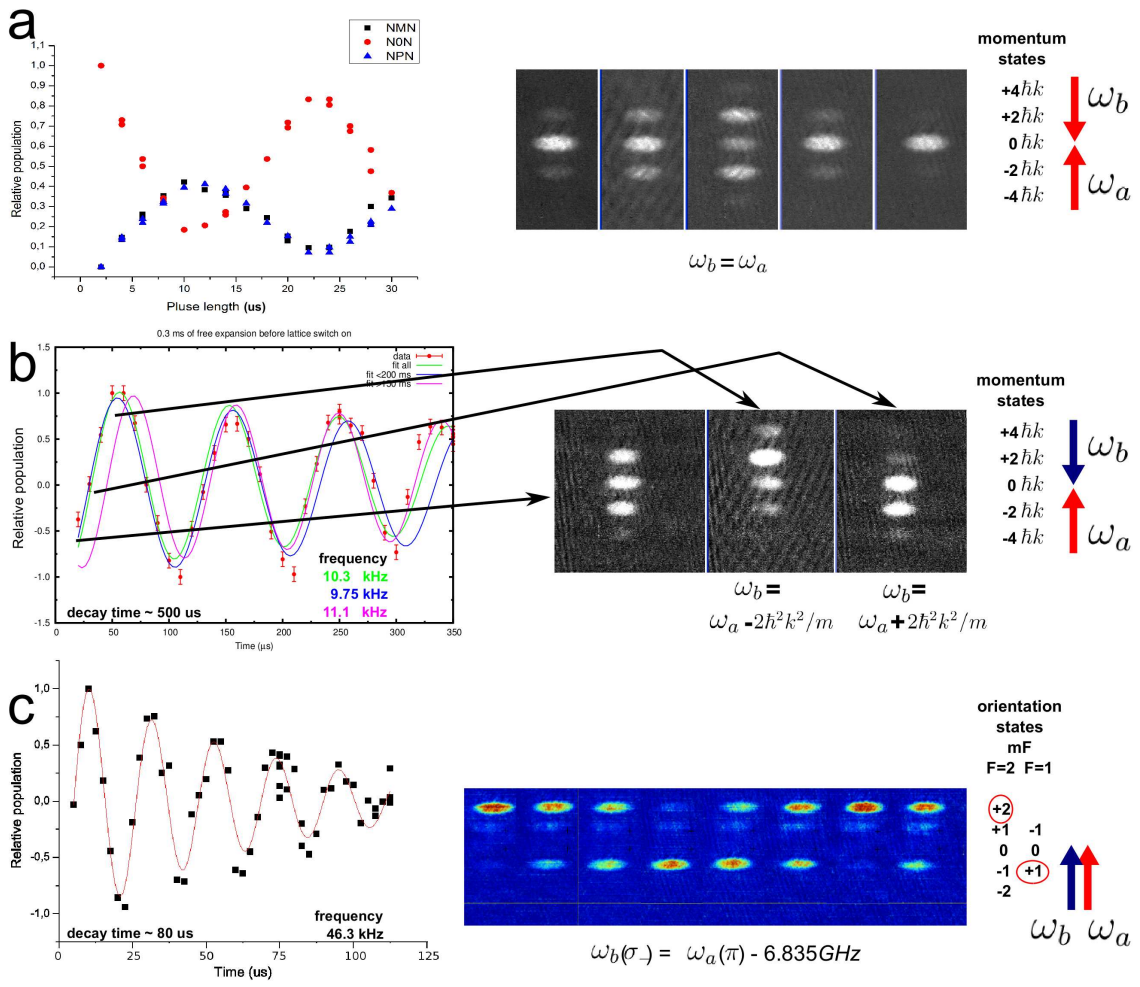


Figure 8.5: **a** - Optical lattice induced oscillations in low power regime [94]. Beams power: $P_{\omega_a} = P_{\omega_b} = 10\,\mu W$; detuning from resonance ($D2$ line) $\Delta = 6.8\,GHz$. **b** - Momentum states Rabi flopping ($P_{\omega_a} = P_{\omega_b} = 2.5\,\mu W$; $\Delta = 6.8\,GHz$). **c** - Hyperfine Rabi flopping obtained for the velocity insensitive Raman transition connecting states $|F = 2, m_F = +2\rangle$ and $|F = 1, m_F = +1\rangle$. $P_{\omega_a} = 10\,\mu W$ ($\pi$ polarization); $P_{\omega_b} = 30\,\mu W$ ($\sigma - \sigma$ polarization); $\Delta = -2.4\,GHz$. The waist of the two beams is $55\,\mu m$ in all the presented cases. **a**,**c**-right: a sequence showing the oscillations in the population distribution is reported. **b**-right: the first image shows the result for an illumination time short enough to ensure a pulse spectrum larger than two times the two-photon recoil energy. In this case, even for $\omega_b$ set equal to $\omega_a + 2\frac{\hbar k^2}{m}$, also the $\omega_b = \omega_a - 2\frac{\hbar k^2}{m}$ condition is fulfilled, and lobes on both sides are present. The second and the third images show population transfer for opposite two-photon recoil energy detunings ($\pm 2\frac{\hbar k^2}{m} = \pm 15\,kHz$).

the fits on short ($\omega_1 = 2\pi \times 9.75\, kHz[rad]$) and on long ($\omega_2 = 2\pi \times 11.1\, kHz[rad]$) times, we gets indeed $\Delta \sim 2\pi \times 5.3\, kHz[rad]$.

# Chapter 9

# The atom chip

In this section I briefly summarize the main characteristics of the apparatus used for the production of the condensate, belonging to the atom chip family. I first describe the general features of such a type of set-up and then give some details on our procedure we have developed to get degenerate samples.

The principal aspect of a mirror-MOT set-up is that, by exploiting the symmetry of the ideal scheme for the MOT, the trap is realized by adding a mirror at the center of the system, thus obtaining some of the light beams from the reflection of the others. As shown in fig.9.1.a, the mirror-MOT works like a slightly misaligned regular MOT. This solution allows one to break free from constraints of optical accessibility from both sides of each direction, as it is in the normal scheme. One gets hence the possibility of placing "objects" very close to the point where the magneto optical trap forms. In this sense the mirror can be exploited even as mechanical support. The most common way to exploit this new possibility is however inserting electric wires for the realization of steep gradient and trapping potential of magnetic field. The field produced by a current carrying wire takes indeed a decreasing profile with the distance as

$$\vec{B}(\vec{r}) = \frac{\mu_0}{2\pi}\frac{I}{r}\bar{I}\times\bar{r} \qquad \bar{A} \text{ indicating a versor: } \vec{A} = \vec{A}/|\vec{A}| \tag{9.1}$$

Moreover, by adding a constant magnetic field $\vec{B}_{bias}$ in a direction perpendicular to the wire it is possible to create a trapping potential [100, 99]. The presence of a bias field produces indeed a zero of the magnetic field all along an axes parallel to the

wire direction, at the height

$$z_{bias} = \frac{\mu_0}{\pi} \frac{I}{|\vec{B}_{bias}|} \tag{9.2}$$

The result is thus a linear guide for atoms in low seeking states, as shown in fig.9.1. The guide can be reduced to a trap by means of the field obtained by two additional current carrying wires set parallel to each other and perpendicular to the first one. Trapping potential are obtained even exploiting a single wire, just by giving it a suitable bending. Quadrupole traps can be obtained indeed with U-shaped wires, while bending the wire into a Z shape it is possible to create a 3D harmonic trap of Ioffe-Pritchard type with a field minimum different from zero. The main characteristics of these traps are related to the reduced size of the conducting element and to its proximity to the sample to trap. The short distance results in a very strong field gradient, so that typical frequencies for these devices are almost unreachable with conductors placed out of the vacuum chamber. On the other hand, the trapping volume and the maximal depth are quite smaller than in the normal case (in our case, e.g., we measure a trapping frequency up to $\omega_\rho \sim 2\pi \times 900\ Hz$ for the strongest confined direction, and the maximal trappable temperature is $\sim 100\mu K$, with a capture volume $\sim (17\mu m \times 17\mu m \times 500\mu m)$). In our set-up the chip is constituted by a plane structure of silica oxide with a gold coating deposition ensuring both the reflective properties required for the functionality of the mirror-MOT and the conductance necessary to sustain high density currents. The ultimate z-shaped wire is indeed carved in the mirror itself, isolating a channel of gold from the rest of the reflecting surface by digging from the two sides until leaving just the silicon oxide; these structures are obtained by means of photolithography techniques.
This wire (cross section $2 \times 125\,\mu m^2$) is the conductive element providing the trap where it is possible to get condensation. The chip is mounted on a ceramic holder[1] with an embedded Z-wire and two U-wires (see fig.6.1). It is placed facing downwards into a high-vacuum glass cell, as shown in fig.9.2. External coils pairs are used to create all necessary magnetic fields for the $MOT$.

The mirror-MOT stage is able to produce cold samples of up to $70 \times 10^6$ atoms at a temperature of $\sim 120\,\mu K$ in about 5 $s$ collection time. The atoms are further

[1] able to electrically isolate the chip while ensuring large thermal conduction, two fundamental properties due to the relative high current applied to the chip (about $2\,A$) for a duration of $3\,s$

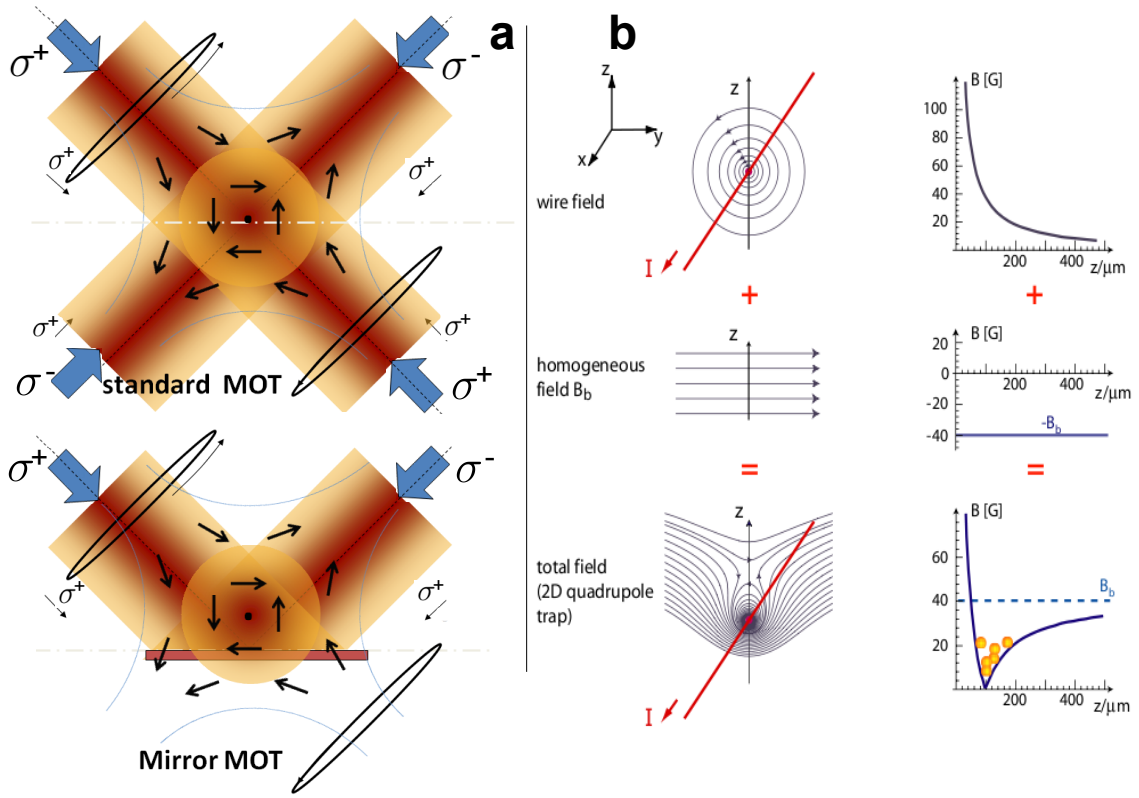


Figure 9.1: **a** - By exploiting the symmetry of the ideal scheme for a MOT, the trap is realized by adding a mirror at the center of the system, thus obtaining some of the light beams from the reflection of the others. This solution allows avoiding the constraint of optical accessibility from both sides of each direction, as it is in the normal scheme.

**b** - Fundamental concept at the basis of microtraps: a current carrying wire produces a magnetic field with cylindric symmetry, decreasing with the distance from the wire. By adding a bias field directed in whatever direction on the plane orthogonal to the wire, a magnetic guide is generated. By changing the direction of the bias field, the guide rotates around the axis of the wire, while, by changing its modulus, the guide gets closer or farther from the wire.

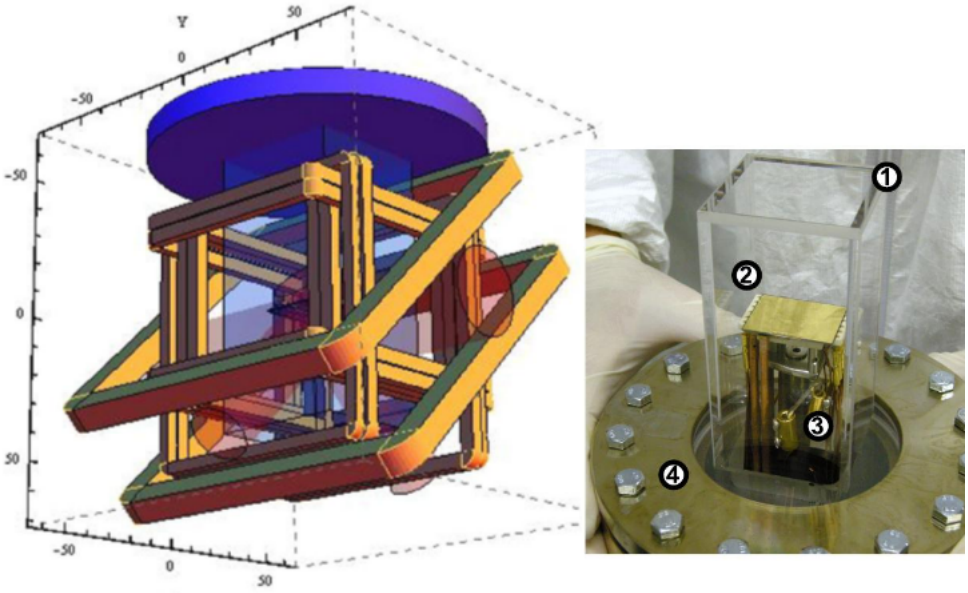


Figure 9.2: Left: representation of the science vacuum cell embedded into the magnetic coils for the control of the bias field. The whole apparatus is contained in a cubic volume of $(20 \times 20 \times 20)cm$. Right: science cell with the atomchip. (1) *Hellma* glass cell, (2) chip, (3) dispenser (atom source), (4) home made flange hosting the glass metal adapter.

cooled down to $10\,\mu K$ by an optical molasses phase. At this stage the cloud has an almost spherical shape of $\sim 700\,\mu m$ diameter.

The sample is then pumped into the $|F = 2, m_F = 2\rangle$ state before being loaded in two-stages into the chip magnetic trap. First, an ancillary magnetic trap is generated $1.2\,mm$ below the chip by the $25\,A$-guiding z-wire in the chip holder. After a while, an almost adiabatic procedure of compression and approach to the chip is performed by simultaneous ramping of the trap and external bias currents. The sample is then transfered to the magnetic trap formed by the $1.7\,A$-guiding z-wire defined on the chip surface at a distance of about $200\,\mu m$ from it. This complicated sequence of operation is made necessary by both the limited depth and capture volume of the magnetic traps. While providing a sufficient depth ($>\sim 100\,\mu K$) in fact, the chip z-wire trap holds a too small capture volume ($\sim (40\,\mu m \times 40\,\mu m \times 500\,\mu m)$) to effectively load the atoms directly from the molasses phase. It is hence better to rely on an intermediate

trap that, even loosing a large part of the sample due to its its weakness (evaluated depth $\sim 10\,\mu K$), presents a wider capture volume ($300\,\mu m \times 300\,\mu m \times 700\,\mu m$) and can take place in a region easily accessible for the MOT ($1.2\,mm > 700\,\mu m =$ size of the cloud).
Once in the chip trap, the sample, which is now constituted by $20 \times 10^6$ atoms at $T \sim 50\,\mu K$, is further compressed, to increase the scattering rate up to a value which lets evaporation until condensation in a time scale shorter than the trapping life time ($\sim 1\,s$ in a $10^{-9}\,mbar$ vacuum). The final frequencies of the chip trap attain the values $(\nu_\rho, \nu_z) = (950\,Hz,\, 46\,Hz)$. The atoms are evaporated to quantum degeneracy by ramping down the frequency of an RF field supplied by an RF generator ($Agilent33250A$) connected to one of the U-wires located in the chip holder. The RF ramp starts from a frequency of $13\,MHz$ and is stopped at $\sim 700\,kHz$, the whole stage takes $2.5\,s$. The obtained $BEC$ is typically formed by $3 \times 10^4$ atoms, with a critical temperature of $0.5\,\mu K$ and is positioned at $150\,\mu m$ from the chip surface. The magnetic field at the bottom of the trap points in the $y$ direction (fig6.1) and can be controlled by an external coils pair. The magnetic field stability is better than $5\,mG$.

## 9.1 Stern-Gerlach analysis

To perform the Stern-Gerlach procedure which allows the detection of the population distribution in the orientation manifold we can exploit two sources of magnetic gradient. The simplest way is to maintain the current on the z-wire for some while (generally it is sufficient $100\,\mu s$) after switching off the bias field on the x axis. In this way the trapping potential is reduced to a decreasing slope of the form of the expression 9.1. Under the effect of the gravitation the atoms start to fall, but the low field seeking states are pushed down a bit more due to the presence of the gradient, while the high field seeking states are held slightly closer to the chip. The separation is performed hence on the $z$ axis (see fig9.3.left). Actually the current used for the trapping stage ($I = 1.7\,A$) provides a potential stronger than gravity, and the latter states eventually hit the chip if the gradient is maintained for a sufficiently long time. The second gradient we can provide is obtained by means of an external coil placed on the $y$ axis (see fig9.3.right). The separation in this case takes place on the plane orthogonal to the gravity force, on the direction of propagation for the interrogation beams (lattice, $EIT$). In this case, to get good discernibility, the gradient has to be held for at least $5\,ms$, and we have to image the atoms after at least $12\,ms$.

The two gradients show complementary properties. The z-wire gradient is stronger and needs for a shorter execution time. Moreover it provides the separation on a direction ($z$ axis) orthogonal to the separation induced by momentum transfer transitions obtained with the interrogation beams, so that it is possible to determine clearly both the internal (orientation) and the external (momentum) state occupied by the cloud(s).
On the other hand, the gradient is applied when the cloud is very close to the chip, so that it is relevant the non linear slope of the field, which ends up in a deformation of the orientation sub-clouds (see fig.9.3.left). No such effect is detected in case of the gradient along the $y$ direction. Moreover the z-wire gradient has a more violent switching transient, so that it works properly just if used by switching off the bias field while leaving the current on the wire. A procedure conceiving a complete switch of the fields responsible for the trapping potential, followed by a "pulse" of gradient, which allows for an interaction under homogeneous magnetic field, has proven to be much less reproducible and coherent. On the contrary, this is the usual way to exploit

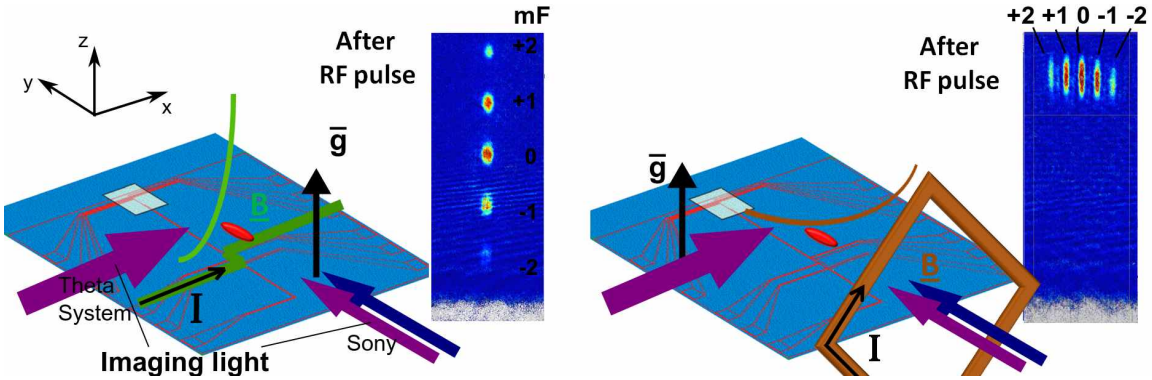


Figure 9.3: The two possible Stern-Gerlach analysis procedures. The first procedure exploits the gradient magnetic field along the $z$ axis generated by the same current carrying wire used for the implementation of the magnetic trap. The second procedure, instead, relies instead on the gradient obtained on the $y$ axis (axis of propagation of the interrogation beams) by means of additional external macroscopic coil. The two procedures show complementary properties (see text).

the y-coil gradient.

## 9.2 Optimization of the thermal cloud

The degenerate sample obtained with the atom chip contains $N \sim 3 \times 10^4$ atoms and occupies a volume of the order of $(2\,\mu m \times 2\,\mu m \times 35\,\mu m)$. Even if the estimate of the optical depth indicates a value of the order of one hundred, the cloud is too small to be used for quantum memory experiments. Indeed the matching between the transversal size of the cloud and that of the light pulse to be stored is a prerequisite in order to obtain a good storage efficiency, but a minimal waist of $2\,\mu m$ is very hard to attain with optical lenses placed out of the vacuum chamber (at least 10 cm far from the cloud). Moreover, to overlap to objects of this size by means of manual alignment looks even more difficult. On the other hand, as already mentioned at the beginning of the chapter 5, degeneracy is not a stringent requirement for the formation of low decay rate coherences. Thus we worked on the loading procedure of the ultracold atomic sample in order to obtain a cloud at sufficiently low temperature to ensure small detrimental effects induced by the magnetic potential, and a sufficiently high number of atoms to ensure a good optical depth even for a transversal size of the order of $50\,\mu m$. The procedure we have elaborated consists in maintaining the same experimental routine as that developed for the production of the condensate until the loading stage of the chip-z trap. At this point the cloud is characterized by a number of atoms $N \sim 20 \times 10^6$ at a temperature of $T \sim 50\,\mu K$, shows a transversal size of $\sim 35\,\mu m$ and is located at a distance from the chip surface of $\sim 200\,\mu m$. Hence, the sample has a good number of atoms, but it is not cold enough, it is too close to the chip and has a too small section[2]. Actually all these parameters can be pushed to the right direction by expanding the trap by means of a reduction of the bias field on the x axis (for the technical detail on the adiabatic deformation of a micro-trap see [54] or [100]). In fig9.4 we report the variation of these parameters as a function of the current feeding the bias x coils. The bias is smoothly reduced in a time period of $1\,s$ in order to ensure adiabatic evolution. Temperature, size and quote of the cloud are determined by means of the imaging on the direction of propagation of the interrogation beams. For the distance from the chip, we take an image of the cloud

[2]as reported in the introduction of chapter 5, the distance from the chip has to be of the order of 3-4 times the waist of the interrogation beam at a *centimeter* from the minimal waist in order to avoid diffraction induced by the surface. More the evaluation of the coherence decay rate induced by the magnetic potential leads to a reasonable upper limit for the temperature of the order of $T \sim 25\,\mu K$

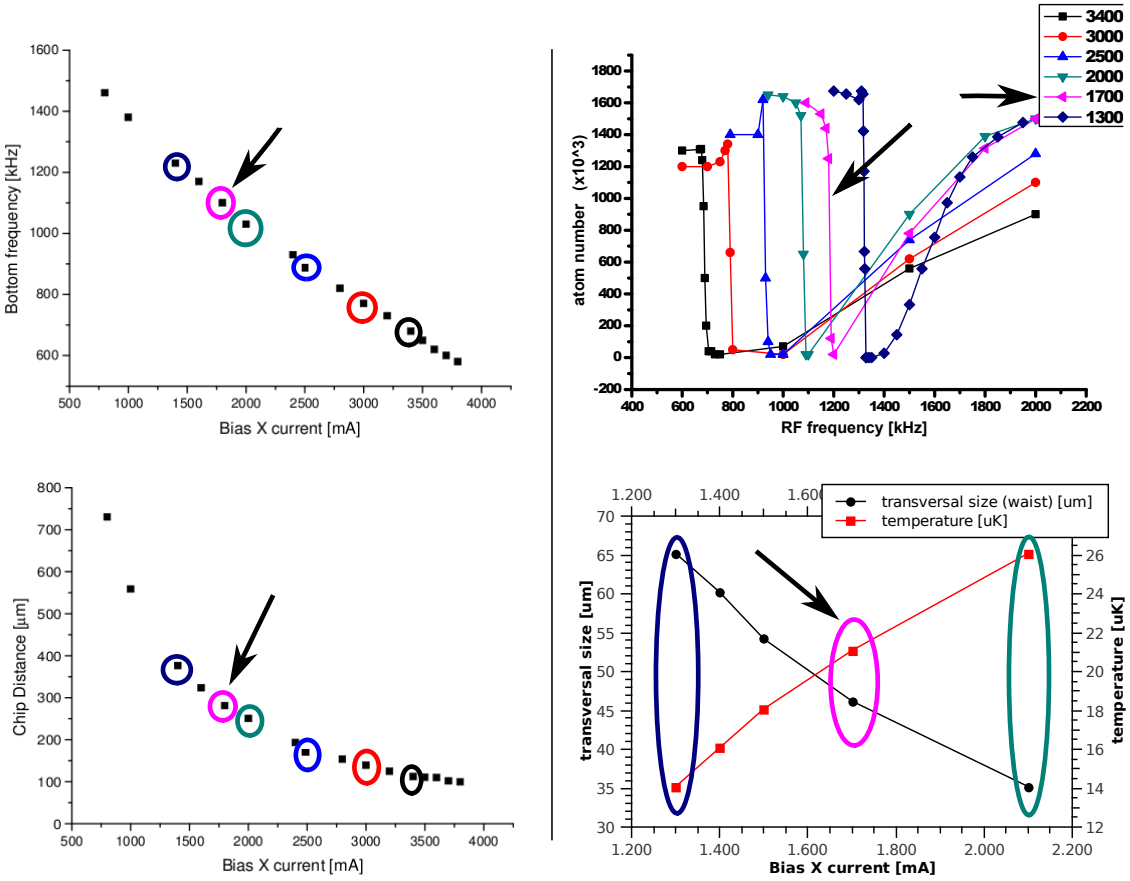


Figure 9.4: Looking for the optimal regime of trapping to maximize the light beam-atomic cloud coupling. Basically all the involved parameters (temperature, transversal section, distance from the chip, bottom frequency) are moved to the direction of interest by lowering the magnetic bias field in the $x$ direction (the bias field responsible for the formation of the trap). Indeed this operation involves both a reduction of the trapping frequencies (which corresponds to a lower temperature and an increased transversal size (bottom-right panel)) and an increase of the distance from the chip (bottom-left panel), which implies also an increase of the bottom frequency (top-left). The graph on the top-right panel shows the number of atoms surviving the application of a $1\,s$ pulse of RF at the fixed frequency reported on the abscissa. The extension of the frequency band in which the RF is able to reduce the number of trapped atoms is related to the temperature of the sample. The colored circles identify the data points referring to the same final state. We chose as regular sample for experiment on *EIT* the configuration marked by pink circles.

when still trapped. For the size, the high optical density along the axis of the cigar-like shape prevents from recovering the information by a direct measurement, so we obtained the reported estimation as a prolongation to the origin of the dynamics of the ballistic expansion of the cloud as function of the free falling time. The graph on the top-right corner of fig9.4 shows the number of atoms surviving the application of a $1\,s$-pulse of RF at the fix frequency reported on the abscissa. The steep edge on the low frequencies side, which characterizes the curves for each value of the bias field, is related to the bottom frequency of the trap, and corresponds to the values reported in the graph in the top-left corner of the figure. The values do not match completely because they depend also on the applied magnetic bias field on the y direction, which is slightly varied day by day to optimize the loading stage. The extension of the frequency band in which the RF is able to reduce the number of trapped atoms is related to the temperature of the sample and it is reduced in the case of a wider expansion of the trap, which corresponds to a lower final temperature.
The chosen configuration for the $EIT$ spectroscopy is noted on the figure by pink cycles and black arrows. It corresponds to: $T \sim 22\,\mu K$, transversal section $\sim 46\,\mu m$, distance from the chip $\sim 250\,\mu m$.

# Chapter 10

# Conclusions

An interface between quantum information carriers (quantum states of light) and quantum information storage and processors (atoms in our case) is an integral part of a full-scale quantum information system. Recent efforts in EU projects have seen diverse systems making key proof-of-principle demonstrations of long storage times, high efficiency, and high fidelities. In the context of quantum communication, the goal for all of these approaches is integration with photonic (flying qubit) systems and their operation in complete quantum repeater architectures and protocols. Putting the accent on miniaturization and compatibility and aiming at a first realistic protocol for a quantum repeater which would allow a direct technological implementation with a tremendous impact on Quantum Communication Technologies. The work reported in this thesis has contributed to the understanding of the mechanisms underlying the storage of pulses of light in atomic media based on electromagnetically induced transparency ($EIT$).

In the first part of the PhD I have collaborated to the characterization of the effects of $EIT$ obtained addressing the $D2$ line in a hot vapor of Cesium. In particular, we have focused the attention on the influence of the inhomogeneous broadening in the case of media showing a multiple excited state structure, as in the case of the $D2$ line of alkali atoms. Significant differences, both in theoretical and experimental results, have been observed with respect to the three-level $\Lambda$ scheme usually considered to describe the interaction. For a Doppler broadened medium, the existence of velocity classes able to destroy the induced transparency has been theoretically

demonstrated. Performing a selective depopulation of these velocity classes in our sample has led to a restoration of the transparency peak, thus verifying the prediction of theoretical model. We have detected an increase of the maximal transmission by a factor 3.5 .
The implementation of the protocol to optimize the memory efficiency based on depopulation of velocity classes has not been implemented in this thesis work due to some technical issues, however the deeper understanding of these processes should allow the optimization of the efficiency of a number of phenomena which are based on electromagnetically induced transparency in complex structures.

In the second part of the PhD I have participated to the construction of an atom chip set-up for the production of degenerate sample of $^{87}Rb$ atoms, which has led to the production of a condensate of $\sim 30 \times 10^3$ atoms.
In the mean time I have worked on the realization of an apparatus for the optical interrogation of the ultracold sample. The system has been designed to produce, starting from a single coherent source, two fields capable of driving Raman transitions between hyperfine ground states plus a third beam usable as a local oscillator. We have verified that the apparatus fulfills the features on pulse shaping, frequency tuning, noise figure, and beam leakage attenuation, required for long lived quantum memories experiments. We have then demonstrated that our sample, with an ad hoc optimized regime of trapping, can provide a high optical depth covering the whole transversal extent of the interrogation field, which is a prerequisite for high efficiency storage. In this configuration, a strong reduction (almost 6 orders of magnitude) in the group velocity of a light pulse has been detected under $EIT$ condition. This result, considered that the exploited $\Lambda$ scheme is not the optimal one, constitutes a promising step towards the realization of high efficient coherent information storage. Exploiting the degenerate sample we have then implemented a multi-state cold-atom interferometer based on RF coupling, fully merged with the atom chip. We demonstrated the narrowing of the interferential fringes induced by the increase of the number of paths and verified the sensitivity of the interferometer to illumination with a far from resonance field. Finally we have developed a method to measure the relative phase of light pulses using atomic interferometry.

# Bibliography


[1] B.P. Anderson and M.A. Kasevich. Macroscopic quantum interference from atomic tunnel arrays. *Science*, 282(5394):1686–1689, 1998.

[2] J. Appel, E. Figueroa, D. Korystov, M. Lobino, and A.I. Lvovsky. Quantum memory for squeezed light. *Physical review letters*, 100(9):93602, 2008.

[3] F.T. Arecchi, E. Courtens, R. Gilmore, and H. Thomas. Atomic Coherent States in Quantum Optics. *PRA*, 6(6):2211–2237, 1972.

[4] E. Arimondo, S. Shepherd, R.R. Moseley, B.D. Sinclair, and M.H. Dunn. Coherent population trapping in laser spectroscopy. *Prog. Opt.*, 35:259–356, 1996.

[5] V. Bagnato, D.E. Pritchard, and D. Kleppner. Bose-Einstein condensation in an external potential. *Physical Review A*, 35:4354–4358, 1987.

[6] M. Bajcsy, A.S. Zibrov, and M.D. Lukin. Stationary pulses of light in an atomic medium. *Nature*, 426(638), 2003.

[7] C.H. Bennett, G. Brassard, et al. Quantum cryptography: Public key distribution and coin tossing. In *Proceedings of IEEE International Conference on Computers, Systems and Signal Processing*, volume 175. Bangalore, India, 1984.

[8] C.H. Bennett and D.P. DiVincenzo. Quantum information and computation. *Nature*, 404(6775):247–255, 2000.

[9] K. Bergmann, H. Theuer, and B.W. Shore. Coherent population transfer among quantum states of atoms and molecules. *Reviews of Modern Physics*, 70(3):1003, 1998.

[10] P. Bicchi, L. Moi, P. Savino, and B. Zambon. Measurement of the diffusion coefficient of oriented Na atoms in different buffer gases. *Il Nuovo Cimento B (1971-1996)*, 55(1):1–14, 1980.

[11] M.S. Bigelow, N.N. Lepeshkin, and R.W. Boyd. Superluminal and slow light propagation in a room-temperature solid. *Science*, 301(5630):200–202, 2003.

[12] E.D. Black. An introduction to Pound–Drever–Hall laser frequency stabilization. *American Journal of Physics*, 69:79, 2001.

[13] H.J. Briegel, W. Dür, J.I. Cirac, and P. Zoller. Quantum repeaters: The role of imperfect local operations in quantum communication. *Physical Review Letters*, 81(26):5932–5935, 1998.

[14] BC Buchler, M. Hosseini, G. Hétet, B.M. Sparkes, and P.K. Lam. Precision spectral manipulation of optical pulses using a coherent photon echo memory. *Optics letters*, 35(7):1091–1093, 2010.

[15] G. Campbell, A. Ordog, and A.I. Lvovsky. Multimode electromagnetically induced transparency on a single atomic line. *New Journal of Physics*, 11:103021, 2009.

[16] S. Chakrabarti, A. Pradhan, B. Ray, and P.N. Ghosh. Velocity selective optical pumping effects and electromagnetically induced transparency for D2 transitions in rubidium. *Journal of Physics B: Atomic, Molecular and Optical Physics*, 38:4321, 2005.

[17] T. Chaneliere, D.N. Matsukevich, S.D. Jenkins, S.Y. Lan, T.A.B. Kennedy, and A. Kuzmich. Storage and retrieval of single photons transmitted between remote quantum memories. *Nature*, 438(7069):833–836, 2005.

[18] K.S. Choi, H. Deng, J. Laurat, and H.J. Kimble. Mapping photonic entanglement into and out of a quantum memory. *Nature*, 452(7183):67–71, 2008.

[19] C. Cohen-Tannoudji, J. Dupont-Roc, and G. Grynberg. Processus d'interaction entre photons et atoms. *EDP Sciences*, 1996.

[20] J. Cviklinski. *Interface quantique atomes-champs en régime de variables continues*. PhD thesis, Université Paris VI, 2008.

[21] J. Cviklinski, J. Ortalo, J. Laurat, A. Bramati, M. Pinard, and E. Giacobino. Reversible quantum interface for tunable single-sideband modulation. *Physical review letters*, 101(13):133601, 2008.

[22] J. Dalibard and C. Cohen-Tannoudji. Dressed-atom approach to atomic motion in laser light: the dipole force revisited. *JOSA B*, 2(11):1707–1720, 1985.

[23] A. Dantan. *Génération, stockage et manipulation détats non classiques pour des ensembles atomiques et des champs électromagnétiques*. PhD thesis, Université Paris VI, 2012.

[24] A. Dantan and M. Pinard. Quantum-state transfer between fields and atoms in electromagnetically induced transparency. *Physical Review A*, 69(4):043810, 2004.

[25] L. Deng, M.G. Payne, and E.W. Hagley. Propagation of light pulse in an ultra-cold atomic vapor: mechanism for the loss of the probe field. *Optics communications*, 198(1-3):129–133, 2001.

[26] D. Deutsch. Quantum theory, the Church-Turing principle and the universal quantum computer. *Proceedings of the Royal Society of London. A. Mathematical and Physical Sciences*, 400(1818):97–117, 1985.

[27] R.W.P. Drever, J.L. Hall, F.V. Kowalski, J. Hough, GM Ford, A.J. Munley, and H. Ward. Laser phase and frequency stabilization using an optical resonator. *Applied Physics B: Lasers and Optics*, 31(2):97–105, 1983.

[28] M.D. Eisaman, A. André, F. Massou, M. Fleischhauer, A.S. Zibrov, and M.D. Lukin. Electromagnetically induced transparency with tunable single-photon pulses. *Nature*, 438(7069):837–841, 2005.

[29] L. Fallani. *Bose-Einstein Condensate in Optical Lattices*. PhD thesis, Lens-Università degli Studi di Firenze, 2005.

[30] M. Fattori, G. Roati, B. Deissler, C. DErrico, M. Zaccanti, M. Jona-Lasinio, L. Santos, M. Inguscio, and G. Modugno. Magnetic Dipolar Interaction in a Bose-Einstein Condensate Atomic Interferometer. *Physical review letters*, 101(19):190405, 2008.

[31] E. Figueroa, M. Lobino, D. Korystov, J. Appel, and A.I. Lvovsky. Propagation of squeezed vacuum under electromagnetically induced transparency. *New Journal of Physics*, 11:013044, 2009.

[32] M. Fleischhauer, A. Imamoglu, and J.P. Marangos. Electromagnetically induced transparency: Optics in coherent media. *Reviews of Modern Physics*, 77(2):633, 2005.

[33] M. Fleischhauer and M.D. Lukin. Dark-state polaritons in electromagnetically induced transparency. *Physical review letters*, 84(22):5094–5097, 2000.

[34] M. Fleischhauer and M.D. Lukin. Quantum memory for photons: Dark-state polaritons. *Physical Review A*, 65(2):022314, 2002.

[35] R. Folman, P. Krüger, D. Cassettari, B. Hessmo, T. Maier, and J. Schmiedmayer. Controlling cold atoms using nanofabricated surfaces: atom chips. *Physical review letters*, 84(20):4749–4752, 2000.

[36] K. Fujii. Dynamics of an n level system of atoms interacting with laser fields. *Journal of Mathematical Sciences*, 153(2):57–69, 2008.

[37] D.J. Fulton, S. Shepherd, R.R. Moseley, B.D. Sinclair, and M.H. Dunn. Continuous-wave electromagnetically induced transparency: A comparison of V, $\Lambda$, and cascade systems. *Physical Review A*, 52(3):2302, 1995.

[38] N.S. Ginsberg, S.R. Garner, and L.V. Hau. Coherent control of optical information with matter wave dynamics. *Nature*, 445(7128):623–626, 2007.

[39] V. Giovannetti, S. Lloyd, and L. Maccone. Quantum-enhanced measurements: beating the standard quantum limit. *Science*, 306(5700):1330–1336, 2004.

[40] R.J. Glauber. Coherent and incoherent states of the radiation field. *Physical Review*, 131(6):2766–2788, 1963.

[41] A.V. Gorshkov, A. André, M. Fleischhauer, A.S. Sørensen, and M.D. Lukin. Universal approach to optimal photon storage in atomic media. *Physical review letters*, 98(12):123601, 2007.

[42] A.V. Gorshkov, A. André, M.D. Lukin, and A.S. Sørensen. Photon storage in Λ-type optically dense atomic media. II. Free-space model. *Physical Review A*, 76(3):033805, 2007.

[43] H.R. Gray, C.R. Stroud, et al. Autler-Townes effect in double optical resonance. *Optics Communications*, 25(3):359–362, 1978.

[44] R. Grimm, M. Weidemüller, and Y.B. Ovchinnikov. Optical dipole traps for neutral atoms. *Advances in atomic, molecular, and optical physics*, 42:95–170, 2000.

[45] C. Gross, T. Zibold, E. Nicklas, J. Esteve, and M.K. Oberthaler. Nonlinear atom interferometer surpasses classical precision limit. *Nature*, 464(7292):1165–1169, 2010.

[46] K. Hammerer, A.S. Sørensen, and E.S. Polzik. Quantum interface between light and atomic ensembles. *Reviews of Modern Physics*, 82(2):1041, 2010.

[47] D.M. Harber, H.J. Lewandowski, J.M. McGuirk, and E.A. Cornell. Effect of cold collisions on spin coherence and resonance shifts in a magnetically trapped ultracold gas.

[48] S.E. Harris. Electromagnetically induced transparency. *Physics Today*, 50:36, 1997.

[49] S.E. Harris, J.E. Field, and A. Imamoglu. Nonlinear optical processes using electromagnetically induced transparency. *Physical review letters*, 64(10):1107–1110, 1990.

[50] L.V. Hau, S.E. Harris, Z. Dutton, and C.H. Behroozi. Light speed reduction to 17 metres per second in an ultracold atomic gas. *Nature*, 397(6720):594–598, 1999.

[51] M.P. Hedges, J.J. Longdell, Y. Li, and M.J. Sellars. Efficient quantum memory for light. *Nature*, 465(7301):1052–1056, 2010.

[52] G. Heinze, A. Rudolf, F. Beil, and T. Halfmann. Storage of images in atomic coherences in a rare-earth-ion-doped solid. *Physical Review A*, 81(1):011401, 2010.

[53] C. Henkel, P. Krüger, R. Folman, and J. Schmiedmayer. Fundamental limits for coherent manipulation on atom chips. *Applied Physics B: Lasers and Optics*, 76(2):173–182, 2003.

[54] I. Herrera. *Bec in microtraps*. PhD thesis, Univesidad de Madrid-Università degli Studi di Firenze, 2012.

[55] G. Hétet, A. Peng, M.T. Johnsson, J.J. Hope, and P.K. Lam. Characterization of electromagnetically-induced-transparency-based continuous-variable quantum memories. *Physical Review A*, 77(1):012323, 2008.

[56] H. Hinderthür, F. Ruschewitz, H.J. Lohe, S. Lechte, K. Sengstock, and W. Ertmer. Time-domain high-finesse atom interferometry. *Physical Review A*, 59(3):2216, 1999.

[57] K. Honda, D. Akamatsu, M. Arikawa, Y. Yokoi, K. Akiba, S. Nagatsuka, T. Tanimura, A. Furusawa, and M. Kozuma. Storage and retrieval of a squeezed vacuum. *Physical review letters*, 100(9):93601, 2008.

[58] S.A. Hopkins, E. Usadi, H.X. Chen, and A.V. Durrant. Electromagnetically induced transparency of laser-cooled rubidium atoms in three-level [Lambda]-type systems. *Optics communications*, 138(1-3):185–192, 1997.

[59] M. Hosseini, G. Campbell, B.M. Sparkes, P.K. Lam, and BC Buchler. Unconditional room-temperature quantum memory. *Nature Physics*, 7(10):795–799, 2011.

[60] M. Hosseini, B.M. Sparkes, G. Campbell, P.K. Lam, and BC Buchler. High efficiency coherent optical memory with warm rubidium vapour. *Nature communications*, 2:174, 2011.

[61] M. Hosseini, B.M. Sparkes, G. Hétet, J.J. Longdell, P.K. Lam, and B.C. Buchler. Coherent optical pulse sequencer for quantum applications. *Nature*, 461(7261):241–245, 2009.

[62] A. Javan, O. Kocharovskaya, H. Lee, and M.O. Scully. Narrowing of electromagnetically induced transparency resonance in a Doppler-broadened medium. *Physical Review A*, 66(1):013805, 2002.

[63] B. Julsgaard, J. Sherson, J.L. Sorensen, and E.S. Polzik. Characterizing the spin state of an atomic ensemble using the magneto-optical resonance method. *Journal of Optics B: Quantum and Semicalssical Optics*, 6:5–14, 2004.

[64] M. Kasevich and S. Chu. Atomic interferometry using stimulated Raman transitions. *Physical review letters*, 67(2):181–184, 1991.

[65] W. Ketterle, D.S. Durfree, and D.M. Stamper-Kurn. Making, probing and understanding Bose-Einstein condensates, Contribution to the proceedings of the 1998 Enrico Fermi summer school on Bose-Einstein condensation in Varenna, Italy, 1998.

[66] M. Kozuma, D. Akamatsu, L. Deng, E.W. Hagley, and M.G. Payne. Steep optical-wave group-velocity reduction and "storage of light without on-resonance electromagnetically induced transparency. *Physical Review A*, 66(3):031801, 2002.

[67] M. Kozuma, L. Deng, E.W. Hagley, J. Wen, R. Lutwak, K. Helmerson, SL Rolston, and W.D. Phillips. Coherent splitting of Bose-Einstein condensed atoms with optically induced Bragg diffraction. *Physical review letters*, 82(5):871–875, 1999.

[68] M. Kubasik, M. Koschorreck, M. Napolitano, S.R. De Echaniz, H. Crepaz, J. Eschner, E.S. Polzik, and M.W. Mitchell. Polarization-based light-atom quantum interface with an all-optical trap. *Physical Review A*, 79(4):043815, 2009.

[69] N.A. Kurnit, I.D. Abella, and S.R. Hartmann. Observation of a photon echo. *Physical Review Letters*, 13(19):567–568, 1964.

[70] B. Lauritzen, J. Minář, H. De Riedmatten, M. Afzelius, N. Sangouard, C. Simon, and N. Gisin. Telecommunication-wavelength solid-state memory at the single photon level. *Physical review letters*, 104(8):80502, 2010.

[71] A. Lezama, A.M. Akulshin, A.I. Sidorov, and P. Hannaford. Storage and retrieval of light pulses in atomic media with "slow and "fast light. *Physical Review A*, 73(3):033806, 2006.

[72] C. Liu, Z. Dutton, C.H. Behroozi, and L.V. Hau. Observation of coherent optical information storage in an atomic medium using halted light pulses. *Nature*, 409(6819):490–493, 2001.

[73] J.J. Longdell, E. Fraval, M.J. Sellars, and N.B. Manson. Stopped light with storage times greater than one second using electromagnetically induced transparency in a solid. *Physical review letters*, 95(6):63601, 2005.

[74] R. Loudon. *The quantum theory of light*. Oxford University Press, 2nd edition, 1983.

[75] M.D. Lukin. Colloquium: Trapping and manipulating photon states in atomic ensembles. *Reviews of Modern Physics*, 75(2):457–472, 2003.

[76] A. MacRae, G. Campbell, and A.I. Lvovsky. Matched slow pulses using double electromagnetically induced transparency. *Optics letters*, 33(22):2659–2661, 2008.

[77] A. Mair, J. Hager, D.F. Phillips, R.L. Walsworth, and M.D. Lukin. Phase coherence and control of stored photonic information. *Physical Review A*, 65(3):031802, 2002.

[78] L. Mandel and E. Wolf. *Optical Coherence and Quantum Optics*. Cambridge University Press, reprinted with corrections edition, 2008.

[79] A.B. Matsko, Y.V. Rostovtsev, O. Kocharovskaya, A.S. Zibrov, and M.O. Scully. Nonadiabatic approach to quantum optical information storage. *Physical Review A*, 64(4):043809, 2001.

[80] A. Messiah. *Quantum mechanics*. Dover Publications, 1999.

[81] R. Miller, T.E. Northup, K.M. Birnbaum, A. Boca, A.D. Boozer, and H.J. Kimble. Trapped atoms in cavity QED: coupling quantized light and matter. *Journal of Physics B: Atomic, Molecular and Optical Physics*, 38:S551, 2005.

[82] F. Minardi, C. Fort, P. Maddaloni, M. Modugno, and M. Inguscio. Time-domain atom interferometry across the threshold for Bose-Einstein condensation. *Physical Review Letters*, 87(17):170401, 2001.

[83] O.S. Mishina, M. Scherman, P. Lombardi, J. Ortalo, D. Felinto, A.S. Sheremet, A. Bramati, D.V. Kupriyanov, J. Laurat, and E. Giacobino. Electromagnetically induced transparency in an inhomogeneously broadened $\Lambda$ transition with multiple excited levels. *Physical Review A*, 83(5):053809, 2011.

[84] C. Monroe, H. Robinson, and C.E. Wieman. Observation of the cesium clock transition using laser-cooled atoms in a vapor cell. *Optics letters*, 16(1):50–52, 1991.

[85] D. Moretti, D. Felinto, and J.W.R. Tabosa. Collapses and revivals of stored orbital angular momentum of light in a cold atomic ensemble. *Arxiv preprint arXiv:0901.0939*, 2009.

[86] M. Nilsson and S. Kröll. Solid state quantum memory using complete absorption and re-emission of photons by tailored and externally controlled inhomogeneous absorption profiles. *Optics communications*, 247(4):393–403, 2005.

[87] M. Notcutt, L.S. Ma, J. Ye, and J.L. Hall. Simple and compact 1-Hz laser system via an improved mounting configuration of a reference cavity. *Optics letters*, 30(14):1815–1817, 2005.

[88] I. Novikova, N.B. Phillips, and A.V. Gorshkov. Optimal light storage with full pulse shape control. *Arxiv preprint arXiv:0805.1927*, 2008.

[89] I. Novikova, Y. Xiao, D.F. Phillips, and R.L. Walsworth. EIT and diffusion of atomic coherence. *Journal of Modern Optics*, 52(16):2381–2390, 2005.

[90] J. Oreg, F.T. Hioe, and J.H. Eberly. Adiabatic following in multilevel systems. *Physical Review A*, 29(2):690, 1984.

[91] J. Ortalo. *Transparence induite électromagnetiquement et mémoire quantique dans une vapeur de césium.* PhD thesis, Université Paris VI, 2009.

[92] J. Ortalo, J. Cviklinski, P. Lombardi, J. Laurat, A. Bramati, M. Pinard, and E. Giacobino. Atomic-ensemble-based quantum memory for sideband modulations. *Journal of Physics B: Atomic, Molecular and Optical Physics*, 42:114010, 2009.

[93] H. Ott, J. Fortagh, G. Schlotterbeck, A. Grossmann, and C. Zimmermann. Bose-Einstein condensation in a surface microtrap. *Physical review letters*, 87(23):230401, 2001.

[94] Y.B. Ovchinnikov, J.H. Müller, M.R. Doery, E.J.D. Vredenbregt, K. Helmerson, SL Rolston, and W.D. Phillips. Diffraction of a released Bose-Einstein condensate by a pulsed standing light wave. *Physical review letters*, 83(2):284–287, 1999.

[95] A. Peters, K.Y. Chung, and S. Chu. Measurement of gravitational acceleration by dropping atoms. *Nature*, 400(6747):849–852, 1999.

[96] J. Petrovic1, I. Herrera, P. Lombardi, F. Schaefer, and F.S. Cataliotti. A Multi-State Interferometer on an Atom Chip. *(submitted).*

[97] D.F. Phillips, M. Fleischhauer, A. Mair, R.L. Walsworth, and M.D. Lukin. Storage of light in atomic vapor. *Physical Review Letters*, 86(5):783–786, 2001.

[98] N.B. Phillips, A.V. Gorshkov, and I. Novikova. Optimal light storage in atomic vapor. *Physical Review A*, 78(2):023801, 2008.

[99] J. Reichel. Microchip traps and Bose–Einstein condensation. *Applied Physics B: Lasers and Optics*, 74(6):469–487, 2002.

[100] J. Reichel, W. Hänsel, and T.W. Hänsch. Atomic micromanipulation with magnetic surface traps. *Physical review letters*, 83(17):3398–3401, 1999.

[101] J. Reichel and V. Vuletić. *Atom Chips.* Wiley-VCH, 2010.

[102] K.F. Reim, P. Michelberger, K.C. Lee, J. Nunn, N.K. Langford, and I.A. Walmsley. Single-photon-level quantum memory at room temperature. *Physical Review Letters*, 107(5):53603, 2011.

[103] M. Scherman. *Transparence induite électromagnetiquement et mémoire quantique sur la raie D2 du césium.* PhD thesis, Université Paris VI, 2012.

[104] M. Scherman, O.S. Mishina, P. Lombardi, E. Giacobino, and J. Laurat. Enhancing electromagnetically-induced transparency in a multilevel broadened medium. *Opt. Express*, 20(4):4346–4351, Feb 2012.

[105] M.O. Scully and M.S. Zubairy. *Quantum Optics*. Cambridge University Press, Cambridge, 1997.

[106] D.W. Sesko and C.E. Wieman. Observation of the cesium clock transition in laser-cooled atoms. *Optics letters*, 14(5):269–271, 1989.

[107] M.S. Shahriar, P.R. Hemmer, et al. Direct excitation of microwave-spin dressed states using a laser-excited resonance Raman interaction. *Physical review letters*, 65(15):1865–1868, 1990.

[108] K. Shinohara, T. Aoki, and A. Morinaga. Atomic Multiple-Beam Interferometer Phase-Shifted by the Multiple Magnetic Pulse Fields. In *Proceedings of the 7th International Symposium on Foundations of Quantum Mechanics in the Light of New Technology: ISQM–Tokyo'01: Advanced Research Laboratory, Hitachi, Ltd., Hatoyama, Saitama, Japan, 27-30 August 2001*, page 148. World Scientific Pub Co Inc, 2002.

[109] I.R. Sola, V.S. Malinovsky, B.Y. Chang, J. Santamaria, and K. Bergmann. Coherent population transfer in three-level A systems by chirped laser pulses: Minimization of the intermediate-level population. *PHYSICAL REVIEW-SERIES A-*, 59:4494–4501, 1999.

[110] M. Stähler, R. Wynands, S. Knappe, J. Kitching, L. Hollberg, A.V. Taichenachev, and V.I. Yudin. Coherent population trapping resonances in thermal $^{85}Rb$ vapor: $D\_1$ versus $D\_2$ line excitation. *Optics letters*, 27(16):1472–1474, 2002.

[111] D.A. Steck. Cesium D Line Data. *http://steck.us/alkalidata*, 2009.

[112] D.A. Steck. Rubidium 87 D Line Data. *http://steck.us/alkalidata*, 2009.

[113] S. Swain. Master equation derivation of quantum regression theorem. *Journal of Physics A: Mathematical and General*, 14:2577, 1981.

[114] J.R. Taylor. *An introduction to error analysis: the study of uncertainties in physical measurements*. Univ Science Books, 1997.

[115] P. Treutlein, P. Hommelhoff, T. Steinmetz, T.W. Hänsch, and J. Reichel. Coherence in microchip traps. *Physical review letters*, 92(20):203005, 2004.

[116] P.K. Vudyasetu, R.M. Camacho, and J.C. Howell. Storage and retrieval of multimode transverse images in hot atomic rubidium vapor. *Physical review letters*, 100(12):123903, 2008.

[117] G. Weihs, M. Reck, H. Weinfurter, and A. Zeilinger. All-fiber three-path MachZehnder interferometer. *Optics letters*, 21(4):302–304, 1996.

[118] M. Weitz, T. Heupel, TW Hänsch, et al. Multiple beam atomic interferometer. *Physical review letters*, 77(12):2356–2359, 1996.

[119] H. Xia, A.J. Merriam, S.J. Sharpe, G.Y. Yin, and S.E. Harris. Electromagnetically induced transparency with spectator momenta. *Physical Review A*, 59(5):3190–3193, 1999.

[120] H. Xia, S.J. Sharpe, A.J. Merriam, and S.E. Harris. Electromagnetically induced transparency in atoms with hyperfine structure. *Physical Review A*, 56(5):3362–3365, 1997.

[121] A. Yariv. *Introduction to Optical Electronics*. Holt, Rinehart and Winston, Inc., New York, NY, 2nd edition, 1976.

[122] C.Y. Ye and A.S. Zibrov. Width of the electromagnetically induced transparency resonance in atomic vapor. *Physical review. A*, 65(2):023806–1, 2002.

[123] B. Zhao, Y.A. Chen, X.H. Bao, T. Strassel, C.S. Chuu, X.M. Jin, J. Schmiedmayer, Z.S. Yuan, S. Chen, and J.W. Pan. A millisecond quantum memory for scalable quantum networks. *Nature physics*, 5(2):95–99, 2008.

[124] R. Zhao, Y.O. Dudin, S.D. Jenkins, C.J. Campbell, D.N. Matsukevich, T.A.B. Kennedy, and A. Kuzmich. Long-lived quantum memory. *Nature Physics*, 5(2):100–104, 2008.

[125] A.S. Zibrov, A.B. Matsko, O. Kocharovskaya, Y.V. Rostovtsev, G.R. Welch, and M.O. Scully. Transporting and time reversing light via atomic coherence. *Physical review letters*, 88(10):103601, 2002.